OUKA
The University of Osaka
Institutional Knowledge Archive

Title	Studies on Physical Properties of Metal Hydrides and Hydrogen Behavior in Zr Alloys
Author(s)	Ito, Masato
Citation	大阪大学, 2008, 博士論文
Version Type	VoR
URL	https://hdl.handle.net/11094/2407
rights	
Note	

The University of Osaka Institutional Knowledge Archive : OUKA

https://ir.library.osaka-u.ac.jp/

The University of Osaka

工学12677

Doctoral Dissertation

Studies on Physical Properties of Metal Hydrides and Hydrogen Behavior in Zr Alloys

2008

Masato Ito

Division of Sustanable Energy and Environmental Engineering
Graduate School of Engineering
Osaka University

Doctoral Dissertation

Studies on Physical Properties of Metal Hydrides and Hydrogen Behavior in Zr Alloys

(金属水素化物の物性ならびに Zr 合金中水素挙動に関する研究)

2008

Masato Ito

Division of Sustanable Energy and Environmental Engineering
Graduate School of Engineering
Osaka University

Abstract

Basic bulk properties of metal – hydrogen system and hydrogen behavior in zirconium alloys were studied in order to contribute to the technological developments of integrity assessments and maintenances of structural materials in the existing and next-generation nuclear power systems.

Flaw-free bulk hydrides of yttrium, hafnium, niobium, and Zr-Gd alloy were successfully produced and their mechanical, electrical, and thermal properties were evaluated. The yttrium and niobium hydrides had higher elastic moduli and Vickers hardness than the respective pure metals, whereas the mechanical properties of the hafnium hydride were lower than those of the pure hafnium. Additionally, the mechanical properties of the yttrium and niobium hydrides increased with increasing hydrogen content, on the contrary those of the hafnium hydride decreased with increasing hydrogen content. The thermal conductivity of yttrium hydride was significantly higher than that of pure yttrium although the hydrides of hafnium and niobium had almost same or less thermal conductivities than the respective pure metals. The thermal conductivity of hydride of Zr-Gd alloy, which was polyphasic material, was higher than that of the zirconium hydride. It was found from the preset study and literatures that although yttrium, titanium, zirconium, and hafnium were adjacent in the periodic table and their hydrides exhibited the same crystal structures, they possessed polymorphic physical properties. It was considered that these results were mutually comparable and they revealed the characteristic nature of metal hydrides since their crystal structure was same. The several important correlations between the basic bulk properties of metal hydrides were found from the present and previous studies.

The electronic structures of the yttrium, titanium, zirconium, hafnium, and niobium hydrogen solid solutions and hydrides were evaluated by ab initio calculations in order to discuss the effects of hydrogen on the characteristics of the metals. The elastic moduli of the yttrium hydrogen solid solution could be evaluated from the ab initio study and the calculated results were good accordance with the present experimental results. From the analysis of the bond order in unit-cell, it was considered that the change of mechanical properties due to hydrogen was correlated to the original covalency of the metals. The calculated bond order of the metal hydrides also qualitatively explained the trends of the hydrogen content dependence of the mechanical properties of the hydrides. The elastic moduli from the total energy calculation were well accordance with the experimental data. The temperature dependence of liner thermal expansion coefficient was evaluated and the results provided better understanding of the

properties of the metal hydrides.

The terminal solid solubility of hydrogen (TSS) of Zr-Nb binary alloys with different niobium concentrations and Nb added Zircaloy-4 was measured, and the effect of niobium addition was evaluated in order to supply fundamental data for the integrity of new-type fuel cladding. It was found that the TSS of αZr was not affected by the solute niobium and that the β Zr precipitant led to increase the TSS in the Zr-Nb alloys. The change in TSS by niobium addition was slightly larger than that by the traditional additive elements. The TSS of Nb added Zircaloy-4 was found to be higher than that of Zircaloy-2 and -4 due to the further effect of β Zr precipitation on top of the traditional additive element effects. The mechanical properties of hydrogenated Zr-Nb binary alloys with different phases were evaluated in order to discuss the effect of hydrogen absorption. The solute hydrogen didn't affect the mechanical properties of the single phase β Zr-20Nb alloy. In the Zr-1.0Nb and Zr-2.5Nb alloys, the solute hydrogen reduced the Young's modulus of the alloys, which was considered to be due to the change in the modulus of αZr matrix phase.

The transient hydrogen diffusion analysis, including the three effects of hydrogen concentration, temperature, and stress, was performed using the finite element method. The effects of several parameters, such as internal pressure, crack number, and its depth, were evaluated. The hydrogen distribution after the internal pressure loading was noticeably different from the initial state and a large amount of hydrogen piled up near the crack tip. The hydrogen diffused into the vicinity of the crack tip and the amount of piled up hydrogen increased with increasing the internal pressure. With increasing the crack length, the more amount of hydrogen piled up around the crack tip and the hydrogen-focusing area significantly spread. The crack number didn't affect the hydrogen behavior near the crack tip. All the results were corresponding to the distribution of the hydrostatic pressure because the contribution of the stress gradient to hydrogen diffusion near the crack tip was larger than the other contributions. It was found that hydrogen increasing rate per unit time increased with growing the crack length and increasing the internal pressure. It was also found that the changing rate from the initial state reached over 10 % for a given short time from the several seconds to several thousands of seconds.

Contents

CHAPTER 1

General Introduction 1

1-1. Background 2

1-2. Metal Hydrides as New Component Materials in Nuclear Field 2

1-3. Hydrogen Embrittlement of High Burn-up Fuel Cladding of Light Water Reactors 3

1-4. Objectives 4

References 5

CHAPTER 2

Basic Bulk Properties of Metal-Hydrogen Systems 9

2-1. Introduction 10

2-1-1. Background 10

2-1-2. Objective 16

2-2. Experimental Procedure 16

2-2-1. Sample Preparation 16

2-2-2. Sample Characterization 19

2-2-3. Measurement Methods 20

2-3. Results and Discussion 23

2-3-1. Y-H System 23

2-3-2. Hf-H System 45

2-3-3. Nb-H System 58

2-3-4. Hydrides of Gd-Zr Alloy 78

2-3-5. Correlations between Several Properties of Metal Hydrides 87

2-4. Summary 93

References 94

CHAPTER 3

Ab initio Study of Metal-Hydrogen Systems 101

3-1. Introduction 102

3-2. Calculation 103

3-2-1. Calculation Codes 103

3-2-2. Elastic Constants 103

3-2-3. Thermal Expansion 105

3-2-4. Calculation Conditions 107

3-3. Results and Discussion 108

3-3-1. Mechanical Properties of Transition Metal Hydrogen Solid Solutions 108

3-3-2. Thermophysical Properties of Transition Metal Hydrides 121

3-4. Summary 141

References 142

CHAPTER 4

Characteristics of Zr-Nb Alloys with Precipitated Hydride and/or Solute Hydrogen 147

4-1. Introduction 147

4-2. Experimental Procedure 152

4-2-1. Sample Preparation 152

4-2-2. Measurement Method 154

4-3. Results and Discussion 156

4-3-1. Terminal Solid Solubility of hydrogen of Zr-Nb Alloys 156

4-3-2. Mechanical Properties of Hydrogenated Zr-Nb Alloys 164

4-4. Summary 173

References 173

CHAPTER 5

Finite Element Analysis of Hydrogen Behavior in LWR Cladding under Gradients of Hydrogen, Temperature, and Stress 177

5-1. Introduction 178

5-2. Calculation 181

5-2-1. Finite Element Models 181
5-2-2. Theory of Hydrogen Diffusion Analysis 185
5-2-3. Analysis Procedure 186
5-3. Results and Discussion 187
5-3-1. Stress and Strain Distribution of Fuel Cladding with Crack 187
5-3-2. Hydrogen Diffusion Behavior under Gradients of Hydrogen, Temperature, and Stress 194
5-4. Summary 207
References 207

CHAPTER 6
Concluding Remarks 211

Acknowlegement 215

Research Activity 216

CHAPTER 1

General Introduction

Chapter 1
General Introduction

1-1. Background

The current electric power generations around the world heavily relies on the burning of fossil fuels, such as oil, gas, and coal. The production of energy by burning the fossil fuels generates pollutants and carbon dioxide. The possibility of global climate change resulting from an increase in the greenhouse gas concentration in the atmosphere is a major global concern. It is considered that reduction of future greenhouse gas emissions largely depends on the progress of generation technologies based on nuclear power and renewable energy sources. The nuclear power generation has such advantages as scarce carbon dioxide emitting, stable power supply, and economical efficiency. Therefore, the nuclear energy has significant potential for solving the energy and environmental problem without losing sustainable development of human societies. On the contrary, there are concerns in the nuclear power system; a concern about production and accumulation of long-lived radioactive waste is one of the most important problems that should be resolved by technical development. From the view point of reducing the burden by disposal of the high level radioactive waste, advanced nuclear power systems including fast reactor are expected [1–4], in which plutonium would be effectively utilized and long-lived minor actinides would change into stable nuclide or short-half-life radionuclide by nuclear transmutation. In addition, burnup extension of light water reactor (LWR) fuels that is now under way for the sake of cost reduction also contributes to reduce radioactive waste generation. However, there are many technical requirements in order to pursue such sophistications of nuclear power systems. Establishing techniques for integrity assessment and maintenance of nuclear materials is one of the most essential points. The present study is intended to contribute to the establishment by means of elucidating basic bulk properties of metal-hydrogen systems and hydrogen behavior in nuclear materials. Importance of these elucidations is described in following sections.

1-2. Metal Hydrides as New Component Materials in Nuclear Field

Metal hydrides have either equaling or surpassing hydrogen atom density per unit of volume as water or liquid hydrogen [5]. Since mass of hydrogen almost equals to that of neutron, parts of kinetic energy of fast neutron can efficiently transfer to hydrogen by

elastic collisions. Therefore, the metal hydrides can be superior moderator of neutron. Hydride fuels have long been expected [6–14] and a project "Assess the feasibility of improving the performance of PWR and BWR by using hydride fuel instead of oxide fuel" is working mainly by groups in University of California since 2002. In addition, new concepts of the nuclear fast reactor core using the metal hydrides as neutron absorber were recently suggested [15–17]. Although the gadolinium containing LWR fuel is used as neutron absorber that is so-called burnable poison in order to extend the burnup of the fuels in safety, there is previously no concept of neutron absorber for the fast reactors. The new concept is as follows: hydrogen atoms in the metal hydrides moderate the fast neutron and then moderated thermal neutron can be efficiently absorbed by the metals such as the gadolinium and hafnium. Therefore, gadolinium containing zirconium hydride and hafnium hydride are candidates for neutron absorber and control rod in the fast reactor. Furthermore, the zirconium and yttrium hydride are widely expected as the neutron moderator and reflector in nuclear reactors [18–23] because of their low induced activity, small neutron absorption cross-section, low hydrogen desorption pressure, high hydrogen density, phase stability, and low cost. Therefore, it is necessary to evaluate several properties such as mechanical and thermal properties of the metal hydrides. The basic bulk properties of metal-hydrogen alloys have been extensively studied [24–25]. However, there is inadequate information on such data of the single-phase metal hydrides. It is because the pure bulk metal hydrides without any defects are hard to be procured. Recently, technique for production of flaw-free bulk metal hydrides with wide-ranging hydrogen contents was established by Yamanaka and Setoyama et al. [26–32]. This is great step towards practical application of the metal hydrides and one can elucidate the properties of pure metal hydrides with unprecedented detail.

1-3. Hydrogen Embrittlement of High Burn-up Fuel Cladding of Light Water Reactors

The extension of burn-up of LWR fuels has proceeded in order to reduce the spent fuel and to increase efficiency of the power generation. The high burn-up have been achieved, 55GWd/t in PWR since 2004, and 45GWd/t in BWR since 1999, and higher burn up will be accomplished in future. The further burnup extension place stricter demands on performance of the nuclear materials, although the components used in current reactors are extremely reliable and has a very low failure rate. Therefore, it is important to continue the enhancement of the reliability of nuclear materials.

Zirconium alloys are extensively used in various types of nuclear reactors for different applications, examples being fuel cladding tubes of LWRs, grids, channels in Boiling Water Reactors (BWRs) as well as pressure and calandria tubes in Pressurized Heavy Water Reactors (PHWRs). This is because that the zirconium has low neutron absorption cross-section, superior corrosion resistance, and good mechanical properties [33–37]. Since the zirconium based alloys have been used for the fuel claddings of the LWRs in 1950's, small amounts of additive elements such as tin, iron, chromium, nickel, and niobium have been alloyed with the zirconium in order to improve the corrosion resistance [38–42]. The production process such as rolling and heat treatment of the zirconium alloys has been optimized for their performance including the mechanical properties and corrosion resistance [43–52]. On the contrary, it is well known that the zirconium alloys absorb a part of evolved hydrogen during operation by the corrosion reaction between zirconium alloy and cooling water as follows:

$$Zr + 2H_2O \rightarrow ZrO_2 + 4H \qquad (1\text{-}1)$$

If the total hydrogen concentration in the alloy exceeds the solubility limit, brittle zirconium hydrides are formed as precipitates in the alloy, which markedly deteriorates the material strength. In recent years, new alloys with high corrosion resistance have been proposed, however, the hydrogen absorption properties are not significantly improved in the alloys. Therefore, the influence of zirconium hydride on the integrity of fuel cladding is observed with keen interest because of longer extended burnup of nuclear fuel. For example, there were some accidents such as outside-in crack of fuel cladding at power ramp test [53], hydride-assisted pellet-cladding mechanical interaction at reactivity initiated accident (RIA) [54] and delayed hydride clacking (DHC) at CANDU reactor [55]. Although corrosion and hydrogen absorption behaviors of the LWR cladding simulating practical uses have been extensively studied [38–52, 56–61], systematic information on the effect of hydrogen on the fundamental properties for the zirconium alloys were not sufficient. For this reason, it is hard to assess the embrittlement behavior due to hydrogen of the high burnup fuel claddings in accurate detail.

1-4. Objectives

From such point of view, the properties of metal hydrides and hydrogen behavior in the fuel cladding are studied. The present dissertation consists of six chapters including this introductory chapter. In chapter 2, the basic bulk properties of metal-hydrogen systems are described. Until now, there has been only limited information on the

properties of the metal hydrides because of the difficulty in producing the bulk hydrides. The author produced several flaw-free bulk metal hydrides to systematically evaluate their thermophysical properties. In chapter 3, ab initio electronic structure calculations for the metal hydrogen solid solutions and hydrides were performed in order to discuss the experimental results obtained in chapter 2. In chapter 4, characteristics of zirconium alloys with precipitated hydride and/or solute hydrogen are described. The terminal solid solubility of hydrogen for niobium containing zirconium alloys which are expected to cope with the higher burnup of the LWR was evaluated. The mechanical properties of hydrogenated Zr-Nb binary alloys with several phases were also evaluated. In chapter 5, the finite element analysis of hydrogen behavior in LWR cladding under the gradients of hydrogen, temperature, and stress is described. The conclusion of the present dissertation is described in chapter 6.

References

[1] M.K. Meyer, R. Fielding, J. Gan, Journal of Nuclear Materials, 371(2007) 281-287.

[2] A.H. Martínez, Y. Kadi, G. Parks, Annals of Nuclear Energy, 34 (2007) 550-563.

[3] A. Abánades, A. Pérez-Navarro, Nuclear Engineering and Design, 237 (2007) 325-333.

[4] T. Aoyama, T. Sekine, S. Maeda, A. Yoshida, Y. Maeda, S. Suzuki, T. Takeda, Nuclear Engineering and Design, 237 (2007) 353-368.

[5] B. Stalinski, Berichte der Bunsen-Gesellschaft, 76 (1972) 724-732.

[6] P. Paetz, K. Lucke, Journal of Nuclear Materials, 43 (1972) 13-27.

[7] M.T. Simnad, F.C. Foushee, G.B. West, Nuclear Technology, 28 (1976) 31-56.

[8] M.T. Simnad, Nuclear Engineering and Design, 64 (1981) 403-422.

[9] T. Yamamoto, H. Suwarno, H. Kayano, M. Yamawaki, Journal of Nuclear Science and Technology, 32 (1995) 260-262.

[10] M. Yamawaki, H. Suwarno, T. Yamamoto, T. Sanda, K. Fujimura, K. Kawashima, K. Konashi, Journal of Alloys and Compounds, 271–273 (1998) 530-533.

[11] K. Kakiuchi, N. Itagaki, T. Furuya, T. Hattori, Y. Nakazono, F. Ono, K. Yamaguchi, M. Yamawaki, Journal of Nuclear Materials, 294 (2001) 28-31.

[12] K. Fujimura, T. Sanda, M. Yamawaki, K. Konashi, Journal of Nuclear Science and Technology, 38 (2001) 879–886.

[13] E. Greenspan, H. Garkisch, J. Malen, M. Moalem, D. Olander, B. Petrovic, Z. Shayer, N. Todreas, Transactions of the American Nuclear Society, 89 (2003) 381.

[14] D.R. Olander and M. Ng, Journal of Nuclear Materials, 346 (2005) 98-108.

[15] M. Yamawaki, K. Konashi, S. Shimada, Journal of the Atomic Energy Society of Japan, 46 (2004) 457-466.

[16] K. Konashi et al., Proceedings of the ICAPP'06, Reno, USA (2006).

[17] K. Konashi, M. Yamawaki, T. Terai, K. Ito, "Development of Hydride Neutron Absorber for FBR," 2007 Fall Meeting of the Atomic Energy Society of Japan, P49.

[18] H. Takahashi, H. Takashita, X. Chen, AIP Conference Proceedings: International Conference on Accelerator-Driven Transmutation Technologies and Applications, (1995) 710-716.

[19] T. Wakabayashi, N. Higano, Progress in Nuclear Energy, 32 (1998) 555-562.

[20] S. Kasai, K. Kubota, H. Hayafune, M. Ichimiya, Progress in Nuclear Energy, 37 (2000) 131-136.

[21] K. Ikeda, T. Kawakita, Y. Ohkubo, Progress in Nuclear Energy, 37 (2000) 163-168.

[22] T. Takeda, D. Sato, T. Yamamoto, W. Hongchun, Progress in Nuclear Energy, 37 (2000) 229-234.

[23] K. Fujimura, T. Sanda, S. Moro, M. Saito, H. Sekimoto, Progress in Nuclear Energy, 40 (2002) 587-596.

[24] W.M. Mueller, J.P. Blackledge, G.G. Libowitz, Metal Hydrides, Academic Press, New York (1968).

[25] Y. Fukai, The Metal-Hydrogen System: Basic Bulk Properties, Springer Series in Materials Science 21 (1993).

[26] S. Yamanaka, K. Yoshioka, M. Uno, M. Katsura, H. Anada, T. Matsuda, S. Kobayashi, Journal of Alloys and Compounds, 293-295 (1999) 23-29.

[27] S. Yamanaka, K. Yoshioka, M. Uno, M. Katsura, H. Anada, T. Matsuda, S. Kobayashi, Journal of Alloys and Compounds, 293-295 (1999) 908-914.

[28] S. Yamanaka, K. Yamada, K. Kurosaki, M. Uno, K. Takeda, H. Anada, T. Matsuda, S. Kobayashi, Journal of Nuclear Materials, 294 (2001) 94-98.

[29] S. Yamanaka, K. Yamada, K. Kurosaki, M. Uno, K. Takeda, H. Anada, T. Matsuda, S. Kobayashi, Journal of Alloys and Compounds, 330-332 (2002) 99-104.

[30] M. Uno, K. Yamada, T. Maruyama, H. Muta, S. Yamanaka, Journal of Alloys and Compounds, 366 (2004) 101-106.

[31] D. Setoyama, J. Matsunaga, H. Muta, M. Uno, S. Yamanaka, Journal of Alloys and Compounds, 381 (2004) 215-220.

[32] M. Ito, D. Setoyama, J. Matsunaga, H. Muta, K. Kurosaki, M. Uno, S. Yamanaka, Journal of Alloys and Compounds, 420 (2006) 25-28.

[33] B. Lustman, F. Kerze, The Metallurgy of Zirconium, McGraw-Hill, New York (1955).

[34] D.L. Douglass, Atomic Energy Review, International Atomic Energy Agency, Vienna (1971).

[35] R. Choubey, J.J. Jonas, B.A. Cheadle, Metallurgical and Materials Transactions, A13 (1982) 1957-1964.

[36] E.F. Ibrahim, B.A. Cheadle, Canadian Metallurgical Quaterly, 24 (1985) 273-281.

[37] C.E. Coleman, B.A. Cheadle, C.D. Cann and J.R. Theaker, Zirconium in the Nuclear Industry, ASTM STP 1295 (1996) 884-898.

[38] D.L. Douglass, The Metallurgy of Zirconium, Vienna, Atomic Energy Review, Supplement 1971.

[39] C.M. Eucken, P.T. Finden, Zirconium in the Nuclear Industry, ASTM STP 1023 (1989) 113-127.

[40] G.P. Sabol, G.R. Kilp, M.G. Balfour, E. Roberts, Zirconium in the Nuclear Industry, ASTM STP 1023 (1989) 227-244.

[41] J.P. Mardon, D. Charquet, J. Senevat, Proceeding of International Topical Meeting on Light Water Reactor Fuel Performance, (1994) 643-649.

[42] G. Garzarolli, E. Steinberg. H.G. Weidinger, Zirconium in the Nuclear Industry, ASTM STP 1245 (1994) 760-778.

[43] I.L. Dillamore, W.T. Roberts, Metals Reviews, 10 (1965) 271.

[44] R.G. Ballinger, R.M. Pelloux, Journal of Nuclear Materials, 97 (1981) 231-253.

[45] E. F. Ibrahim, R. Choubey, J. J. Jonas, Journal of Nuclear Materials, 126 (1984) 44-52.

[46] S. Shimada, Y. Etoh, K. Tomida, Journal of Nuclear Materials, 248 (1997) 275-280.

[47] T. Kido, K. Kanasugi, M. Sugano, K. Komatsu, Journal of Nuclear Materials, 248 (1997) 281-287.

[48] R.E. Logé, J. W. Signorelli, Y. B. Chastel, M. Y. Perrin, R. A. Lebensohn, Acta Materialia, 48 (2000) 3917-3930.

[49] Y.H. Jeong, K.O. Lee, H.G. Kim, Journal of Nuclear Materials, 302 (2002) 9-19.

[50] K. Kapoor, C. Padmaprabu, S.V. Ramana Rao, T. Sanyal, B.P. Kashyap, Journal of Nuclear Materials, 312 (2003) 125-133.

[51] A.R. Massih, M. Dahlbäck, M. Limbäck, T. Andersson, B. Lehtinen, Corrosion Science, 48 (2006) 1154-1181.

[52] K.L. Murty, I. Charit, Progress in Nuclear Energy, 48 (2006) 325-359.

[53] S.Shimada, E. Etoh, H. Hayashi, Y. Tukuta, Journal of Nuclear Materials, 327 (2004) 97-113.

[54] K. Edsinger, J.H. Davies, R.B. Adamson, Zirconium in the Nuclear Industry, ASTM STP 1354 (2000) 316-339.

[55] B. Cox, Journal of Nuclear Materials, 170 (1990) 1-23.

[56] I. Aitchison, Zirconium in the Nuclear Industry, ASTM STP 458 (1969) 160.

[57] S.C. Lin, M. Hamasaki, Y.D. Chuang, Nuclear Science and Engineering, 71 (1979) 251.

[58] J.H. Huang, S.P. Huang, Journal of Nuclear Materials, 208 (1994) 166-179.

[59] J.B. Bai, C. Prioul, S. Lansiart, C. Francois, Scripta Metallurgica et Materialia, 25 (1994) 2559-2563.

[61] H.S. Hong, D.R. Olander, Journal of Nuclear Materials, 297 (2001) 107-112.

[60] Y.S. Kim, W.E. Wang, D.R. Olander, S. K. Yagnik, Journal of Nuclear Materials, 246 (1997) 43-52.

[62] L. Lanzani, M. Ruch, Journal of Nuclear Materials 324 (2004) 165-176.

[63] H.S. Hong, L. Sihver, D.R. Olander, L. Hallstadius, Journal of Nuclear Materials, 336 (2005) 113-119.

CHAPTER 2

Basic Bulk Properties of Metal-Hydrogen Systems

Chapter 2

Basic Bulk Properties of Metal-Hydrogen Systems

2-1. Introduction

2-1-1. Background

Transition metals and their alloys are useful materials because many of them have high chemical durability as well as high strength. Therefore they have been extensively utilized in various fields. Especially in nuclear power system, zirconium alloys such as Zircaloy and Zr–Nb alloy have been widely employed as pressure tubes and fuel claddings of nuclear reactors, and titanium alloys are major candidate as overpacks for geological disposal of high level radioactive wastes. On the other hand, the transition metals are known to absorb large quantities of hydrogen. The transition metals form hydrogen solid solutions at low hydrogen content and hydrides at higher hydrogen content. The hydrogen absorption leads to decrease intensity of structural materials [1-7], which is called hydrogen embrittlement. The hydrogen embrittlement can become a serious problem associated with safeness of the system; in particular the hydrides are just awful nuisance to the materials. However, the physico-chemical properties of the metal hydrides are virtually unknown, which is caused by difficulties in production of them. As well as the hydrides, the properties of the metal hydrogen solid solutions are poorly studied. It is because the transition metal hydrogen solid solutions had been unnoticed until report [8] which indicated that solute hydrogen in metallic lattice affected and accelerated creep rate of the zirconium alloy. Until now, the thermophysical properties of the titanium and zirconium hydrides and hydrogen solid solutions have been previously investigated by Yamanaka and Setoyama et al. [9-23]. Subsequently, a lot of discussions on the effect of hydrogen on their properties have been held. However, the mechanism of hydrogen effect is not comprehensively known and further research is required.

Although the metal hydrides have the negative face, they have an amount of potential. For instance, the densities of hydrogen atoms in some transition metal hydrides greater than in water or in liquid hydrogen [24]. Various metal hydrides have attracted much interest as hydrogen storage media. Hydrogen is the most effective moderator for neutron, therefore a variety of use has been also suggested for the metal hydrides in nuclear engineering field such as moderator, reflector and shielding components for fast reactors and accelerator-driven transmutation system. These applications need such properties as high melting point, low induced activity, small

neutron absorption cross-section, low hydrogen desorption pressure, high hydrogen density, phase stability, and low cost.

(a) Y-H system

The yttrium hydride satisfies the above-mentioned conditions and therefore it is expected as one of the good candidate as the neutron control material and reflector components for the fast breeder reactor (FBR) [25]. The yttrium–hydrogen system has been widely focused over the several years. Thin film system allowed the fabrication of the yttrium hydride and the hydrogenation changed optical properties of the yttrium, therefore the thin yttrium film was expected to be a switching mirror [26-30]. Rare earths including the yttrium form the hydrogen solid solutions, the di-hydrides and tri-hydrides exothermally. Fig. 2.1.1 shows the phase diagram for yttrium-hydrogen system [31]. The yttrium hydrogen solid solution (α phase), the di-hydride (δ phase), and tri-hydride (ε phase) are appeared in the phase diagram. In the α phase region, the hydrogen atoms interstice in the tetrahedral site of the hcp yttrium metallic lattice. The di-hydride crystallizes in the fcc fluorite structure and has metallic properties. The tri-hydride has an hcp structure, the tetrahedral and octahedral sites of which are occupied with hydrogen, and has semiconductor properties. The optical switching is contributed to the metal-semiconductor transition.

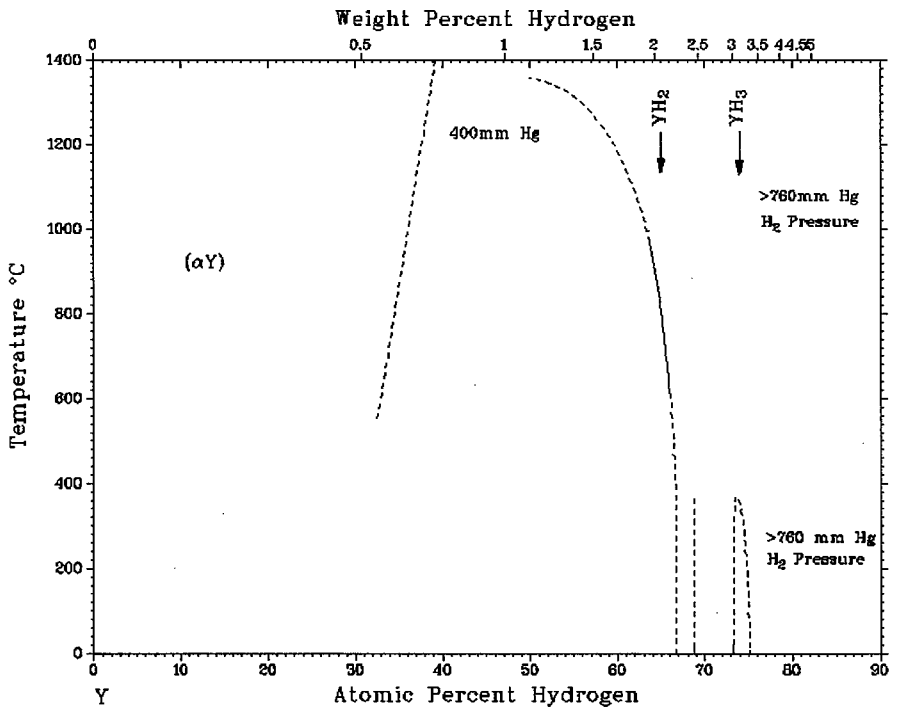


Fig. 2.1.1. Phase diagram for Y-H system [31].

However, the thin film system is confined to a few measurements of properties because of its dimensional restriction. The application is also limited. Therefore, if flaw-free bulk yttrium hydrides can be prepared, it is very meaningful and interesting from the prospective of research and practical use of them.

(b) Hf-H system

Although existing control rods for fast reactors are predominantly boron carbide, the use of the boron carbide control rod is limited by Pellet-Cladding Mechanical Interaction (PCMI) failure due to swelling. Helium gas is produced and accumulated in the boron carbide control rod by the nuclear reaction of boron, this causes the swelling. On the other hand, the helium gas production doesn't occur in the nuclear reaction process of hafnium with neutron. The nuclear reaction is expressed as follows:

$$Hf^{177}(n,\gamma)Hf^{178}(n,\gamma)Hf^{179} \qquad (2\text{-}1\text{-}1)$$

The daughter radionuclide Hf^{178} also has a large absorption cross-section of thermal neutron as well as the parent nuclide Hf^{177}. Since hydrogen can moderate the fast neutrons and the hafnium has superior absorptive property of the thermal neutron, the hafnium hydride can efficiently absorb the fast neutrons. Therefore, the hafnium hydride is expected as an advance control rod that has the excellent and long-life worth for the fast reactors.

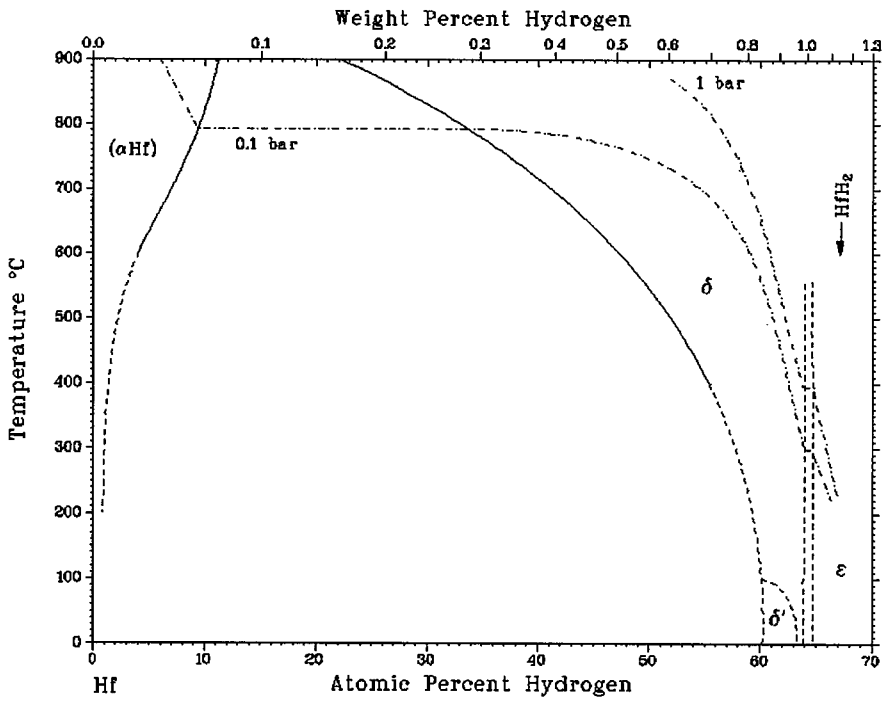


Fig. 2.1.2. Phase diagram for Hf-H system [32].

Fig. 2.1.2 shows the phase diagram for hafnium-hydrogen system [32]. The hafnium hydrogen solid solution (α phase) and the two types of di-hydride (δ and ε phase) are appeared in the phase diagram. This is very similar to titanium- and zirconium–hydrogen systems. However, it is reported [33–35] that there exist another crystal structure of the hafnium hydride which has a pseudocubic defect fluorite type structure (δ' phase). The hydrogen content of the δ' phase is slightly lower than that of δ phase, as confirmed in Fig. 2.1.2. In order to use the hafnium hydrides in practice, their characteristics should be evaluated.

(c) Nb-H system

Niobium alloys and niobium containing alloys are useful materials in various kinds of plants because of their excellent mechanical properties, high-corrosion resistance, high melting point, and small neutron absorption cross section. Therefore, they have been extensively utilized and expected as the pressure tubes of CANDU, high performance nuclear fuel claddings, the ITER divertor, and ultra-high temperature materials [36–40]. However, hydrogen is generated by corrosion processes in use environments, and some of the hydrogen is absorbed into these alloys. This would lead to the hydrogen embrittlement. Additionally, the niobium and its alloys are widely expected as a hydrogen permeation membrane because their hydrogen permeability is much higher than that of the existing material such as palladium and its alloys [41, 42]. However, the niobium alloys are broken down by the hydrogen embrittlement and subsequently can not be utilized as the hydrogen permeation membrane. Therefore, it is important to investigate the behavior of niobium hydrogen solid solutions and hydrides. Fig. 2.1.3 shows the phase diagram of niobium-hydrogen system [43]. Niobium absorbs hydrogen and forms a single phase (bcc_A2, α -phase) solid solution up to a hydrogen content $C_H = 0.059$ in atomic ratio [H/Nb] at room temperature. A Nb-H phase with face-centered orthorhombic structure mono-hydride (β phase) exists, in which the hydrogen occupation is restricted to four tetrahedral interstitial sites forming an ordered arrangement. Although the fluorite type structure di-hydride (δ phase) is also confirmed in the phase diagram, the phase can be stable only at a significantly high ambient pressure of hydrogen gas. The investigation of the β phase niobium hydride is important for elucidation of the hydrogen embrittlement of the niobium alloys around room temperature.

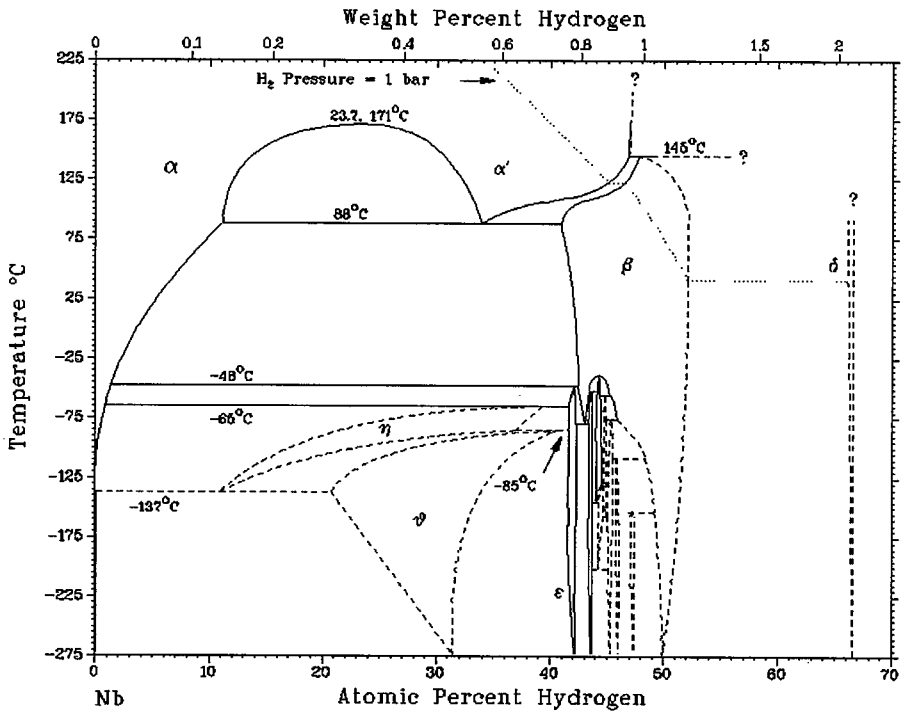


Fig. 2.1.3. Phase diagram for Nb-H system [43].

(d) Hydride of Zr-Gd alloy

New concepts of nuclear fast reactor core using metal hydrides as neutron absorber were recently suggested [44–46]. Although the gadolinium containing light water reactor (LWR) fuel is used as neutron absorber that is so-called burnable poison in order to extend the burnup of the fuels in safety, there is previously no concept of neutron absorber for the fast reactors. The new concept is as follows: hydrogen in metal hydrides moderates the fast neutron and then moderated thermal neutron can be efficiently absorbed by the gadolinium. Therefore, hydrides of Zr-Gd alloys are candidates for neutron absorber and controller materials in the fast reactor. Fig. 2.1.4 and Fig. 2.1.5 show the phase diagram for the gadolinium and zirconium -hydrogen system, respectively [47, 48]. The gadolinium also forms the hydrogen solid solutions (α phase), the di-hydrides (δ phase), and tri-hydrides (ε phase) exothermally. The zirconium hydrogen solid solution (α phase) and two types of di-hydride (δ and ε phase) are appeared in the phase diagram. Recently, the zirconium hydride is keenly noticed. Yamanaka et al. [9, 12, 13, 15, 16, and 19] investigated the mechanical and thermal properties of δ phase zirconium hydride. Tsuchiya et al. [49, 50] reported the thermal properties of ε phase zirconium hydride. However, the quite limitary information on the hydrides of gadolinium and zirconium-gadolinium alloys is available.

For the practical use, the hydrogen content region from 1.5 to 2.0 in atomic ratio is favorable for the gadolinium-zirconium alloys. In the case, δ phase di-hydrides would be important for both the metal-hydrogen systems.

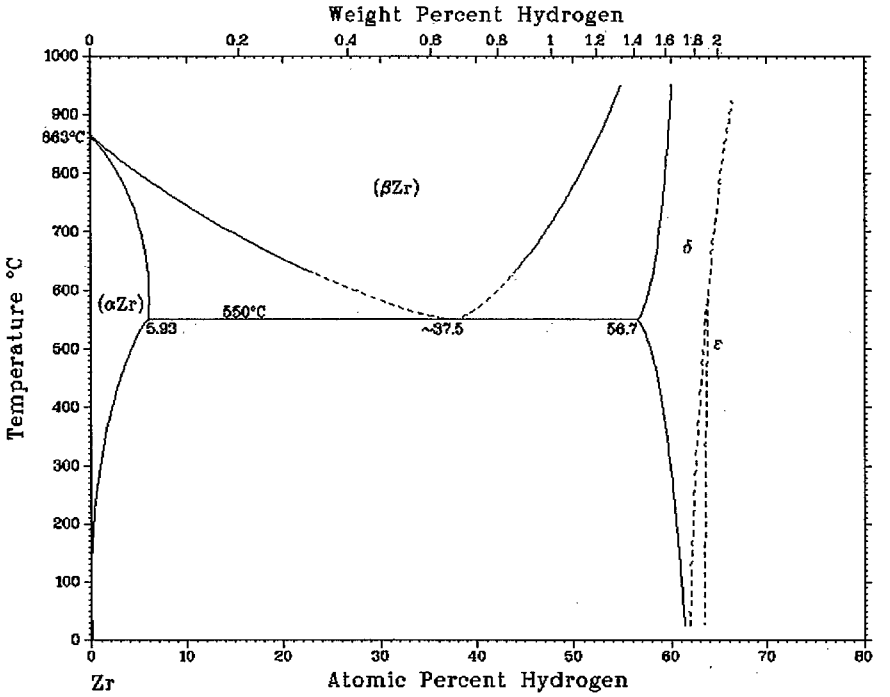


Fig. 2.1.4. Phase diagram for Zr-H system [47].

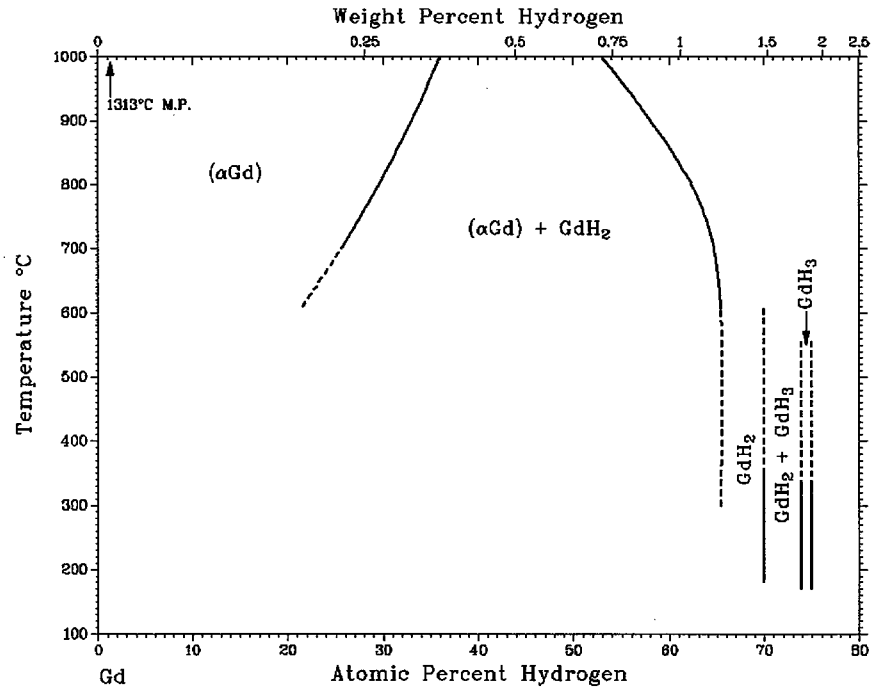


Fig. 2.1.5. Phase diagram for Gd-H system [48].

2-1-2. Objective

The basic bulk properties of metal-hydrogen alloys have been extensively studied [51–53]. However, there is inadequate information on such data of the single-phase metal hydrides although much data is needed for practical use. It is because the pure bulk metal hydrides without any defects are hard to be procured. Recently, technique for production of flaw-free bulk metal hydrides with wide-ranging hydrogen contents was established by Yamanaka and Setoyama et al. [9–13, 21]. This was great step towards practical application of the metal hydrides and we have elucidated the properties of pure metal hydrides with unprecedented detail. In this study, the author looked for the method to produce the bulk hydrides of yttrium, hafnium, niobium, and Zr-Gd alloy and have succeeded in them. The details are given in section 2-2. The yttrium, hafnium and gadolinium have a same crystal structure of hcp_A3 (α phase) as the titanium and zirconium, and their hydrides have also a same crystal structure of fcc_C1 (δ phase) as the titanium and zirconium hydrides. Therefore the information on the physico-chemical properties of the metal-hydrogen systems are comparable with those of zirconium- and titanium–hydrogen system and have a great deal with potential in theory of the transition metal – hydrogen system. In addition the change of hydrogen content may affect thermal and mechanical properties of the hydrided materials. Therefore, since a high reliability of nuclear materials is required under various severe conditions, the evaluation of hydrogen amount influences on the properties of the metal hydrides are also considered to be necessary. With such background, study for the basic bulk properties of metal-hydrogen systems with wide ranging hydrogen content is very important from the viewpoint of both academic interest and material engineering. In this chapter, the physico-chemical properties of the yttrium and niobium hydrogen solid solutions are studied. Bulk hydrides of the yttrium, hafnium, niobium, and Zr-Gd alloy are produced and their physico-chemical properties are systematically investigated.

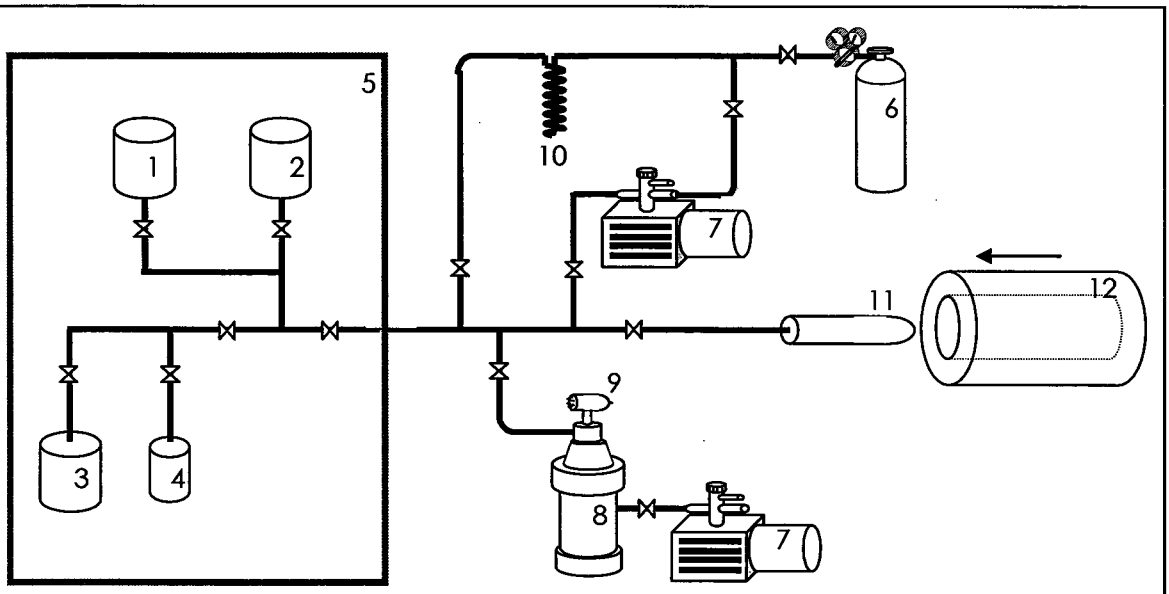
2-2. Experimental Procedure

2-2-1. Sample Preparation

Hydrogenation was carried out in a modified Sieverts' UHV apparatus in this study. Fig.2.2.1 shows the schematic view of the apparatus.

The preparation procedures for the hydrogen solid solution of yttrium and niobium were almost identical. The pure (99.9 %) yttrium and niobium polycrystalline was used

as the starting material for their hydrogen solid solutions. Firstly, the pure samples were degreased in acetone. After evacuating below 10^{-6} Pa in the Sieverts' apparatus, the sample was annealed at 1073 K for 10 hours in order to remove the residual stress and impurity gases. Then, the highly pure hydrogen gas (7N) was passed through a liquefied nitrogen trap and then introduced to the reaction chamber up to predetermined pressures. After the keeping this condition for 1 hour, the sample was air cooled. The hydrogen content during the hydrogenation is figured out by the temperature and the equilibrium hydrogen pressure.



1. Capacitance manometer (~10 Torr)
2. Capacitance manometer (~1000 Torr)
3. Standard volume (528.406 ml)
4. Standard volume (4.04 ml)
5. Low temperature incubator (298 K)
6. High purity hydrogen gas (7N)
7. Rotary vacuum pump
8. Turbo-molecular pump
9. Ionization vaccum gauge
10. Liquid nitrogen trap
11. Quartz tube
12. Electric resistance furnace

Fig. 2.2.1. Schematic view of the modified Sieverts' apparatus.

On the other hand, the production procedures for the hydrides of yttrium, hafnium, niobium, and Zr-Gd alloy were quite different from that for the hydrogen solid solution. The reason of this difference was attributed to the phase transition accompanied with the large volumetric expansion from the metal phase to the hydride phase during

hydrogenation, and to the original material strength of the hydrides. Therefore it has been said that the production of flaw-free bulk metal hydrides is almost impossible [54, 55]. In the present study, the authors have succeeded to prepare various shapes of bulk hydrides of yttrium, niobium, hafnium, and Zr-Gd alloy without cracks and voids. The production technique was different for each metal hydride due to the difference of nature for each metal-hydrogen system.

Bulk yttrium hydrides were produced directly from various shapes of yttrium polycrystalline rods with 99.9 wt% purity. Firstly, the pure yttrium was degreased in acetone and then introduced in the Sieverts' apparatus. After evacuating below 10^{-6} Pa in the apparatus, the sample was annealed at 1073 K for 10 hours. Then, the highly pure hydrogen gas (7N) was passed through a liquefied nitrogen trap and then introduced to the reaction chamber up to predetermined pressure. As previously mentioned, there is difficulty in the production of flaw-free bulk metal hydride. From the previous researches by Yamanaka and Setoyama, the destruction during hydrogenation was thought to be aftereffects of the differences of volume and crystal structure between metal and hydride. Therefore, the hydrogenating rate on crossing the ($\alpha + \delta$) field should be kept very slowly for producing flaw-free bulk yttrium hydride. Since the equilibrium hydrogen pressure of the yttrium – hydrogen system is quite low, all the introduced hydrogen gas below atmospheric pressure is immediately absorbed into the sample even at high temperature. Therefore, the hydrogen flow rate into reaction chamber was regulated and 50 hours were taken to progress the phase transformation from α phase to δ phase. At the end of this process, hydrogen absorption of yttrium almost finished. Finally, the sample was cooled to room temperature at –40 K/hr.

Various shapes of pure (99.9 %) hafnium polycrystalline rods were used as starting materials for the bulk hafnium hydrides. Note that commercially grade pure hafnium contains a few percent of zirconium. After the annealing at 1123 K in vacuum for 12 hours, the pure hydrogen gas was passed through a liquefied nitrogen trap and then introduced to the reaction chamber. Then, the sample was gradually cooled to 723 K for hydrogen absorption. According to the Le Chatelier's law, when the temperature of the system in the reaction chamber is becoming lower, the exothermic hydrogenation reaction of hafnium is proceeding in order to counteract the temperature change. Therefore, it is possible to control the hydrogenating rate by controlling the cooling rate. Since the hafnium hydride has comparatively low equilibrium hydrogen pressure, both the hydrogen flow rate into reaction chamber and the rate of the subsequent cooling

should be keep quite low. Therefore, 50 hours were taken for the hydrogen gas introduction and the cooling rate from 1123 to 723 K was set to –10 K/hour. Such quite slow cooling rate allowed us to produce the crack and void free bulk hydride. After reaching 723 K, the sample was furnace-cooled to room temperature. Hydrogen absorption during the furnace cool is scarce.

Polycrystalline pure (99.95 %) niobium was used as starting material for the bulk niobium hydride. After the annealing at 1073 K in vacuum for 12 hours, the pure hydrogen gas was introduced to the reaction chamber. Then, the sample was gradually cooled to 623 K for hydrogen absorption. The cooling rates in this case were –10 K/hour. Finally, after reached to 623 K, the sample was furnace-cooled to room temperature.

The pure zirconium and gadolinium were used as starting materials for the hydride of Zr-Gd alloy (Zr : Gd = 10 : 1). The purity of the zirconium and gadolinium is 99.9 wt%. The source materials were melted in an arc furnace under argon atmosphere at 0.05 MPa. For homogeneity, the specimen was turned over and melted more than 5 times. The obtained ingot was cut into various shapes for measurements. After annealing at 1073 K in vacuum for 10 hours, the pure hydrogen gas was introduced into the reaction chamber. Although the gadolinium hydride has quite low equilibrium hydrogen pressure, the zirconium hydride has comparatively high equilibrium hydrogen pressure. Therefore, both the hydrogen flow rate into reaction chamber and the rate of the subsequent cooling should be kept quite low. In this case, 50 hours were taken for the hydrogen gas introduction and the cooling rate from 1073 to 723 K was set to –10 K/hour. After reaching 723 K, the sample was furnace-cooled to room temperature.

These hydrogenation processes enable the production of various shapes of the bulk metal hydrides. For all the bulk metal hydrides, the hydrogen absorption is confirmed to finish at enough high temperature for hydrogen to homogenize in the samples.

2-2-2. Sample Characterization

The hydrogen content of the specimens was measured by a hydrogen analyzer (EMGA-621, HORIBA Ltd.). The analyzer measures change in thermal conductivity which is affected by the hydrogen gas extracted from the sample, and then hydrogen content is computed. In this study, the measurements were repeated 5 times for all samples, and the average value was adopted from the data obtained. The phase of the prepared samples and lattice parameters were evaluated by a high-temperature X-ray diffractometer (RINT-2000/PC, Rigaku Corp.) using CuKα radiation in the He flow atmosphere. The errors of the lattice parameter values are within 0.0001 nm. The

surface condition of the sample was obtained by an optical microscope (BX51M, OLYMPUS), a confocal scanning laser microscope (OLS310, OLYMPUS), and a field emission type scanning electron microscope (FE-SEM) (JSM-6500F, JEOL). The information of the inside of sample also obtained after an argon ion milling treatment (SM-09010: Cross Section Polisher, JEOL). Crystallographic orientation measurement of the sample was performed using the FE-SEM equipped with an electron backscatter diffraction patterns (EBSP) system (OIM400, TSL). The surface of the sample for the EBSP measurement was treated by a mechano-chemical polishing (CMP), i.e. a mechanical polishing with a chemical treatment using colloidal silica nano-particles, or the argon iron milling.

2-2-3. Measurement Methods

(a) Mechanical Properties

The longitudinal and shear sound velocity measurement was carried out by an ultrasonic pulse-echo method (Echometer1062, Nihon Matech Corp.) at room temperature. The sound velocity was obtained by following equation:

$$V = \frac{2L}{T_2 - T_1} \tag{2-2-1}$$

where V is the sound velocity of the sample, L is the length of the sample, T_1 is the reflection time of the pulse from incidence face, and T_2 is the reflection time from the rear face, respectively. 5.0 MHz longitudinal wave pulse and shear wave pulse were used for measuring the longitudinal sound velocity (V_L) and the shear sound velocity (V_S), respectively.

Then the shear modulus G, the Young's modulus E, the bulk modulus B, the Poisson's ratio σ and the Debye temperature θ_D are calculated in terms of the longitudinal velocity V_L and the shear velocity V_S as follows:

$$G = \rho V_S^{\,2} \tag{2-2-2}$$

$$E = \rho V_S^{\,2} \times \frac{3V_L^{\,2} - 4V_S^{\,2}}{V_L^{\,2} - V_S^{\,2}} \tag{2-2-3}$$

$$B = \rho\left(V_L^{\,2} - \frac{4}{3}V_S^{\,2}\right) \tag{2-2-4}$$

$$\sigma_P = \frac{1}{2} \times \frac{V_L^{\,2} - 2V_S^{\,2}}{V_L^{\,2} - V_S^{\,2}} \tag{2-2-5}$$

$$\theta_D = \frac{h}{k}\sqrt[3]{\frac{9N}{4\pi V_{uc}(1/V_L^3 + 2/V_S^3)}} \quad (2\text{-}2\text{-}6)$$

where ρ is the density of the sample, h the Planck constant, k the Boltzmann constant, N the number of metal atoms in a unit cell and V_{uc} is unit cell volume.

The Vickers hardness was also measured using a Vickers harness tester (MHT-1, Matsuzawa Co. Ltd.) at room temperature. The applied load and load time for the indentation were 1.0 kgf and 10 sec, respectively. The measurements were repeated more than 10 times for all samples, and the average hardness was estimated from the data obtained. The Vickers hardness H_V was calculated using the following equation:

$$H_V[GPa] = \frac{2P_H \sin(\phi/2)}{d^2} \quad (2\text{-}2\text{-}7)$$

where ϕ is the indenter apex angle (136°), P_H the applied load and d the mean length of diagonals. In the present study, the unit "GPa" is adopted to express the hardness instead of a *general* hardness number, "kgf/mm^2," for comparison with such mechanical properties as the Young's modulus.

(b) Electrical Properties

The electrical resistivity was measured by the standard four-probe dc method (ZEM-1, ULVAC-RIKO Inc.) in helium atmosphere from room temperature to about 773 K. Fig.2.2.3 shows the schematic view of the apparatus. The resistivity of the sample was evaluated from following equation:

$$\rho = \frac{V_{ref}}{V_{AB}}\rho_{ref}\frac{A}{L} \quad (2\text{-}2\text{-}8)$$

where ρ is the resistivity of the sample, V_{ref} and V_{AB} are the voltage of the reference resistor and the voltage between two probes, A is the area of cross section of the sample, and L is the distance between two electrodes, respectively. In the present study, the measurement was carried out in the temperature range from 353 K to about 773 K. The measurements were repeated 3 times at same temperature with different temperature gradient (20 K, 30 K, and 40 K).

(c) Thermal Properties

The thermal expansion was measured in a high purity argon (99.999%) atmosphere with a flow rate of 100 ml/min using by the differential thermodilatometry (TD5020, Bruker Axs) from room temperature to about 773 K. The α-Al_2O_3 was used as a reference sample.

The heat capacity was measured in a high purity argon (99.999%) atmosphere with

a flow rate of 100 ml/min using a differential scanning calorimetry (Triple-cell DSC, ULVAC-RIKO Inc.) from room temperature to about 773 K. The apparatus which has "a triple-cell system and adiabatic temperature control system" was originally developed by Takahashi et al. [56]. The temperature differences between the sample side and empty side, and the reference side and the empty side were detected simultaneously by R-type thermocouples under the condition of constant heating rate. The specific heat capacity of the sample was determined by comparing each of the signals of sample side and empty side. The value of reference, α-Al_2O_3 standard, was also determined to check the accuracy of the measurement. In this study, two methods, a scanning method and an enthalpy method, were carried out. In the scanning method, the difference in ordinate displacement between the reference and blank and between the sample and blank were measured for a given temperature range of a scan. The enthalpy method refers to heat capacity measurements in which all the output signals during a temperature scan are integrated to give the total enthalpy change (ΔH) for the given temperature interval (ΔT). The quantity $\Delta H / \Delta T$ is adopted as the value of the heat capacity at the middle point of the temperature interval. The measurement was carried out at intervals of 50 K and heating rates of 5 K/min. The isothermal baselines at initial and final temperature were interpolated linearly to give the baseline values for temperatures within the interval. The ordinate values during and after scan were then integrated, taking into account the interpolated baseline. This procedure was performed on the results of scans on the sample, the reference and the blank runs. The enthalpy change of the sample was calculated by subtracting the integrated area for the determined by comparing the observed enthalpy change of the sample with that of the reference, by taking into account the calibration constant.

The thermal diffusivity was measured by the laser flash method (TC-7000, ULVAC-RIKO Inc.) from room temperature to about 773 K in vacuum (10^{-4} Pa). The technique is based on transiently heating one surface of the sample with an energy pulse from a ruby laser. The temperature change on the opposite surface was monitored with an indium antimonide infrared detector. The thermal diffusion equation is expressed from the experimental rear surface temperature history of the sample after being flashed by a laser pulse, using following equation [57]:

$$\ln(t_{1/2} \cdot T) = \ln\left[2 \cdot T_m \left(L^2 / \pi D\right)^{1/2}\right] - \left(L^2/4D\right) \cdot 1/t \qquad (2\text{-}2\text{-}9)$$

where $t_{1/2}$ is the time to one-half the maximum temperature rise T_m at rear surface of the sample, T is the temperature at rear surface of the sample at that time t, L is the

sample thickness, D is the thermal diffusivity, respectively. In the equation, $\ln(t_{1/2} \cdot T)$ was assumed to be in reverse proportion to temperature T and then the value for the slope is $L^2/4D$. Therefore, the thermal diffusivity was obtained by the following equation:

$$\alpha = L^2 / 4t_{1/2} \qquad (2\text{-}2\text{-}10)$$

2-3. Results and Discussion

2-3-1. Y-H system

(a) Sample Characterization of Yttrium Hydrogen Solid Solution

It is found from the literature [31] that hydrogen can dissolve up to 0.25 in atomic ratio [H/Y] at room temperature. The hydrogen content of the prepared sample was in the range from 0.00 to 0.20 in atomic ratio [H/Y]. From the X-ray diffraction analysis all the prepared samples were confirmed to have an hcp_A3 α-Y(H) single phase. Fig. 2.3.1 shows the lattice parameters a and c at room temperature as a function of hydrogen content C_H [H/Y], together with literature data by Spedding [58], Beaudry [59], and Khatamian [60]. The lattice parameter of yttrium hydrogen solid solution increases by hydrogen addition as expressed as follows:

$$a\,[\mathrm{nm}] = 0.3646 + 1.029 \times 10^{-2} \times C_H\ (\mathrm{H/Y}) \qquad (2\text{-}3\text{-}1)$$

$$c\,[\mathrm{nm}] = 0.5722 + 3.363 \times 10^{-2} \times C_H\ (\mathrm{H/Y}) \qquad (2\text{-}3\text{-}2)$$

The present results are well accorded with the literature data. It was also confirmed that the densities of yttrium hydrogen solid solution determined from weight and dimensional measurements approximately equaled to the theoretical density calculated from the lattice parameter. The linear expansion coefficient of c-axis on the hydrogen content, $\lambda_c = (1/c)(\partial c/\partial C_H)$, is 3.36×10^{-2}, which is larger than the coefficient of a-axis, $\lambda_a = (1/a)(\partial a/\partial C_H)$, 1.03×10^{-2}. It is considered that this difference is the actual c/a ratio for yttrium (1.57) being smaller than the ideal ratio for hcp structure ($\sqrt{8/3} = 1.63$).

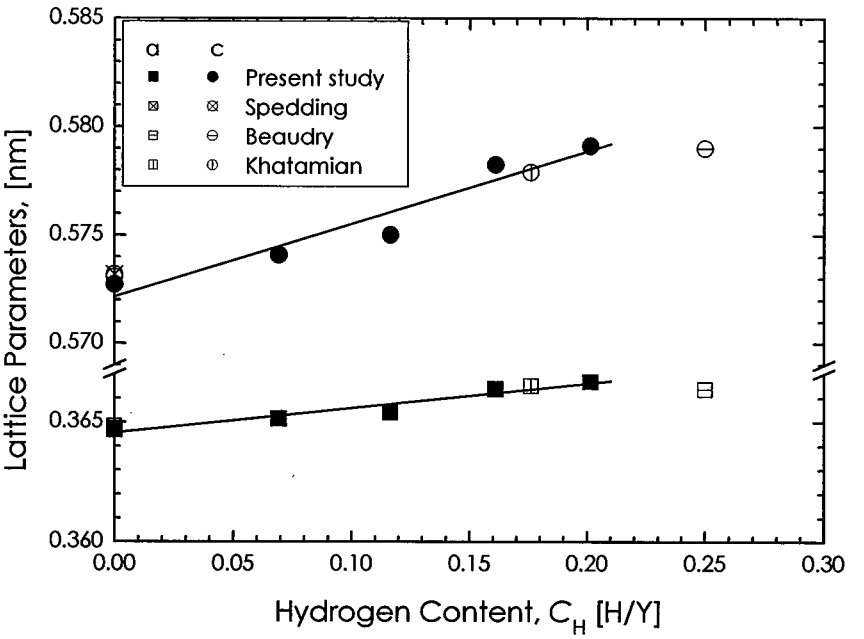


Fig. 2.3.1. Lattice parameters at room temperature of yttrium hydrogen solid solution as a function of hydrogen content, together with literature data [58-60]

(b) Mechanical Properties of Yttrium Hydrogen Solid Solution

Fig. 2.3.2 shows the longitudinal V_L and shear V_S sound velocities of the yttrium hydrogen solid solutions at room temperature as the function of hydrogen content C_H [H/Y]. The velocities increase by hydrogen addition as expressed as follows:

$$V_L[\mathrm{m/s}] = 4193 + 1848 \times C_H(\mathrm{H/Y}) \quad (2\text{-}3\text{-}3)$$

$$V_S[\mathrm{m/s}] = 2425 + 404 \times C_H(\mathrm{H/Y}) \quad (2\text{-}3\text{-}4)$$

Fig. 2.3.3 shows the Young's modulus E, shear modulus G, and Bulk modulus B at room temperature of the yttrium hydrogen solid solutions as a function of hydrogen content C_H [H/Y]. As same as the sound velocities, the elastic moduli of the yttrium hydrogen solid solution increases with increasing the hydrogen content. Therefore, it is found that the yttrium becomes elastically hard by the effect of hydrogen dissolution. The dependences of elastic moduli on the hydrogen content are expressed as follows:

$$E[\mathrm{GPa}] = 65.0 + 32.7 \times C_H(\mathrm{H/Y}) \quad (2\text{-}3\text{-}5)$$

$$G[\mathrm{GPa}] = 26.0 + 9.15 \times C_H(\mathrm{H/Y}) \quad (2\text{-}3\text{-}6)$$

$$B[\mathrm{GPa}] = 43.1 + 60.2 \times C_H(\mathrm{H/Y}) \quad (2\text{-}3\text{-}7)$$

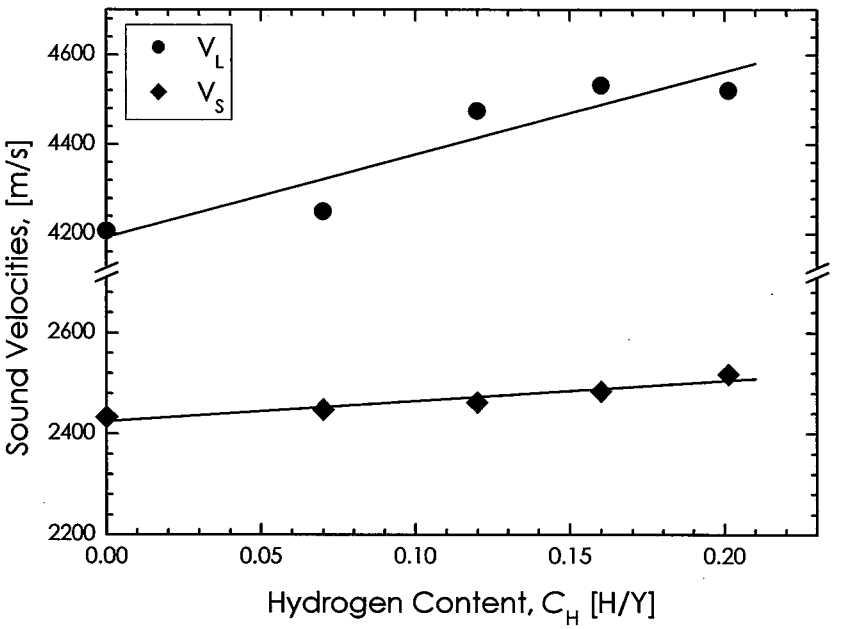


Fig. 2.3.2. Sound velocities at room temperature of yttrium hydrogen solid solution as a function of hydrogen content.

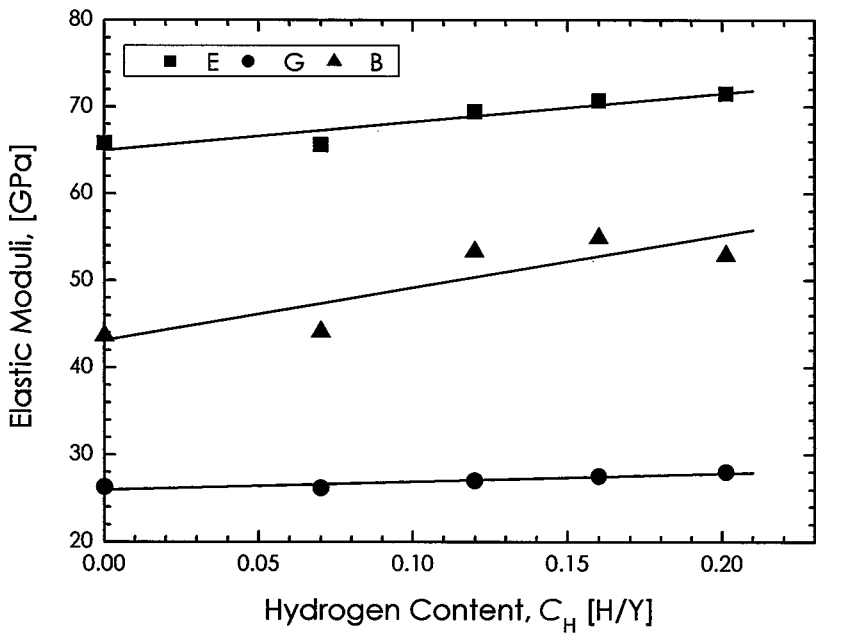


Fig. 2.3.3. Elastic moduli of yttrium hydrogen solid solutions as a function of hydrogen content.

Fig. 2.3.4 shows the Debye temperature θ_D at room temperature of the yttrium hydrogen solid solution as a function of hydrogen content C_H [H/Y], together with literature data by Heiniger [61]. The Debye temperature of the yttrium is increased by hydrogen addition as expressed as follows:

$$\theta_D[K] = 250 + 37.4 \times C_H(H/Y) \quad (2\text{-}3\text{-}8)$$

The present result is smaller than the low temperature limit value (280 K) [61], this difference is caused by the difference of measurement technique and temperature condition.

Fig. 2.3.5 shows the Vickers hardness H_V at room temperature of the yttrium hydrogen solid solutions as a function of hydrogen content C_H [H/Y]. The Vickers hardness also increases with increasing the hydrogen content as empirically expressed as follows:

$$H_V[GPa] = 0.870 + 2.43 \times C_H(H/Y) \quad (2\text{-}3\text{-}9)$$

Therefore, it is also found that the yttrium becomes plastically hard by the effect of hydrogen dissolution.

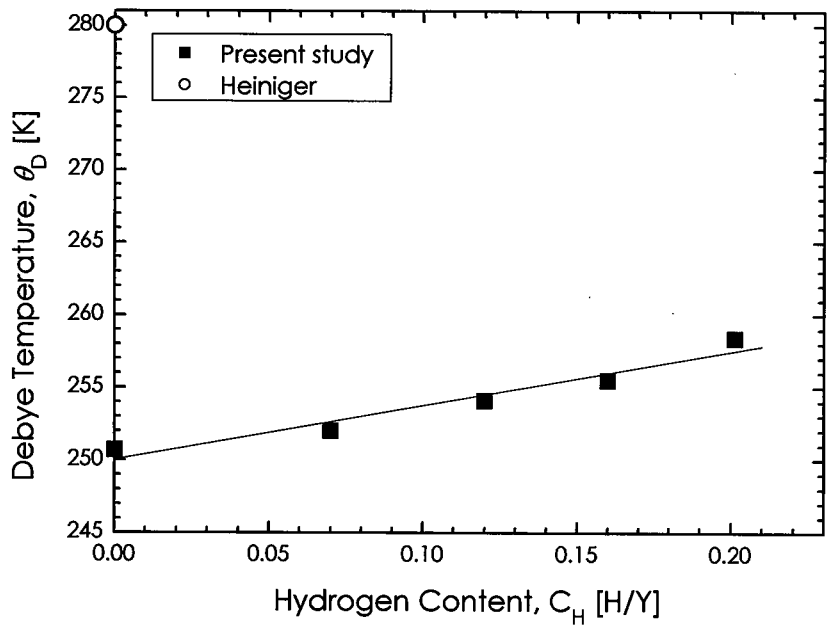


Fig. 2.3.4. Debye temperature of yttrium hydrogen solid solution as a function of hydrogen content, together with literature data [61].

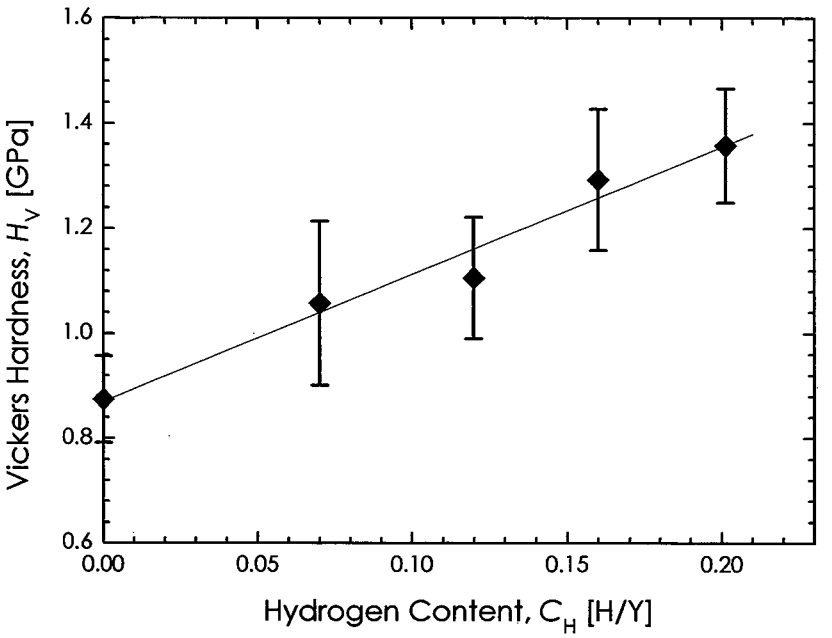


Fig. 2.3.5. Vickers hardness at room temperature of yttrium hydrogen solid solutions as a function of hydrogen content.

(c) Electrical Properties of Yttrium Hydrogen Solid Solution

The temperature dependence of the electrical resistivity ρ of yttrium hydrogen solid solution is shown in Fig. 2.3.6. The electrical resistivity of yttrium hydrogen solid solution exhibits metallic temperature dependence and is gradually increased by hydrogen addition. It is confirmed from Fig. 2.3.7 that the electrical resistivity linearly increases with increasing hydrogen content up to C_H=0.16. The interstitial hydrogen plays a role as electron scattering point and the Matthiessen's rule is fulfilled. Therefore, linear fitting could be performed with using following equation:

$$\rho^{Y-H(T)} = \rho^{Y(T)} + C_H \rho^H \qquad (2\text{-}3\text{-}10)$$

where $\rho^{Y-H(T)}$, $\rho^{Y(T)}$, and ρ^H are the electrical resistivity of yttrium hydrogen solid solution, that of pure yttrium, and added resistivity for one H atom, respectively. The added resistivity with hydrogen interstice in the yttrium is $4.41\times10^{-6}\ \Omega\cdot m$/(H/Y) in the temperature range from 373 K to 773 K. Bonnet [62] reported the values $(2.34 \sim 2.48)\times10^{-6}\ \Omega\cdot m$/(H/Y) as the added resistivities of yttrium hydrogen solid solution with hydrogen content in the temperature range from 4.2 K to 300 K. The present value is larger than the literature values, which may be attributed to the difference of the

measuring temperature between them.

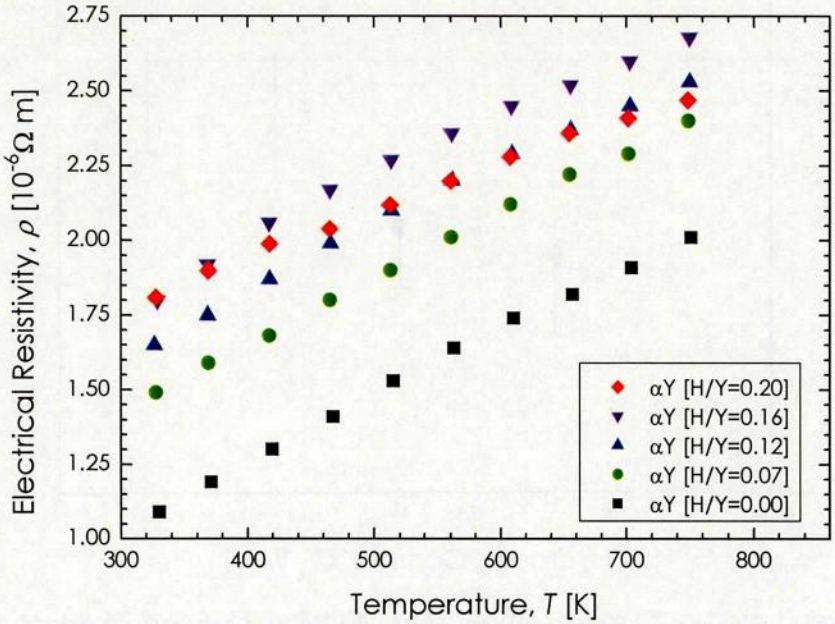


Fig. 2.3.6. Temperature dependence of electrical resistivity of yttrium hydrogen solid solution.

The electrical resistivities decreases on reaching a maximum near C_H=0.16 in the temperature range from 373 K to 773 K and this tendency becomes significant with increasing temperature. It is considered that the electronic structure of yttrium is changed by large amount of interstitial hydrogen and therefore their electrical resistivities disobey the Matthiessen's rule at above the maximum hydrogen content. The maxima of the electrical resistivity appear and shift to lower hydrogen content with increasing temperature. This result implies that there are other factors to affect with the resistivity and subsequently the limit of hydrogen content for the Mathiesen's rule becomes smaller with increasing temperature. The electron density of states of the yttrium hydrogen solid solution dominates in the vicinity of the Fermi level, which explains the metal-like temperature dependence of the electrical resistivity. The temperature factor could not be considered by the first principle calculation, therefore the further discussion is limited. However, there is one simple assumption. The pure yttrium is strongly anisotropic in the electrical resistivity, originally. Zinov'yev [63] showed that the anisotropy for the electrical resistivity $\rho_{\perp} / \rho_{//}$ of the pure yttrium single crystal decreased with increasing temperature, which was related to that the ratio c/a for pure

yttrium also got near to the ideal ratio for hcp structure ($\sqrt{8/3}$) with increasing temperature ($\rho_{\perp}$ was the electrical resistivity perpendicular to the direction of c axis and $\rho_{//}$ was the resistivity parallel to the direction of c axis). This can be easily understood by spread of electron's path. As is noted earlier, the ratio of the lattice parameter c/a for yttrium hydrogen solid solution get near to the ideal ratio for hcp structure ($\sqrt{8/3}$) with increasing the hydrogen content. In the temperature range the maxima of the electrical resistivity appear, the $\rho_{\perp}$ would decrease with the lattice expansion by hydrogen addition. The electrical resistivity of the polycrystalline ρ_{POLY} is known to be expressed as:

$$\rho_{POLY} = 2/3\rho_{\perp} + 1/3\rho_{//} \qquad (2\text{-}3\text{-}11)$$

Therefore, this assumption is borne out by the large effect on the ρ_{POLY} of the $\rho_{\perp}$ and the small effect on the resistivity of hydrogen as the impurity [53].

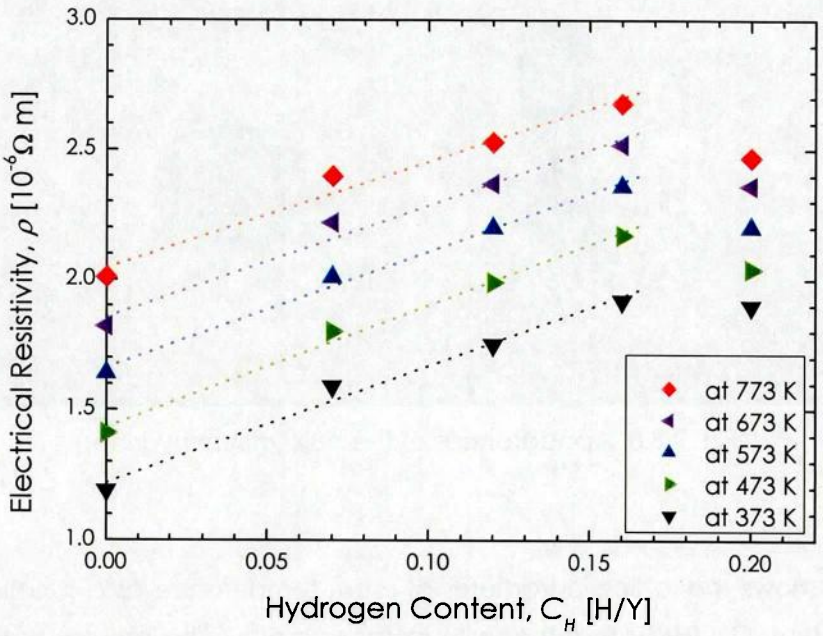


Fig. 2.3.7. Electrical resistivity of yttrium hydrogen solid solution as a function of hydrogen content; Dotted lines are fitting in the hydrogen content range from 0.00 to 0.16 in atomic ratio.

(d) Sample Characterization of Yttrium Hydride

Various shapes of bulk yttrium hydrides could be prepared. Fig. 2.3.8 shows the appearances of the prepared samples. Metallic gray color of the yttrium metal changed to dark blue of the yttrium hydride. Hydrogen contents C_H of the prepared samples were in the range from 1.72 to 2.01 in atomic ratio [H/Y]. Fig. 2.3.9 shows the X-ray diffraction patterns of $YH_{1.72}$ and $YH_{2.01}$, together with literature data by Markin [64]. From the analysis, it is found that all of the samples prepared in the present study show a fluorite type structured fcc_C1 (δ-phase).

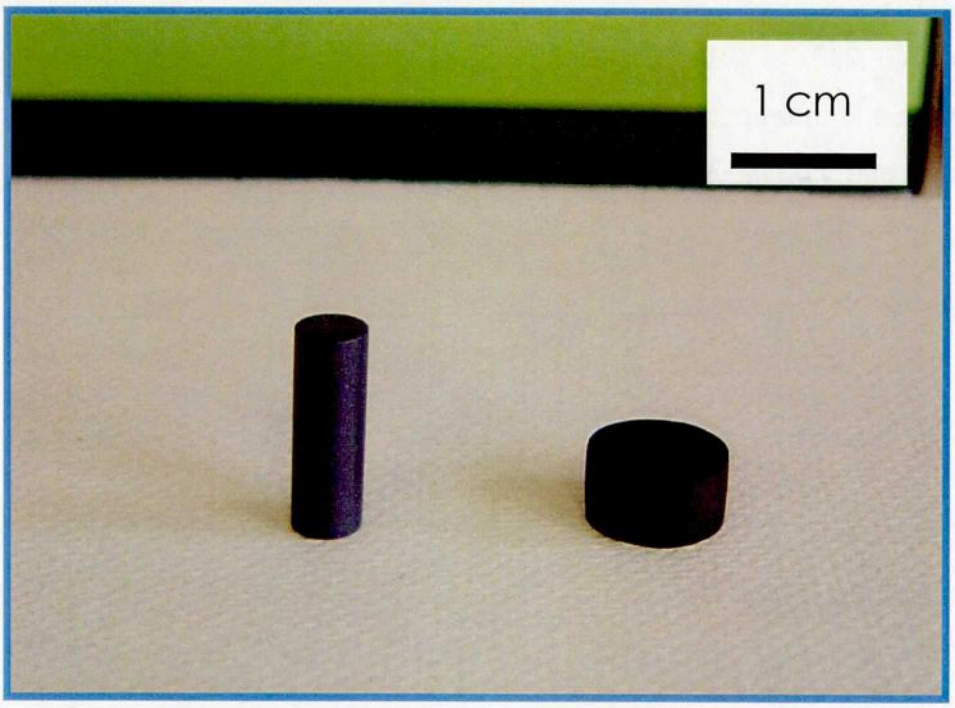


Fig. 2.3.8. Appearances of the bulk yttrium hydride.

Fig. 2.3.10 shows the lattice parameter at room temperature as a function of the hydrogen content C_H [H/Y], together with literature data. The present results are in good agreement with the results of Landin [65], Khatamian [66], Lundin [67], and Daou [68]. It is found from this figure that the lattice parameter slightly decreases with increasing the hydrogen content, according to the following relationship:

$$a\,[\mathrm{nm}] = 0.5216 - 4.367\times10^{-4}\times C_H\,(\mathrm{H/Y}) \qquad (2\text{-}3\text{-}12)$$

It was confirmed that the densities of the hydrides determined from weight and dimensional measurements approximately equaled to the theoretical density, which

was calculated from the lattice parameter. Therefore it is considered that there exist scarce voids in the sample. Micro cracks or voids were not found on the surface and inside of the samples from the confocal scanning laser microscope observation.

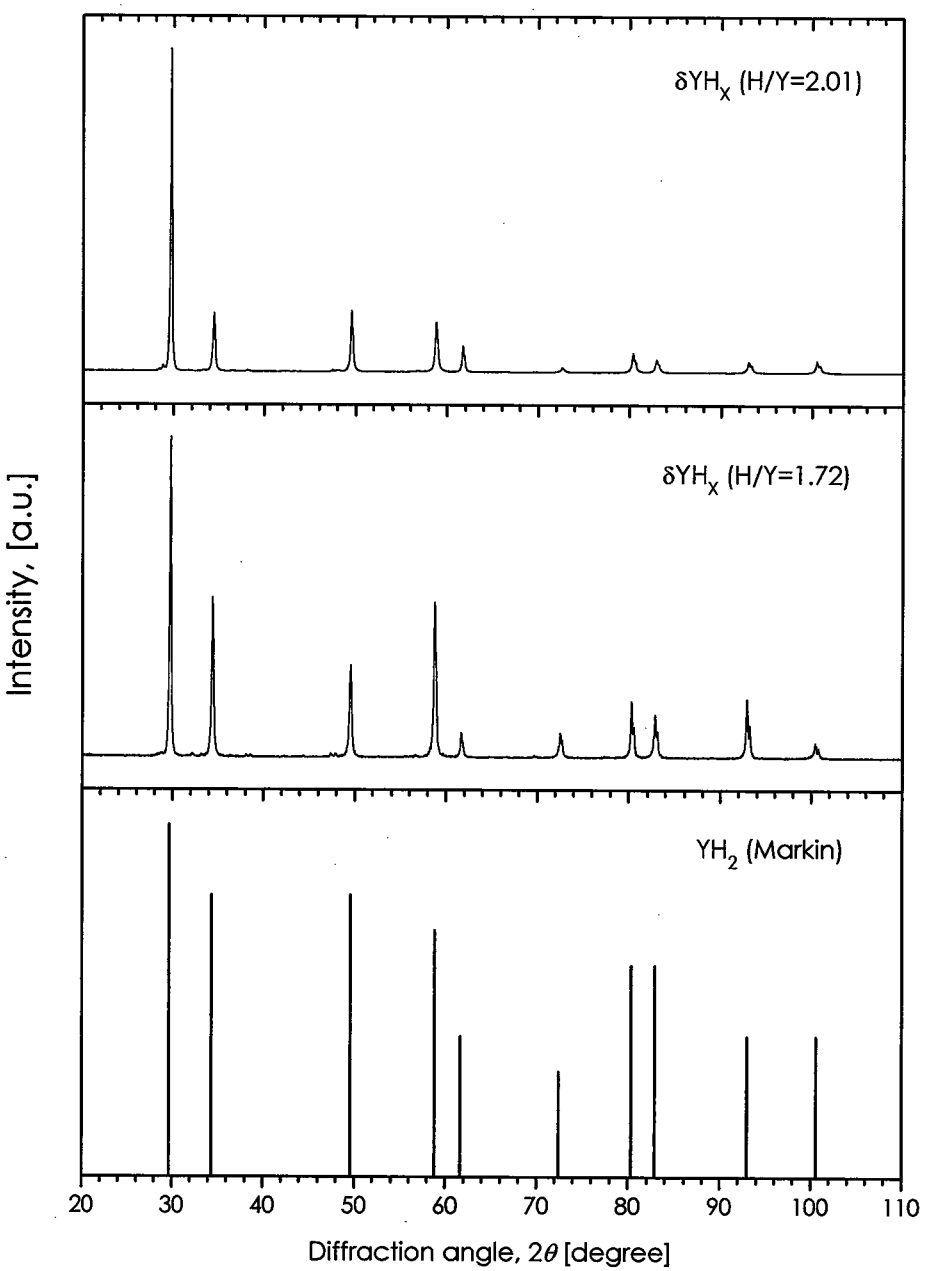


Fig. 2.3.9. X-ray diffraction patterns of yttrium hydride, together with literature data [64].

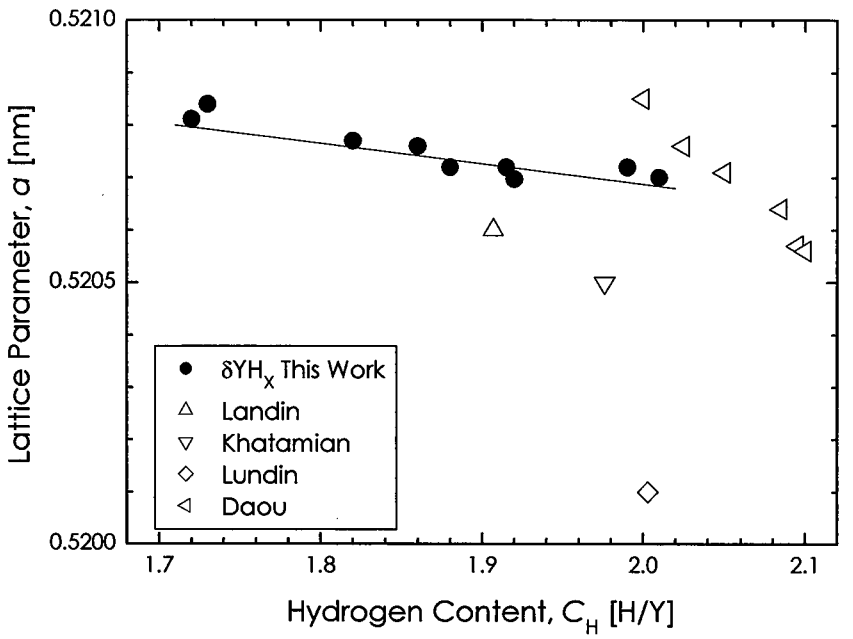


Fig. 2.3.10. Lattice parameter at room temperature of yttrium hydride as a function of hydrogen content, together with literature data [65-68].

Fig. 2.3.11 shows the density at room temperature of the hydrided yttrium as a function of hydrogen content C_H [H/Y]. In the α phase region, the density of the yttrium decreases with hydrogen addition, due to lattice expansion. In the $(\alpha+\delta)$ two phase region, the density of hydrided yttrium is supposed to decrease with increasing the hydrogen content, because the density of the yttrium hydride is smaller than that of the yttrium hydrogen solid solution. In the δ phase region, the density gradually increases with the hydrogen content due to lattice shrinking. From the measurements using electron backscattering diffraction pattern (EBSP) as shown in Fig. 2.3.12, the grain sizes of the samples are found to be around 77 μm, which is larger than those of titanium and zirconium hydrides. It is considered that the difference in hydrogen absorption temperature described in section 2-2 would contribute to this difference. Apparent crystalline orientation in the samples was not confirmed from the many time EBSP measurements. It is considered that the prepared samples are isotropic polycrystalline materials.

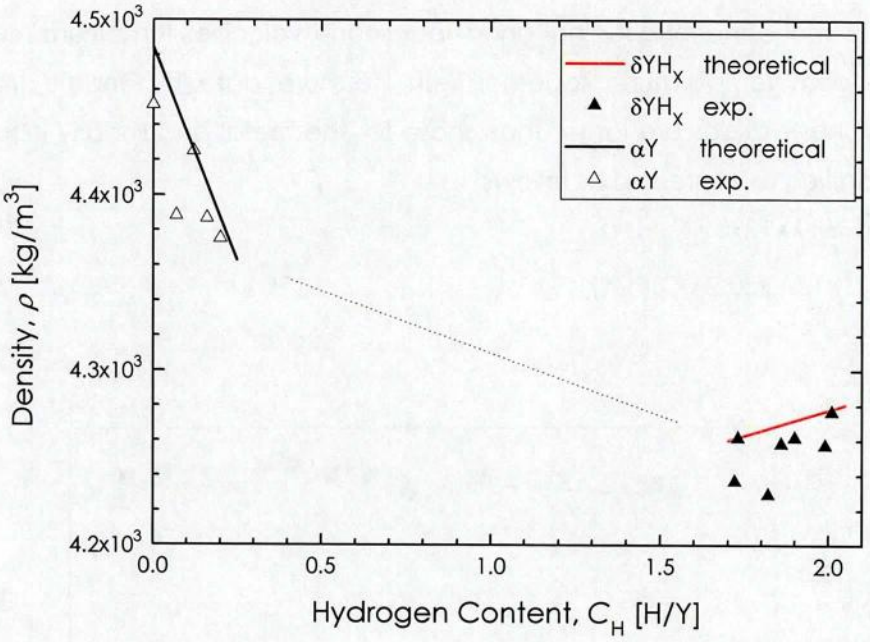


Fig. 2.3.11. Density at room temperature of the hydrided yttrium as a function of hydrogen content.

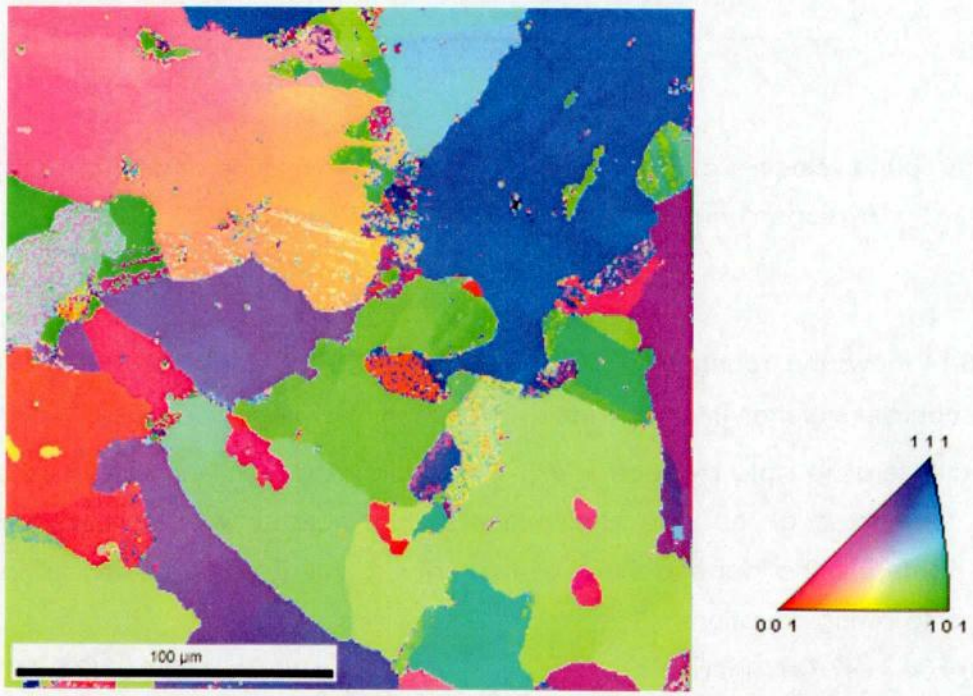


Fig. 2.3.12. Crystal orientation map of yttrium hydride $YH_{1.86}$.

(e) Mechanical Properties of Yttrium Hydride

Fig. 2.3.13 shows the longitudinal and shear sound velocities for yttrium metal and hydrides at room temperature, together with literature data by Beattie [69]. The velocities for the hydrides are larger than those for the metal and linearly increase by hydrogen addition as expressed as follows;

$$V_L[\mathrm{m/s}] = 3640 + 1295 \times C_H(\mathrm{H/Y}) \quad (2\text{-}3\text{-}13)$$

$$V_S[\mathrm{m/s}] = 1813 + 930.2 \times C_H(\mathrm{H/Y}) \quad (2\text{-}3\text{-}14)$$

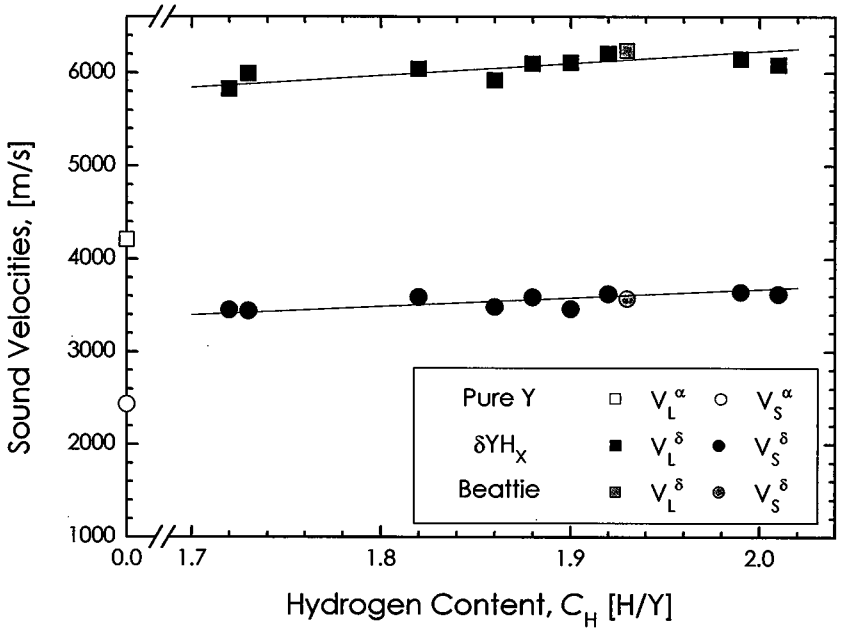


Fig. 2.3.13. Sound velocities at room temperature of yttrium hydride as a function of hydrogen content, together with literature data [69].

Fig. 2.3.14 shows the Young's modulus E, shear modulus G, and bulk modulus B at room temperature of the yttrium hydride as a function of hydrogen content C_H [H/Y], together with literature data by Beattie [69]. The elatic moduli of the yttrium hydride are larger than those of the pure yttrium and slightly increase with increasing the hydrogen content. The dependences of hydrogen content on these moduli are described as following equations:

$$E[\mathrm{GPa}] = 38.7 + 49.7 \times C_H(\mathrm{H/Y}) \quad (2\text{-}3\text{-}15)$$

$$G[\mathrm{GPa}] = 15.2 + 20.4 \times C_H(\mathrm{H/Y}) \quad (2\text{-}3\text{-}16)$$

$$B[\mathrm{GPa}] = 27.4 + 29.5 \times C_H(\mathrm{H/Y}) \quad (2\text{-}3\text{-}17)$$

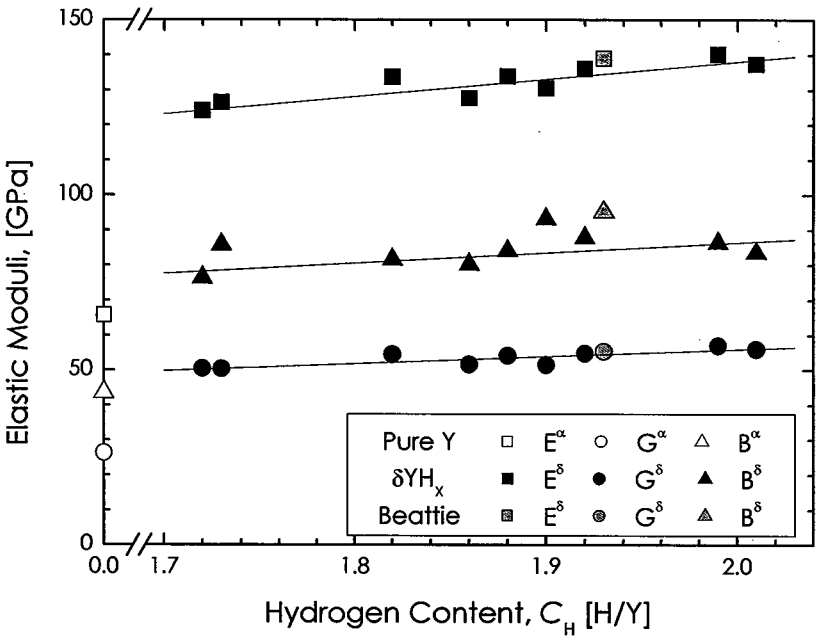


Fig. 2.3.14. The elastic moduli at room temperature of yttrium hydride as a function of hydrogen content, together with literature data [69].

Fig. 2.3.15 shows the Poisson's ratio of the yttrium hydride as a function of hydrogen content. It is found from this figure that the Poisson's ratio is not changed by hydrogen addition. Therefore, the crystal of the yttrium hydride is considered to become isotropically harder due to hydrogen addition. Fig. 2.3.16 shows the Debye temperatures at room temperature of the yttrium hydride as a function of hydrogen content, together with the value that estimated from the literature data by Beattie. Beattie calculated the Debye temperature of $YH_{1.93}$ as 537 K, determining that the N in the equation (2-2-6) was equal to the number of all atoms in the unit cell. In this figure, the author re-calculated the Debye temperature as 375 K assuming that N was 4, for comparing with the results of the present study, and for the unification with the previous studies for the titanium and zirconium hydrides [9, 13, 16, and 21]. The Debye temperature of the hydride is higher than that of the pure yttrium and increases with increasing the hydrogen content as expressed as follows:

$$\theta_D[K] = 234 + 66.2 \times C_H(H/Y) \qquad (2\text{-}3\text{-}18)$$

The increase is caused because the yttrium hydride is elastically harder than the pure yttrium.

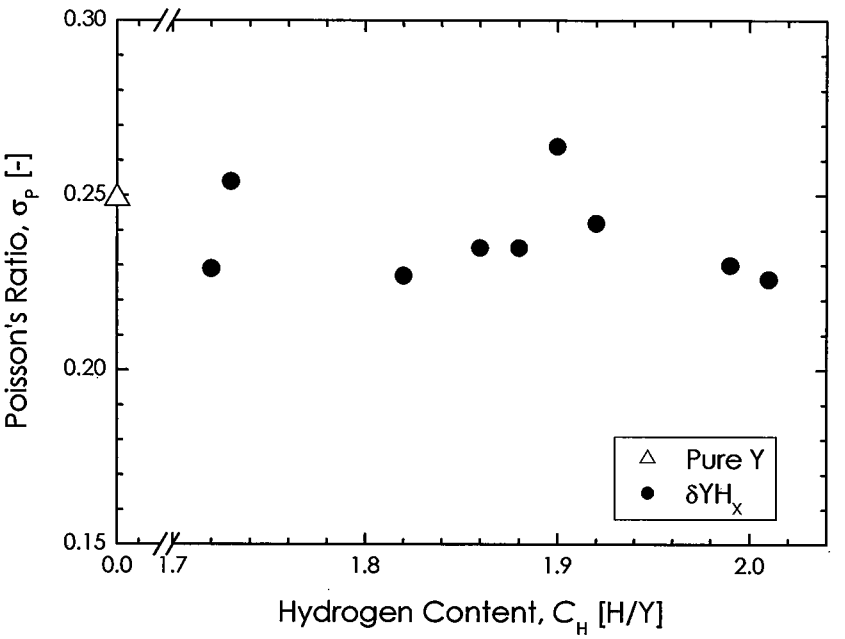


Fig. 2.3.15. Possion's ratio at room temperature of yttrium hydride as a function of hydrogen content.

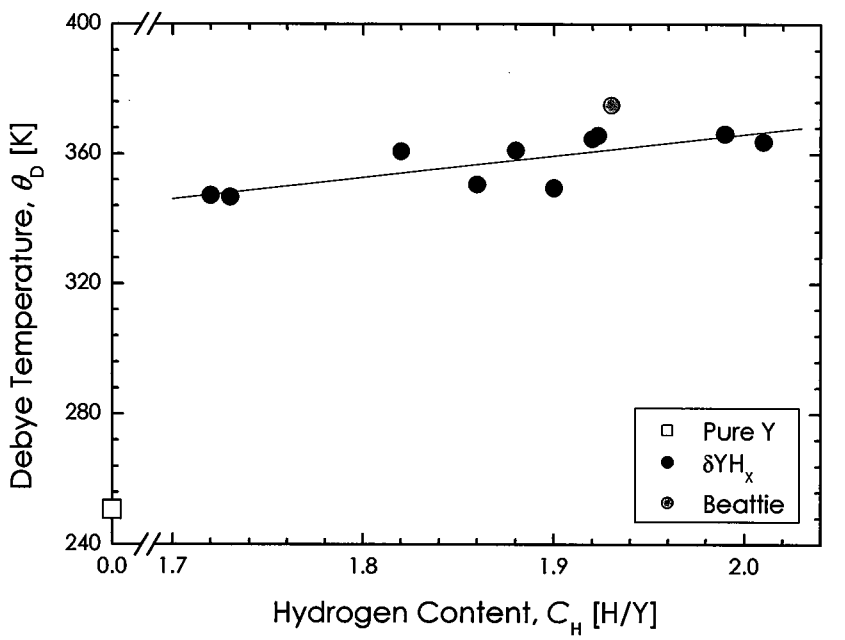


Fig. 2.3.16. Debye temperature of yttrium hydride as a function of hydrogen content, together with the value that estimated from literature data [69].

Fig. 2.3.17 shows the Vickers hardness at room temperature of the yttrium hydride, together with literature data by Parker [70]. The hardness values of the hydrides are also larger than that of the pure yttrium and slightly increase with the hydrogen addition, expressed as follows:

$$H_V[\mathrm{GPa}] = 1.90 + 3.00 \times C_H(\mathrm{H/Y}) \qquad (2\text{-}3\text{-}19)$$

Lundin [71] reported that the increase of hydrogen content induced the increase of hardness of yttrium hydride. Therefore it is considerable that this accordance of the increasing hardness between Lundin and the present study indicate that hydrogen addition hardens the hydride.

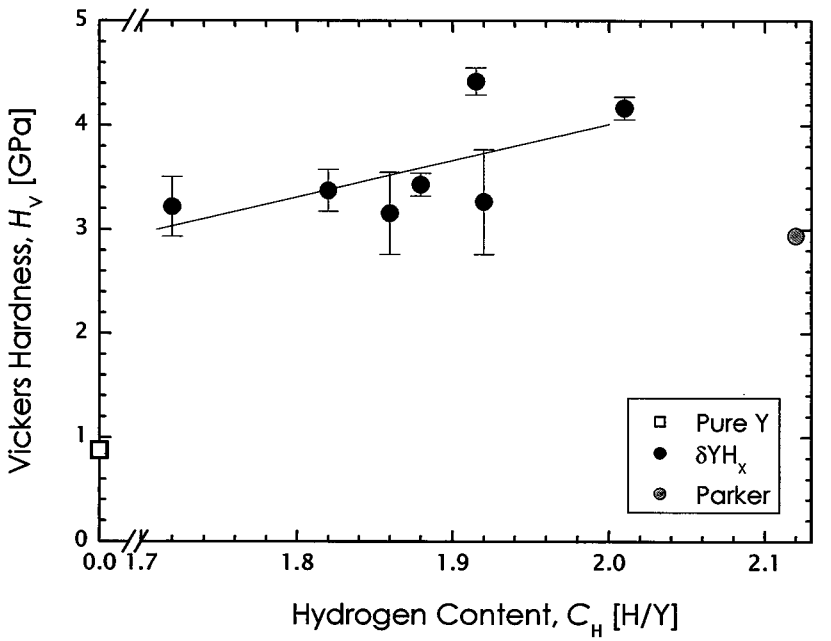


Fig. 2.3.17. Vickers hardness at room temperature of yttrium hydride as a function of hydrogen content, together with literature data [70].

(f) Electrical and Thermal Properties of Yttrium Hydride

Fig. 2.3.18 shows the temperature dependence of electrical resistivity of yttrium hydride, together with literature data by Daou [72]. The electrical resistivity of yttrium hydride shows metallic temperature dependence and is drastically lower than that of the pure yttrium. This drastic decrease also reported in literatures [72, 73]. The increase of the Debye temperature is one of the reasons for the significant decrease of

the resistivity with hydrogenation. It is considered that the number of electrons as carriers of yttrium hydride is smaller than those of the pure yttrium because some free electrons are utilized in the metal-hydrogen bond. Therefore, the decrease in electrical resistivity should be attributed to the increase in mobility of the carriers. The first principle electronic structure calculations on same rare-earth metal and hydrogen system were previously performed by Gupta et al. [74-76]. They indicated that the electron-phonon interaction of the lanthanum hydride was smaller than that of pure lanthanum, which resulted in reduction of its electrical resistivity due to hydrogenation. The similar discussion can be hold for the yttrium-hydrogen system because the yttrium and lanthanum are same rare-earth metals.

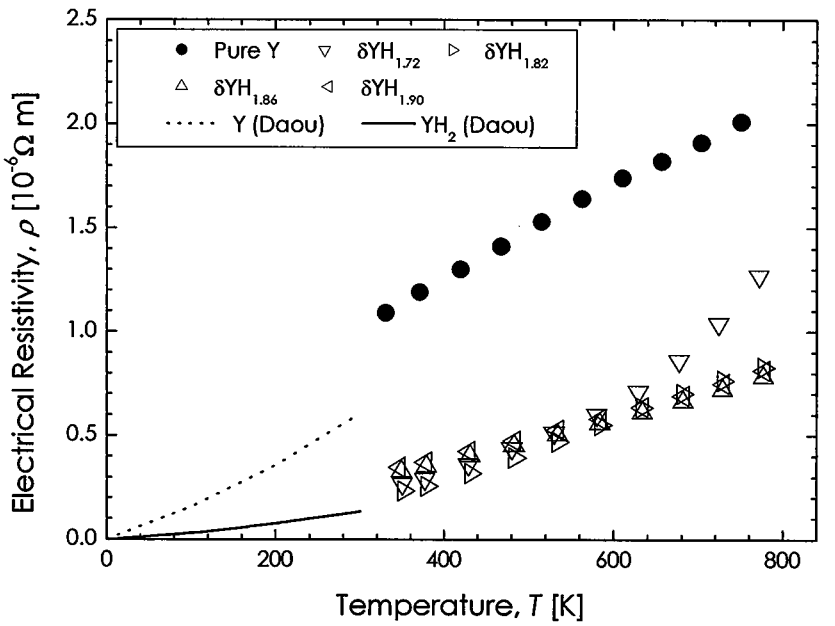


Fig. 2.3.18. Temperature dependence of electrical resistivity of yttrium hydride, together with literature data [72].

Fig. 2.3.19 and Fig. 2.3.20 show the temperature dependence of thermal expansion and linear thermal expansion coefficient (LTEC) of the yttrium hydrides, together with the literature data by Nolting [77], Touloukian [78], and Lundin [79]. The present data are good accordance with the literatures. The LTECs of the yttrium hydrides are almost same as that of the pure yttrium but slightly increase with increasing temperature and hydrogen content.

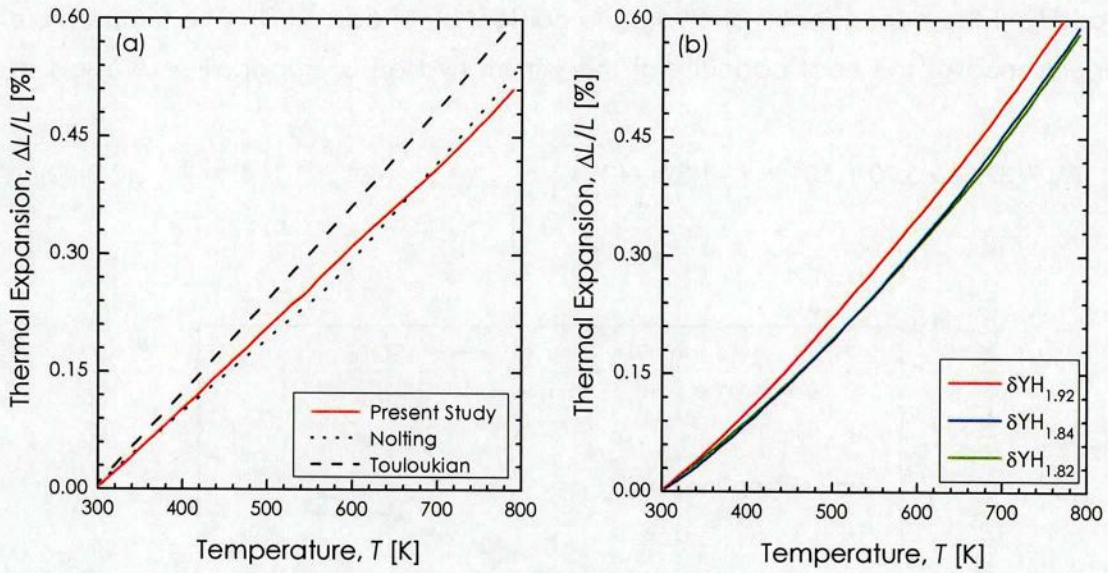


Fig. 2.3.19. Temperature dependence of thermal expansion; (a) Pure Y, (b) Yttrium hydride, together with literature data [76, 77].

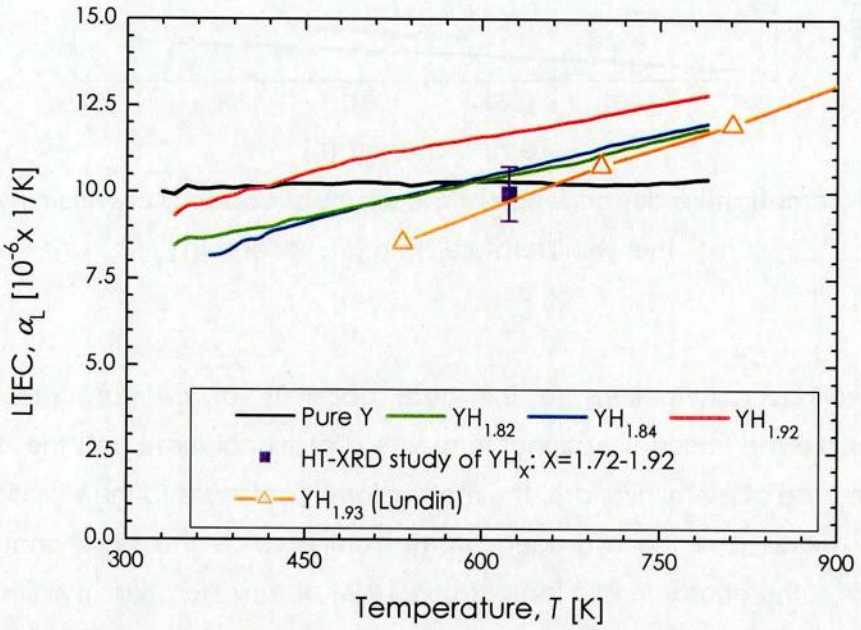


Fig. 2.3.20. Temperature dependence of linear thermal expansion coefficient (LTEC) of yttrium hydride, together with literature data [79].

Fig. 2.3.21 shows the temperature dependence of specific heat capacities C_P of the pure yttrium and the yttrium hydrides, together with literature data [51, 80, and 81].

The specific heat capacity of yttrium hydride is much higher than that of the pure yttrium. In addition, the dependence on hydrogen content is not observed. The temperature dependence of the heat capacity of the yttrium hydride is empirically expressed as follows:

$$C_P = 37.28 + 5.707 \times 10^{-2} \times T - 1.391 \times 10^{6} \times T^{-2} \quad \text{(2-3-20)}$$

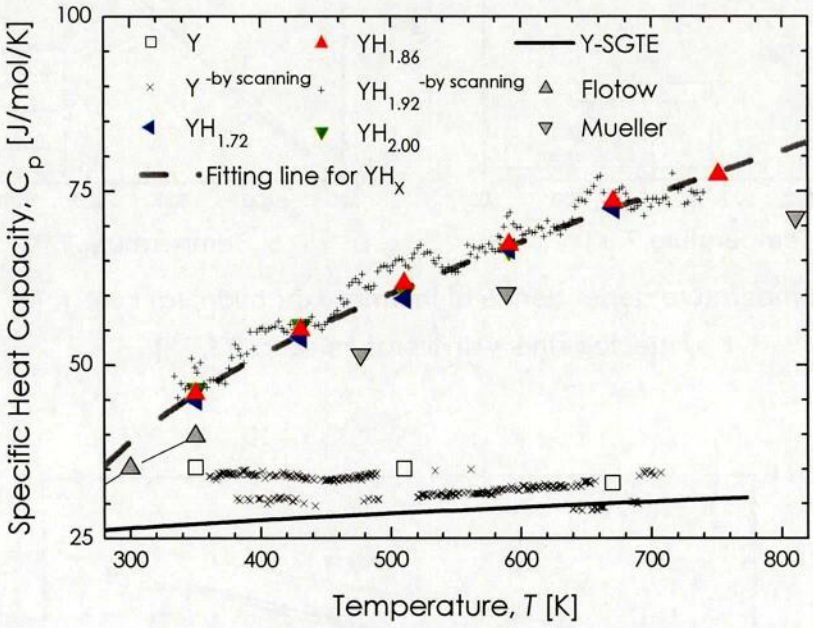


Fig. 2.3.21. Temperature dependence of specific heat capacity of yttrium hydride, together with literature data [51, 80, and 81].

There are various contributions to the heat capacity at constant pressure: the contributions are the lattice vibrational term, the dilatational term, and the electronic term. In the case of metal hydrides, the metal atoms contribute to the vibrational term for acoustic mode and the hydrogen atoms contribute to the vibrational term for optical mode. The characteristic temperature θ [K] of their vibrations is quite different from each other because of their large difference in the mass between the metallic atoms and the hydrogen atom. Therefore the total heat capacity C_P is approximately expressed as follows:

$$C_P = C_V{}^{Y} + C_d + C_{el} + C_V{}^{H} \quad \text{(2-3-21)}$$

where the $C_V{}^{Y}$ is the vibrational term for the acoustic mode, the C_d is the dilatational

term, the C_{el} is the electronic term, and C_V^H is the vibrational term for the optical mode, respectively. The acoustic vibrational term of metal C_V^M can be calculated by means of the Debye approximation using the following equation:

$$C_V^Y = 9R\left(\frac{T}{\theta_D}\right)^3 \int_0^{\theta_D/T} \frac{x^4 e^x}{\left(e^x - 1\right)^2} dx \qquad (2\text{-}3\text{-}22)$$

where θ_D is the Debye temperature that can be adopted from the present experimental data and R is the gas constant. The dilatational term is estimated as follows:

$$C_d = \alpha_L^2 V_m B T / 9 \qquad (2\text{-}3\text{-}23)$$

where α_L is the linear thermal expansion coefficient, V_m is the molar volume, and B is the bulk modulus. The present experimental data were utilized for calculating the term. The electronic term can be also calculated as the following equation:

$$C_{el} = \gamma T \qquad (2\text{-}3\text{-}24)$$

The reference data of the coefficient of electronic heat capacity γ by Flotow [80] was adopted for the yttrium hydride. The optical vibrational term of hydrogen C_V^H can be calculated by means of Einstein approximation using the following equation:

$$C_V^H = 3C_H R\left(\frac{\theta_E}{T}\right)^2 \frac{\exp(\theta_E / T)}{\{\exp(\theta_E / T) - 1\}^2} \qquad (2\text{-}3\text{-}25)$$

where C_H is the hydrogen content in atomic ratio [H/M], and $\theta_E = h\nu / k$ is the Einstein temperature reported by Semekov [82]. The calculation was carried out with the presumption that these input parameters were independent of temperature.

Fig. 2.3.22 shows the calculated heat capacity of YH_2, together with experimental results. The calculated heat capacity is slightly lower than the experimental results obtained in the present study. It is found that the acoustic mode of the lattice vibration is the most dominant below 200 K, whereas the heat capacity from the hydrogen optical mode increases with temperature above room temperature.

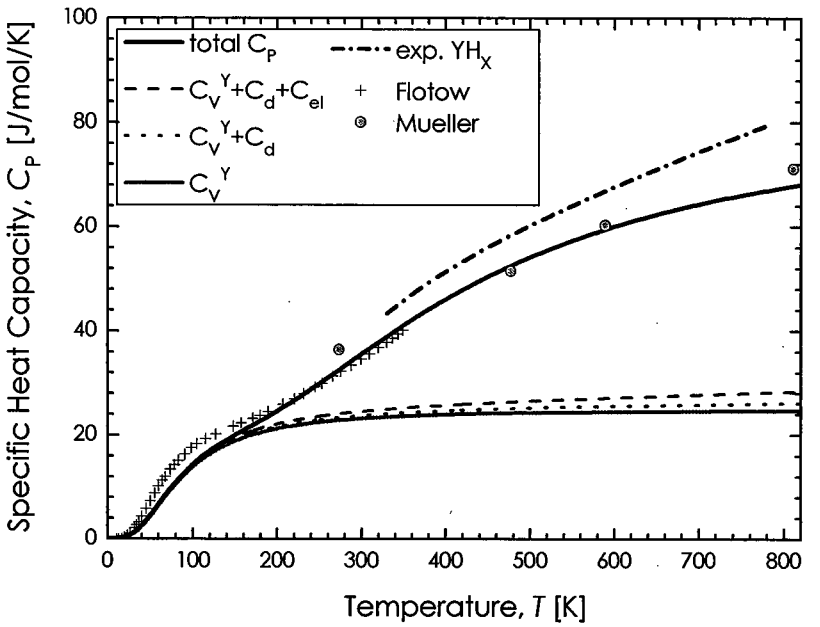


Fig. 2.3.22. Temperature dependence of the calculated heat capacity of yttrium hydride, together with the experimental results.

Fig. 2.3.23 shows the temperature dependence of thermal diffusivities α of the yttrium hydride. The thermal diffusivity of the yttrium hydride decreases with increasing temperature. The diffusivities of the hydrides are higher than that of the pure yttrium in the temperature range from room temperature to 700 K and not affected by the hydrogen content. This characteristic becomes much more pronounced as temperature decreases. The temperature dependence of the thermal diffusivity of δYH_X for the present study is expressed as follows:

$$\alpha[m^2/s] = \frac{0.160}{T} - 1.31\times10^{-5} \qquad (2\text{-}3\text{-}26)$$

The thermal conductivity κ was derived from the thermal diffusivity α, the heat capacity C_P, and the density ρ:

$$\kappa = \alpha C_P \rho \qquad (2\text{-}3\text{-}27)$$

Fig. 2.3.24 shows the estimated thermal conductivity of the yttrium hydride, which is higher than that of the pure yttrium. As with the diffusivity, the thermal conductivity of the hydride decreases with temperature increases, whereas that of the pure metal stays almost constant. A slight dependence on the hydrogen content of the conductivity is observed.

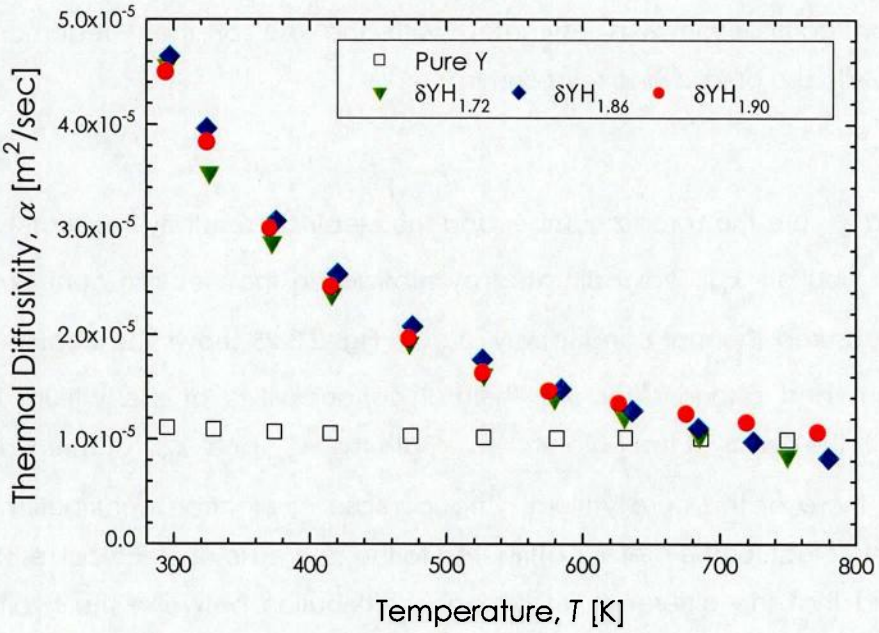


Fig. 2.3.23. Temperature dependence of thermal diffusivity of yttrium hydride.

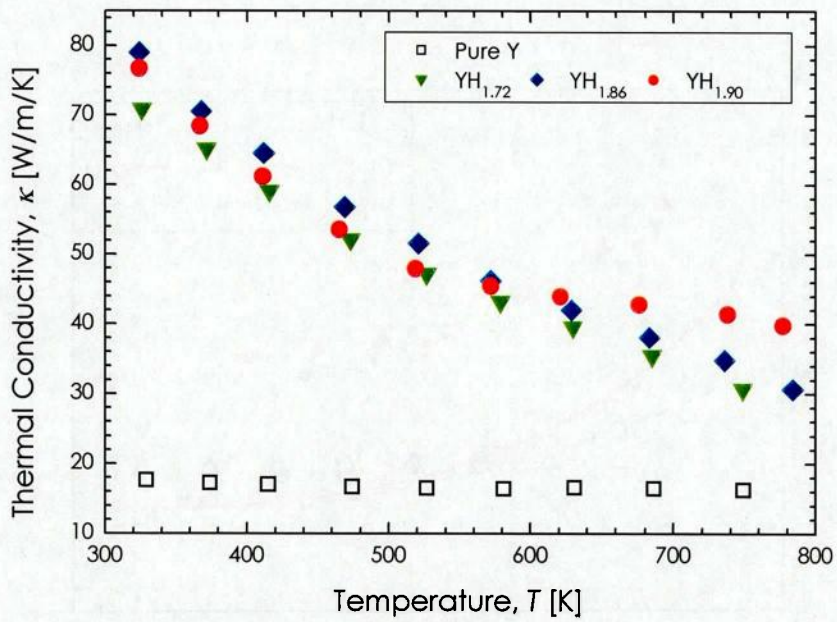


Fig. 2.3.24. Temperature dependence of thermal conductivity of yttrium hydride.

The total thermal conductivity can be approximately represented as the sum of the electron (κ_{el}) and phonon (κ_{ph}) components as follows:

$$\kappa_{total} = \kappa_{el} + \kappa_{ph} \qquad (2\text{-}3\text{-}28)$$

The electron contribution was estimated with the use of the Wiedemann–Franz relationship with use of following relationship:

$$\kappa_{el} = \frac{LT}{\rho} \qquad (2\text{-}3\text{-}29)$$

where L and ρ are the Lorentz number and the electrical resistivity, respectively. The phonon contribution κ_{ph} was estimated by subtracting the electron contribution κ_{el} from the measured thermal conductivity κ_{total}. Fig. 2.3.25 shows the contributions of the electrons and phonons for the thermal conductivities of the yttrium hydride, together with the results of the pure yttrium. Both the κ_{el} and κ_{ph} of the hydride are larger than those of the pure yttrium. The increase of electron contribution for the hydride against that for the metal is attributed to the decrease of electrical resistivity. It is considered that the difference of phonon contribution between the hydride and metal is caused by the difference of the Debye temperature. The thermal conductivities of titanium and zirconium hydrides showed a nearly constant value of 20 W/m/K against Temperature [12, 13, and 23]. Therefore the yttrium hydride is superior to the titanium and zirconium hydrides in regard of heat removal.

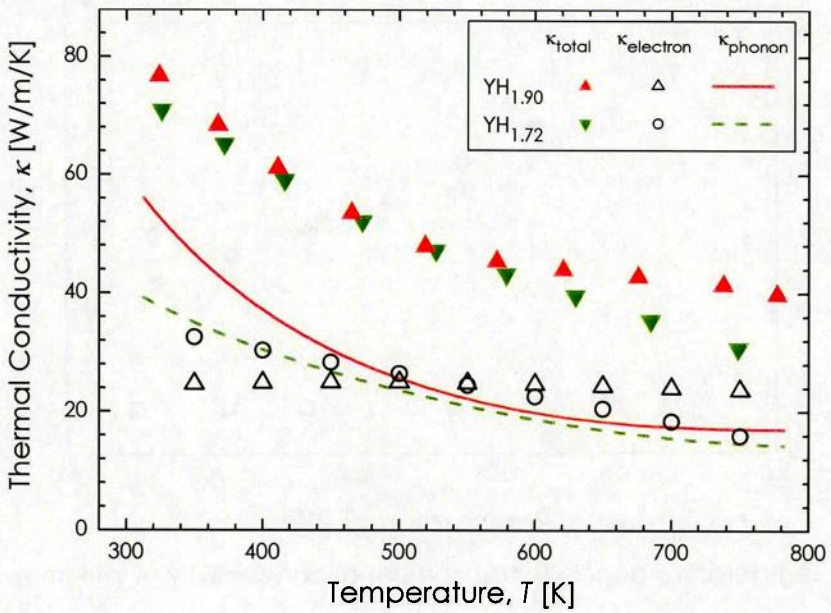


Fig. 2.3.25. Contributions of the electrons and phonons for the thermal conductivity of yttrium hydride.

2-3-2. Hf-H system

(a) Sample Characterization of Hafnium Hydride

Various shapes of bulk hafnium hydrides could be produced. Fig. 2.3.26 shows the appearances of the prepared samples that is silver-gray colored. Hydrogen contents C_H of the prepared samples were in the range from 1.54 to 1.73 in atomic ratio [H/Hf]. Fig. 2.3.27 shows the X-ray diffraction patterns at room temperature of the hafnium hydride, together with literature data by Sidhu [83]. From the analysis, it was found that the samples prepared in the present study are a fluorite type structured fcc_C1 (δ) single phase or a δ' single phase. It was confirmed that the sample whose hydrogen content was below 1.58 in atomic ratio had the δ' phase.

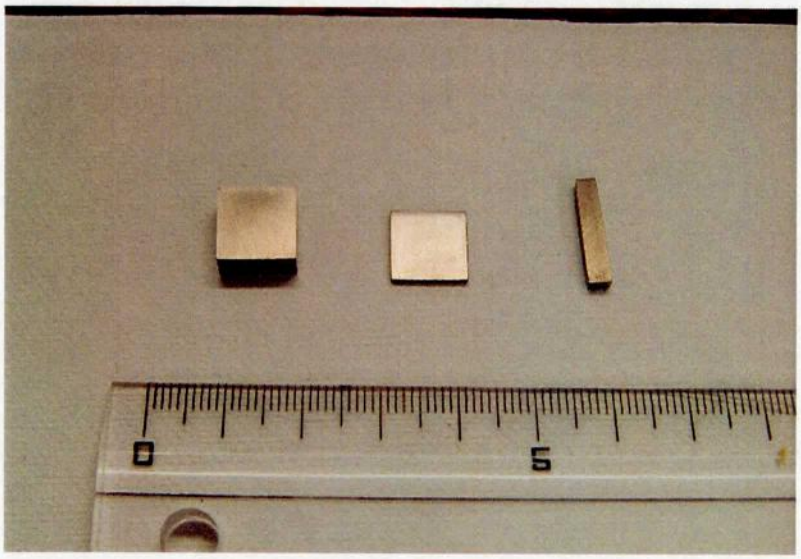


Fig. 2.3.26. Appearance of various shapes of the bulk hafnium hydride.

Fig. 2.3.28 shows the lattice parameter at room temperature of the hafnium hydride δHfH_X as a function of the hydrogen content C_H [H/Hf], together with literature data by Sidhu [33, 83], Espagno [34], Katz [84], and Lewis [52]. The present results are in good agreement with the literature data. It is found from this figure that the lattice parameter linearly increases with increasing the hydrogen content, according to the following empirical relationship:

$$a[nm] = 0.4295 + 2.513 \times 10^{-2} \times C_H(H/Hf) \qquad (2\text{-}3\text{-}30)$$

The densities of the samples determined from weight and dimensional measurements

were found to be about 97% to the theoretical density that was calculated from the lattice parameter. The density of the pure hafnium used in the present study was also about 97% to the theoretical density. The commercial grade hafnium contains a few percent impurity of zirconium, which would cause the smaller densities of the present samples than their theoretical densities. Micro cracks or voids were not found on the surface and inside of the samples from the confocal scanning laser microscope observation. From the EBSP measurements as shown in Fig. 2.3.29, the grain sizes of the samples are found to be around 15μm, which is similar to those of hydrides of titanium and zirconium those are congener elements. Apparent crystalline orientation in the samples was not confirmed from the many time EBSP measurements. It is considered that the prepared samples are isotropic polycrystalline materials.

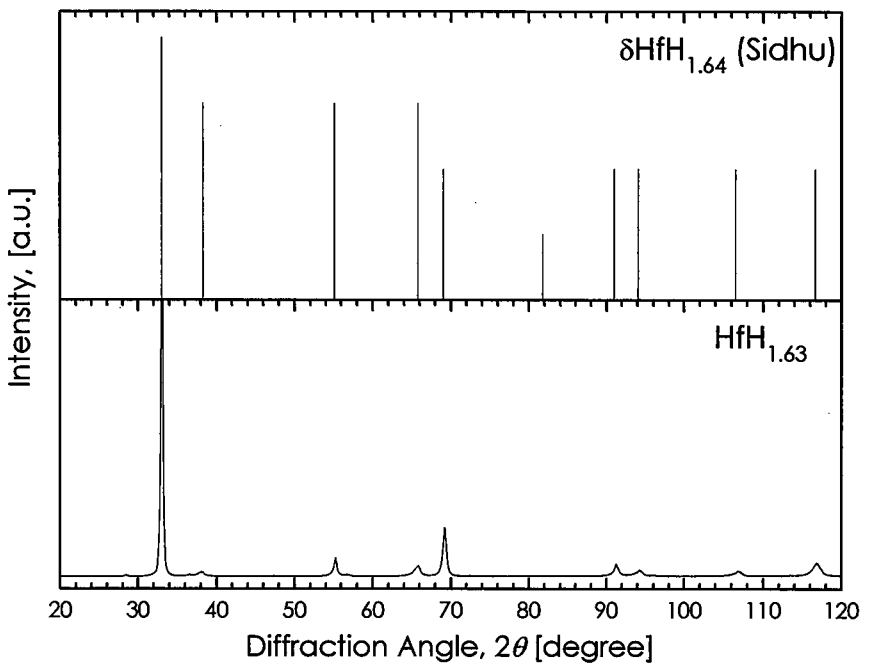


Fig. 2.3.27. X-ray diffraction patterns at room temperature of hafnium hydride, together with reference data [83].

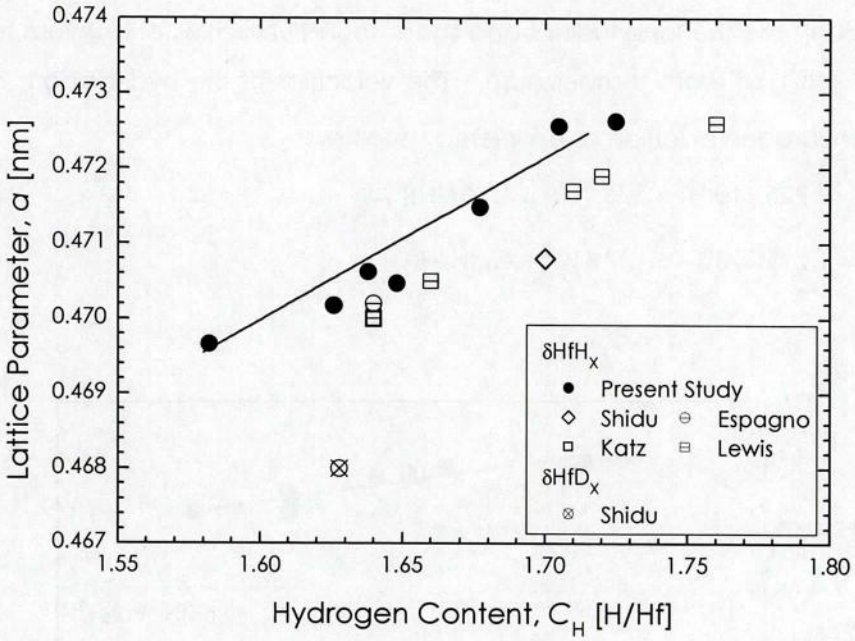


Fig. 2.3.28. Lattice parameters at room temperature of hafnium hydride as a function of hydrogen content, together with literature data [33, 34, 52, 83, and 84].

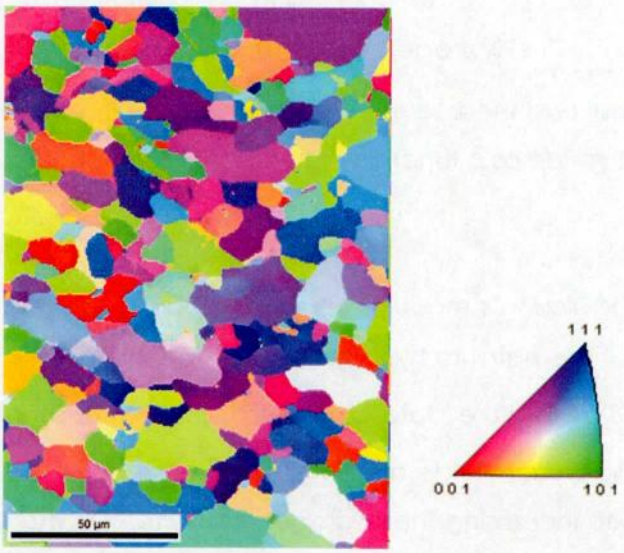


Fig. 2.3.29. Crystal orientation map of hafnium hydride $\delta HfH_{1.68}$

(b) Mechanical Properties of Hafnium Hydride

Fig. 2.3.30 shows the longitudinal and shear sound velocities of hafnium metal and the hydride δHfH_X at room temperature. The velocities of the hydrides are drastically reduced by hydrogen addition as expressed as follows;

$$V_L[m/s] = 9.925\times10^3 - 3.375\times10^3 \times C_H(H/Hf) \quad (2\text{-}3\text{-}31)$$

$$V_S[m/s] = 1.215\times10^4 - 6.187\times10^3 \times C_H(H/Hf) \quad (2\text{-}3\text{-}32)$$

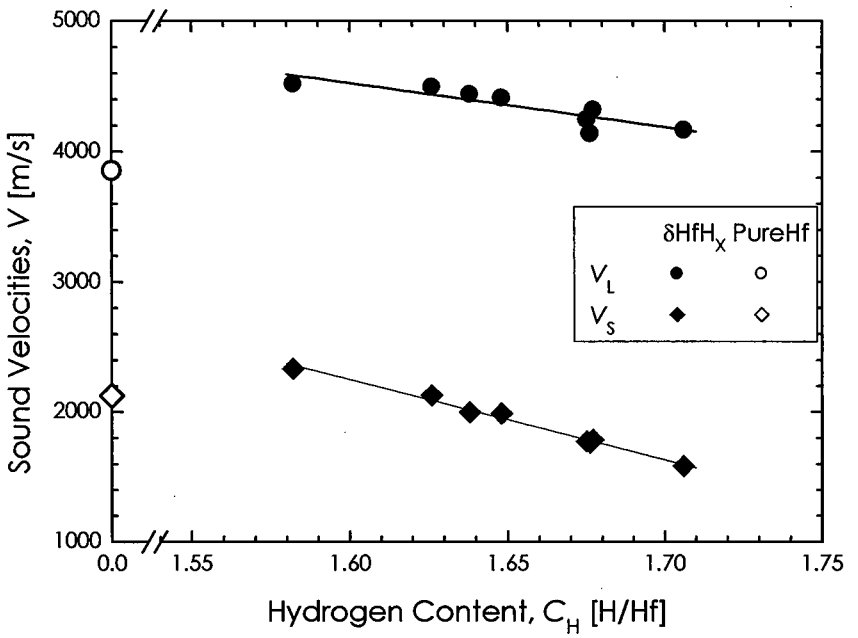


Fig. 2.3.30. Longitudinal and shear sound velocities at room temperature of hafnium hydride as a function of hydrogen content.

Fig. 2.3.31 shows the Young's modulus E, shear modulus G, and bulk modulus B at room temperature of the hafnium hydride δHfH_X as a function of hydrogen content C_H [H/Hf], together with literature data by Gorecki [85]. The Young's modulus and shear modulus of the hafnium hydride are lower than those of the hafnium metal, and drastically decrease with increasing the hydrogen content. On the contrary, the bulk modulus of the hydride is higher than that of the pure hafnium and almost independent of the hydrogen content. The dependencies of hydrogen content on these moduli are empirically described as following equations:

$$E[GPa] = 1.17\times10^3 - 6.40\times10^2 \times C_H(H/Hf) \quad (2\text{-}3\text{-}33)$$

$$G[\mathrm{GPa}] = 4.88\times10^{2} - 2.70\times10^{2}\times C_{H}(\mathrm{H/Hf}) \quad (2\text{-}3\text{-}34)$$

$$B[\mathrm{GPa}] = 2.09\times10^{2} - 3.39\times10^{1}\times C_{H}(\mathrm{H/Hf}) \quad (2\text{-}3\text{-}35)$$

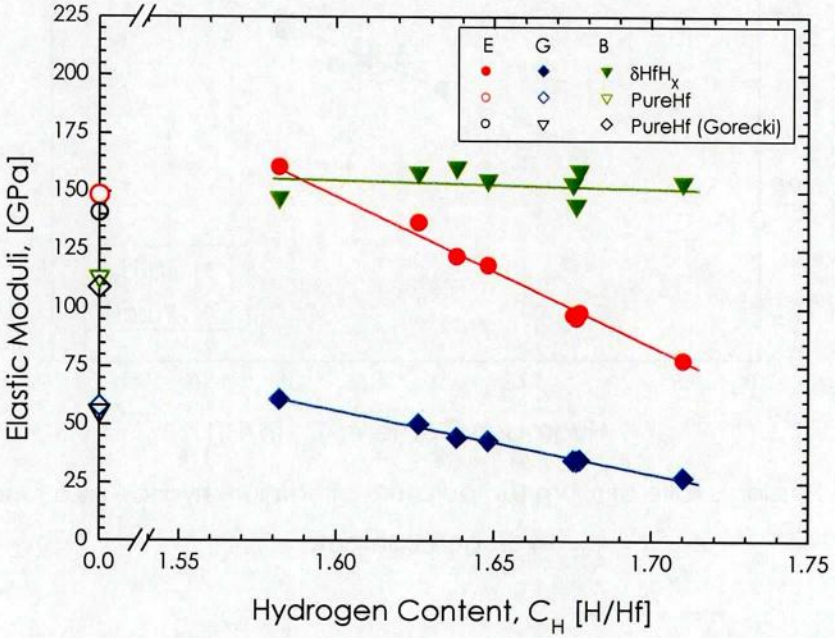


Fig. 2.3.31. Elastic moduli at room temperature of hafnium hydride as a function of hydrogen content, together with literature data [85].

Fig. 2.3.32 shows the Poisson's ratio of the hafnium hydride δHfH_x as a function of hydrogen content C_H [H/Hf]. The Poisson's ratio of the hydride is higher than that of the pure hafnium and increases with increasing the hydrogen content. The dependence of the hydrogen content is described as following equations:

$$\sigma[-] = -0.869 + 0.754\times C_{H}(\mathrm{H/Hf}) \quad (2\text{-}3\text{-}36)$$

The mechanical instability of crystal against all kinds of shear deformations increases with increasing the Poisson's ratio. In other words, the higher Poisson's ratio a crystal has, the lower elastic moduli such as the Young's modulus and shear modulus of the crystal are. Therefore, it is considered that the hydrogen content in the hafnium hydride affects its anisotropic deformation behaviors such as lateral and shear deformations but not the behavior of isotropically elastic deformation. As a result, the hafnium becomes elastically softer by the hydrogenation.

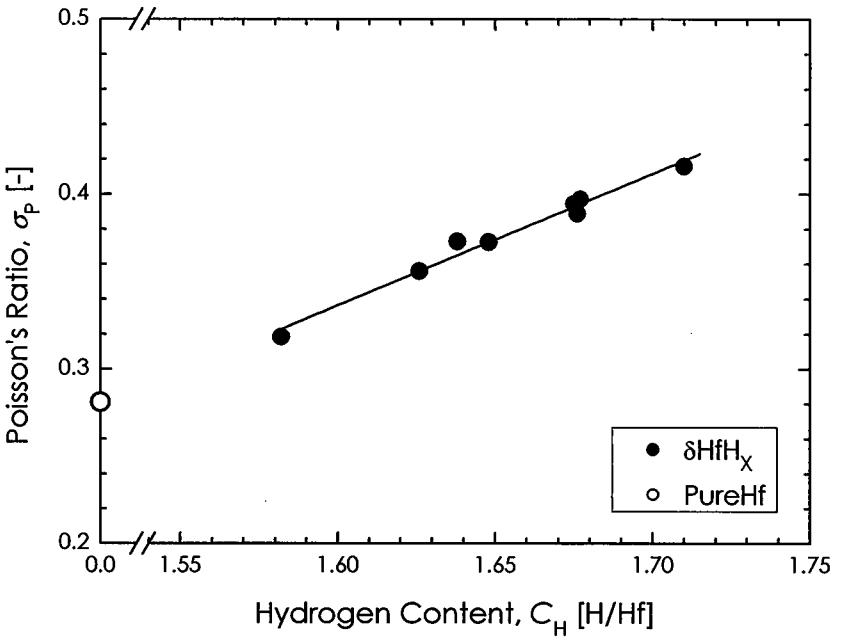


Fig. 2.3.32. Possion's ratio at room temperature of hafnium hydride as a function of hydrogen content.

Fig. 2.3.33 shows the Debye temperatures at room temperature of the hafnium hydride δHfH$_X$ as a function of hydrogen content, together with literature data of low temperature limit by Kittel [86]. The Debye temperature of the hydride is lower than that of the pure hafnium and decreases with increasing the hydrogen content as empirically expressed as follows:

$$\theta_D[K] = 1.05 \times 10^3 - 5.35 \times 10^2 \times C_H(H/Hf) \quad (2\text{-}3\text{-}37)$$

The mechanism of this decrease is same as the decrease of the elastic moduli.

Fig. 2.3.34 shows the Vickers hardness at room temperature of the hafnium hydride δHfH$_X$ as a function of hydrogen content C_H [H/Hf]. The hardness values of the hydrides are higher than that of the pure hafnium. As well as elastic moduli, the hardness decreases with increasing the hydrogen content, expressed as follows:

$$H_V[GPa] = 9.56 - 4.10 \times C_H(H/Hf) \quad (2\text{-}3\text{-}38)$$

The effect of hydrogenation on the mechanical properties for the hafnium is very similar to that of the titanium [21] which is congener element.

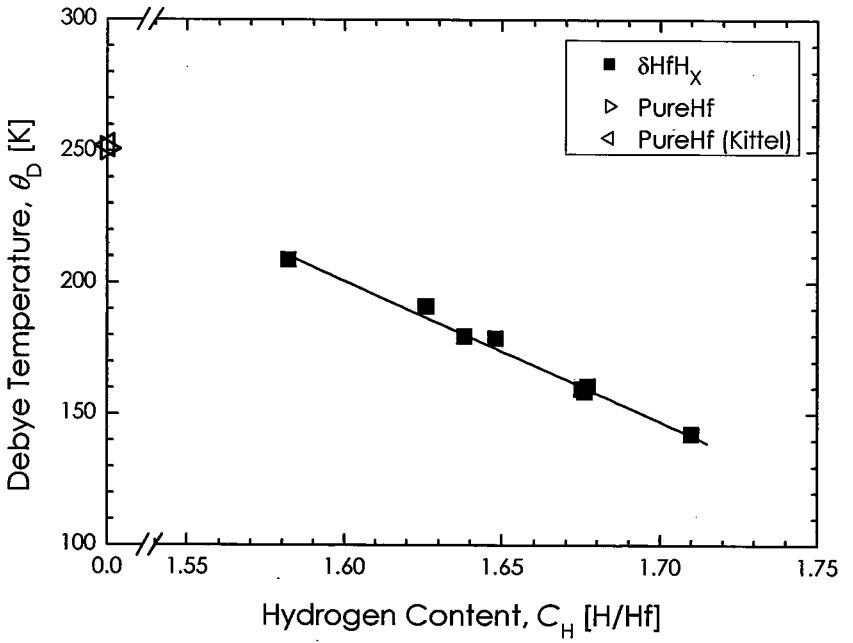


Fig. 2.3.33. Debye temperature of hafnium hydride as a function of hydrogen content, together with literature data [86].

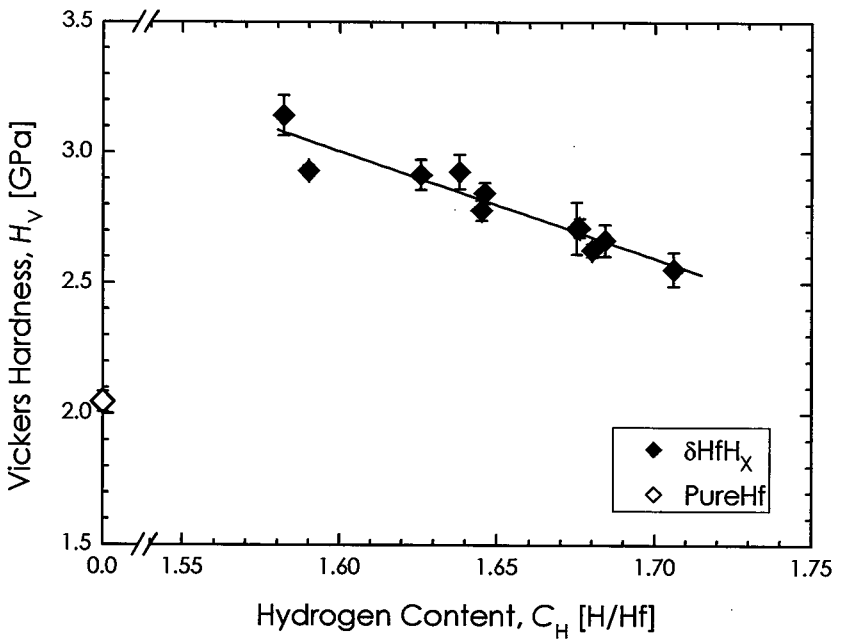


Fig. 2.3.34. Vickers hardness at room temperature of hafnium hydride as a function of hydrogen content.

(c) Electrical and Thermal Properties of Hafnium Hydride

Fig. 2.3.35 shows the temperature dependence of electrical resistivity of hafnium hydride, together with literature data by Rossiter [87] and Andrievskii [88]. The electrical resistivity of hafnium hydride shows metallic temperature dependence and is almost same as that of pure hafnium. The increasing rate with temperature of the hydride is slightly lower than that of the pure metal. These trends are similar to the titanium and zirconium hydride. On the contrary, the hydride sample that has lower hydrogen content than 1.58 in atomic ratio indicates anomalous temperature dependence of the resistivity below 400 K. This is attributed to the δ prime to δ phase transition.

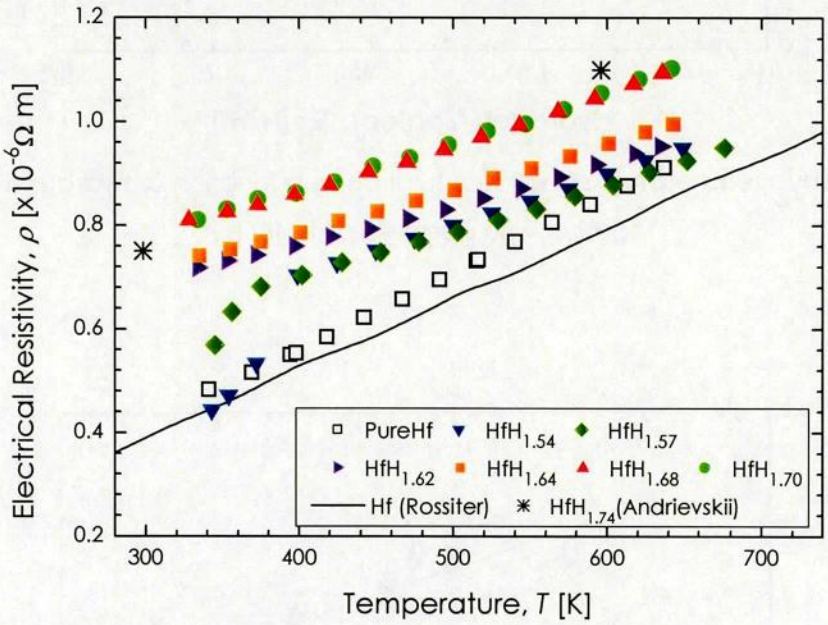


Fig. 2.3.35. Temperature dependence of electrical resistivity of hafnium hydride, together with literature data [87, 88].

Fig. 2.3.36 shows the thermal expansion $\Delta L/L$ of the hafnium hydrides, together with the literature data by Touloukian [77]. There is inflection point at about 400 K in the thermal expansion of the hydride that has lower hydrogen content than 1.58 in atomic ratio. For these samples, the data below about 400 K are for the δ prime phase and the data above the temperature are for the δ phase. The inflection temperature appears to decrease with increasing the hydrogen content. The thermal expansion of the hafnium hydride is higher than that of the pure hafnium and gradually decreases with increasing hydrogen content. The thermal expansion of δ prime phase is slightly

lower than that of the δ phase; the sample expands due to the δ'-δ phase transition.

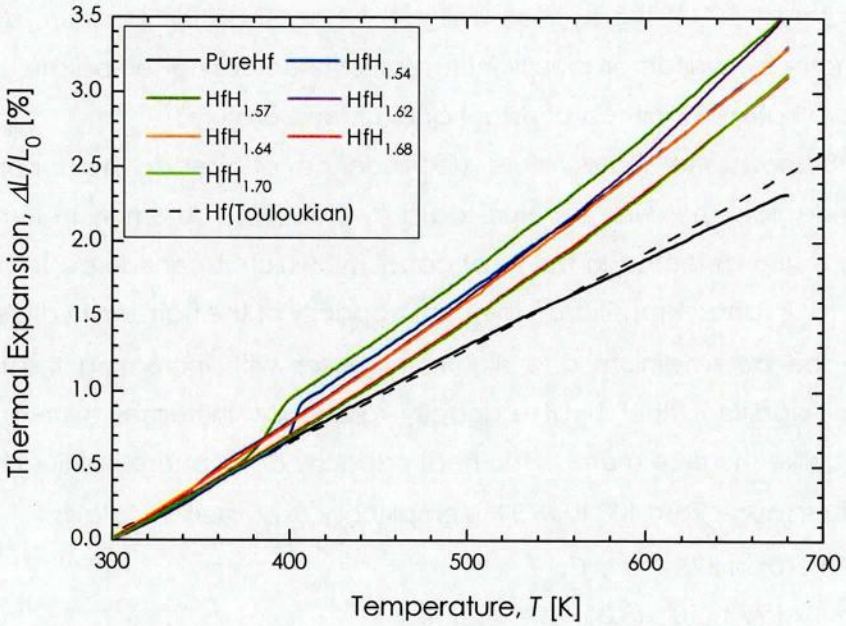


Fig. 2.3.36. Thermal expansion of hafnium hydride, together with literature data [77].

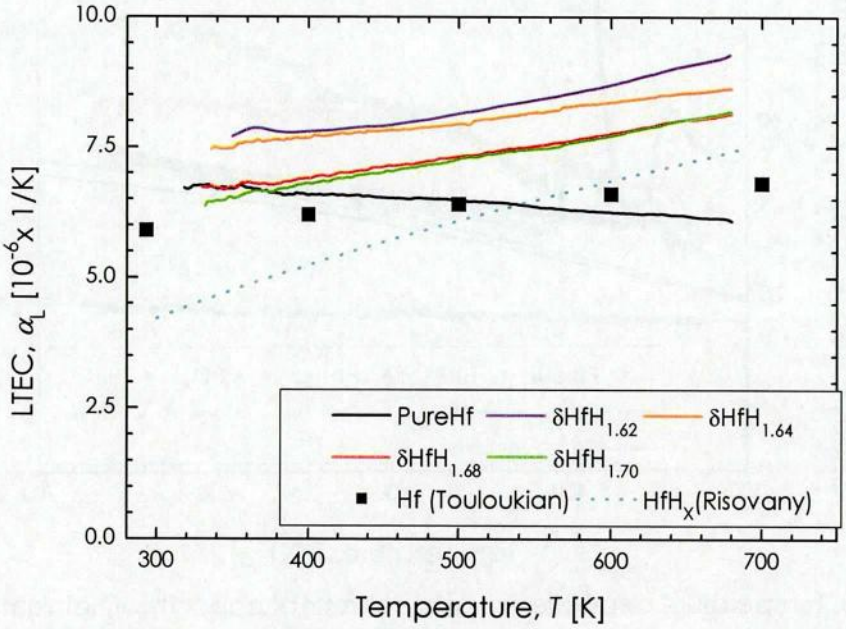


Fig. 2.3.37. Temperature dependence of linear thermal expansion coefficient (LTEC) of hafnium hydride, together with literature data [77, 89].

Fig. 2.3.37 shows the temperature dependence of linear thermal expansion coefficient (LTEC) of the hafnium hydrides, together with the literature data by Risovany [89]. The present LTEC of the hydride is slightly higher than the literature data. The LTEC of the hafnium hydride gradually increases with increasing temperature whereas that of the pure hafnium is almost constant against temperature.

Fig. 2.3.38 shows the temperature dependence of specific heat capacity of hafnium hydride, together with literature data by Cox [90]. Anomaly in temperature dependence is also detected in the heat capacity, which is considered to be due to the δ prime to δ phase transition. The heat capacity of the hafnium hydride is higher than that of the pure hafnium and slightly increases with increasing the hydrogen content. In addition, the heat capacity gradually increases with increasing temperature unlike the pure metal. The heat capacity of δ phase hafnium hydride in the temperature range from 400 to 673 K is empirically expressed as follows:

$$C_P = -7.70\times10^{2} + 4.96\times10^{2}\times C_H + (5.93\times10^{-1} - 3.35\times10^{-1}\times C_H)\cdot T + (8.42\times10^{7} - 5.25\times10^{7}\times C_H)\cdot T^{-2} \quad (2\text{-}3\text{-}39)$$

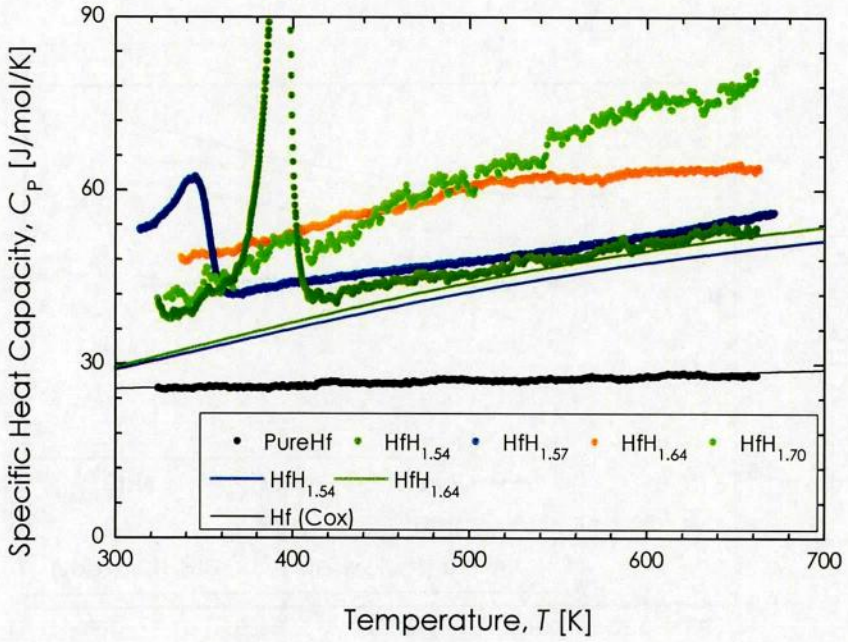


Fig. 2.3.38. Temperature dependence of specific heat capacity of hafnium hydride, together with literature data [90].

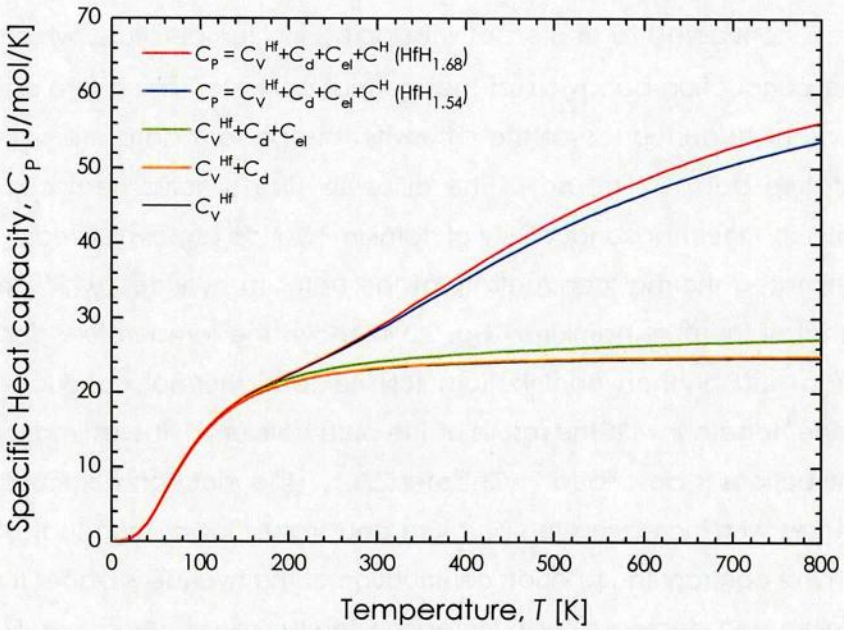


Fig. 2.3.39. Calculated specific heat capacity of hafnium hydride.

Fig. 2.3.39 shows the calculation results specific heat capacity of hafnium hydride. The calculation procedure is described in Chapter 2.3.1. The author couldn't find literature data of the characteristic frequency of optical hydrogen vibration and electronic heat capacity coefficient of the hafnium hydride. Therefore, these data on hydride of titanium that is the congeneric element alternatively utilized for the calculation of the heat capacity [91, 92]. The experimental data are slightly higher than the calculated heat capacities. However, the calculation indicates the qualitative understanding on the heat capacity behavior. The elevations with temperature and hydrogen content are attributable to the excitation of the optical hydrogen vibration.

Fig. 2.3.40 shows the temperature dependence of thermal diffusivities of the hafnium hydride, together with literature data by Tsuchiya [93] and Toloukian [94]. Anomaly in the temperature dependence of the hydride with lower hydrogen content is also detected in the diffusivity, which is considered to be due to the δ prime to δ phase transition. Throughout the electrical and thermal properties, the inflection temperature seems to decrease with increasing the hydrogen content, which is corresponding to the phase diagram information of the hafnium-hydrogen system [32]. The thermal diffusivity of the δ phase hydride is lower than that of the pure hafnium

and slightly decreases due to the hydrogen addition. The thermal diffusivity of the δ' phase hydride drastically decreases with increasing temperature. The lattice stability of the δ' phase is considered to decreases with increasing temperature, which probably influences the conduction behaviors of the thermal carriers. Taking into account the hydrogen content dependence of the diffusivity, the present data are slightly higher than the literature data. With use of the diffusivity, the specific heat capacity, the sample density, the thermal conductivity of hafnium hydride are evaluated. Fig. 2.3.41 shows the estimated thermal conductivity of the hafnium hydrides, which are slightly higher than that of the pure hafnium. Fig. 2.3.42 shows the temperature dependence of the electron and phonon contributions for the total thermal conductivity of the hafnium hydride, together with the results of the pure hafnium. The estimation method of these contributions is described in Chapter 2.3.1. The electron contribution of the hydride increases with increasing temperature and slightly lower than that of the pure hafnium. On the contrary the phonon contribution of the hydride is higher than that of the pure hafnium and decreases with increasing temperature. Accordingly, the total thermal conductivity is almost independent of temperature.

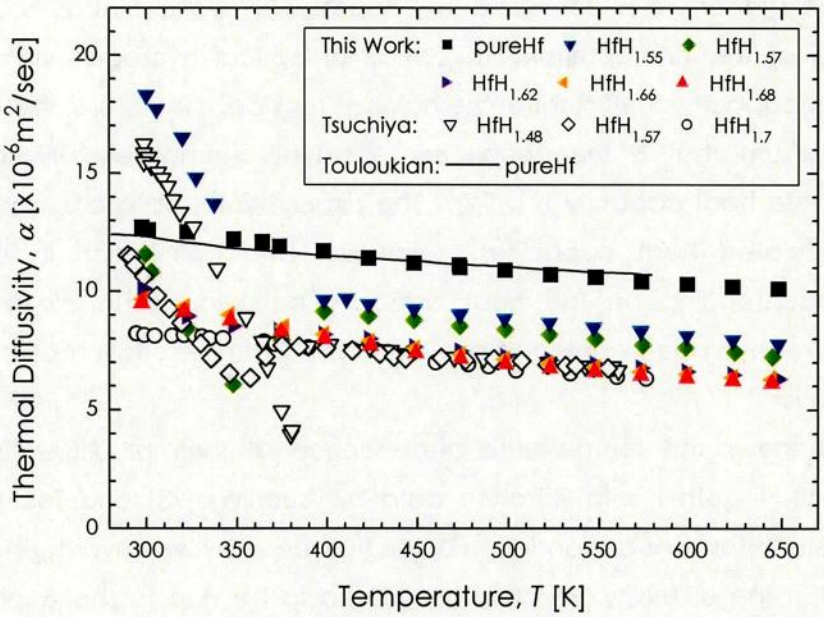


Fig. 2.3.40. Temperature dependence of thermal diffusivity of hafnium hydride, together with literature data [93, 94].

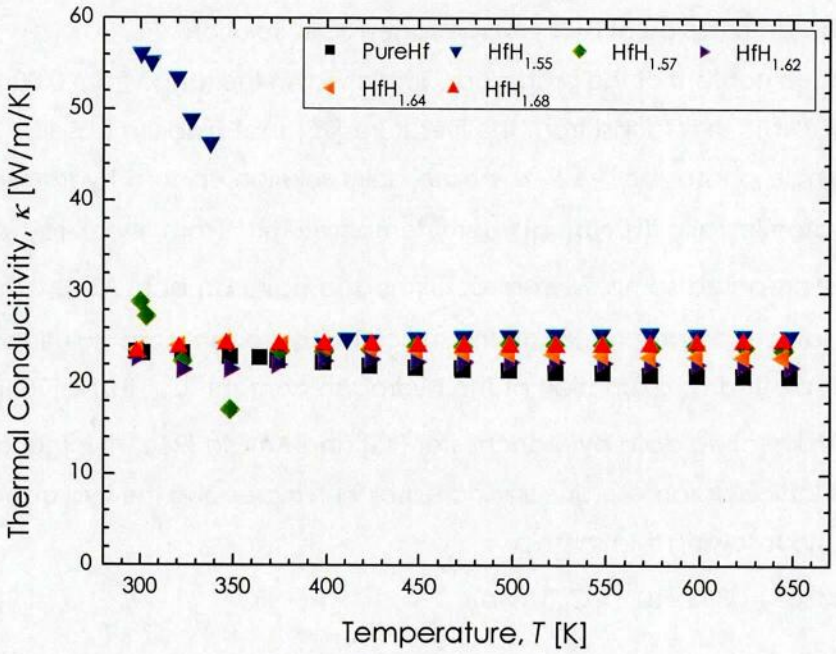


Fig. 2.3.41. Temperature dependence of thermal conductivity of hafnium hydride.

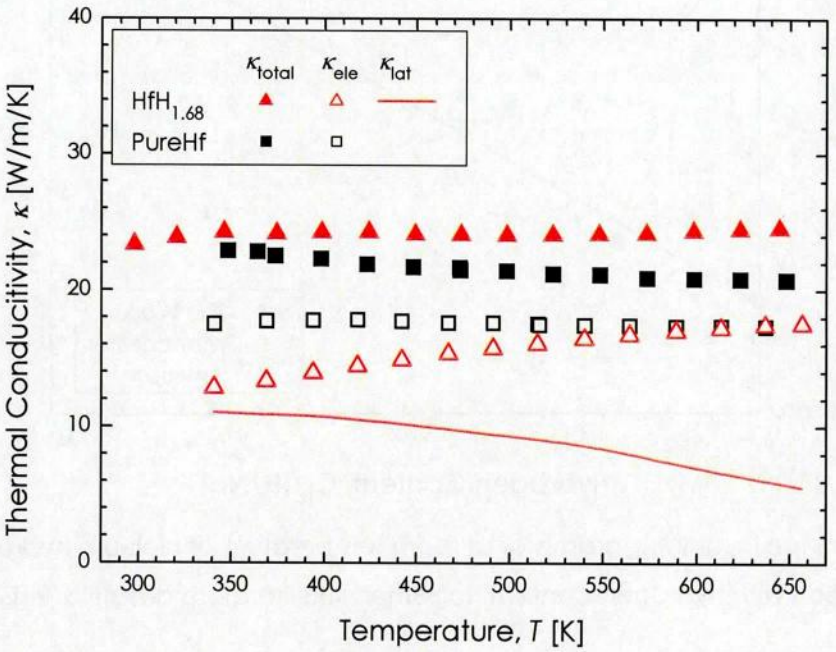


Fig. 2.3.42. Temperature dependence of the electron and lattice contribution to thermal conductivity of hafnium hydride.

2-3-3. Nb-H system

(a) Sample Characterization of Niobium Hydrogen Solid Solution

The hydrogen content of the prepared sample was in the range from 0.00 to 0.032 in atomic ratio [H/Nb]. It is found from the literature [95] that niobium absorbs hydrogen and forms a single phase (bcc_A2, α-phase) solid solution up to a hydrogen content C_H=0.059 in atomic ratio [H/Nb] at room temperature. From the X-ray diffraction analysis all the prepared samples were confirmed to have an bcc_A2 α-Nb(H) single phase. The lattice parameter a of the niobium hydrogen solid solution at room temperature is plotted as a function of the hydrogen content C_H [H/Nb] in Fig. 2.3.43, compared with literature data by Manchester [43] and Amato [96]. It is found from this figure that the lattice parameter linearly increases with increasing the hydrogen content, according to the following relationship:

$$a[\text{nm}] = 0.3303 + 1.382\times10^{-2}\times C_H(\text{H/Nb}) \qquad (2\text{-}3\text{-}40)$$

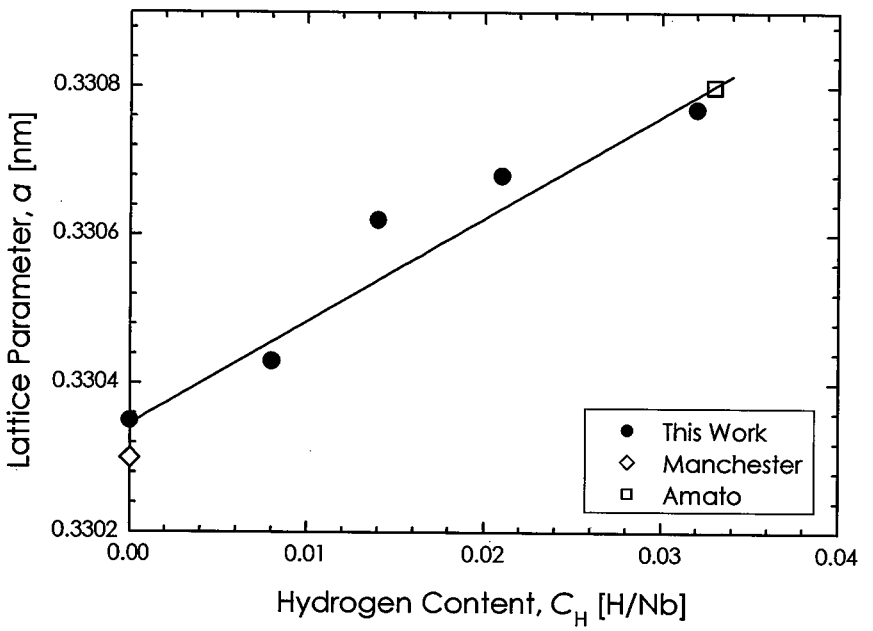


Fig. 2.3.43. Change in lattice parameter at room temperature of niobium hydrogen solid solution with hydrogen content, together with literature data [43, 96].

It has been reported that hydrogen-induced volume expansions in the metals are in the range $2.6 \sim 3.2\times10^{-3}[\text{nm}^3/(\text{H/M})]$. The present hydrogen-induced volume expansion

value is $2.62\times10^{-3}[nm^3/(H/M)]$ and is therefore in good accordance with the literature. It is also found that the geometrical density of the sample, which is determined from the weight and dimensional measurements, is approximately equal to the theoretical density, which is determined from the lattice parameter.

(b) Mechanical Properties of Niobium Hydrogen Solid Solution

Fig. 2.3.44 shows the change in the longitudinal and shear sound velocities of the niobium hydrogen solid solutions at room temperature with the hydrogen content C_H [H/Nb]. It is found from this figure that the sound velocities increases with hydrogen addition as empirically expressed as follows:

$$V_L[m/s] = 5060 + 1.45\times10^3 \times C_H(H/Nb) \quad (2\text{-}3\text{-}41)$$

$$V_S[m/s] = 2050 + 1.00\times10^3 \times C_H(H/Nb) \quad (2\text{-}3\text{-}42)$$

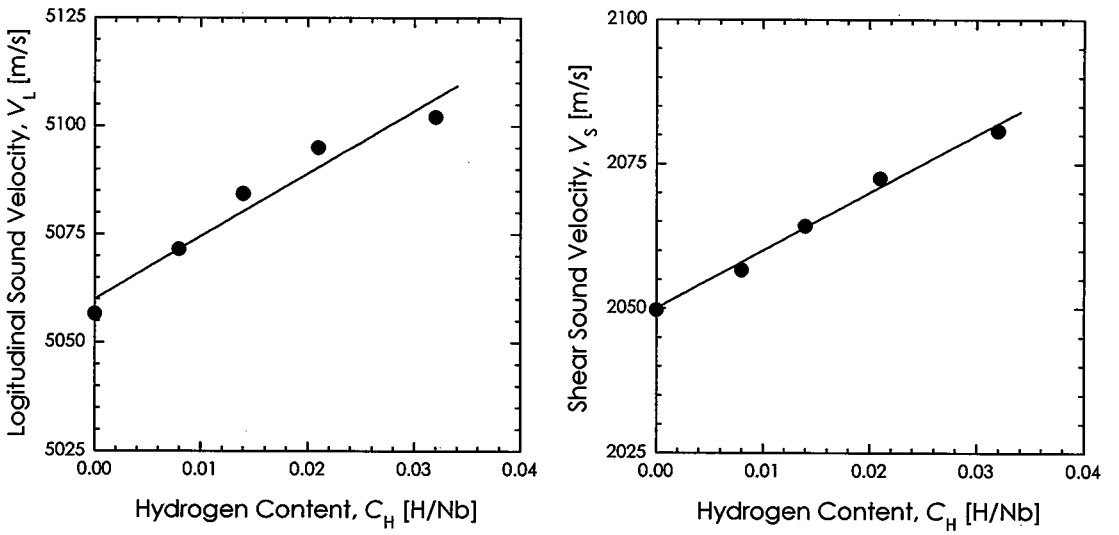


Fig. 2.3.44. Change in longitudinal and shear sound velocities at room temperature of niobium hydrogen solid solution with hydrogen content.

Fig. 2.3.45 shows the Young's modulus and shear modulus of the niobium hydrogen solid solutions as a function of hydrogen content C_H [H/Nb], together with literature data by Fisher [97] and Wriedt [98]. As same as the sound velocities, the elatic moduli of the niobium hydrogen solid solution increases with increasing the hydrogen content. The present result of change in the Young's modulus qualitatively agrees with the literatures. The difference with Fisher in absolute values is acceptable because these

reported values are approximately calculated from the elastic constants of single crystals; the present study expresses more precisely the characteristics of polycrystalline niobium hydrogen solid solution. The dependence of elastic moduli on the hydrogen content in this study is described by the following empirical equations:

$$E[\mathrm{GPa}] = 101 + 84.0 \times C_H(\mathrm{H/Nb}) \quad (2\text{-}3\text{-}43)$$

$$G[\mathrm{GPa}] = 35.9 + 31.2 \times C_H(\mathrm{H/Nb}) \quad (2\text{-}3\text{-}44)$$

Fig. 2.3.46 shows the change in the Debye temperature at room temperature of the niobium hydrogen solid solution as a function of hydrogen content C_H [H/Nb], together with the data obtained from Kittel [86]. The Debye temperature increases with the hydrogen addition as expressed by the following empirical equation:

$$\theta_D[\mathrm{K}] = 264 + 1.16 \times 10^2 \times C_H(\mathrm{H/Nb}) \quad (2\text{-}3\text{-}45)$$

The present result is smaller than the value of low temperature limit (275 K). This difference arises from the use of both different measurement techniques and temperature conditions.

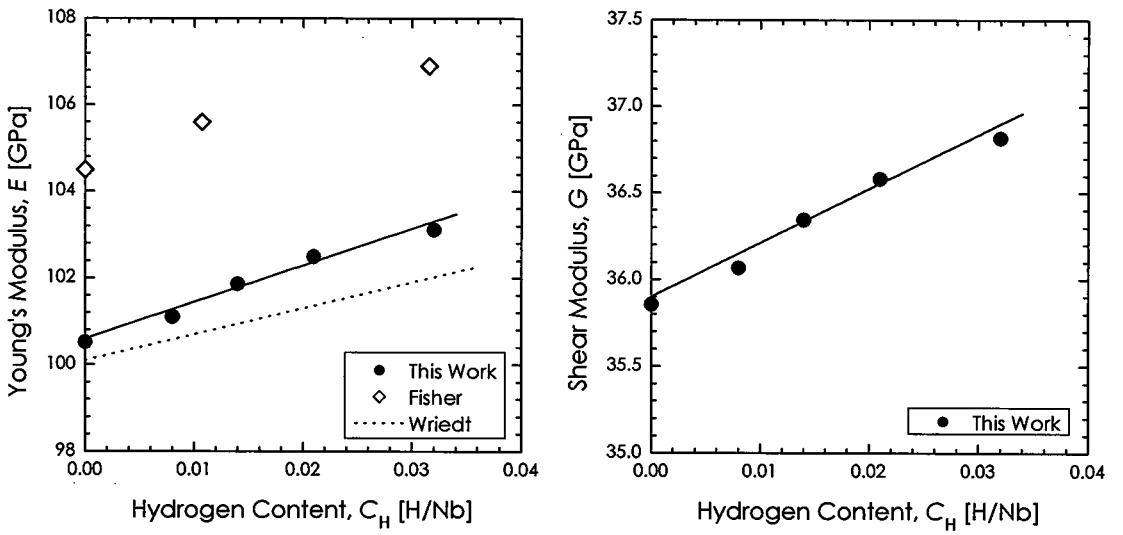


Fig. 2.3.45. Change in Young's and shear moduli at room temperature of niobium hydrogen solid solution with hydrogen content, together with literature data [97, 98].

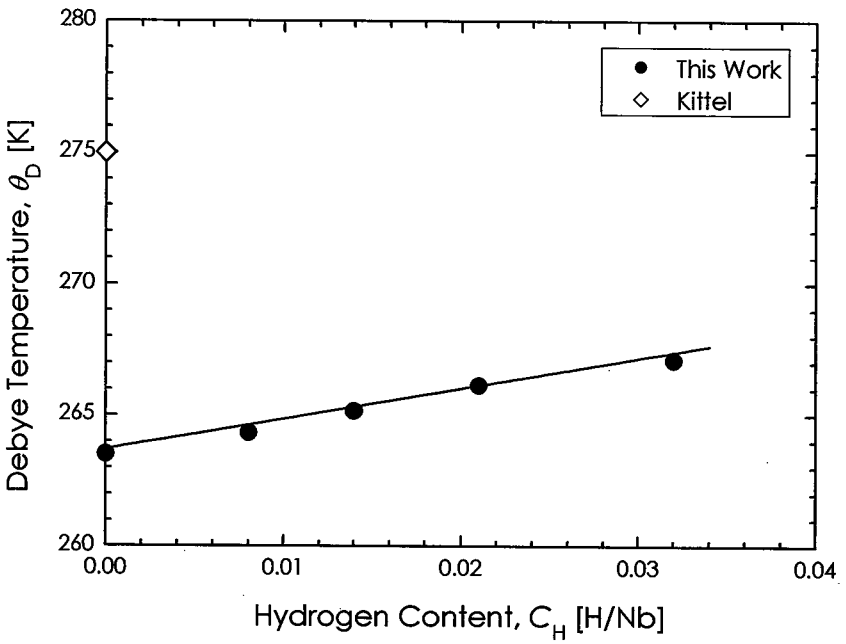


Fig. 2.3.46. Change in Debye temperature of niobium hydrogen solid solution with hydrogen content, together with literature data [86].

Fig. 2.3.47 shows the Vickers hardness H_V at room temperature of the niobium hydrogen solid solutions as a function of hydrogen content C_H [H/Nb]. The Vickers hardness also increases with increasing the hydrogen content as expressed as follows:

$$H_V[\text{GPa}] = 0.536 + 4.83 \times C_H(\text{H/Nb}) \qquad (2\text{-}3\text{-}46)$$

Therefore, it is considered that the niobium is elastically and plastically hardened by the effect of hydrogen dissolution. The elastic moduli and hardness of the titanium and zirconium hydrogen solid solutions, which had hcp crystal structure, were reported to decrease with increasing hydrogen content. On the contrary, the solute hydrogen enhances the mechanical properties of the yttrium hydrogen solid solution that has hcp crystal structure as well as the niobium hydrogen solid solution that has bcc crystal structure. Therefore, the interstitial hydrogen effect appears to be independent of crystal structures. In Chapter 3, the difference of hydrogen effect is discussed in terms of electronic structure.

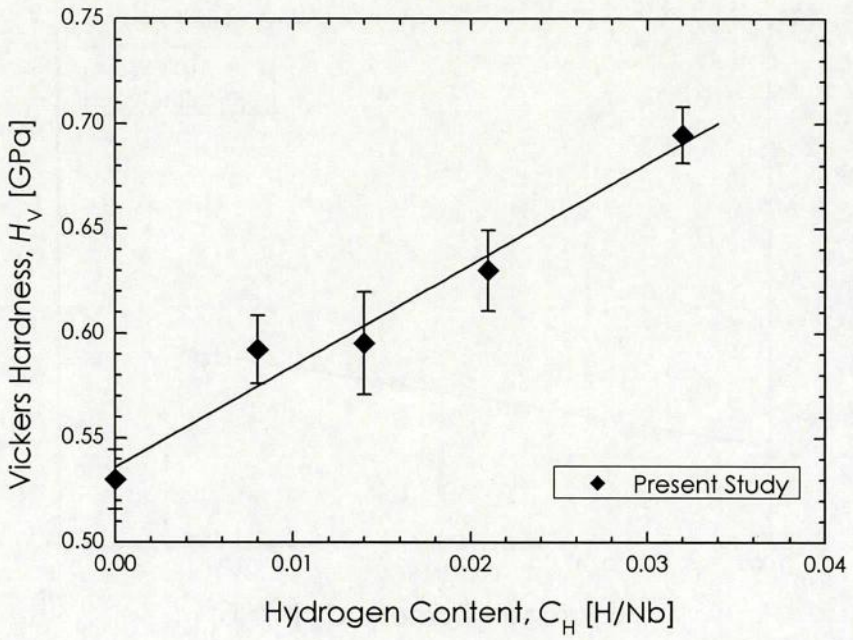


Fig. 2.3.47. Change in Vickers hardness of niobium hydrogen solid solution with hydrogen content.

(d) Sample Characterization of Niobium Hydride

Various shapes of bulk niobium hydrides could be produced. Fig. 2.3.48 shows the appearances of the prepared samples, which has silver-gray color. Hydrogen contents C_H of the prepared samples were in the range from 0.72 to 0.84 in atomic ratio [H/Nb].

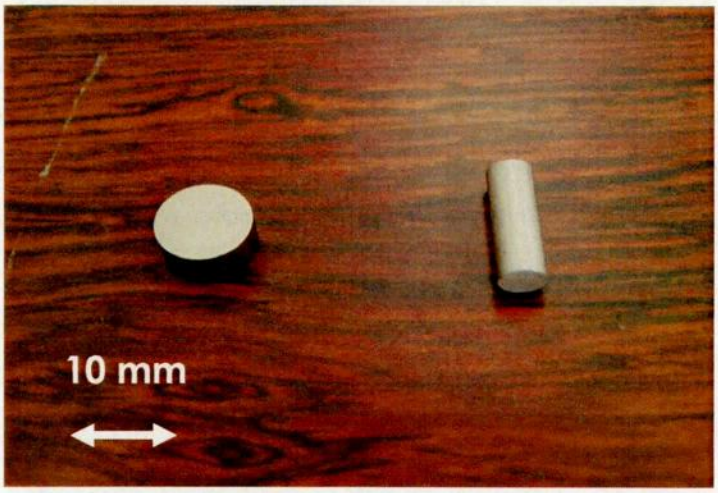


Fig. 2.3.48. Appearances of the bulk niobium hydride.

Fig. 2.3.49 shows the X-ray diffraction pattern of the sample, together with literature data by Rashid [99]. From the analysis, it was found that all of the samples prepared in the present study showed a face-centered orthorhombic (fco) structure (β-phase in the phase diagram). Fig. 2.3.50 shows the lattice parameters at room temperature of the niobium hydride βNbH_X as a function of the hydrogen content C_H [H/Nb], together with literature data by Sakamoto [100], Amoto [96], Rashid [99], and Baden [101]. The present results are in good agreement with the literature. It is found from this figure that the lattice parameters linearly increase with increasing the hydrogen content, according to the following empirical relationship:

$$a[\text{nm}] = 0.4748 + 9.864 \times 10^{-3} \times C_H(\text{H/Nb}) \quad (2\text{-}3\text{-}47)$$

$$b[\text{nm}] = 0.4754 + 1.554 \times 10^{-2} \times C_H(\text{H/Nb}) \quad (2\text{-}3\text{-}48)$$

$$c[\text{nm}] = 0.3307 + 1.584 \times 10^{-2} \times C_H(\text{H/Nb}) \quad (2\text{-}3\text{-}49)$$

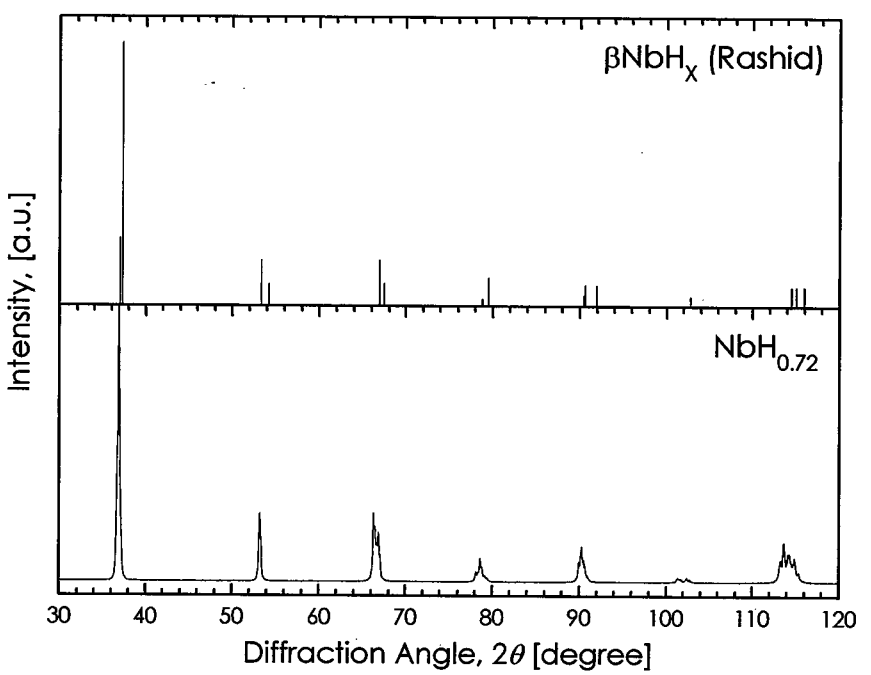


Fig. 2.3.49. X-ray diffraction patterns of niobium hydride, together with literature data [99].

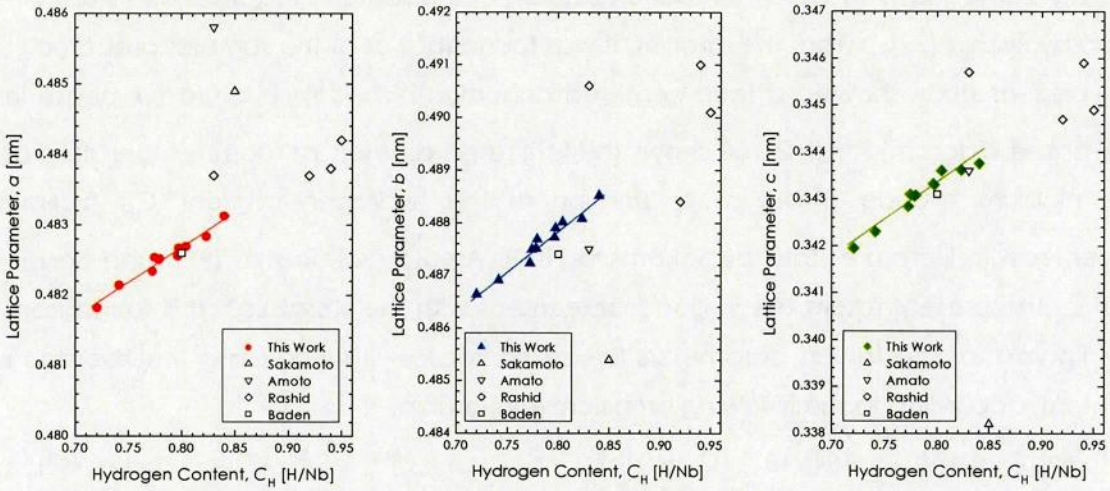


Fig. 2.3.50. Lattice parameters at room temperature of niobium hydride as a function of hydrogen content, together with literature data [96, 99-101].

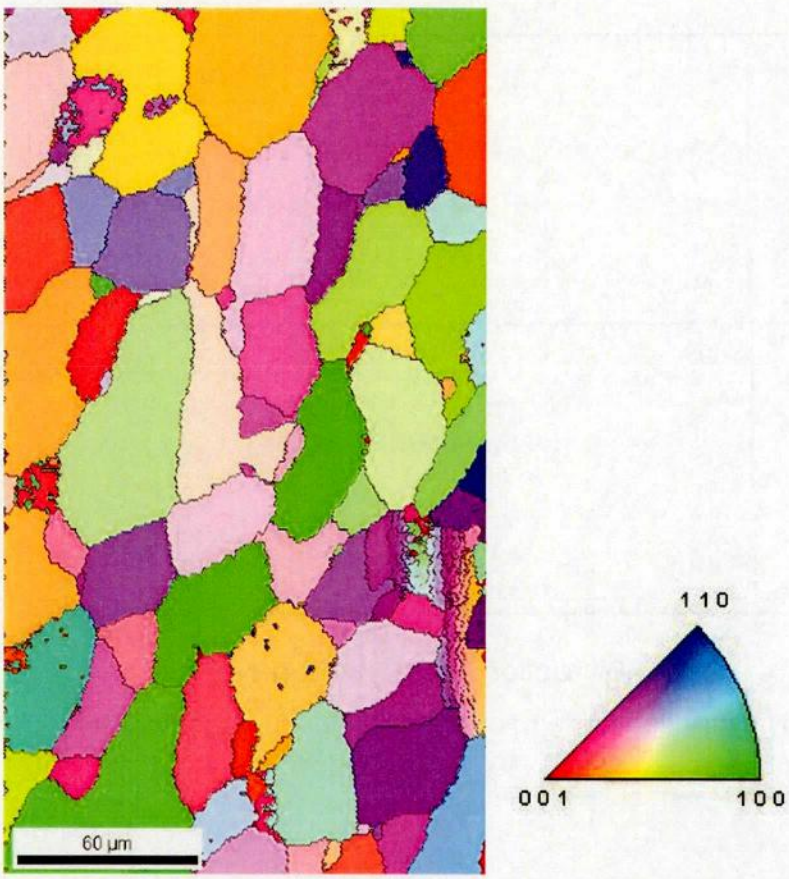


Fig. 2.3.51. Crystal orientation map of niobium hydride $NbH_{0.80}$.

It was also found that the densities of the hydrides determined from weight and dimensional measurements were approximately equal to the theoretical density, which was estimated from the lattice parameter. Therefore it is considered that there exist scarce voids in the sample. Micro cracks or voids were not found on the surface and inside of the samples from the confocal scanning laser microscope observation. From the EBSP measurements as shown in Fig. 2.3.51, the grain sizes of the samples are found to be around 25μm. Apparent crystalline orientation in the samples was not confirmed from the many time EBSP measurements. It is considered that the prepared samples are isotropic polycrystalline materials.

(e) Mechanical Properties of Niobium Hydride

Fig. 2.3.52 shows the longitudinal and shear sound velocities at room temperature of the niobium hydride βNbH_X as a function of hydrogen content C_H [H/Nb]. It is found from this figure that the longitudinal and shear sound velocities of the niobium hydrides are higher than those of the pure niobium and linearly increase with increasing the hydrogen content as empirically expressed as follows;

$$V_L[m/s] = 4679 + 1407 \times C_H(H/Nb) \quad (2\text{-}3\text{-}50)$$

$$V_S[m/s] = 924 + 2204 \times C_H(H/Nb) \quad (2\text{-}3\text{-}51)$$

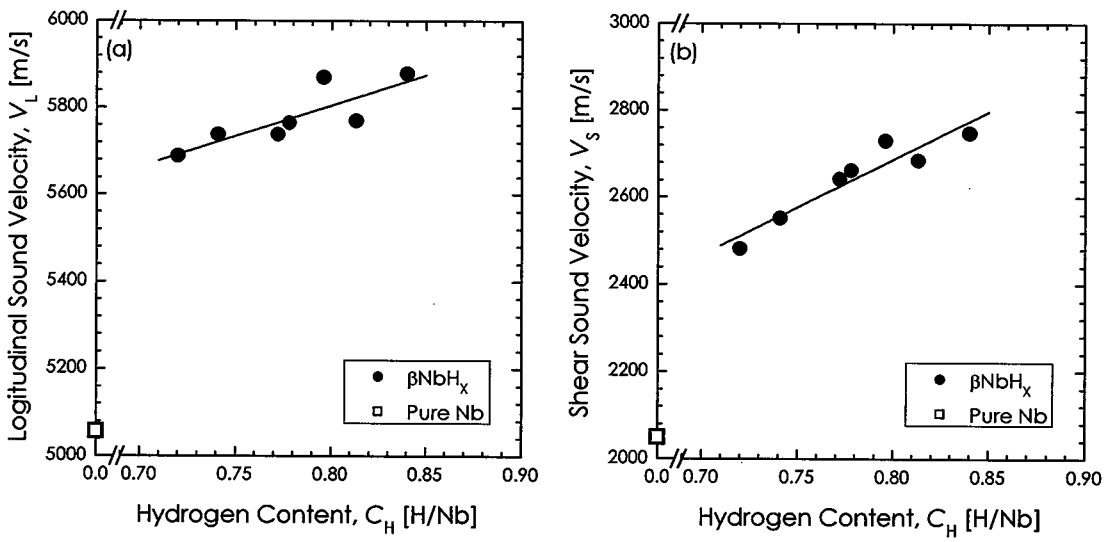


Fig. 2.3.52. Sound velocities at room temperature of niobium hydride as a function of hydrogen content; (a) Longitudinal sound velocity, (b) Shear sound velocity.

Using these results, several elastic moduli can be evaluated. Fig. 2.3.53 shows the Young's modulus and shear modulus at room temperature of the niobium hydride βNbH_X as a function of hydrogen content C_H [H/Nb]. These elatic moduli of the niobium hydride are larger than that of the pure niobium, and increase with increasing the hydrogen content. The dependences of hydrogen content on these moduli are described as following empirical equations:

$$E[GPa] = -25.5 + 220 \times C_H(H/Nb) \quad (2\text{-}3\text{-}52)$$

$$G[GPa] = -15.0 + 87.9 \times C_H(H/Nb) \quad (2\text{-}3\text{-}53)$$

Serdobintsev et al. investigated the dynamic elastic properties of the niobium hydrides by the kHz frequency acoustic spectroscopy [102]. It can be confirmed from their results that higher hydrogen content of the niobium hydride around room temperature leads to higher dynamic elastic modulus. Therefore, it is considered from the present study and the literature that the hydrogen addition in the niobium hydride enhances the mechanical properties. On the contrary, the bulk modulus of the niobium hydride is about 184 GPa, which is also higher than that of the pure niobium (171 GPa), but almost independent of the hydrogen content.

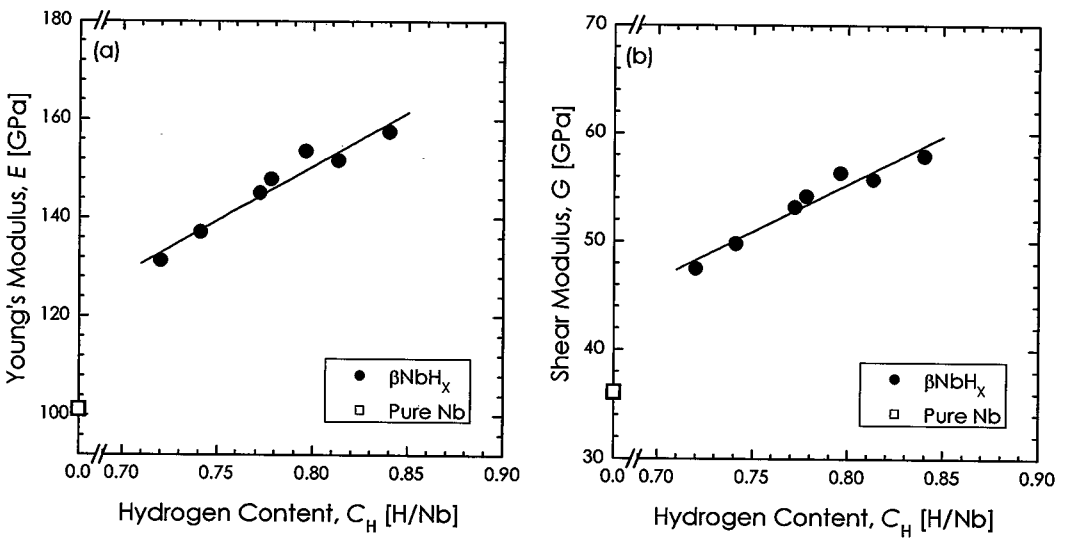


Fig. 2.3.53. Elastic moduli at room temperature of niobium hydride as a function of hydrogen content; (a) Youngs' modulus, (b) Shear modulus.

Fig. 2.3.54 shows the Poison's ratio at room temperature of the niobium hydride βNbH_X as a function of hydrogen content C_H [H/Nb]. The Poison's ratio of the

niobium hydride decreases with increasing the hydrogen content and the dependence of hydrogen content is described as following equations:

$$\sigma[-] = 0.519 - 0.195 \times C_H(\mathrm{H/Nb}) \qquad (2\text{-}3\text{-}54)$$

Therefore, it is considered that the hydrogen content in niobium hydride affects the anisotropic deformation behaviors such as lateral and shear deformations but not the behavior of isotropically elastic deformation. Fig. 2.3.55 shows the Debye temperatures at room temperature of the niobium hydride βNbH_X as a function of hydrogen content C_H [H/Nb]. The Debye temperature of the hydride are higher than that of the pure niobium and increases with increasing hydrogen content as expressed as follows:

$$\theta_D[\mathrm{K}] = 128 + 254 \times C_H(\mathrm{H/Nb}) \qquad (2\text{-}3\text{-}55)$$

The mechanism of this increase is same as the increase of the elastic moduli.

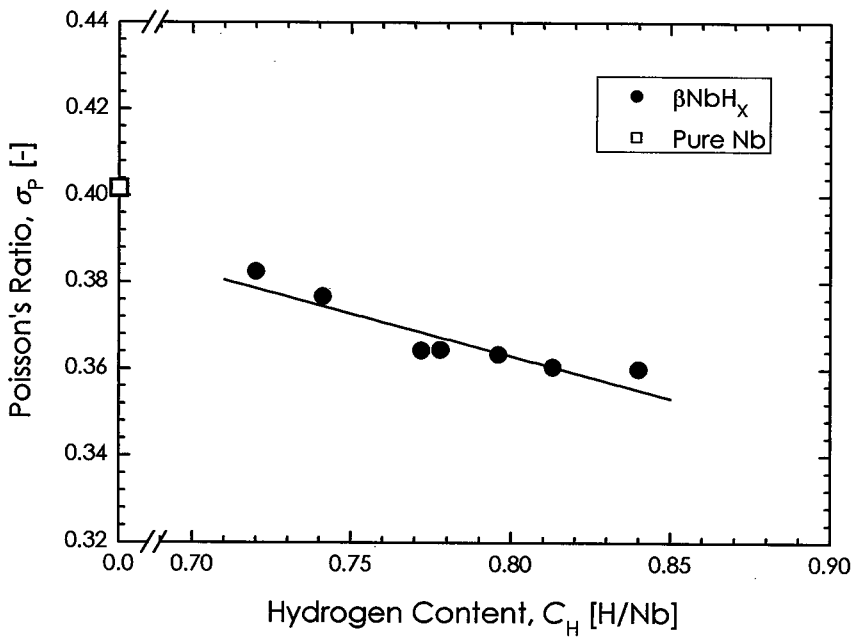


Fig. 2.3.54. Possion's ratio at room temperature of niobium hydride as a function of hydrogen content.

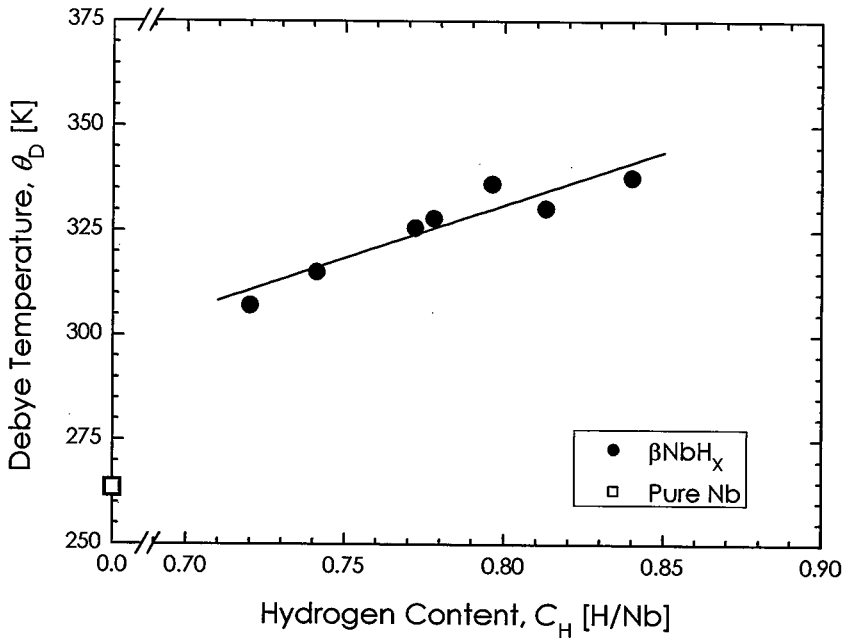


Fig. 2.3.55. Debye temperature of niobium hydride as a function of hydrogen content.

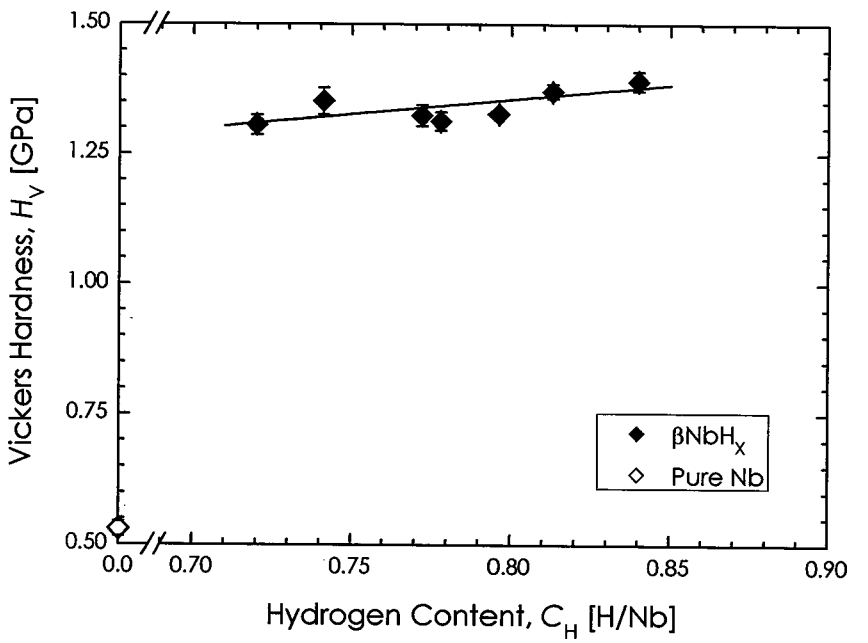


Fig. 2.3.56. Vickers hardness at room temperature of niobium hydride as a function of hydrogen content.

Fig. 2.3.56 shows the Vickers hardness at room temperature of the niobium hydride βNbH_X as a function of hydrogen content C_H [H/Nb]. The hardness of the hydride is also higher than that of the pure niobium and slightly increases with hydrogen addition, empirically expressed as follows:

$$H_V[GPa] = 0.896 + 0.574 \times C_H(H/Nb) \quad (2\text{-}3\text{-}56)$$

Therefore, the hydrogenation is considered to elastically and plastically harden the niobium.

(f) Thermal and Electrical Properties of Niobium Hydride

Fig. 2.3.57 shows a part of the results of high-temperature X-ray diffraction analysis of niobium hydride at room temperature and at 473 K, together with literature data by Rashid [99]. It was confirmed that the βNbH_X transforms into $\alpha' NbH_X$ above about 400 K, which agreed with information from the phase diagram [43].

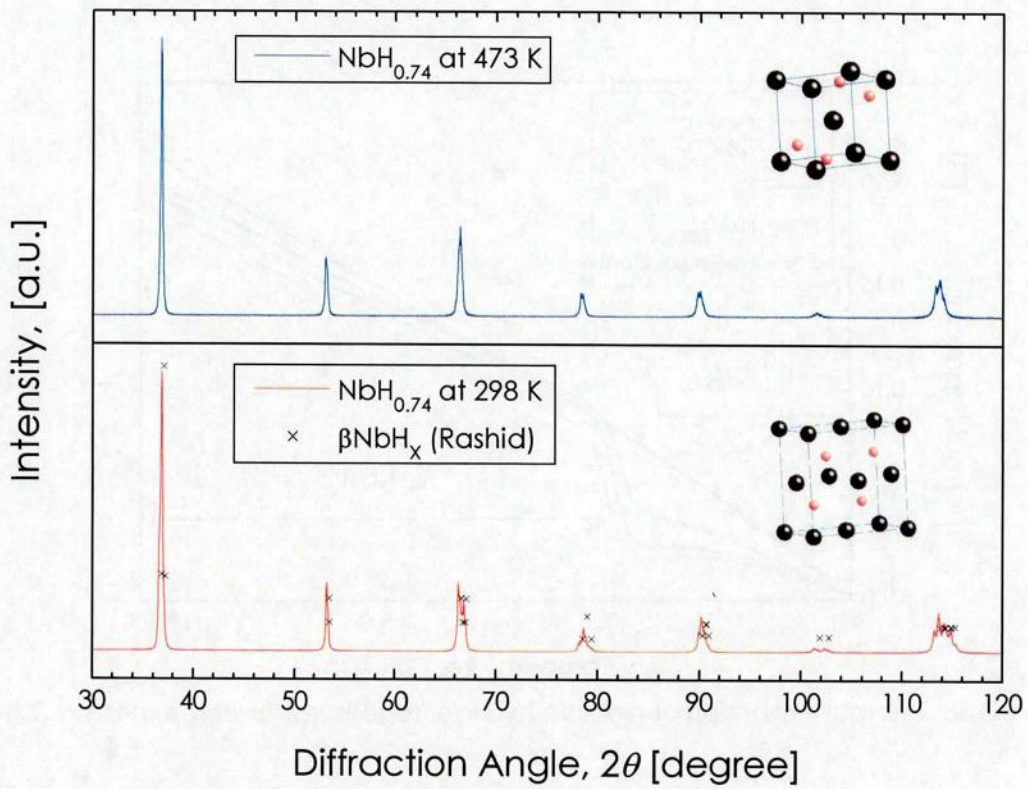


Fig. 2.3.57. X-ray diffraction patterns of α – and β – $NbH_{0.74}$ together with literature data [99]; (a) at room temperature, (b) at 473 K.

Fig. 2.3.58 shows thermal expansion $\Delta L / L$ of the niobium hydride, together with literature data by Touloukian [77]. It is considered that the data below about 375 K are for the βNbH_X and the data above about 400 K are for the $\alpha' NbH_X$. The thermal expansion of the βNbH_X is significantly lower than that of the pure niobium and gradually decreases with increasing hydrogen content. Wlosewicz el al. reported the temperature dependence of crystallographic properties of niobium hydride below the room temperature [103]. It is also found from their study that the lattice volume of βNbH_X almost independent of temperature. However, the reported lattice parameters of the orthorhombic crystal had a margin of error. The further experimental and theoretical investigations on the crystallographic properties are required. The sample significantly expands at the $\beta + \alpha'$ biphasic temperature region. This phenomenon is also found in the literature by Sorokina [104]. The thermal expansion of $\alpha' NbH_X$ is slightly lower than that of the pure niobium and appear to be almost independent of the hydrogen content.

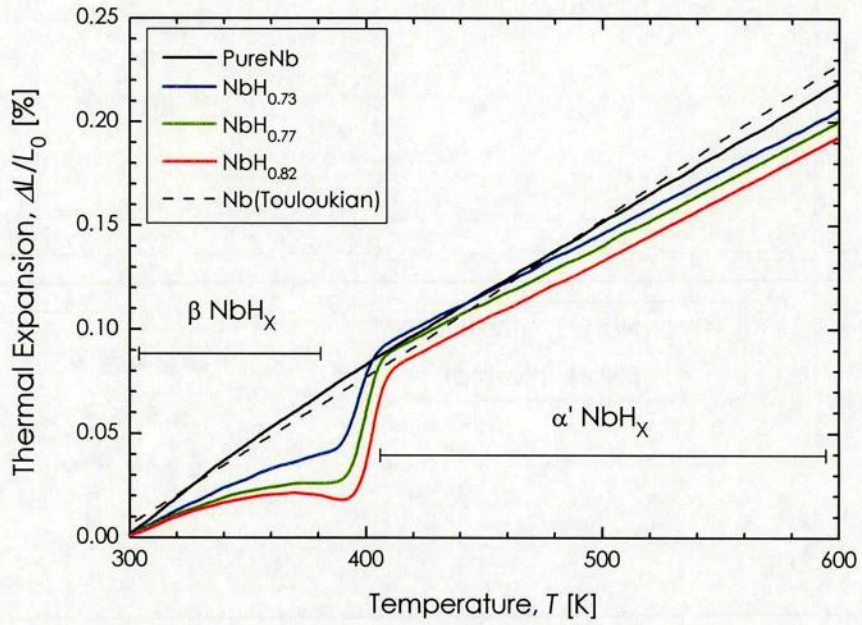


Fig. 2.3.58. Thermal expansion of niobium hydride, together with literature data [77].

Fig. 2.3.59 shows the temperature dependence of electrical resistivity of niobium hydride, together with literature data by Rossiter [87] and Andrievskii [88]. The electrical resistivities of both the βNbH_X and $\alpha' NbH_X$ show metallic temperature dependence.

The resistivity of the βNbH_X is slightly higher than that of the pure niobium. On the other hand, the $\alpha' NbH_X$ shows significantly higher electrical resistivity than the pure niobium. This difference would be attributed the differences in the electronic structure and the carrier scattering due to optical hydrogen vibration between the βNbH_X and $\alpha' NbH_X$. Fig. 2.3.60 shows the electrical resistivity of the niobium hydride at 323 K and at 423 K as a function of hydrogen content C_H [H/Nb]. It is found that the resistiivty gradually reduces with increasing the hydrogen content for the both phase. This is attributed that the Debye temperature increases with increasing the hydrogen content. The literature data by Andrievskii is slightly lower than the present data, which is cased by the difference in the hydrogen content.

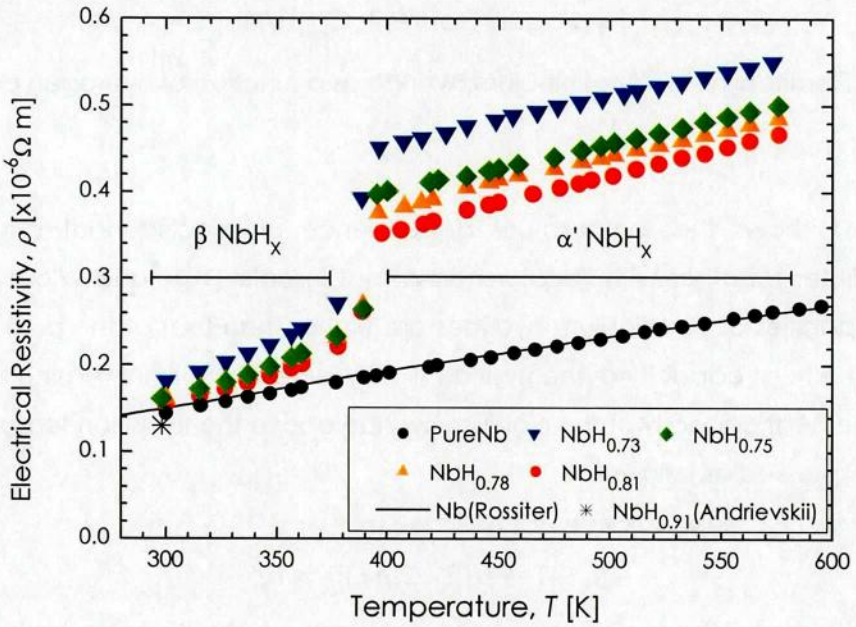


Fig. 2.3.59. Temperature dependence of electrical resistivity of niobium hydride, together with literature data [87, 88].

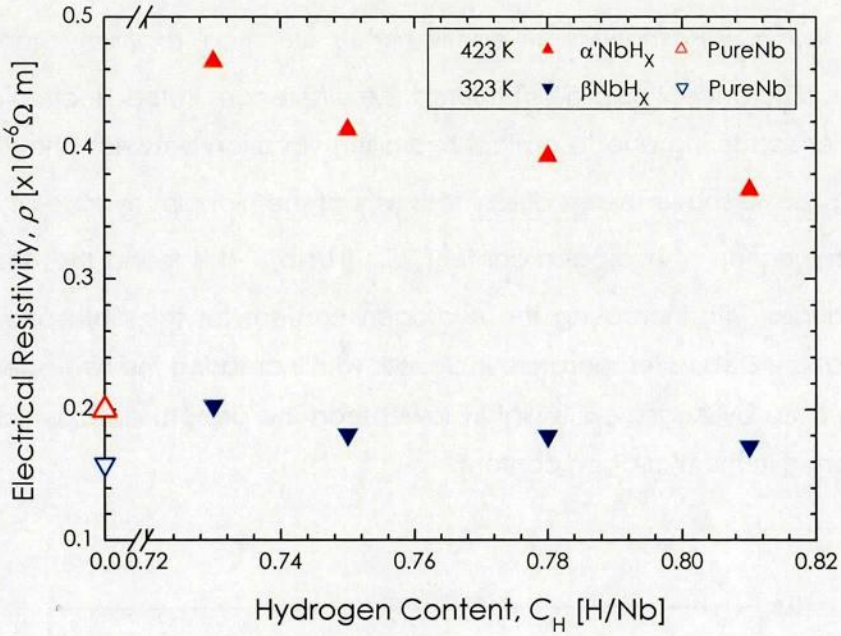


Fig. 2.3.60. Electrical resistivity of niobium hydride as a function of hydrogen content.

Fig. 2.3.61 shows the temperature dependence of specific heat capacity of niobium hydride, together with literature data by Dinsdale [105] and Wlosewicz [99]. The heat capacities of the niobium hydrides are higher than that of the pure niobium. In addition, the heat capacity of the hydride slightly increases with increasing hydrogen content. The heat capacity of the niobium hydride above the transition temperature is empirically expressed as follows:

$$C_P = 121.9 \times C_H - 58.93 + (7.738 - 9.179 \times C_H) \times 10^{-2} \times T + (6.641 - 9.012 \times C_H) \times 10^{6} \times T^{-2} \quad (2\text{-}3\text{-}57)$$

Fig. 2.3.62 shows the calculated heat capacity of the niobium hydride. The calculation procedure is described in Chapter 2.3.1 and the reference data on the Einstein temperatures reported by Alefeld [106] and the coefficient of electronic heat capacity by Ohlendorf [107] were adopted. In the niobium-hydrogen system, the Einstein frequencies of the hydrogen subset are $\theta_E = 1400\,\mathrm{K}$ and twice degenerated, $\theta_E = 1900\,\mathrm{K}$. Therefore, the equation (2-3-25) is converted into the following equation;

$$C_V^{\,H} = (1/3) \times 3C_H R(1400/T)^2 \exp(1400/T)/[\exp(1400/T) - 1]^2 + (2/3) \times 3C_H R(1900/T)^2 \exp(1900/T)/[\exp(1900/T) - 1]^2 \quad (2\text{-}3\text{-}58)$$

Additionally, note that the coefficient of electronic heat capacity for λ' phase which exists below 130 K is alternatively utilized. The calculated heat capacities are good

accordance with the experimental results. Above room temperature, the heat capacity of the niobium hydride is higher than that of the pure niobium and slightly increases with increasing temperature. The calculation indicated that they were attributable to the optical phonon due to hydrogen vibration.

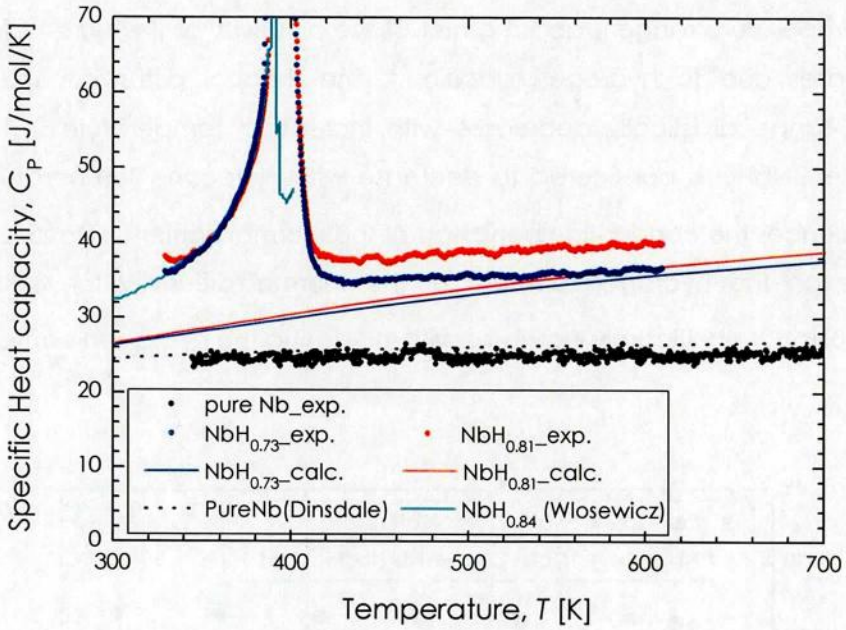


Fig. 2.3.61. Temperature dependence of specific heat capacity of niobium hydride, together with literature data [99, 105].

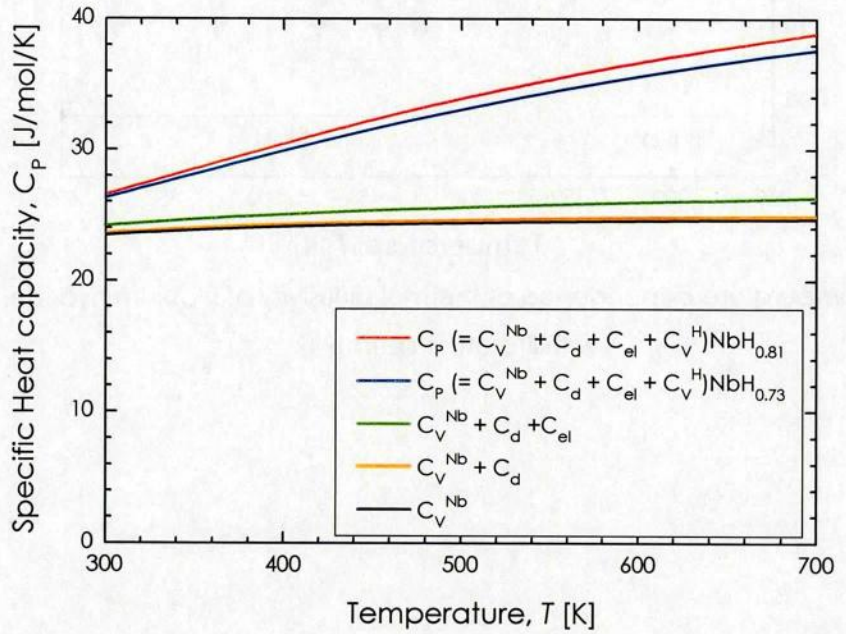


Fig. 2.3.62. Calculated specific heat capacity of niobium hydride.

Fig. 2.3.63 shows the temperature dependence of thermal diffusivities of the niobium hydride, together with literature data by Touloukian [94]. The present diffusivity of pure niobium is slightly higher than the literature. Anomaly in the temperature dependence is also detected in the diffusivity of the hydride, which is considered to be due to the phase transition from the βNbH_X to $\alpha' NbH_X$. The thermal diffusivity of the hydrides at the higher temperature range is about a half of the diffusivity of the pure hafnium and slightly increases due to hydrogen addition. The thermal diffusivity at the lower temperature range drastically decreases with increasing temperature. The lattice stability of the βNbH_X is considered to decrease with increasing temperature, which probably influences the conduction behaviors of the thermal carriers. Despite the slight dependence on the hydrogen content of the thermal diffusivity for $\alpha' NbH_X$, the diffusivity of βNbH_X significantly increases with increasing the hydrogen content.

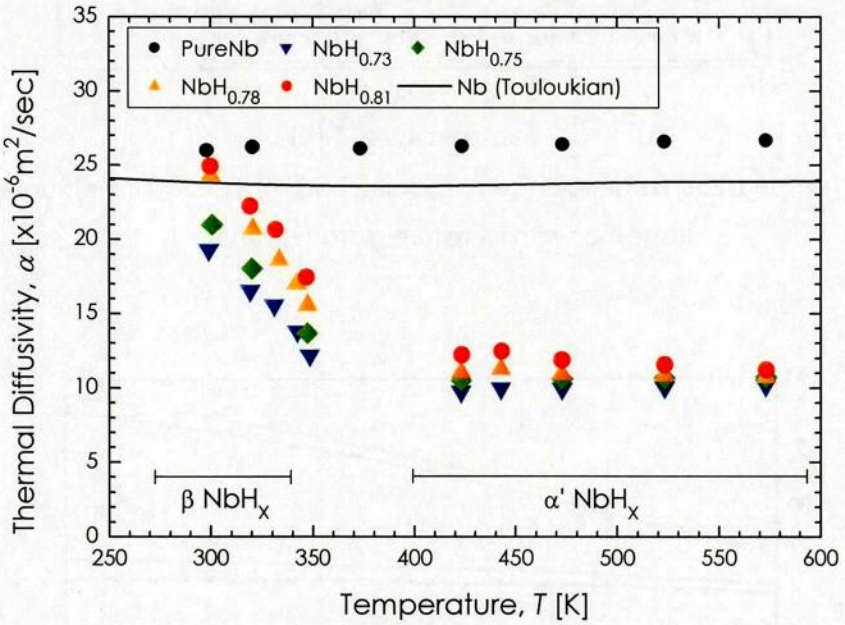


Fig. 2.3.63. Temperature dependence of thermal diffusivity of niobium hydride, together with literature data [94].

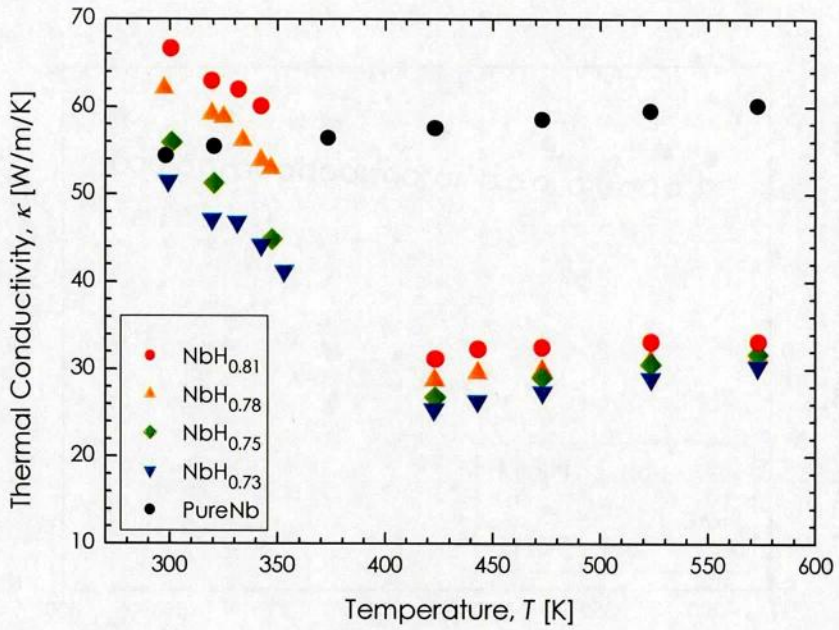


Fig. 2.3.64. Temperature dependence of thermal conductivity of niobium hydride.

The thermal conductivity κ was derived from the thermal diffusivity α, the heat capacity C_P, and the density ρ. Fig. 2.3.64 shows the estimated thermal conductivity of the niobium hydride, which shows similar temperature dependence of the thermal diffusivity. This is because the temperature dependence of the heat capacity of the niobium hydride is not so large. Fig. 2.3.65 shows the temperature dependence of electron contribution to the thermal conductivity of the niobium hydride, together with the results of the pure niobium. The estimation method of these contributions is described in Chapter 2.3.1. It is found from this figure that the electron contribution is major component of the thermal conductivity. The rest contribution is considered to mainly consist of the phonon contribution. Fig. 2.3.66 and Fig. 2.3.67 show the hydrogen content dependence of the electron and phonon contributions to the thermal conductivity of niobium hydride, respectively. From these figures, the increase of thermal conductivity of the βNbH_X with the hydrogen content is mainly attributed to the increase of the phonon contribution. This is considered to be because the Debye temperature of the βNbH_X increases with increasing the hydrogen content. On the contrary, the phonon contribution of $\alpha' NbH_X$ is extremely low. The further investigations such as the high temperature measurements of the Debye temperature are required in order to discuss the result.

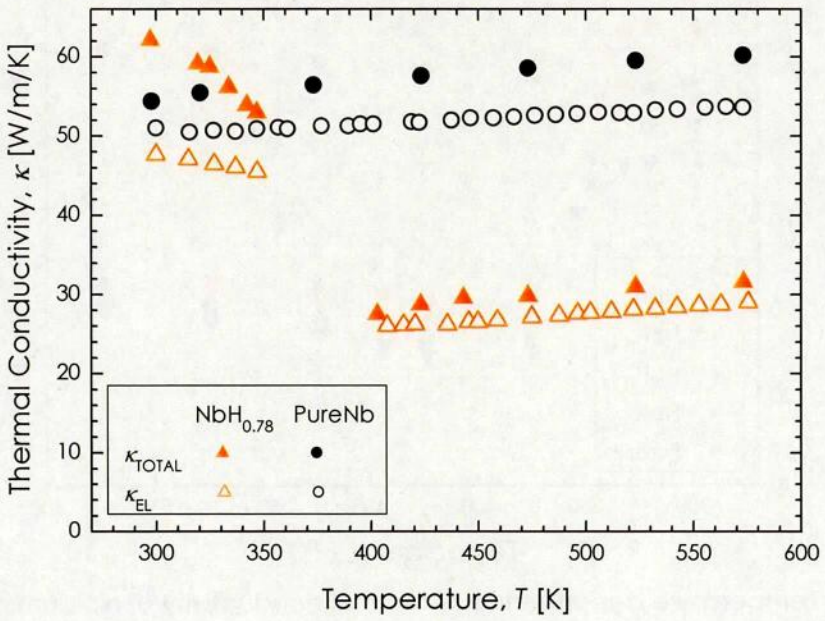


Fig. 2.3.65. Temperature dependence of the electron contribution to thermal conductivity of niobium hydride.

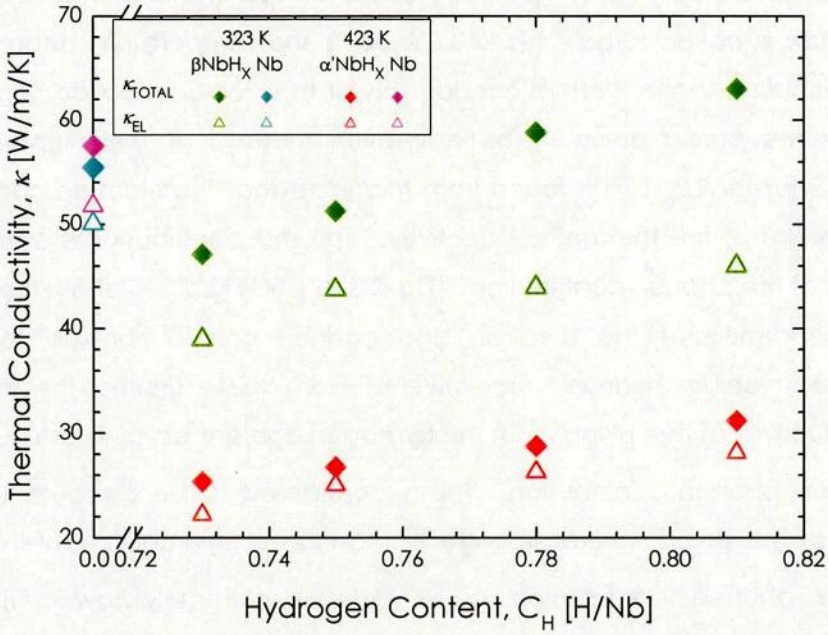


Fig. 2.3.66. Hydrogen content dependence of electron contribution to thermal conductivity of niobium hydride.

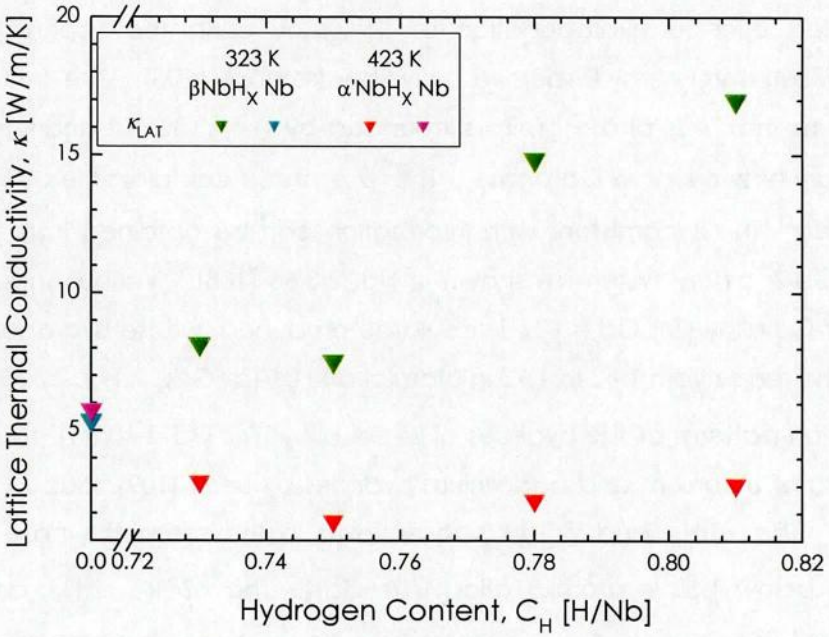


Fig. 2.3.67. Hydrogen content dependence of phonon contribution to thermal conductivity of niobium hydride.

2-3-4. Hydrides of Gd-Zr Alloy

(a) Sample Characterization of Hydrides of Gd-Zr Alloy

Analysis on phase and composition of the arc-melted Zr-Gd alloy (Zr : Gd = 10 : 1) was performed prior to hydrogenation of the alloy using the Scanning Electron Microscope (SEM) and Energy Dispersive X-ray Spectroscopy (EDS). The Zr-Gd alloy has phase structure that α Zr phase grains surrounded by very thin but nearly continuous grain-boundary network of α Gd phase. The α Zr phase contains little of gadolinium, and vice versa. This is consistent with information can be obtained from the phase diagram of Gd-Zr binary system as shown in Fig. 2.3.68 [108]. Various shapes of bulk hydrides of Zr-Gd alloy (Zr : Gd = 10 : 1) could be produced, whose hydrogen contents C_H were in the range from 1.42 to 1.93 in atomic ratio [H/(Zr+Gd)]. Fig. 2.3.69 shows the X-ray diffraction patterns of the hydrides of Zr-Gd alloy (Zr : Gd = 10 : 1), together with literature data of zirconium and gadolinium hydrides by Beck [109], Riabou [110], and Sturdy [111]. The δZrH_X and δGdH_X phase exist in the samples whose hydrogen contents are below 1.53 in atomic ratio [H/(Zr+Gd)]. The δZrH_X, εZrH_X, and δGdH_X exist in the sample whose hydrogen content is 1.75 in atomic ratio [H/(Zr+Gd)]. The εZrH_X and δGdH_X exist in the sample whose hydrogen content is 1.93 in atomic ratio [H/(Zr+Gd)].

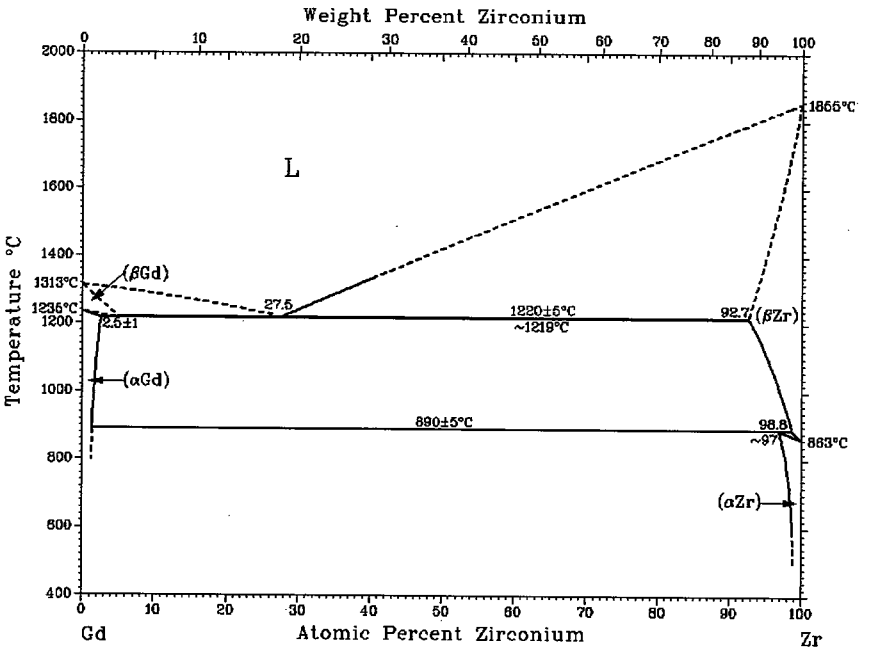


Fig. 2.3.68. Phase diagram of Gd-Zr binary system [108].

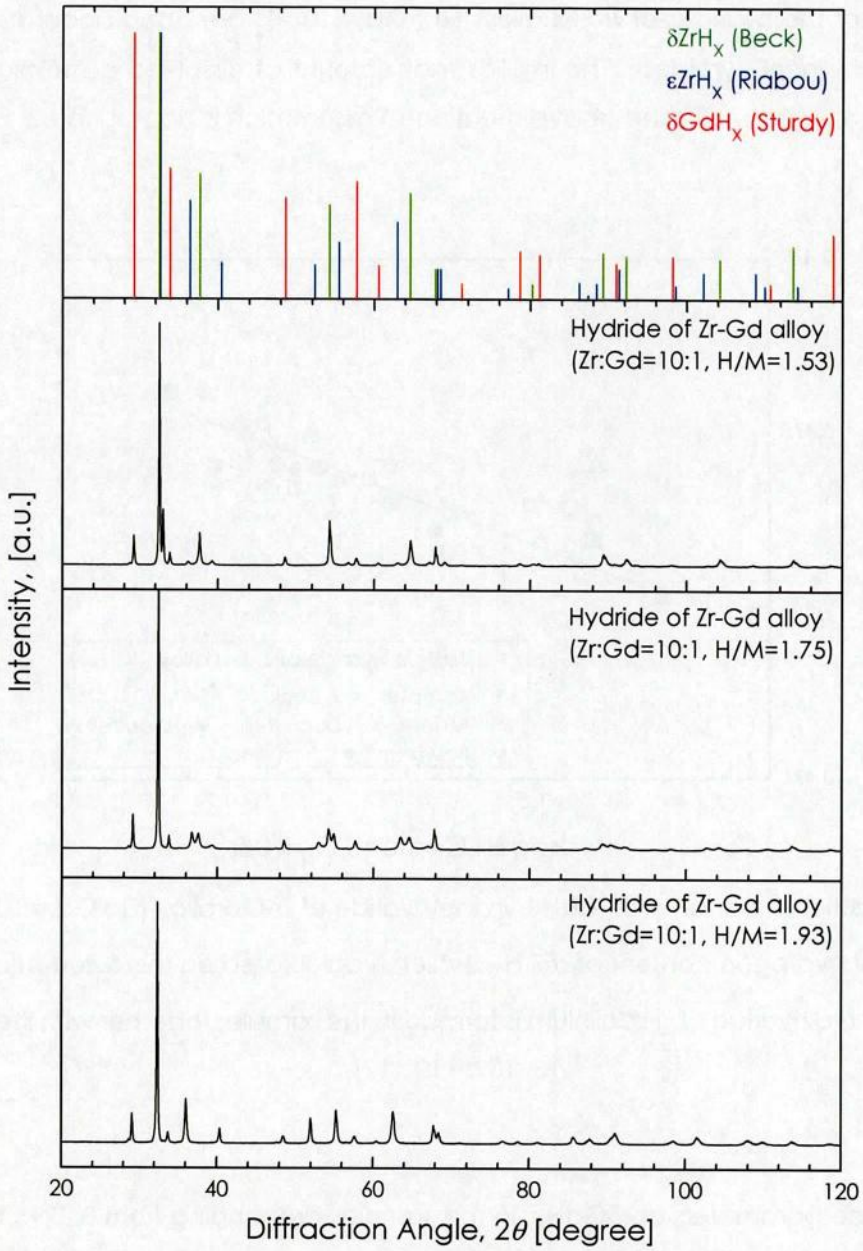


Fig. 2.3.69. X-ray diffraction patterns of the hydrides of Zr-Gd alloys (Zr : Gd = 10 : 1), together with literature data [109-111].

Fig. 2.3.70 and Fig. 2.3.71 show the lattice parameter of δZrH_X and εZrH_X in the hydrides of Zr-Gd alloys (Zr : Gd = 10 : 1) as a function of hydrogen content C_H, together with literature data by Kempter [112], Beck [109], Sidhu [113], Moore [114], Ducastelle [115], Cantrell [116], Bowman [117], Yamanaka [9, 13], and Barradough [118]. In these figures, the hydrogen content is estimated on the assumption that stoichiometric

dihydride of gadolinium is formed in the sample. From the analysis, the lattice parameters of the hydrides of Zr-Gd alloys (Zr : Gd = 10 : 1) are good accordance with those of Zr-H binary hydrides. This implies that amount of dissolved gadolinium in the δZrH_X is vanishingly small if the above-mentioned assumption is appropriate.

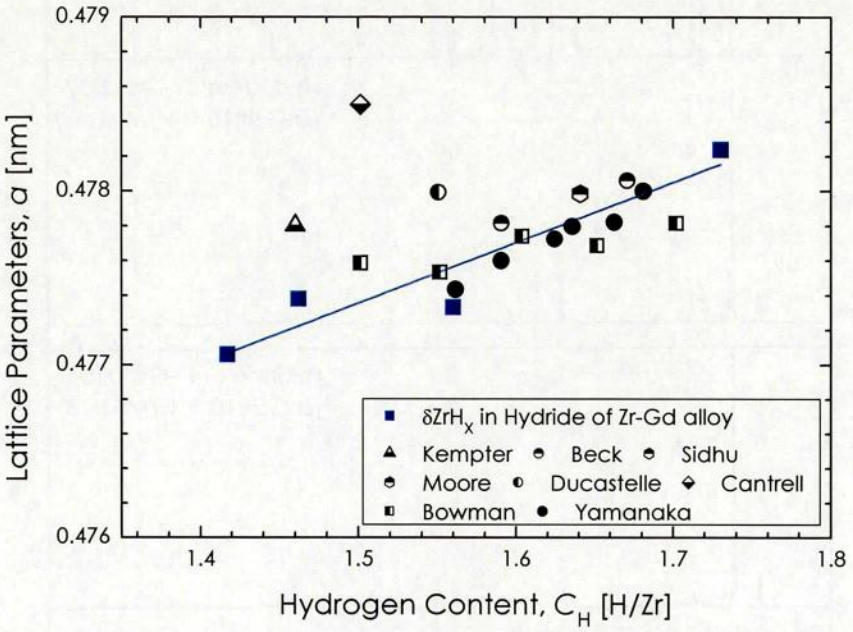


Fig. 2.3.70. Lattice parameter of δZrH_X in the hydride of Zr-Gd alloy (Zr : Gd = 10 : 1) as a function of hydrogen content of δZrH_X, which is calculated on the assumption that stoichiometric dihydride of gadolinium is formed in the sample, together with literature [9, 13, 109, 112-117].

The lattice parameters of δGdH_X in the samples are ranging from 0.5295 to 0.5302 nm, which almost agrees with the reported value (0.5301 nm) of stoichiometry dihydride of gadolinium by Bonnet [119]. Since the low-angle and small peak were used for the lattice parameter evaluation in the case of gadolinium hydride, a concern remains about accuracy of the present lattice parameter. Therefore, further discussions, such as the effects of hydrogen content and zirconium dissolution in the phase, on the lattice parameter are limited. The hydrogen content analysis for each phase is considered to be required. It was also found that the densities of the hydrides determined from weight and dimensional measurements were approximately equal to the theoretical density, which was estimated from the lattice parameter. Therefore it is considered

that there exist scarce voids in the sample. Micro cracks or voids were not found on the surface and inside of the samples from the confocal scanning laser microscope observation.

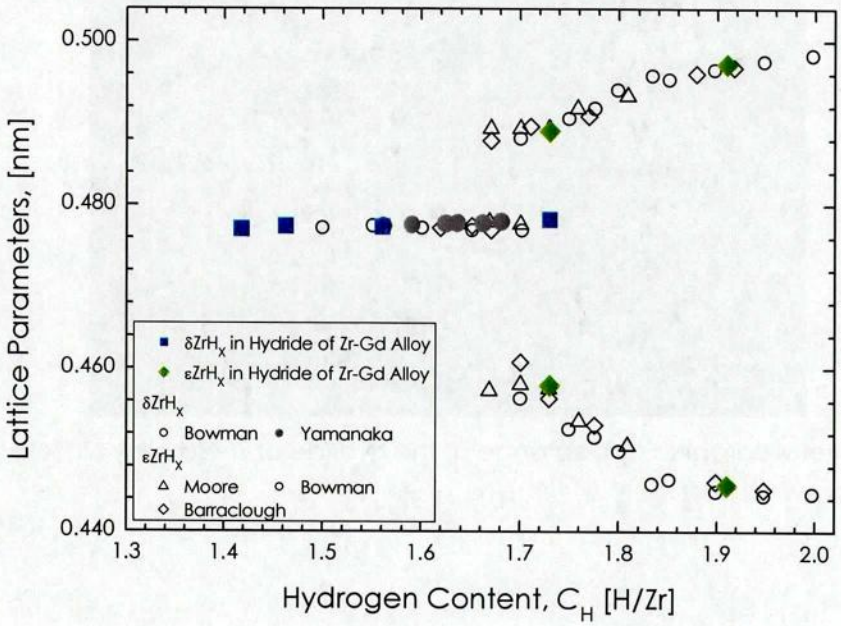


Fig. 2.3.71. Lattice parameter of δZrH_X and εZrH_X in the hydride of Zr-Gd alloy (Zr : Gd = 10 : 1) as a function of hydrogen content, which is calculated on the assumption that stoichiometric dihydride of gadolinium is formed in the sample, together with the literatures [9, 13, 114, 117, and 118].

Fig. 2.3.72 shows metallographic appearance of the hydride of Zr-Gd alloy. Silver color grain, whose size is several dozens of micro-meter, surrounded by very thin but nearly continuous grain-boundary network of dark color phase is observed. The dark phase also disperses in the silver grain. Fig. 2.3.73 and Fig. 2.3.74 show the distribution of oxygen, zirconium, and gadolinium elements in the hydride of Zr-Gd alloy (Zr : Gd = 10 : 1). The several dozens of micro-meter grain mainly contains zirconium; on the other hand the surrounded area mainly contains gadolinium. The oxygen content of gadolinium hydride area appears to be slightly higher than zirconium hydride area. The grain structure was similar to that of the alloy before the hydrogenation.

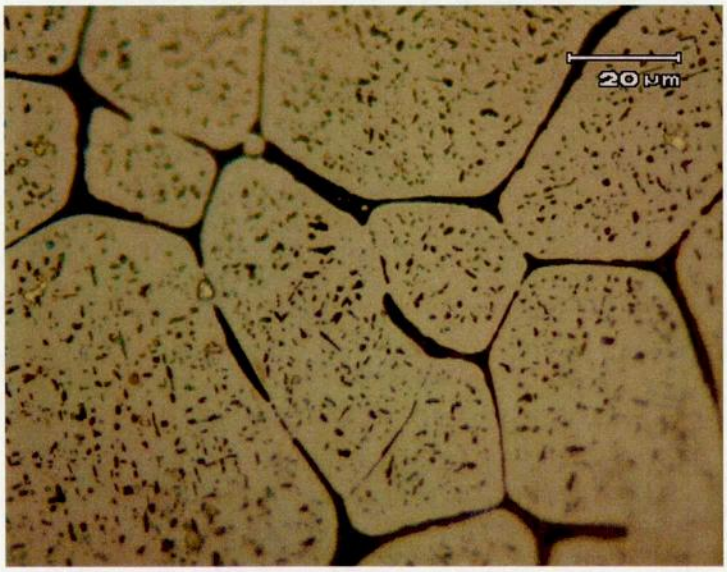


Fig. 2.3.72. Metallographic appearance of the hydride of Zr-Gd alloy (Zr : Gd = 10 : 1, H/M=1.93).

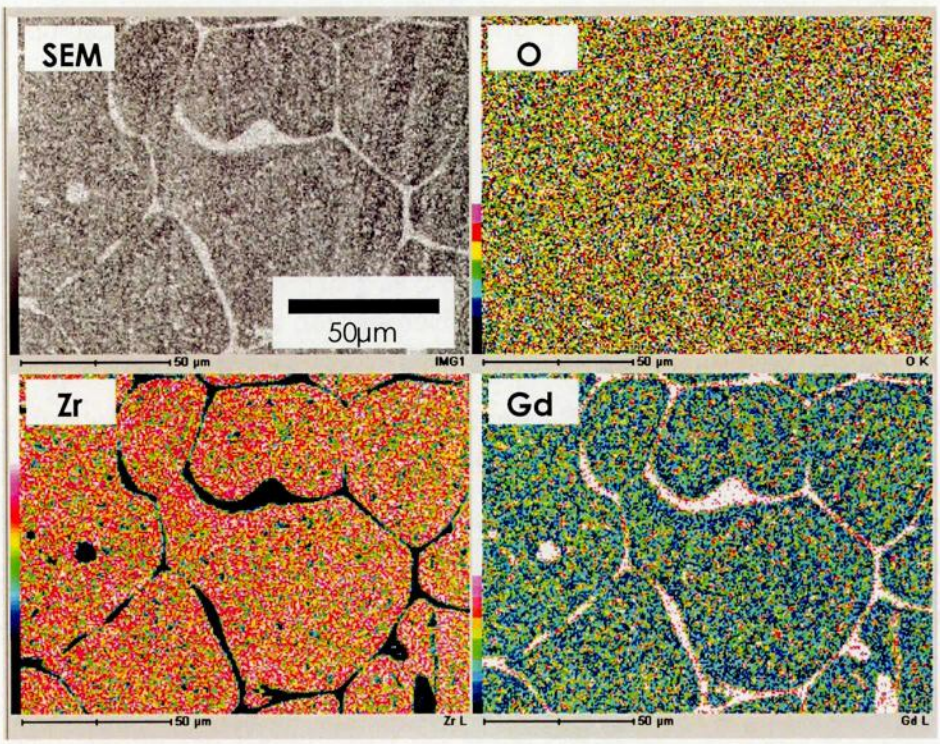


Fig. 2.3.73. Distribution of oxygen, zirconium, and gadolinium elements in the hydride of Zr-Gd alloy (Zr : Gd = 10 : 1, H/M=1.93).

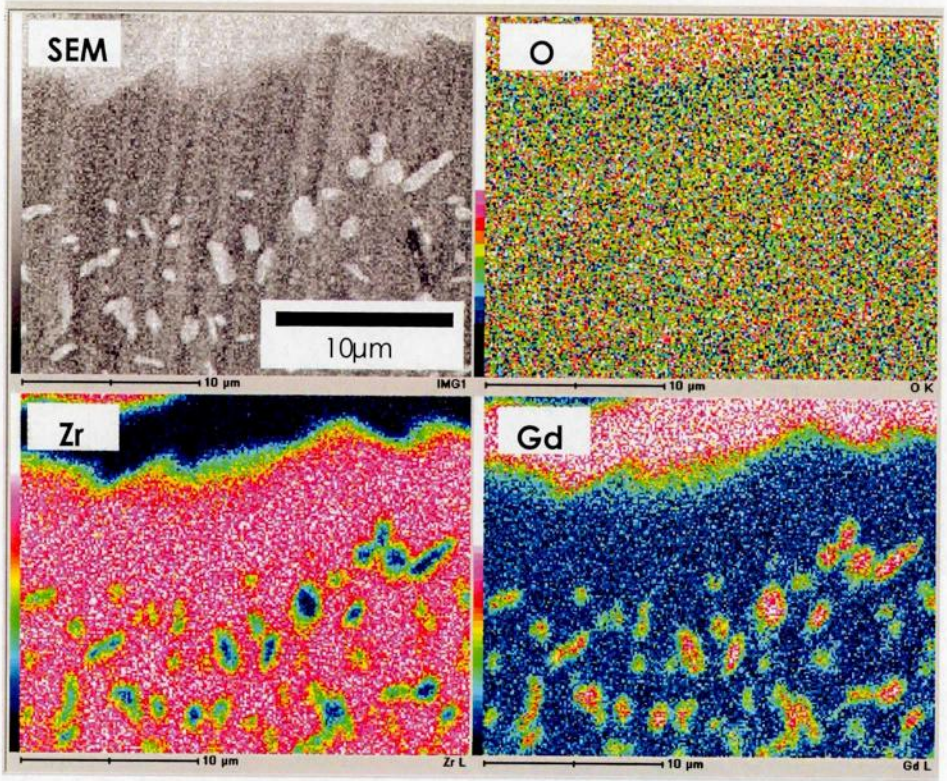


Fig. 2.3.74. Distribution of oxygen, zirconium, and gadolinium elements in the hydride of Zr-Gd alloy (Zr : Gd = 10 : 1, H/M=1.93).

(b) Mechanical Properties of Hydrides of Gd-Zr Alloy

From the pulse-echo sound velocity measurement, the elastic moduli of the hydride of Zr-Gd alloy (Zr : Gd = 10 : 1) were evaluated. Fig. 2.3.75 shows the Young's modulus E and shear modulus G of the hydride of Zr-Gd alloy at room temperature, together with literature data of Zr-H binary system by Yamanaka [9, 13, 16]. The elastic moduli of the hydride of Zr-Gd alloy are larger than those of the Zr-Gd alloy. This trend is similar to that of the Zr-H system, but the present elastic moduli are lower than that of the zirconium hydride. This would be due to that the gadolinium hydride has lower elastic moduli than the zirconium hydride. Fig. 2.3.76 shows the Vickers hardness at room temperature of the hydride of Zr-Gd alloy, together with literature data of Zr-H binary system by Yamanaka [9, 13, 16]. The Vickers hardness of the hydride of Zr-Gd alloy is also higher than that of the Zr-Gd alloy and almost independent of the hydrogen content. However, the hardness is lower than that of the zirconium hydride, which is probably attributed that the gadolinium hydride has lower hardness than the zirconium hydride.

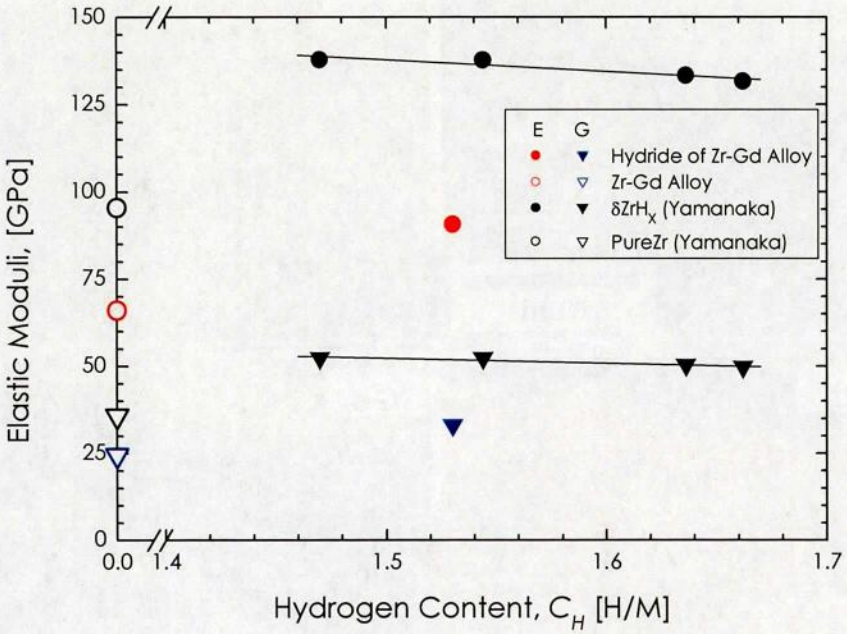


Fig. 2.3.75. Elastic moduli of the hydride of Zr-Gd alloy (Zr : Gd = 10 : 1), together with literature data [9, 13, and 16].

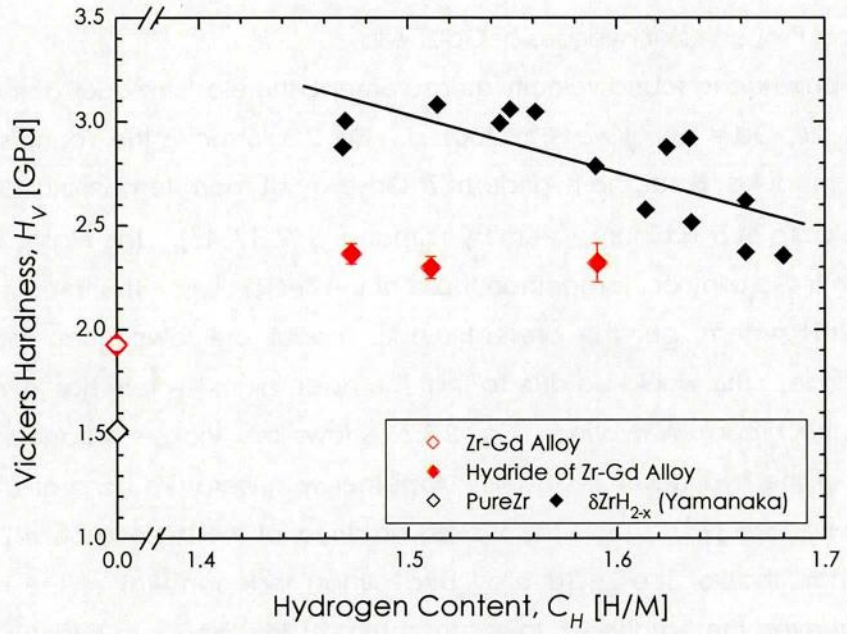


Fig. 2.3.76. Vickers hardness of the hydride of Zr-Gd alloy (Zr : Gd = 10 : 1), together with literature data [9, 13, and 16].

(g) Thermal Properties of Hydrides of Gd-Zr Alloy

It is considered that the specific heat capacity C_P of the hydride of Zr-Gd alloy can be estimated using following equation:

$$C_P[\mathrm{J/g/K}] = \frac{10(\mathrm{mol}) \times C_P{}^{ZrH_x}(\mathrm{J/mol/K}) + 1(\mathrm{mol}) \times C_P{}^{GdH_2}(\mathrm{J/mol/K})}{10(\mathrm{mol}) \times M_{Zr}(\mathrm{g/mol}) + 1(\mathrm{mol}) \times M_{Gd}(\mathrm{g/mol})} \quad (2\text{-}3\text{-}59)$$

where M is the atomic mass number. The detailed information of the heat capacity of zirconium hydride is available. Yamanaka et al. [12] reported the temperature dependence of heat capacity of zirconium hydride at different hydrogen content as follows:

$$C_P{}^{ZrH_x}[\mathrm{J/mol/K}] = 25.02 + 4.746 \times C_H + (3.103 \times 10^{-3} + 2.008 \times 10^{-2} \times C^H) \times T - (1.943 \times 10^5 + 6.358 \times 10^5 \times C_H)/T^2 \quad (2\text{-}3\text{-}60)$$

The specific heat capacity of the yttrium hydride, which is the congeneric element, was alternatively utilized as the heat capacity of the gadolinium hydride in the equation (2-3-59).

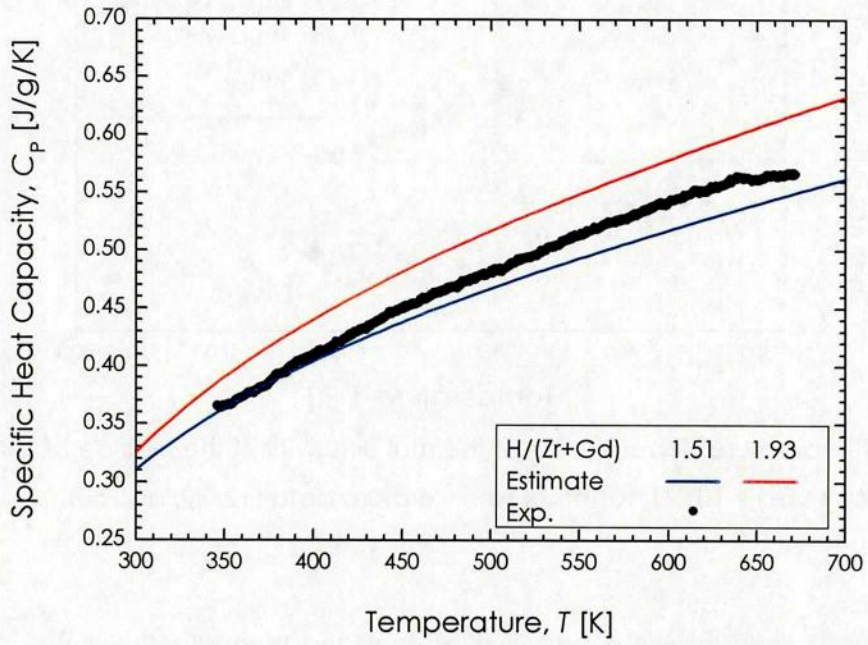


Fig. 2.3.77. Temperature dependence of specific heat capacity of the hydride of Zr-Gd alloy (Zr : Gd = 10 : 1).

Fig. 2.3.77 shows the experimental and estimated results of the temperature dependence of the specific heat capacity of the hydride of Zr-Gd alloy (Zr : Gd = 10 : 1).

The estimated heat capacity is good accordance with the experimental results. The heat capacity of the hydride of Zr-Gd alloy increases with increasing temperature, which is considered to be due to the excitation of optical hydrogen vibration mode in the hydrides. Fig. 2.3.78 shows the temperature dependence of thermal diffusivities α of the hydride of Zr-Gd alloy, together with literature data of zirconium hydrides by Yamanaka [12] and Tsuchiya [49, 50]. The thermal diffusivities of the hydrides decrease with increasing temperature. The diffusivity of the hydride that has lower hydrogen content is higher than that of δZrH_X with similar hydrogen content. On the contrary, the diffusivity of the hydride that has higher hydrogen content is almost same as reported data of εZrH_X with similar hydrogen content.

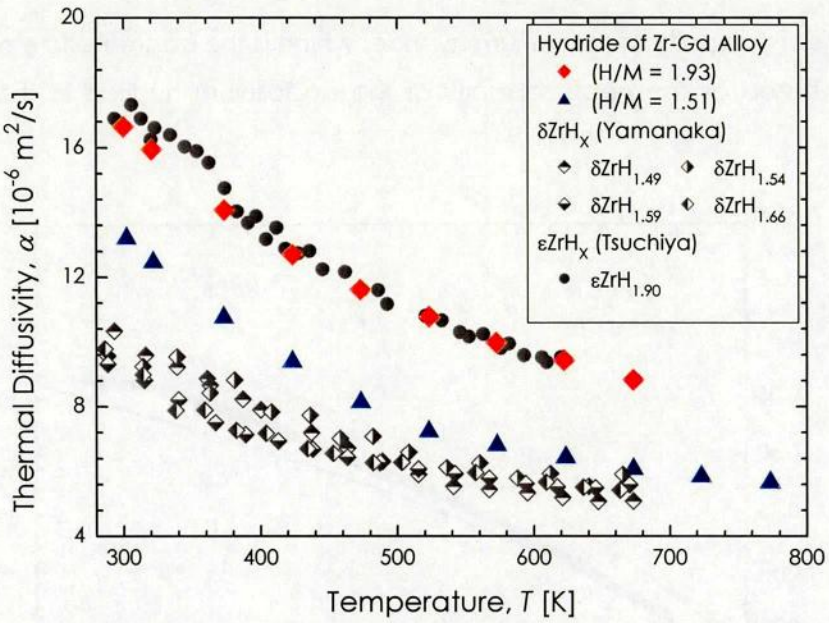


Fig. 2.3.78. Temperature dependence of thermal diffusivity of the hydride of Zr-Gd alloy (Zr : Gd = 10 : 1), together with literature data [12, 49, and 50].

The thermal conductivity κ was derived from the thermal diffusivity α, the heat capacity C_P, and the density ρ. Fig. 2.3.79 shows the estimated thermal conductiviy of the hydride of Zr-Gd alloy. Contrary to the diffusivities, the thermal conductivities of the hydrides are almost independent of temperature. It is found that the hydrogen addition enhances the thermal conductivity of the hydride of Zr-Gd alloy. The conductivity of the hydride that has lower hydrogen content is higher than those of

δZrH_x. On the contrary, the conductivity of the hydride that has higher hydrogen content is slightly lower than the conductivity of εZrH_x. Therefore, since the thermal conductivity would reduce due to scattering of thermal carriers by the phase boundary, it is considered that the precipitant of gadolinium hydride has comparable thermal conductivity to the εZrH_x. The experimental investigations on the thermophysical properties of gadolinium hydride are required.

In the present section, the thermophysical properties of the hydrides of Zr-Gd alloy were reviewed from parts of achievements in the task "Research and development of innovative fast reactor core with use of hydride as neutron absorbers" [120].

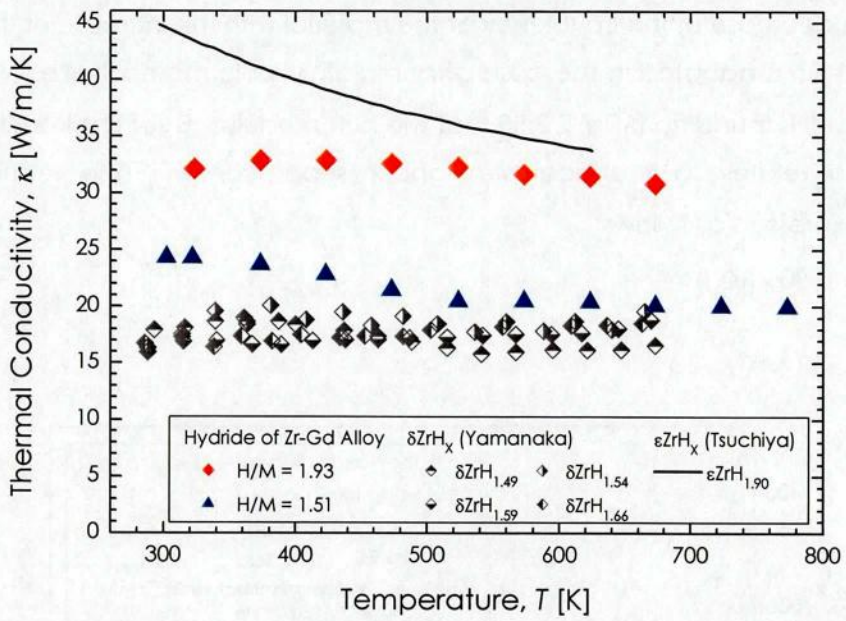


Fig. 2.3.79. Temperature dependence of thermal diffusivity of the hydride of Zr-Gd alloy (Zr : Gd = 10 : 1), together with literature data [12, 49, and 50].

2-3-5. Correlations between Several Properties of Metal Hydrides

Fig. 2.3.80 shows the relationship between the bulk modulus B and the nearest-neighbor separation d of the metal hydrides, together with literature data by Setoyama [21], Yamanaka [9], Beatties [69], Kittel [85], Tosi [121], and Cohen [122]. Cohen demonstrated that the nearest-neighbor separation for several compounds related to the bulk modulus as expressed as follows;

$$B[GPa] = (1971 - 220\lambda) \times (10d)^{-3.5} \qquad (2\text{-}3\text{-}61)$$

This equation indicates that smaller interatomic distance results in larger elastic moduli of the materials. It is found from the literature [122] that this expression was appropriated for group-IV (λ=0), III-V (λ=1) and II-VI (λ=2) materials in the diamond and zinc-blende structure in the center of the Periodic Table. The larger value of λ indicates the decrease of the covalency of the material with the increase of the ionicity of them. λ=6.5 is adopted in the case of completely ionic materials like I-VII rocksalt compounds. It is found from Fig. 2.3.80 that the bulk modulus B of the transition metal hydrides also relates to the nearest-neighbor separation d. The relationship is empirically expressed as follows;

$$B[GPa] = 1480 \times (10d)^{-3.5} \qquad (2\text{-}3\text{-}62)$$

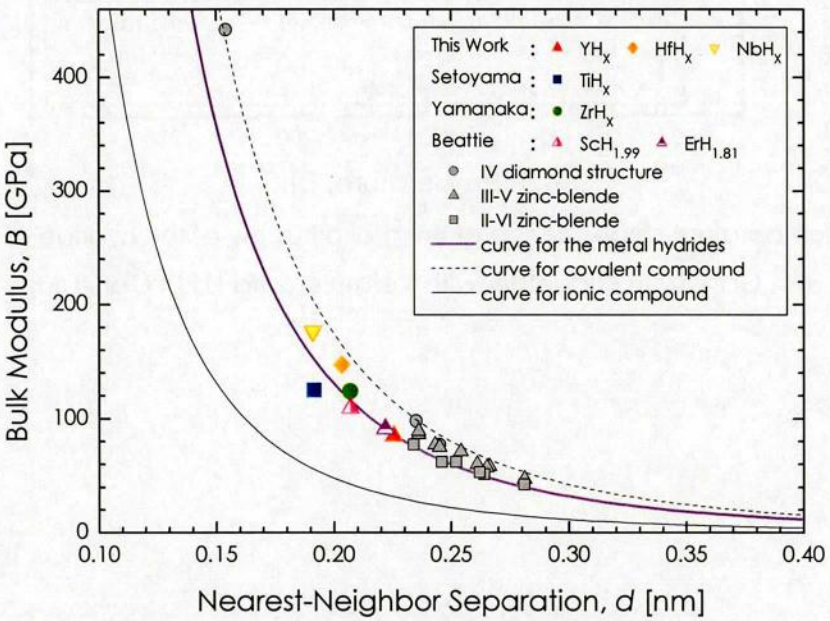


Fig. 2.3.80. Relationship between bulk modulus B and nearest-neighbor separation d of the metal hydrides, together with literature data [9, 21, 69, 85, 121, and 122].

In the case of the metal hydrides, λ =2.2 is applicable in the equation (2-3-62). Therefore, it is considered that the covalency of the transition metal hydrides is smaller than the materials in the diamond and zinc-blende structure and much larger than the ionic materials.

It is also considered that the changes in the mechanical properties of these hydrides are related to those in the density and the bond-length which are determined by the lattice parameters. Fig. 2.3.81 shows the relationship between the changing rate for the elastic moduli and for the lattice parameter da/dC_H of the fluorite-structured metal hydrides [9, 13, 16, and 21].

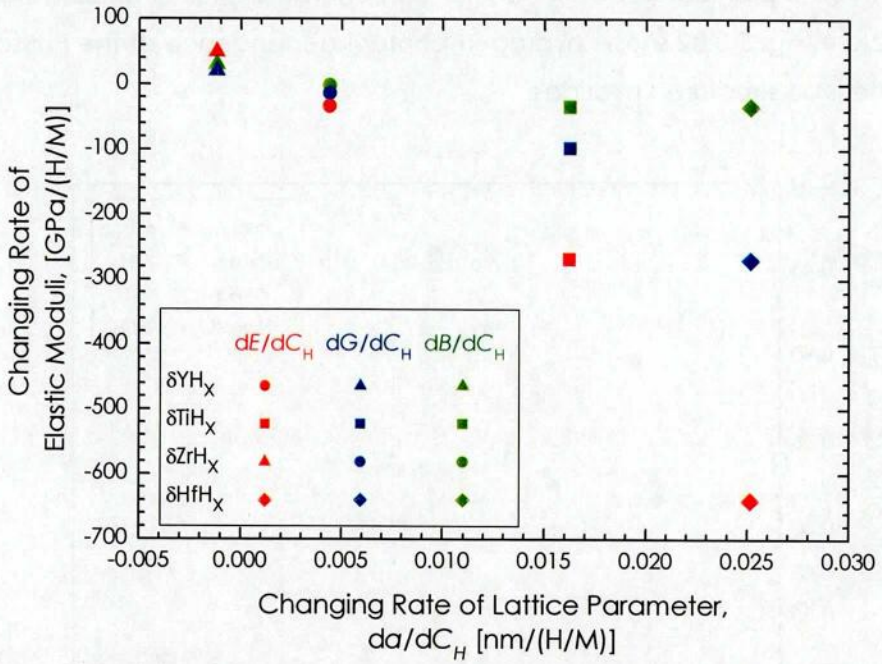


Fig. 2.3.81. Relation between changing rates of elastic moduli and changing rates of lattice parameters da/dC_H of fluorite-structured metal hydrides, together with literature data [9, 13, 16, and 21].

It is found that the degree of lattice expansion of the hydrides appear to affect that of their Young's modulus reductions whereas the lattice shrinking of the yttrium hydride enhances its Young's modulus. Similar behavior is also observed in the relationship between the changing rate for the shear modulus dG/dC_H and for the lattice parameter da/dC_H of the hydrides. On the contrary, the bulk moduli of the hydrides almost unchanged by the hydrogen content because the change in the absolute value

of lattice parameters by hydrogen addition are 5 %/(H/M) at the highest.

It is important to remember that the mechanical properties of the non-stoichiometric hydrides are also affected by variations in the binding state involved with the change in the amount of hydrogen and the lattice volume. Actually, the Young's and shear moduli of the niobium hydride increase with increasing the hydrogen content although the lattice parameters of the hydride increase due to hydrogen addition. Generally, super hard materials such as beryllium and diamond have very small values of the Poisson's ratio; soft materials have large values of the Poisson's ratio. When the Cauthy relation is valid and also the elasticity of crystal is isotropic, the Poisson's ratio equals to 0.25. Therefore, it is considered that the Poisson's ratio relies heavily on the mechanical stability of crystal and characteristics of binding state in the crystal structure. Fig. 2.3.82 shows hydrogen content dependence of the Poisson's ratio of the fluorite type structured hydrides.

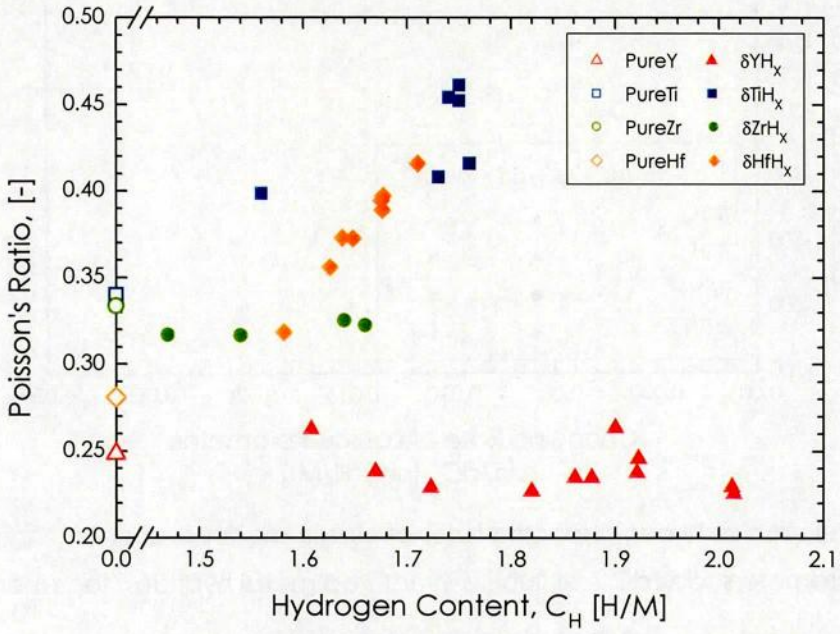


Fig. 2.3.82. Hydrogen content dependence of Poisson's ratio of the fluorite-structured metal hydrides, together with literature data [9, 13, 16, and 21].

The Poisson's ratio of the hydride that has the comparatively small changing rate of the Young's modulus with hydrogen content is found to be almost independent of the hydrogen content. On the contrary, for the hydride whose Young's modulus drastically reduces by hydrogen addition, the Poisson's ratio is also drastically changed with the

hydrogen content. In addition, comparatively high Poisson's ratios of the pure metals appear to correspond to the comparatively high Poisson's ratios of the metal hydride, and vice versa.

Fig. 2.3.83 shows the relationship between the changing rates of the Young's modulus and changing rates of the Poisson's ratio of the metal hydrides. In this figure, the data of niobium hydride is also plotted in order to declare the importance of Poisson's ratio. As described in the section 2-3-3, the elastic moduli of niobium hydride increase with increasing the hydrogen content although its lattice spreads by hydrogen addition. It is found from this figure that the changing rate of the Young's modulus with the hydrogen content is also related to that of the Poisson's ratio. Therefore, the mechanical stability and/or characteristics of binding state of metal hydrides are considered to be also changed with the hydrogen content. This is important to give a more detailed explanation about the drastic changes in the Young's and shear moduli although the change in the mechanical properties of metal hydrides with the hydrogen content is certainly related to the lattice volume change. For further discussion, the electronic structure calculations for the metal-hydrogen systems are necessary, which are described in Chapter 3.

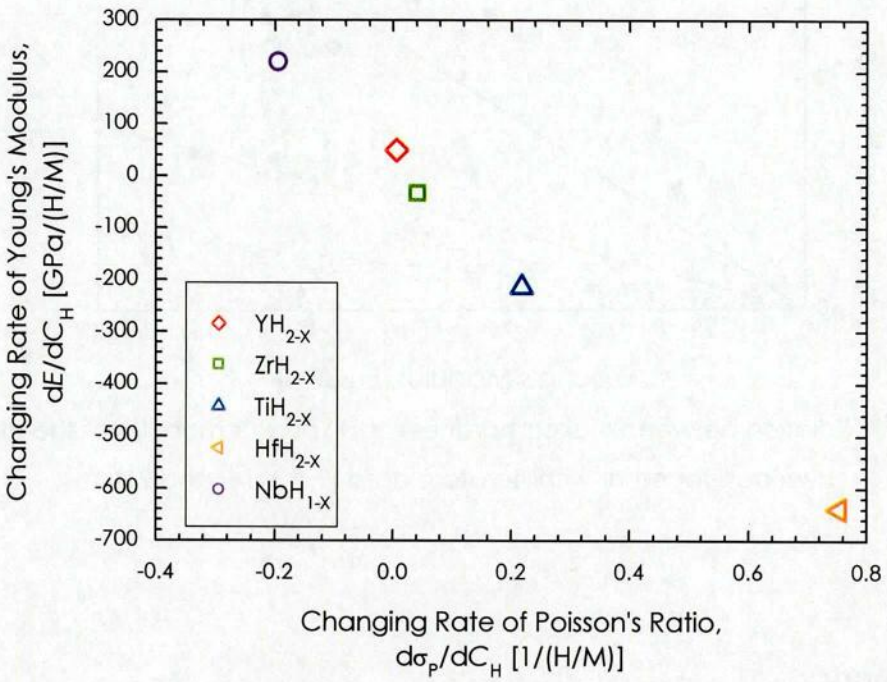


Fig. 2.3.83. Relationship between changing rates of Young's modulus dE/dC_H and changing rates of Poisson's ratio $d\sigma_P/dC_H$ of the metal hydrides, together with literature data [9, 13, 16, and 21].

The hardness (H_V)/Young's modulus (E) ratio is known to be a factor to categorize plastic or elastic materials [123]. For example, the H_V / E for carbide or oxide ceramics was reported as about 0.05, and that for bcc, fcc and hcp metal is 0.006, 0.003, 0.004, respectively. Fig. 2.3.84 shows the relation between the Young's modulus and the Vickers hardness of the metal hydrides, together with literature data [9, 13, 16, and 21]. The H_V / E for the fluorite-type structured hydrides is 0.0215, which is a middle value between metal and ceramics. Therefore, it is considerable that deformation mechanism of the fluorite-type structured hydrides is unique and different from that of the metals or ceramics. The H_V / E for the niobium hydride is 0.00921 and is slightly smaller than that of the fluorite-type structured hydrides. This difference is considered to come from the differences in the crystal structure and hydrogen content.

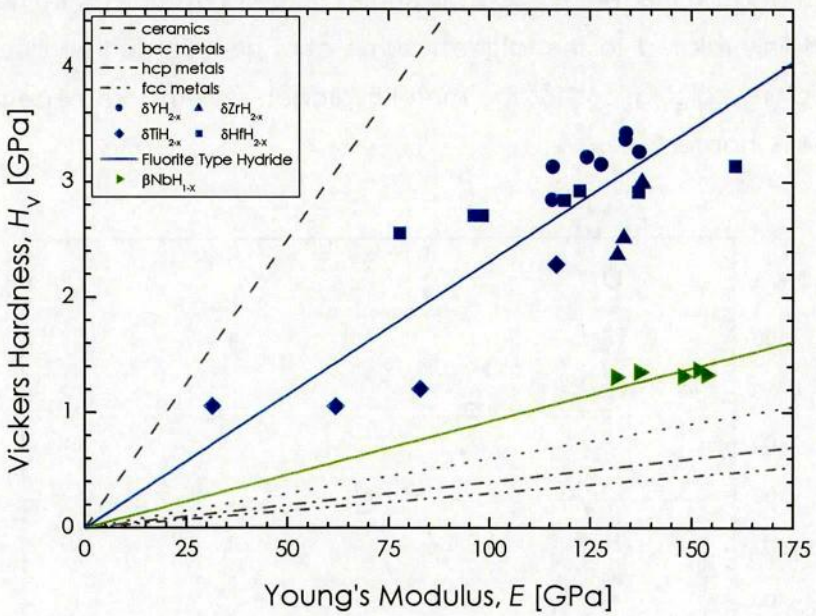


Fig. 2.3.84. Relation between Vickers hardness and Young's modulus of the metal hydrides, together with literature data [9, 13, 16, and 21].

2-4. Summary

In this chapter, the basic bulk properties of the metal-hydrogen systems, i.e. the mechanical properties of metal hydrogen solid solutions and the thermophysical properties of metal hydrides, were evaluated.

The mechanical properties of single phase hydrogen solid solutions of the yttrium and niobium were measured. The elastic moduli of the hydrogen solid solutions increased with increasing hydrogen content. The Vickers hardness of the hydrogen solid solutions also increased with increasing hydrogen content. Therefore, it was considered that the yttrium and niobium were elastically and plastically hardened by the effect of hydrogen dissolution. This trend differed from the titanium and zirconium hydrogen solid solutions, whose elastic moduli and hardness reduced by hydrogen addition. The interstitial hydrogen effect appeared to be independent of crystal structures. For further discussion, the electronic structure of the hydrogen solid solutions was required to be evaluated.

The author succeeded in the production of bulk metal hydrides of yttrium, hafnium, niobium, and Zr-Gd alloy, without cracks and voids. The yttrium and niobium hydrides had higher elastic moduli and Vickers hardness than the respective pure metals, whereas the mechanical properties of the hafnium hydride were lower than those of the pure hafnium. Additionally, the mechanical properties of the yttrium and niobium hydrides increased with increasing hydrogen content, on the contrary those of the hafnium hydride decreased with increasing hydrogen content. The thermal conductivity of yttrium hydride was significantly higher than that of pure yttrium although the hydrides of hafnium and niobium had almost same or less thermal conductivities than the respective pure metals. Some of the thermophysical properties of hydride of Zr-Gd alloy, which was polyphasic material, were similar to that of the zirconium hydride. Investigation on the gadolinium hydride was considered to be important. It was found from the preset study and the literatures that although yttrium, titanium, zirconium, and hafnium were adjacent in the periodic table and their hydrides exhibited the same crystal structures, they possessed polymorphic physical properties. It was considered that these results were mutually comparable and they revealed the characteristic nature of metal hydrides since their crystal structure was same. The several important correlations between the basic bulk properties of metal hydrides were found from the present and previous studies.

References

[1] J.F. Fernández, F. Cuevas, M. Algueró, C. Sánchez, Journal of Alloys and Compounds, 231 (1995) 78-84.

[2] F. Nagase, T. Otomo, H. Uetsuka, JAERI-Research 1998-064, Japan Atomic Energy Research Institute, (1998).

[3] F. Nagase, T. Otomo, H. Uetsuka, JAERI-Research 2000-046, Japan Atomic Energy Research Institute, (2000).

[4] M. Kuroda, S. Yamanaka, F. Nagase, H. Uetsuka, Nuclear Engineering and Design, 203 (2001) 185-194.

[5] S. Yamanaka, M. Kuroda, D. Setoyama, M. Uno, K. Takeda, H. Anada, F. Nagase, H. Uetsuka, Journal of Alloys and Compounds, 330-332 (2002) 400-403.

[6] M. Kuroda, S. Yamanaka, Journal of Nuclear Science and Technology, 39 (2002) 234-240.

[7] J.L. Feng, A.G. Varias, Y.K. Sui, International Journal of Solids and structures, 43 (2006) 2174-2192.

[8] 原子力発電技術機構燃料部, 平成 12 年度リサイクル燃料資源貯蔵施設安全性解析コード改良試験等に関する報告書 (2002).

[9] S. Yamanaka, K. Yoshioka, M. Uno, M. Katsura, H. Anada, T. Matsuda, S. Kobayashi, Journal of Alloys and Compounds, 293-295 (1999) 23-29.

[10] S. Yamanaka, K. Yoshioka, M. Uno, M. Katsura, H. Anada, T. Matsuda, S. Kobayashi, Journal of Alloys and Compounds, 293-295 (1999) 908-914.

[11] M. Kuroda, S. Yamanaka, F. Nagase, H. Uetsuka, Nuclear Engineering and Design, 203 (2001) 185-194.

[12] S. Yamanaka, K. Yamada, K. Kurosaki, M. Uno, K. Takeda, H. Anada, T. Matsuda, S. Kobayashi, Journal of Nuclear Materials, 294 (2001) 94-98.

[13] S. Yamanaka, K. Yamada, K. Kurosaki, M. Uno, K. Takeda, H. Anada, T. Matsuda, S. Kobayashi, Journal of Alloys and Compounds, 330-332 (2002) 99-104.

[14] M. Kuroda, S. Yamanaka, D. Setoyama, M. Uno, K. Takeda, H. Anada, F. Nagase, H.i Uetsuka, Journal of Alloys and Compounds, 330-332, (2002) 404-407.

[15] S. Yamanaka, M. Kuroda, D. Setoyama, M. Uno, K. Takeda, H. Anada, F. Nagase and H. Uetsuka, Journal of Alloys and Compounds, 330-332 (2002) 400-403.

[16] 山中伸介, 黒田雅利, 瀬戸山大吾, 日本原子力学会和文論文誌, Vol. 1, No. 4 (2002) 323-327.

[17] M. Kuroda , D. Setoyama , M. Uno, S. Yamanaka, Journal of Alloys and Compounds, 368 (2004) 211-214.

[18] M. Uno, K. Yamada, T. Maruyama, H. Muta, S. Yamanaka, Journal of Alloys and Compounds, 366 (2004) 101-106.

[19] S. Yamanaka, D. Setoyama, H. Muta, M. Uno, M. Kuroda, K. Takeda, T. Matsuda,

Journal of Alloys and Compounds, 372 (2004) 129-135.

[20] D. Setoyama, S. Yamanaka, Journal of Alloys and Compounds, 379 (2004) 193-197.

[21] D. Setoyama, J. Matsunaga, H. Muta, M. Uno, S. Yamanaka, Journal of Alloys and Compounds, 381(1-2) (2004) 215-220.

[22] D. Setoyama, J. Matsunaga, H. Muta, M. Uno, S. Yamanaka, Journal of Alloys and Compounds, 385 (2004) 156-159.

[23] M. Ito, D. Setoyama, J. Matsunaga, H. Muta, K. Kurosaki, M. Uno, S. Yamanaka, Journal of Alloys and Compounds, 420 (2006) 25-28.

[24] B. Stalinski, Berichte der Bunsen-Gesellschaft, 76 (1972) 724-732.

[25] H. Takahashi, H. Takashita, X. Chen, AIP Conference Proceedings: International Conference on Accelerator-Driven Transmutation Technologies and Applications, (1995) 710-716.

[26] J.H. Singleton, L.N. Yannopoulos, Journal of Vacuum Science & Technology, 12 (1975) 414.

[27] P.H.L. Notten, M. Kremers, R. Griessen, Journal of the Electrochemical Society, 143 (1996) 3348-3353.

[28] R. Griessen, Europhysics News, Vol. 32 (2001) No. 2.

[29] M. Dornheim, A. Pundt, R. Kirchheim, S. J. van der Molen, E. S. Kooij, J. Kerssemakers, R. Griessen, H. Harms and U. Geyer, Journal of Applied Physics, 93 (2003) 8958-8965.

[30] M.M. Sanchez-Lopez, P. Velasquez, R. Castaner, A. Gutierrez, J. Costa-Quintana, F. Lopez-Aguilar, Proceedings SPIE—International Society for Optical Engineering, 4829 (2003) 797-798.

[31] D. Khatamian, F.D. Manchester, Phase Diagrams of Binary Hydrogen Alloys, 11 (1990) 293-304.

[32] H. Okamoto, Journal of Phase Equilibria, 12 (1991).

[33] S.S. Sidhu, J.C. McGuire, Journal of Applied Physics, 23 (1952) 1257-1261.

[34] L. Espagno, P. Azou, P. Bastien, Comptes Rendus, 250 (1960) 4352.

[35] R.K. Edwards, E. Veleckis, The Journal of Physical Chemistry, 66 (1962) 1657-1661.

[36] H.M. Yun, R.H. Titran In: J.J. Stephens, T.M.S. Ahmad, (Editors), High Temperature Nb Alloys, (1991) 83.

[37] D.M. Shah, D.L. Anton, D.P. Pope, Material Science & Engineering A, 192–193 (1995) 658-672.

[38] D. Khatamian, V.C. Ling, Journal of Alloys and Compounds, 253–254 (1997) 162-166.

[39] D.A. Petti, K.A. McCarthy, Fusion Engineering and Design, 54 (2001) 537-545.

[40] L. Lanzani, M. Ruch, Journal of Nuclear Materials, 324 (2004) 165-176.

[41] Y. Nakamura, S. Sengoku, Y. Nakahara, N. Suzuki, H. Suzuki, N. Ohyabu, A. Busnyuk,

M. Notkin and A. Livshits, Journal of Nuclear Materials, 278,(2000) 312-319.

[42] Y. Zhang, T. Ozaki, M. Komaki and C. Nishimura, Journal of Membrane Science, 224 (2003) 81.

[43] F.D. Manchester, J. Pitre, In: F.D. Manchester (Eds.), "Phase Diagrams of Binary Hydrogen Alloys," ASM International, Materials Park, OH, (2000).

[44] M. Yamawaki, K. Konashi, S. Shimada, Journal of the Atomic Energy Society of Japan, 46 (2004) 457.

[45] K. Konashi et al., Proceedings of the ICAPP'06, Reno, USA (2006).

[46] K. Konashi, M. Yamawaki, T. Terai, K. Ito, "Development of Hydride Neutron Absorber for FBR," 2007 Fall Meeting of the Atomic Energy Society of Japan, P49.

[47] E. Zuzek, J.P. Abriata, A. San-Martin, F.D. Manchester, Phase Diagrams of Binary Hydrogen Alloys, 11 (1990) 309.

[48] T. Massalski, H. Okamoto, P.R. Subramanian, L. Kacprzak, Binary Alloys Phase Diagrams (2nd Edition) (1990), 1883.

[49] B. Tsuchiya, J. Huang, K. Konashi, M. Teshigawara, M. Yamawaki, Journal of Nuclear Materials, 289 (2001) 329.

[50] B. Tsuchiya, M. Teshigawara, K. Konashi, M. Yamawaki, Journal of Alloys and Compounds, 330-332 (2002) 357.

[51] W.M. Mueller, J.P. Blackledge, G.G. Libowitz, "Metal Hydrides", Academic Press, New York (1968).

[52] F.A. Lewis, A. Aladjem, "Hydrogen Metal Systems", Scitec Publications Ltd., Balaban Publishers, Zürich, Switzerland (1996).

[53] Y. Fukai, "The Metal-Hydrogen System: Basic Bulk Properties", Springer Series in Materials Science 21 (1993).

[54] B. Tsuchiya, S. Nagata, T. Shikama, K. Konashi, M. Yamawaki, Journal of Alloys and Compounds, 356-357 (2003) 223.

[55] J. Xu, S. Q. Shi, Journal of Nuclear Materials, 327 (2004) 165.

[56] Y. Takahashi, M. Asou, Thermochimica Acta, 223 (1993) 7.

[57] Y. Takahashi, Netsu Sokutei, 15 (1988) 103.

[58] F.H. Spedding, B.J. Beaudry, Journal of the Less-Common Metals, 25 (1971) 61.

[59] B.J. Beaudry, F.H. Spedding, Metallurgical Transactions, B6 (1975) 419.

[60] D. Khatamian, C. Stassis, B.J. Beaudry, Physical Review, B23 (1981) 624.

[61] F. Heiniger, E. Bucher, J. Muller, Physik der Kondensiterten Materie, 5 (1966) 243.

[62] J.E. Bonnet, C. Juckum, A. Lucasson, Journal of Physics, F12 (1982) 699.

[63] V.E. Zinov'yev, "Metals at High Temperatures: Standard Handbook of Properties," Hemisphere Publishing Corp., New York, (1990).

[64] V.Ya. Markin, G.N. Parkhuta, V.A. Savin, V.I. Solovei, R.S. Yurkova, Izvestiya Akademii Nauk SSSR, Serija Neorganicheskie Materialy, 19 (1983) 1470.

[65] N.A. Landin, L.A. Izhvanov, A.S. Chernikov, V.P. Kalinin, Russian Journal of Inorganic Chemistry, 16 (1971) 274.

[66] D. Khatamian, W.A. Kamitakahara, R.G. Barnes, D.T. Peterson, Physical Review, B21 (1980) 2622.

[67] C.E. Lundin, J.P. Blackledge, Journal of the Electrochemical Society, 109 (1962) 838.

[68] J.N. Daou, P. Vajda, Physical Review, B45 (1992) 10907.

[69] A.G. Beattie, Journal of Applied Physics, 43 (1972) 3219.

[70] D.S. Parker, USAEC Report APEX-588, General Electric Company, (1960).

[71] C.E. Lundin, D.T. Klodt, Quarterly Progress Report No. 6, USAEC Report APEX-308, Denver Research Institute, (1957).

[72] J.N. Daou, A. Lucasson, P. Vajda, J.P. Burger, Journal of Physics, F14 (1984) 2983.

[73] R. Griessen, J.N. Huiberts, M. Kremers, A.T.M. van Goch, N.J. Koeman, J.P. Notten, Journal of Alloys and Compounds, 253-254 (1997) 44.

[74] M. Gupta, Solid State Communications, 27 (1978) 1355-1359.

[75] M. Gupta, J.P. Burger, Physical Review, B22 (1980) 6074.

[76] M. Gupta, Solid State Communications, 50 (1984) 439.

[77] H.J. Nolting, C.R. Simmons, J.J. Klingenberg, Journal of Inorganic and Nuclear Chemistry, 14 (1960) 208-216.

[78] Y.S. Touloukian, R.K. Kirby, R.E. Taylor, P.D. Desai, "Thermal expansion: Metallic elements and alloys", Thermophysical Properties of Matter, 12, IFI/Plenum, New York, (1975).

[79] C.E. Lundin, D.T. Klodt, Quarterly Progress Report No. 6, USAEC Report APEX-308, Denver Research Institute, (1957).

[80] H.E. Flotow, D.W. Osborne, K. Otto, The Journal of Chemical Physics, 36 (1962) 866.

[81] The SGTE Pure Substance and Solution database, GTT-DATA SERVICES, 1996.

[82] V.A. Semenov, Y.V. Lisichkin, Soviet Physics. Solid State, 27 (1985) 158.

[83] S.S. Sidhu, L.R. Heaton, D.D. Zauberis, Acta Crystallographica, 9 (1956) 607.

[84] O.M. Katz, J.A. Berger, Transaction of the Metallurgical Society of AIME, 233 (1965) 1017.

[85] T. Gorecki, Material Science and Engineering, 43 (1980) 225-230.

[86] C. Kittel, "Introduction to Solid State Physics", Wiley, New York, (1996)

[87] P.L. Rossiter, "The electrical resistivity of metals and alloys", Cambridge solid state science series, Cambridge University Press, Cambridge ; New York, (1991).

[88] R.A. Andrievskii, V.I. Savin, R.A. Lyutikov, Zhurnal Neorganicheskoi Khimii, 17 (1972)

915-19.

[89] V.D. Risovany, E.P. Kolochkov, V.B. Ponomarenko, "Hafnium in Nuclear Engineering," Russian Materials Monograph Series, American Nuclear Society, USA (2001).

[90] J.D. Cox, D.D. Wagman, V.A. Medvedev, CODATA Key Values for Thermodynamics, Hemisphere, New York, (1989).

[91] K. Bohmhammel, G. Wolf, G. Gross, H. Mädge, Journal of Low Temperature Physics, 43 (1981) 521.

[92] S. Ikeda, N. Watanabe, K. Kai, Physica, B+C 120 (1983) 131.

[93] B. Tsuchiya, M. Teshigawara, K. Konashi, S. Nagata, T. Shikama, Journal of Alloys and Compounds, 446-447 (2007) 439-442.

[94] Y.S. Touloukian, "Thermal diffusivity", Thermophysical Properties of Matter, 10, IFI/Plenum, New York, (1973)

[95] T. Schober, H. Wenzl In: G. Alefeld, J. Völkl (Editors), Hydrogen in Metals II. Topics in Applied Physics vol. 29, Springer-Verlag, Berlin, (1978) 32.

[96] I. Amato, A. Negro, Journal of the Less-Common Metals, 16 (1968) 468.

[97] E.S. Fisher, D.G. Westlake, S.T. Ockers, Physica Status Solidi, A28 (1975) 591.

[98] H.A. Wriedt, R.A. Oriani, Scripta Metallurgica et Materialia, 8 (1974) 203.

[99] M. S. Rashid, T. E. Scott, Journal of the Less-Common Metals, 30 (1973) 399.

[100] M. Sakamoto, Journal of the Physical Society of Japan, 19 (1964) 1862-1866.

[101] W. Baden, A. Weiss, ZEITSCHRIFT FUER METALLKUDE, 74 (1983) 89.

[102] V.I. Serdobintsev, N.L. Arabajian, I. Ratishvili, V.M. Tavkhelidze, Journal of Alloys and Compounds, 356-357 (2003) 100-104.

[103] D. Wlosewicz, T. Plackowski, N.I. Sorokina, Physica, B212 (1995) 113-118.

[104] N.I. Sorokina, O.V. Basargin, V.I. Savin, Soviet Physics. Solid State, 33 (1991) 3565-3569.

[105] A.T. Dinsdale, SGTE data for pure elements, Calphad 15 (1991).

[106] G. Alefeld, J. V61kl (eds.), "Hydrogen in Metals", Parts I and II, Springer, Berlin, (1978).

[107] D. Ohlendorf, E. Wicke, The Journal of Physics and Chemistry of Solids, 40 (1979) 721.

[108] T. Massalski, Binary Alloys Phase Diagrams (2nd Edition), (1990).

[109] R.L. Beck, Transactions of American Society for Metals, 55 (1962) 542.

[110] A.B. Riabou, V.A. Yartys, H.Fjellvag, B.C. Hauback, M.H. Sorby, Journal of Alloys and Compounds, 296 (2000) 312.

[111] G.E. Sturdy, R.N.R. Mulford, Journal of the American Chemical Society, 78 (1956)

1083.

[112] C.P. Kempter, R.O. Elliott, K.A. Gschneidner, Jr., The Journal of Chemical Physics, 33 (1960) 837.

[113] S.S. Sidhu, N.S.S. Murthy, F.P. Campos, D.D. Zauberis, Advances in Chemistry Series, 39 (1963) 87.

[114] K.E. Moore, W.A. Young, Journal of Nuclear Materials, 27 (1968) 316.

[115] F. Ducastelle. R. Caudron, P. Costa, Journal de Physique, 31 (1970) 57.

[116] J.S. Cantrell, R.C. Bowman Jr., D.B. Sullenger, The Journal of Physical Chemistry, 88 (1984) 918.

[117] R.C. Bowman, B.D. Craft Jr., J.S. Cantrell, E.L. Venturini, Physical Review, B31 (1985) 5604.

[118] K.G. Barraclough, C.J. Beevers, Journal of Nuclear Materials, 34 (1970) 125-34.

[119] J.E. Bonnet, J.N. Daou, Journal of Applied Physics, 48 (1977) 964.

[120] 文部科学省原子力システム研究開発事業, 平成18年度成果報告書 水素化物中性子吸収材を用いた革新的高速炉炉心に関する研究開発 (2007).

[121] M.P. Tosi, Solid State Physics, 16 (1964) 1.

[122] M.L. Cohen, Physical Review, B32, 12 (1985) 7988-7991.

[123] K. Tanaka, H. Koguchi and T. Mura, International Journal of Engineering Science, 27 (1989) 11.

CHAPTER 3

Ab initio Study of Metal-Hydrogen Systems

Chapter 3
Ab initio Study of Metal-Hydrogen Systems

3-1. Introduction

The band structure of the rare earth and transition metal hydrides, especially the stoichiometric hydrides, has long been a subject of considerable interest and controversy [1–10]. However, the ab initio electronic state calculation that pays attention to the effect of the wide-ranging hydrogen content on the physical properties of metal-hydrogen system is not so many. In fact, the metal-hydrogen alloys form the hydrogen solid solutions and some nonstoichiometric hydrides. Setoyama [11] and Yamanaka [12] reported that the elastic moduli and Vickers hardness of titanium and zirconium hydrogen solid solutions decreased with increasing hydrogen content. Contrary to these cases, the Chapter 2 of the present dissertation reveals that the yttrium and niobium become elastically and plastically hard due to the interstitial hydrogen. Wriedt [13] revealed that the solute hydrogen enhanced the Young's moduli of the VA transition metal hydrogen solid solutions. These trends are summarized in Table 3.1. The electronic structure calculations are necessary in order to evaluate the changes in the bonding state of the metals due to hydrogenation.

There is very scarce information on the thermophysical properties of the metal hydrides, except for the titanium and zirconium hydrides [14–15]. Therefore, the study by the ab initio calculation also plays an important role for the investigation on the metal hydrides. In the present dissertation, it is found that the elastic moduli and Vickers hardness of the yttrium hydride are higher than those of the pure yttrium and gradually increase with increasing the hydrogen content. Additionally, it is found that the elastic moduli and hardness of the hafnium hydride significantly reduce with increasing the hydrogen content. Setoyama et al. [14] clarified that the elastic moduli and the Vickers hardness of titanium hydride was smaller than that of pure titanium and drastically decreased with increasing hydrogen content. Yamanaka et al. showed that the zirconium hydride had larger elastic moduli and hardness than the pure metal, and those of the hydride decreased with increasing hydrogen content [15]. Thus, it is found from the present study and the literatures that the metal hydrides possess polymorphic physical properties.

From such viewpoint, the ab initio electronic structure calculations were executed in order to elucidate the origin of the physical properties of the metal hydrogen solid solutions and hydrides with different hydrogen contents.

Table 3.1. Hydrogen content dependence of Young's modulus of the transition metal hydrogen solid solutions.

$E = E_0 + k_1 C_H + k_2(T - 273)$			
Material	E_0 [GPa]	k_1 [GPa/(H/M)]	k_2 [10^{-2}xGPa/K]
α-Y(H) (Chapter 2)	65.0	32.7	-
α-Ti(H) (Setoyama)	122.2	-147.3	-6.81
α-Zr(H) (Yamanaka)	97.1	-225.3	-6.04
α-V(H) (Wriedt)	126	61	-
α-Nb(H) (Chapter 2)	101.4	83.1	-
α-Ta(H) (Wriedt)	188	14	-

3-2. Calculation

3-2-1. Calculation Codes

The total energy calculations were performed using the Cambridge Serial Total Energy Package (CASTEP), which is a pseudopotential plane-wave code based on the density functional theory (DFT) originally developed in the Theory of Condensed Matter Group at Cambridge University [16]. The molecular orbital (MO) calculations were performed using the Discrete Variational (DV)-Xα method, based on the Hartree-Fock-Slater one-electron theory in order to estimate the electronic structure. The DV-Xα method is a non-relativistic first principles method using Slater's Xα potential as the exchange-correlation term. The molecular orbitals are constructed by a linear combination of numerically generated atomic orbitals (LCAO). The details of the DV-Xα method have been discussed at length in literatures [17–19].

3-2-2. Elastic Constants

Elastic constant calculations were carried out on the CASTEP-code. The elastic constants of a material describe its response to an applied stress or, conversely, the stress required to maintain a given deformation. To calculate the elastic constant, the strain applied to the crystal and then the stress of the system was calculated. Both stress and strain have three tensile and three shear components, giving six components in total. The linear elastic constants form a 6×6 symmetric matrix C_{ij} (i, j = 1 – 6). The

stress-strain relation was expressed using the following equation:

$$\sigma_i = C_{ij}\varepsilon_j \tag{3-1}$$

where the σ_i is the stress in matrix and the ε_j is the strain in matrix (i, j=1...6=xx, yy, zz, yz, zx, xy). Any symmetry present in the structure may make some of these components equal and others may be fixed at zero. For a cubic system there are only three independent elastic constants, namely C_{11}, C_{12}, and C_{44}. For a hexagonal system there are five independent elastic constants, namely C_{11}, C_{12}, C_{13}, C_{33}, and C_{44}. The stress theory of Nielsen and Martin [20] enables us to calculate the stress tensor σ_{ij} of a given crystal structure from a self-consistent field obtained by DFT. By this theory, the equilibrium lattice constant a_0 can be linearly interpolated at the pressure P=0 in between different lattice constants, while the bulk modulus is given by

$$B = -\frac{a_0}{3}\frac{dP}{da}\bigg|_{a=a_0} \tag{3-2}$$

for a cubic system. To obtain the independent elastic constants of a cubic system, the author applied volume-conserving homogeneous deformations on the equilibrium unit cell. The strain tensor u_{ij} of the orthorhombic deformation is denoted by a single strain parameter ε as

$$\{u_{ij}\} = \begin{pmatrix} \varepsilon & 0 & 0 \\ 0 & -\varepsilon/(1+\varepsilon) & 0 \\ 0 & 0 & 0 \end{pmatrix} \tag{3-3}$$

And that of the shear deformation by γ as

$$\{u_{ij}\} = \begin{pmatrix} 0 & \gamma/2 & 0 \\ \gamma/2 & 0 & 0 \\ 0 & 0 & 0 \end{pmatrix} \tag{3-4}$$

Under the condition $\varepsilon, \gamma << 1$. Hooke's law gives

$$C_{11} - C_{12} = (\sigma_1 - \sigma_2)\left(\varepsilon + \frac{\varepsilon}{1+\varepsilon}\right)^{-1} \tag{3-5}$$

$$C_{44} = \sigma_4/\gamma \tag{3-6}$$

Since the bulk modulus is related to the elastic constants as

$$B = \frac{1}{3}(C_{11} + 2C_{12}) \tag{3-7}$$

Consequently, we can obtain the elastic constants using the bulk modulus from equation (3-2) and following equations:

$$C_{11} = B + \frac{2}{3}(C_{11} - C_{12}) \tag{3-8}$$

$$C_{12} = B - \frac{1}{3}(C_{11} - C_{12}) \tag{3-9}$$

The calculation results were obtained in the case of single crystal. The elastic moduli for polycrystalline were calculated from the elastic stiffness using the Voigt's approximation [21]. Voigt's theory assumes that the strain in the polycrystalline aggregate to the external strain is uniform.

3-2-3. Thermal Expansion

The Helmholtz energy of a vibrating system comprises the total energy from ab initio electronic total-energy calculations E_{total}, the free energy of the vibrating lattice, F_D, and the contribution due to the thermal excitations of electrons, F_{el}:

$$\begin{aligned} F(T,V) &= E_{total}(V) + F_D(T,V) + F_{el}(T,V) \\ &= E_{total}(V) + E_D(V,T) - T \times S_D(V,T) + E_{el}(V,T) - T \times S_{el}(V,T) \end{aligned} \tag{3-10}$$

According to the Debye model, the E_D and S_D can be estimated as follows:

$$E_D(T,V) = \frac{9}{8} N k_B \theta_D + 3 N k_B T D\left(\frac{\theta_D}{T}\right) \tag{3-11}$$

$$S_D(T,V) = 3 N k_B \left[\frac{4}{3} D\left(\frac{\theta_D}{T}\right) - \ln\left(1 - \exp\left(-\frac{\theta_D}{T}\right)\right)\right] \tag{3-12}$$

where $D(\theta_D / T)$ denotes the Debye function that is listed in mathematic tables or calculated by numerical methods. Note that the Debye temperature, θ_D is a function of volume in order to introduce anharmonic effects and the Grüneisen parameter. When the free energy is expressed as function of T and V, the equilibrium $V(T)$ and thus linear thermal expansion coefficient (LTEC) can be calculated through the minimum of $F(T,V)$, i.e. $\partial F(T,V)/\partial V$ equals to zero. Additionally, other thermodynamic properties, such as heat capacity and entropy, can be calculated once the equilibrium volume is determined. In order to include the volume dependence of the Debye temperature, the following relation is used.

$$\theta_D / \theta_{D,0K} = (V_0 / V)^{\gamma_G} \tag{3-13}$$

where $\theta_{D,0K}$ is the Debye temperature corresponding to the equilibrium volume V_0 at 0 K. The Grüneisen parameter, γ_G, as well as $\theta_{D,0K}$ and V_0, can be derived from ab initio calculated total-energy curve, i.e. E_{total}, at 0 K. However, the equation (3-13) implies that

$$\gamma_G = -\frac{\ln\theta_D - \ln\theta_{D,0K}}{\ln V - \ln V_0} \tag{3-14}$$

which is only an approximation of the definition of the Grüneisen parameter,

$$\gamma_G(V) = -\frac{\partial \ln\theta_D}{\partial \ln V} \tag{3-15}$$

This approximation is valid in the vicinity of V_0. Moruzzi et al. [22] showed that the theoretical calculated CLEs agreed well with experiments below 300 K. Note that in Moruzzi's scheme, the initial γ_G used to evaluate the Debye temperatures was derived at the equilibrium volume at 0 K and it was a constant, whereas the resulting Morse-fitted values of γ_G were increasing with increasing temperatures. This may be a further indication that Moruzzi's scheme was not fully self-consistent. Wang et al. [23] realized this problem and derived a general expression for the relation between θ_D and volume from a mean-field potential. Lu et al. [24] shows that it was possible to derive an equivalent $\theta_D - V$ relation from the above definition for γ_G in a straightforward way, and also to incorporate it into the Debye–Grüneisen model instead of the equation (3-13).

There are three well-known approximate ways to calculate the Grüneisen parameter γ_G for a monoatomic solid, and they can be combined using the following expression:

$$\gamma(V) = \frac{1}{3}(\lambda - 1) - \frac{V}{2}\frac{\partial^2 \left[PV^{(2/3)(\lambda+1)}\right]/\partial V^2}{\partial \left[PV^{(2/3)(\lambda+1)}\right]/\partial V} \tag{3-16}$$

where P is pressure. When $\lambda = -1$, one obtains the Slater approximation [25], which considers the material as an elastic medium and assumes the independence of Poisson's ratio on volume. When $\lambda = 0$, it reduces to the expression proposed by Dugdale and MacDonald [26], who assumed that in a cubic crystal all the force constants have the same volume dependence. When $\lambda = 1$, the expression takes the same form as proposed by the free volume theory [27]. In the present study, the Slater approximation is adopted. When integrating the equation (3-15) from both sides and using the equation (3-16), we obtains

$$\theta_D(V) = DV^{2/3}\left[-\frac{\partial P(V)}{\partial V} - \frac{2(\lambda+1)}{3}\frac{P(V)}{V}\right]^{1/2} \tag{3-17}$$

where D is the integral constant that is to be determined. Usually the quantity in the bracket is positive as it is related to the bulk modulus or the curvature of the total energy curve. However, there exists a critical V, above which the quantity in the bracket in

the equation (3-17) will be negative. Fortunately in the case of normal thermal expansion, this critical V will hardly ever be reached. We can thus use the equation (3-17) to make the following derivation simple and clear. When $\lambda = -1$, i.e. Slater's expression is chosen, the equation (3-17) is transformed to

$$\theta_D(V) = DV^{2/3}\left[-\frac{\partial P(V)}{\partial V}\right]^{1/2} \tag{3-18}$$

On the other hand, the Debye temperature is proportional to the Debye sound velocity, υ_D:

$$\theta_D(V) = \frac{\hbar}{k_B}\left(\frac{6\pi^2 N}{V}\right)^{1/3}\upsilon_D \tag{3-19}$$

In the vicinity of the equilibrium volume V_0, the corresponding pressure is very small and the second term in the equation (3-17) can be neglected considering that the bulk modulus usually has a magnitude of hundreds GPa. Thus the equation (3-17) is approximately true. This relation indicates that the $\theta_D - V$ relation is independent of the choice of expression for the Grüneisen parameter (γ_G) at small volume expansion. At volumes much larger than the V_0, the author assumed that the integral constant in the equation (3-17) remained unchanged, yielding

$$\theta_D(V) = k(\nu)\frac{\hbar}{k_B\sqrt{m}}\left(6\pi^2 N\right)^{1/3}V^{2/3}\times\left[-\frac{\partial P(V)}{\partial V}\right]^{1/2} \tag{3-20}$$

$$k(\nu) = \left[\frac{1}{3}\left[\left[\frac{1+\nu}{3(1-\nu)}\right]^{3/2} + 2\left[\frac{2(1+\nu)}{3(1-2\nu)}\right]^{3/2}\right]\right]^{-1/3} \tag{3-21}$$

where ν is the Poisson's ratio. The Poisson's ratio can be obtained from the elastic constant calculation. The author could numerically evaluate the $\theta_D(V)$ and therefore $F(V)$ using only information from ab initio electronic total-energy calculations at 0 K. The effect of hydrogen optical vibration was also estimated in the equations (3-11) and (3-12) with using the Einstein function instead of the Debye function. The electronic terms are excluded into the present calculation assuming that its effect is negligible small.

3-2-4. Calculation Conditions

For the CASTEP total energy calculation, the exchange-correlation potential was treated by using functional of GGA-PW91 (generalized-gradient-corrected local density approximation of Perdew and Wang) [28]. The ultra-soft pseudopotential was applied

to describe the electron-ion interaction. Each selfconsistent field calculation of the total energy is converged within 5.0×10^{-7} eV. The cutoff energies of the wave functions are selected to be 350, 430, 340, and 350 eV for the yttrium, titanium, zirconium, and hafnium hydrides, respectively. A k point mesh of 16x16x16 was chosen. The elastic constant calculations were performed for the yttrium hydrogen solid solutions and the hydrides of yttrium, titanium, zirconium, and hafnium with different hydrogen contents. Thermal expansions of the stoichiometric di-hydrides of yttrium, titanium, zirconium, and hafnium were evaluated.

The DV-Xα calculation was executed with 100,000 sample points per atom in the selfconsistent field. The calculations were continued until the difference of the orbital population of all the atoms between the initial and final state comes to less than 0.002. In order to improve the convergence time, a smearing technique [29, 30] was applied with a smearing parameter of 0.05 eV. The electronic structures, such as the density of states for electrons, the bond order, and the distribution of the electron density, can be calculated from the Milliken analysis [31]. These electronic structures of the yttrium, titanium, zirconium, hafnium, and niobium hydrogen solid solutions with different hydrogen contents were evaluated. These electronic structure calculations were also performed for the yttrium, titanium, zirconium, and hafnium hydrides with different hydrogen contents.

3-3. Results and Discussion

3-3-1. Mechanical Properties of Metal Hydrogen Solid Solutions

Rare-earth metals including the yttrium have large terminal solid solubility of hydrogen even at room temperature. Therefore, the author can make a super-cell model for the ab initio total energy calculation of the yttrium hydrogen solid solution with a reasonable size, as shown in Fig. 3.1. With use of these super-cell models, the elastic constant calculations were carried out. Table 3.2 shows the calculation results of the elastic stiffness constant C_{ij} for pure yttrium with the reference data for single crystal yttrium by Smith [32]. The calculated values give close agreement with the experimental literature data, and therefore the discussion on hydrogen effects could be meaningful. Fig. 3.2 shows the calculated Young's modulus and shear modulus of yttrium hydrogen solid solution, together with experimental results obtained in Chapter 2. These calculated elastic moduli are in good accordance with the experimental results. It is also found from the ab initio calculation that the elastic moduli of yttrium increases

by interstitial hydrogen in the metallic lattice.

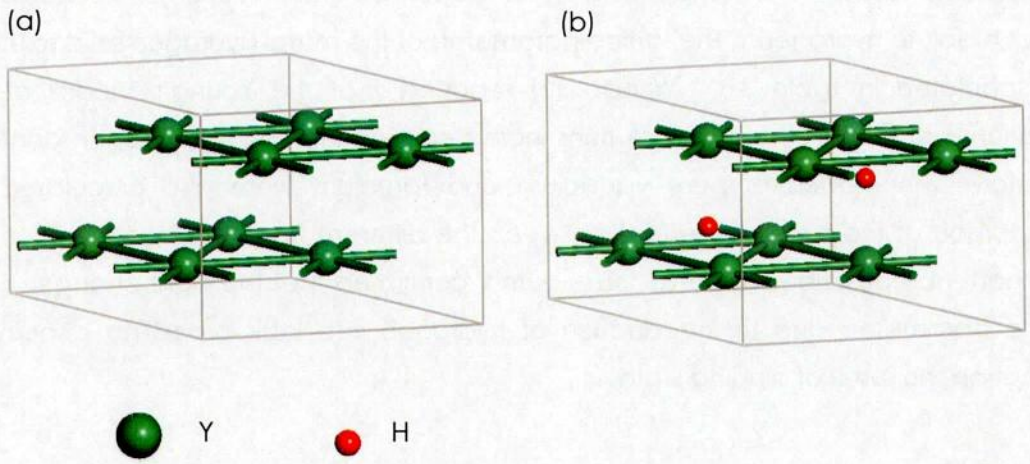


Fig. 3.1. Super-cell models of yttrium hydrogen solid solutions for CASTEP calculation; (a) Y_8H_0 and (b) Y_8H_2.

Table 3.2. The calculated elastic constant of pure yttrium, together with literature data [32].

Elastic stiffness	Calculation	Literature
C_{11} [GPa]	73.3	77.9
C_{12} [GPa]	19.5	28.5
C_{13} [GPa]	18.6	21.0
C_{33} [GPa]	72.2	76.9
C_{44} [GPa]	23.5	24.3

In order to discuss the difference in the hydrogen effects on mechanical properties between the transition metals, the molecular orbital calculations were performed. The binding states, such as density of state, electron density distribution, and bond order, of

several transition metal hydrogen solid solutions were evaluated. Fig. 3.3 and Fig. 3.4 show cluster models of metal hydrogen solid solutions used in the present study. These calculations applied to the yttrium, titanium, zirconium, and niobium hydrogen solid solutions; the results were comparable under the same condition in order to discuss the effect of solute hydrogen. The lattice parameters of the metal hydrogen solid solutions are tabulated in Table 3.3. Wriedt [13] reported that the Young's moduli of VA transition metal hydrogen solid solutions increased with increasing hydrogen content. Therefore, the models of pure vanadium and tantalum were also calculated for comparison of the hydrogen effect between the different transition metals, which will hereinafter be described in detail. The author confirmed that the slight change of the lattice parameters due to introduction of hydrogen into lattice had no discernible impact on the result of binding state.

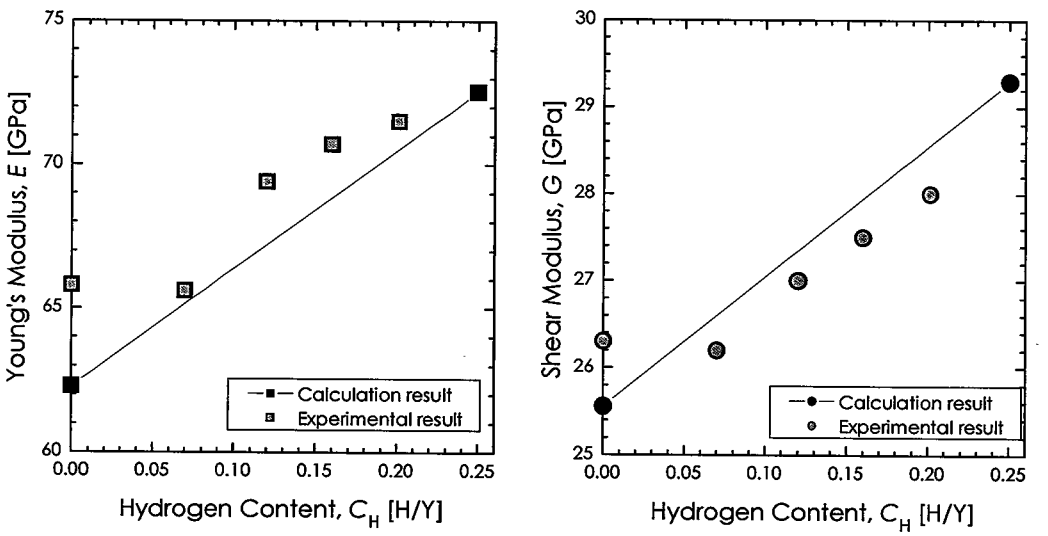


Fig. 3.2. Calculated Young's modulus and shear modulus of yttrium hydrogen solid solution, together with experimental results.

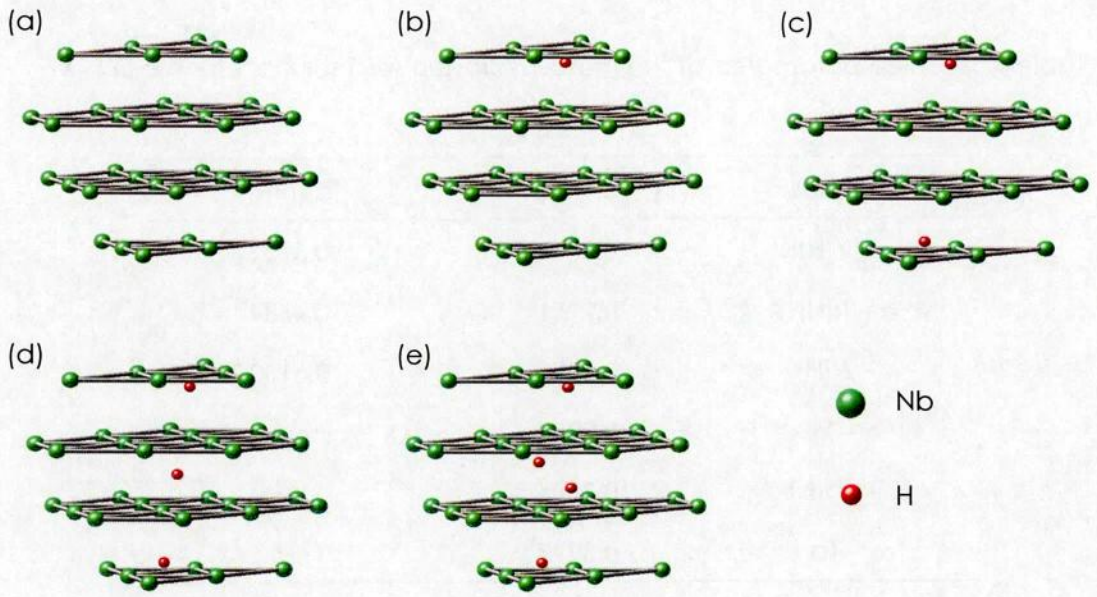


Fig. 3.3. Cluster models of metal hydrogen solid solutions for DV-Xα calculation; (a) M_{36}, (b) $M_{36}H_1$, (c) $M_{36}H_2$, (d) $M_{36}H_3$, and (e) $M_{36}H_4$, where M = Y, Ti, and Zr.

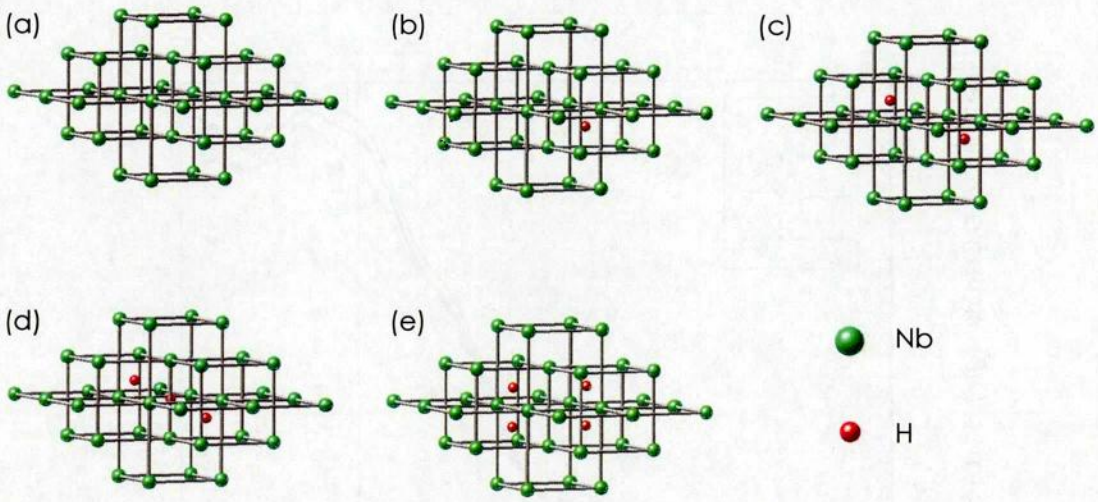


Fig. 3.4. Cluster models of niobium hydrogen solid solutions for DV-Xα calculation; (a) Nb_{36}, (b) $Nb_{36}H_1$, (c) $Nb_{36}H_2$, (d) $Nb_{36}H_3$, and (e) $Nb_{36}H_4$.

Table 3.3. Lattice parameters of the metal hydrogen solid solutions for the DV –Xα clusters.

Material	a [nm]	c [nm]
α – Y(H)	0.3648	0.5732
α – Ti(H)	0.2951	0.4684
α – Zr(H)	0.3230	0.5150
α – V	0.3028	-
α – Nb(H)	0.3304	-
α – Ta	0.3297	-

Fig. 3.5 shows total electron density of states of the yttrium hydrogen solid solutions with different hydrogen contents. The zero of the energy scale corresponds to the Fermi level. The units are states/eV/unit-cell. Due to interstitial hydrogen, the electrons in the vicinity of the Fermi energy of yttrium gradually reduce and the peak at about 6 eV below the Fermi energy simultaneously appears.

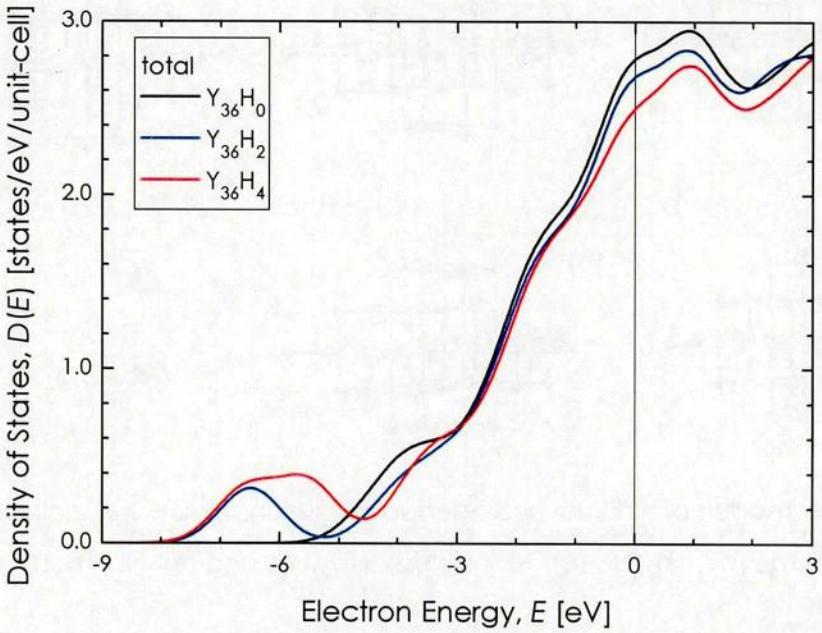


Fig. 3.5. Total density of states of yttrium hydrogen solid solutions with different hydrogen contents. The zero of the energy scale corresponds to the Fermi level.

Fig. 3.6 (a)-(d) show partial density of states of valence electrons of the yttrium hydrogen solid solutions with different hydrogen contents. For the Y 4d and 5s electrons, the state near the Fermi energy decreases with hydrogen addition, and the new peak at about 6 eV below the Fermi energy appears simultaneously. The appearance of density of states for H 1s around 6 eV below the Fermi energy induces these shifts of electron energy. This result indicates that the metal-metal covalent bonding, which has important role in characteristics of the transition metals, reduce by hydrogen addition and the metal-hydrogen bonding is simultaneously created.

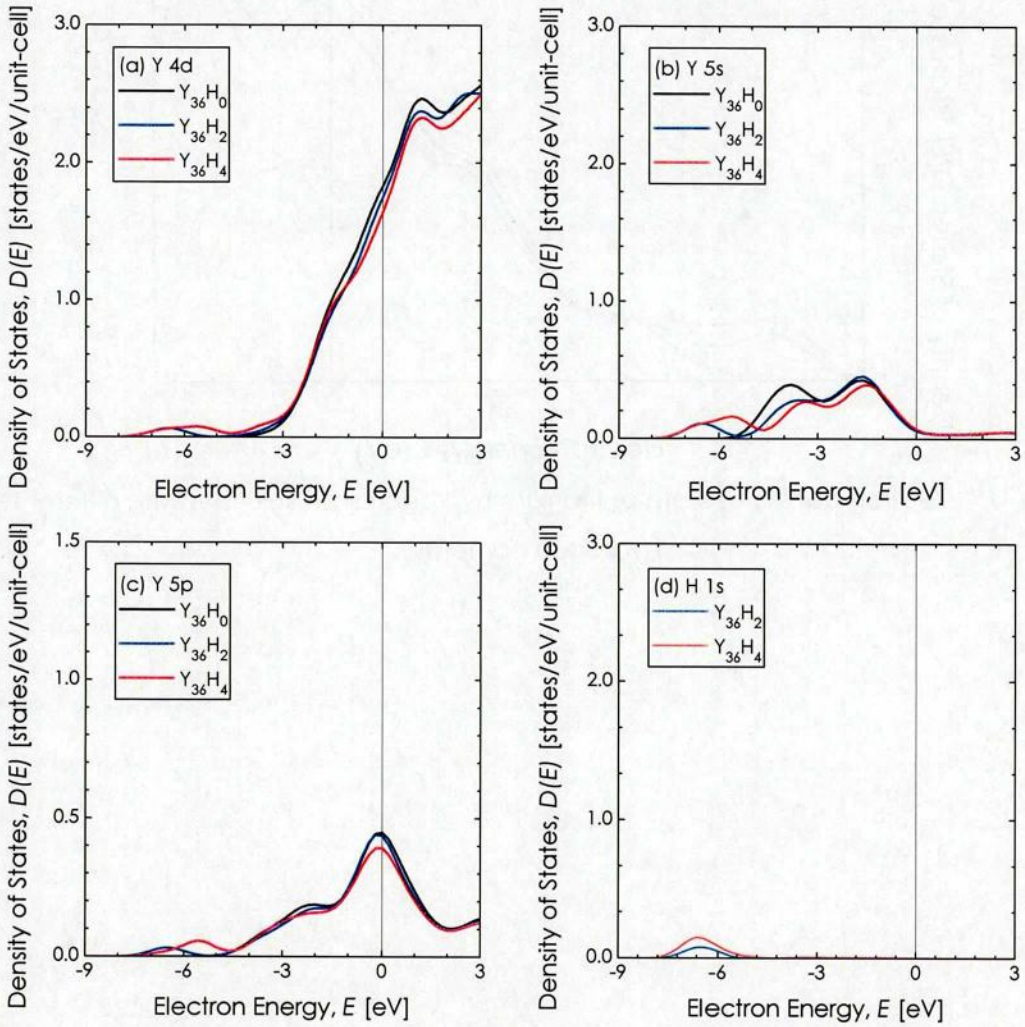


Fig. 3.6. Partial density of states of yttrium hydrogen solid solutions with different hydrogen contents; (a) Y 4d, (b) Y 5s, (c) Y 5p, and (d) H 1s.

Fig. 3.7, Fig. 3.8, and Fig. 3.9 show the electron density of state of titanium, zirconium, and niobium hydrogen solid solutions with different hydrogen contents. It is found from these figures that a new hydrogen-related band appears at about 5 eV for the titanium hydrogen solid solution and at about 7 eV for the zirconium and niobium hydrogen solid solutions. As discussed above, the changes of electronic states due to hydrogen addition indicates the creation of metal-hydrogen bonding.

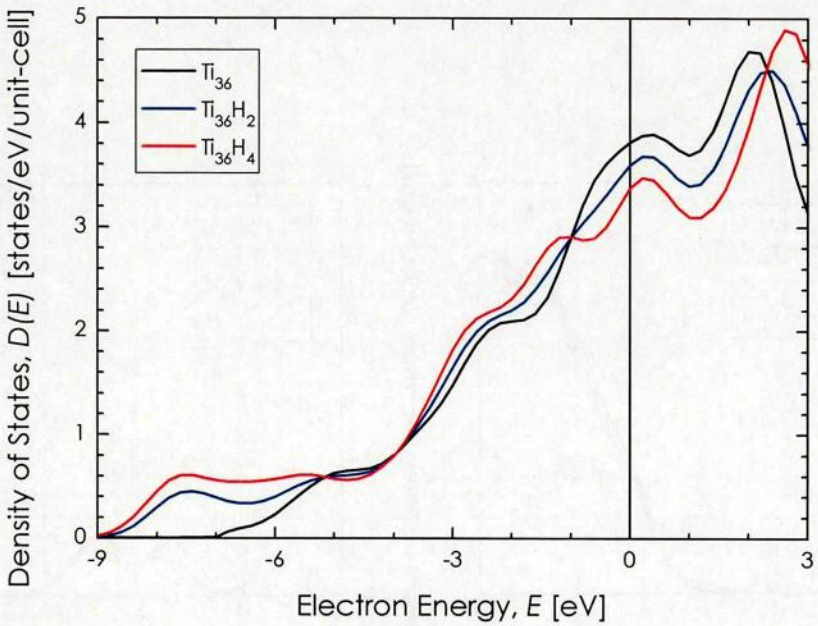


Fig. 3.7. Electron density of state of titanium hydrogen solid solutions with different hydrogen contents.

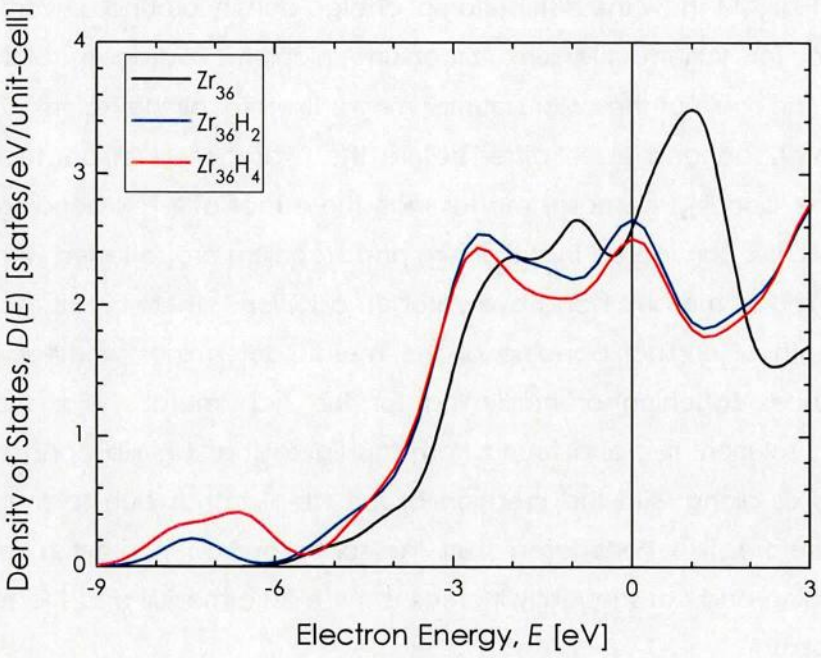


Fig. 3.8. Electron density of state of zirconium hydrogen solid solutions with different hydrogen contents.

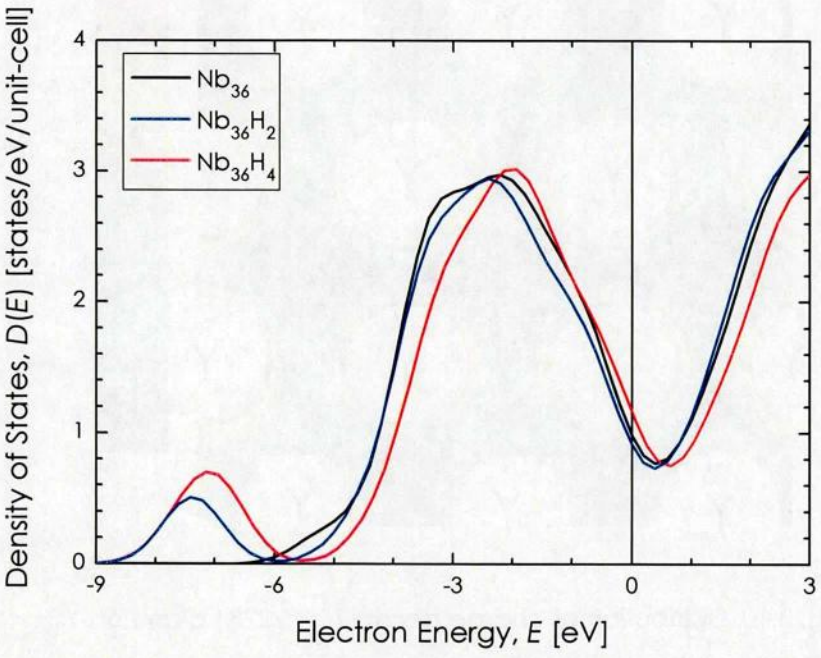


Fig. 3.9. Electron density of state of niobium hydrogen solid solutions with different hydrogen contents.

Fig. 3.10 – Fig. 3.14 show the distribution of charge density around a hydrogen atom in the clusters for yttrium, titanium, zirconium, niobium hydrogen solid solutions, respectively. The scale of the color counter map is fixed for all the results. The yttrium atoms are loosely bonded each other before the hydrogen addition, therefore the reduction of Y-Y bonding is smaller matter than the effect of Y-H-Y bonding creation. On the contrary, it is considered that titanium and zirconium are softened with the result of the weakening of metallic bond by hydrogen addition. Therefore, it is considered that the strength of original bonding of the metals determines whether the solute hydrogen induces softening or hardening for the hcp metals. For the niobium hydrogen solid solution, it is also found from this figure that Nb–Nb bond population slightly decreases along with the creation of the Nb–H bonds due to the hydrogen addition. Therefore, it is considered that the solute hydrogen plays a role for the Nb–H–Nb bonding and consequently increases the elastic moduli and the hardness in the case of niobium.

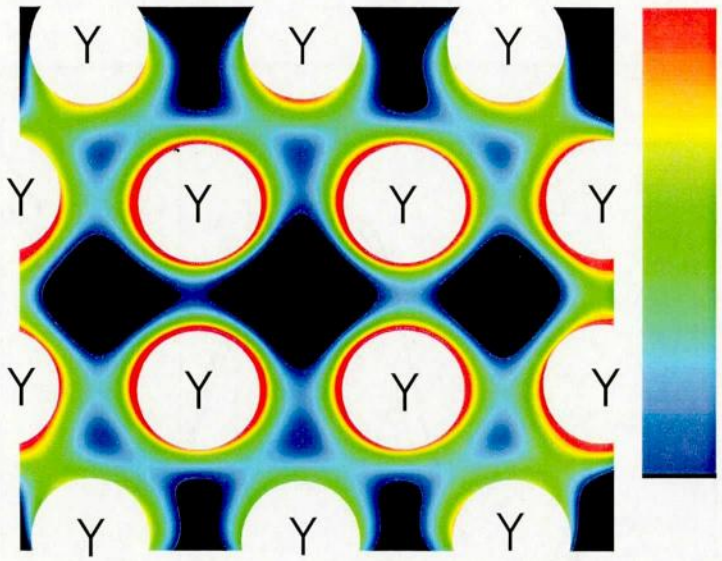


Fig. 3.10. Distribution of charge density for ($20\bar{2}3$) plane of Y_{36} .

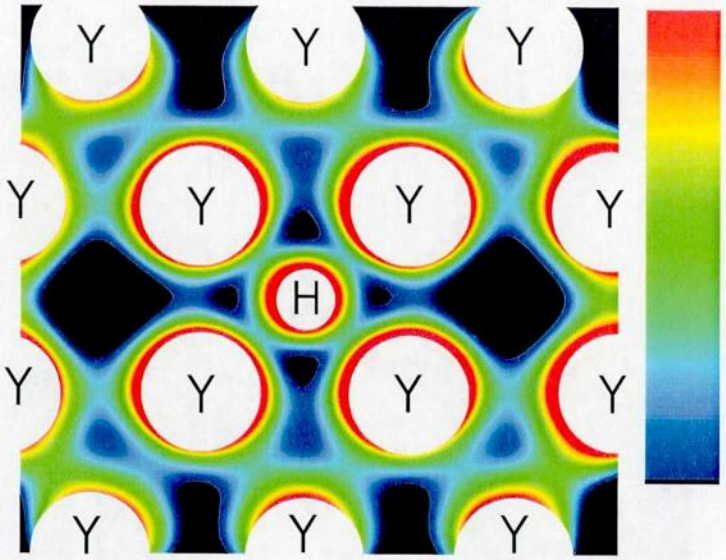


Fig. 3.11. Distribution of charge density for $(20\bar{2}3)$ plane of $Y_{36}H_3$.

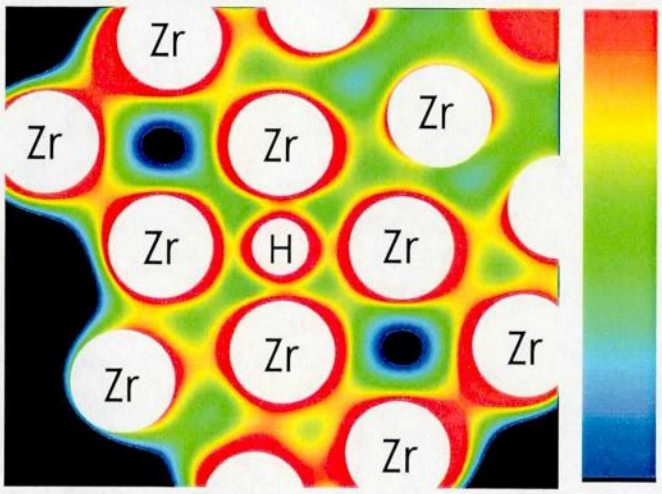


Fig. 3.12. Distribution of charge density for $(20\bar{2}3)$ plane of $Zr_{36}H_3$.

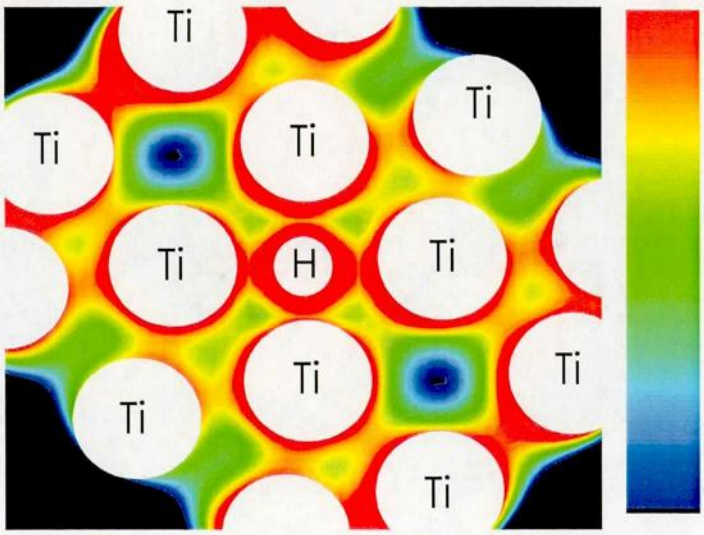


Fig. 3.13. Distribution of charge density for ($20\bar{2}3$) plane of $Ti_{36}H_3$.

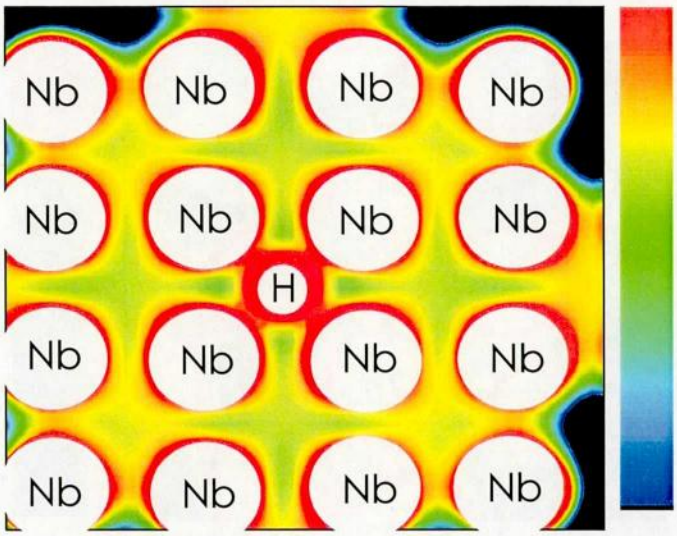


Fig. 3.14. Distribution of charge density for (100) plane of $Nb_{36}H_3$.

The authors focused on the difference on the values of bond orders in unit-cell between the yttrium, titanium, zirconium and niobium hydrogen solid solutions. The bond order is the population of electrons participating in the covalent bonding [30], which has adopted in order to give the qualitative interpretation for the elastic and plastic characteristics [33-36]. The value in the unit-cell was adopted in order to avoid the difference in the number of nearest neighbor atoms between the hcp and bcc. Fig. 3.15 shows bond orders in unit-cell for the M hydrogen solid solutions as a function of hydrogen content. The decreasing rates of metal-metal bond orders for yttrium, titanium, zirconium, and niobium are almost same as well as increasing rates of M-H bond orders. The difference between the metals is absolute values of metal-metal bond orders in unit-cell. Fig. 3.16 shows the relation between the metal-metal bond order in unit-cell and the changing rate of Young's modulus with hydrogen content of the metal hydrogen solid solutions. The changing rates were obtained from the Chapter 2 in the present dissertation and literatures by Setoyama [11], Yamanaka [12], and Wriedt [13]. It is found from this figure that the changing rate of Young's modulus decreases with increasing the bond order in unit-cell. It is considered that the change of mechanical properties due to hydrogen is correlated to the original covalency of the metals.

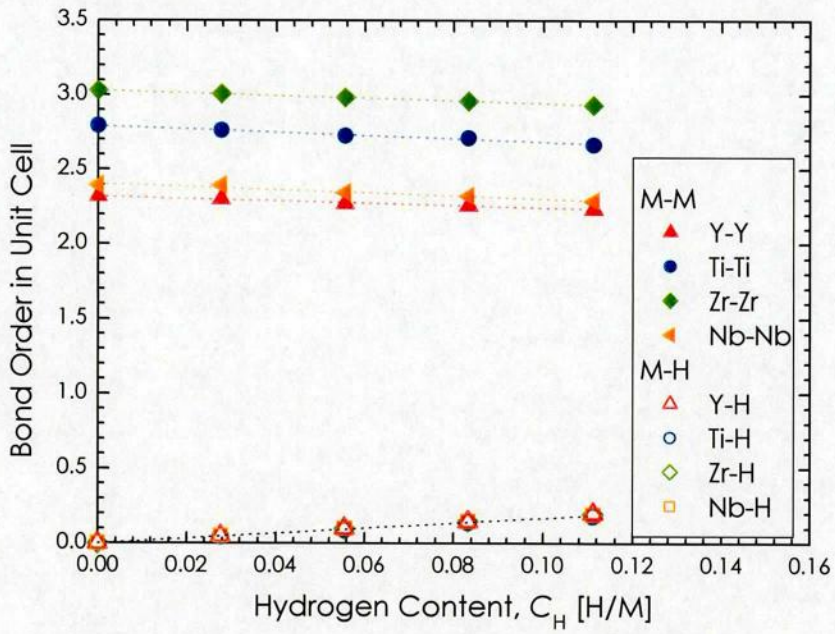


Fig. 3.15. Bond orders in unit-cell for the M hydrogen solid solutions as a function of hydrogen content, where M = Y, Ti, Zr, and Nb.

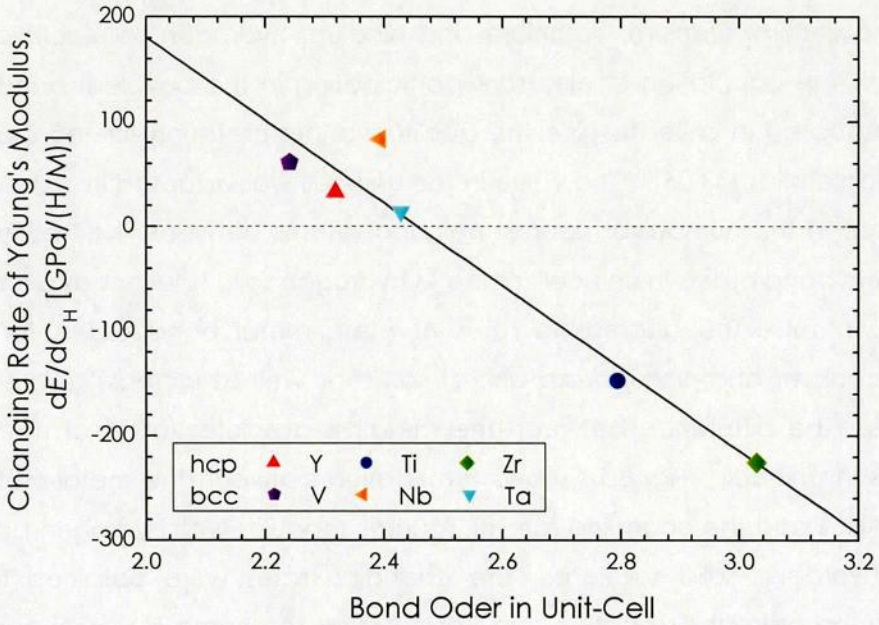


Fig. 3.16. Relation between the metal-metal bond order in unit-cell and the changing rate of Young's modulus with hydrogen content of M hydrogen solid solutions, where M = Y, Ti, Zr, V, Nb, and Ta [11-13]. The line is empirical linear fitting.

3-3-2. Thermophysical Properties of Metal Hydrides

The density of states and the bond order were calculated by the DV-Xα method in order to clarify mechanism on the creation of bonding. Fig. 3.17 shows the cluster models and Table 3.4 shows the input lattice parameters for the calculation. This calculation applied to yttrium, titanium, zirconium, and hafnium hydrides. These results are considered to be comparable under the same condition in order to discuss the effect of hydrogen.

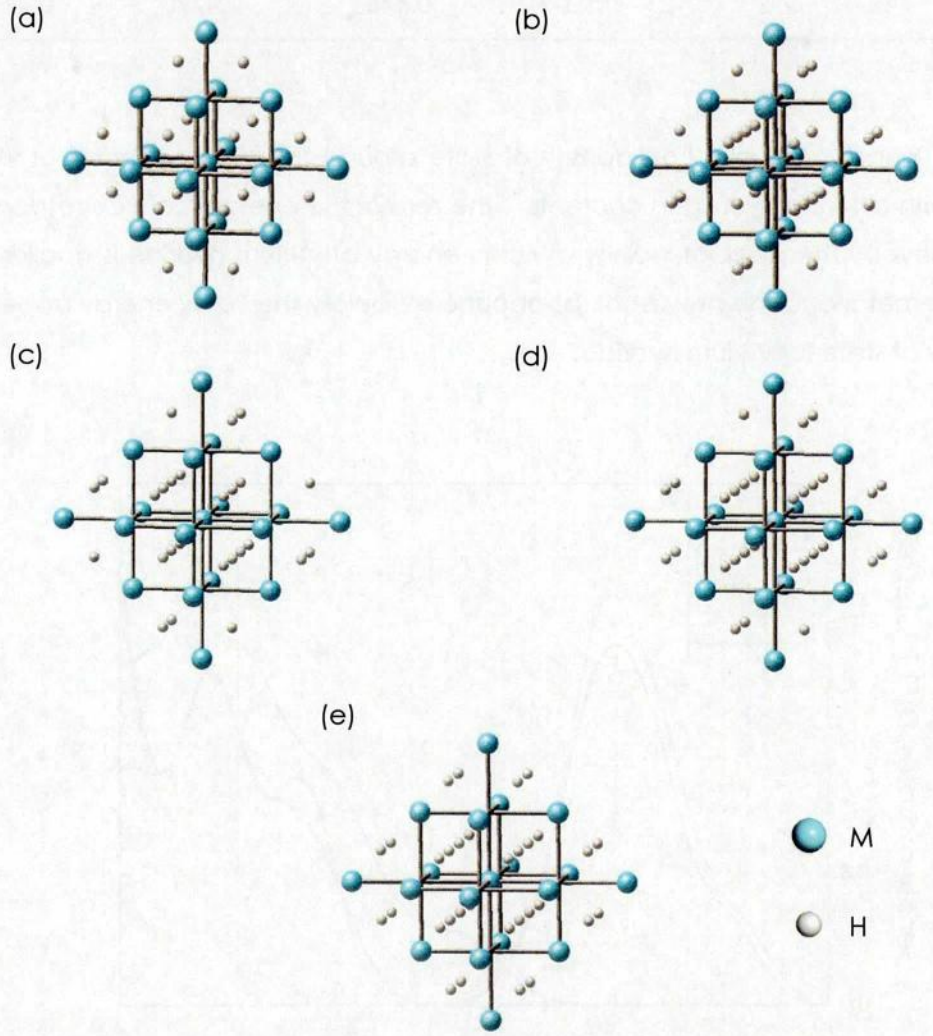


Fig. 3.17. Cluster models of metal hydrides for DV-Xα calculation; (a) $M_{19}H_{16}$, (b) $M_{19}H_{24}$, (c) $M_{19}H_{26}$, (d) $M_{19}H_{30}$, and (e) $M_{19}H_{32}$, where M = Y, Ti, Zr, and Hf.

Table 3.4. Lattice parameters of the clusters for the DV – Xα calculation.

Cluster Model	C_H [H/M]	Lattice Parameters, a [nm]			
		δYH_X	δTiH_X	δZrH_X	δHfH_X
$M_{19}H_{16}$	1.0		0.4465	0.4750	0.4687
$M_{19}H_{24}$	1.5		0.4465	0.4770	0.4715
$M_{19}H_{26}$	1.6	0.5211			
$M_{19}H_{30}$	1.8	0.5210			
$M_{19}H_{32}$	2.0	0.5209	0.4465	0.4790	0.4743

Fig. 3.18 shows the electron density of state around the valence band of yttrium hydrides with different hydrogen contents. The zero of the energy scale corresponds to the Fermi level. The peak at vicinity of Fermi energy of yttrium hydride is smaller than that of the metal and the new peak at about 6 eV below the Fermi energy appears in the density of state for yttrium hydride.

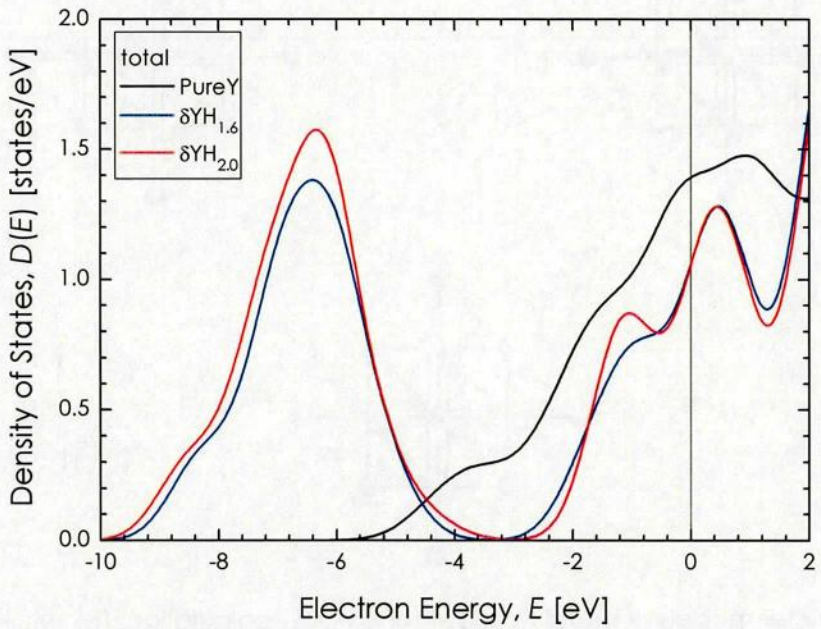


Fig. 3.18. Electron density of state of yttrium hydrides with different hydrogen contents. The zero of the energy scale corresponds to the Fermi level.

Fig. 3.19 shows partial density of states of the valence electrons of yttrium hydrides with different hydrogen contents. Along with the appearance of 1s peak of hydrogen at about 6 eV below the Fermi energy, Y 4d, 5s and 5p electrons near the Fermi energy decrease by hydrogenation and shift to around 6 eV below the Fermi energy. This indicates that the electrons of yttrium and hydrogen interact with each other and then the bonding between yttrium and hydrogen is created.

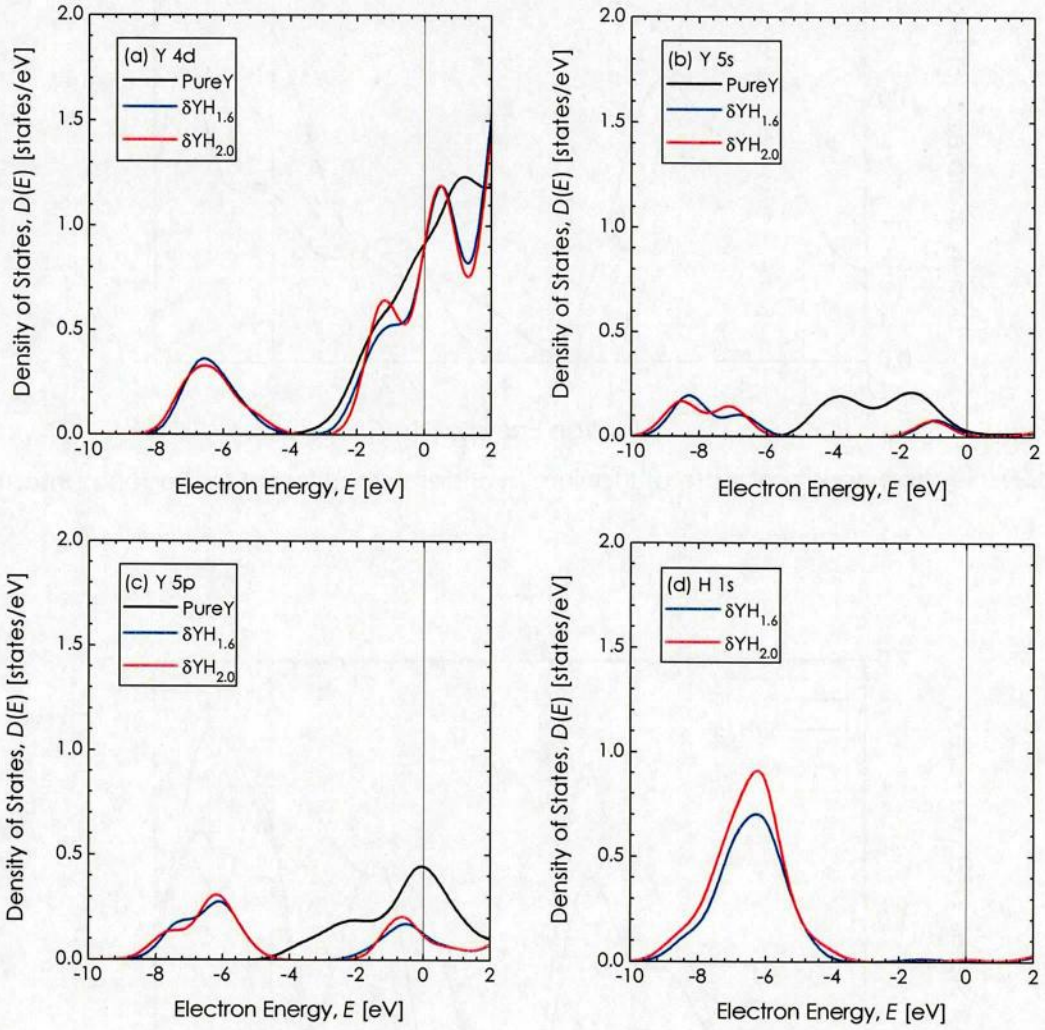


Fig. 3.19. Partial density of states of yttrium hydrides with different hydrogen contents; (a) Y 4d, (b) Y 5s, (c) Y 5p, and (d) H 1s.

Fig. 3.20–22 show the electron density of state of titanium, zirconium, and hafnium hydrides with different hydrogen contents. A new hydrogen-related band appears at

about 5 ~ 7 eV just below the d band in the hydrides. It is considered that there is common mechanism for the change in the density of states between the metal hydrides and hydrogen solid solutions.

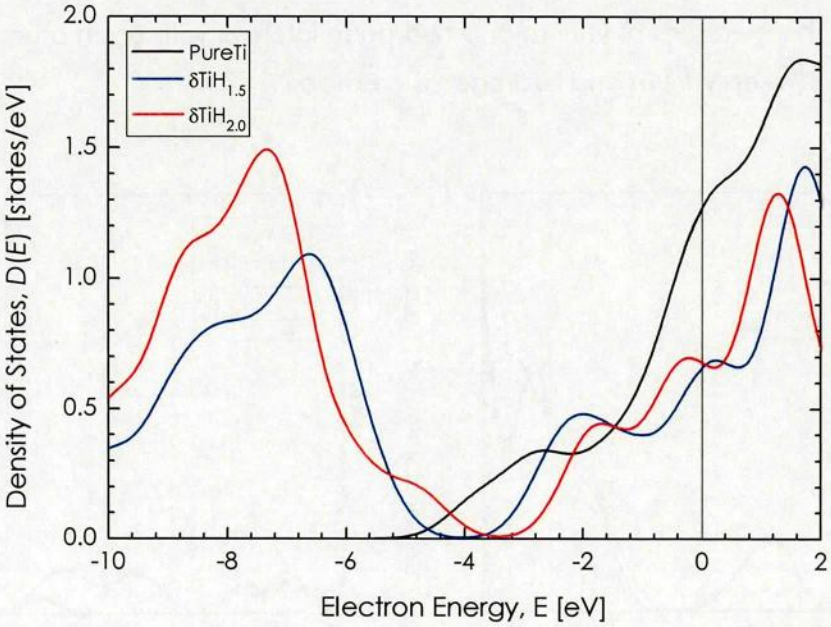


Fig. 3.20. Electron density of state of titanium hydrides with different hydrogen contents.

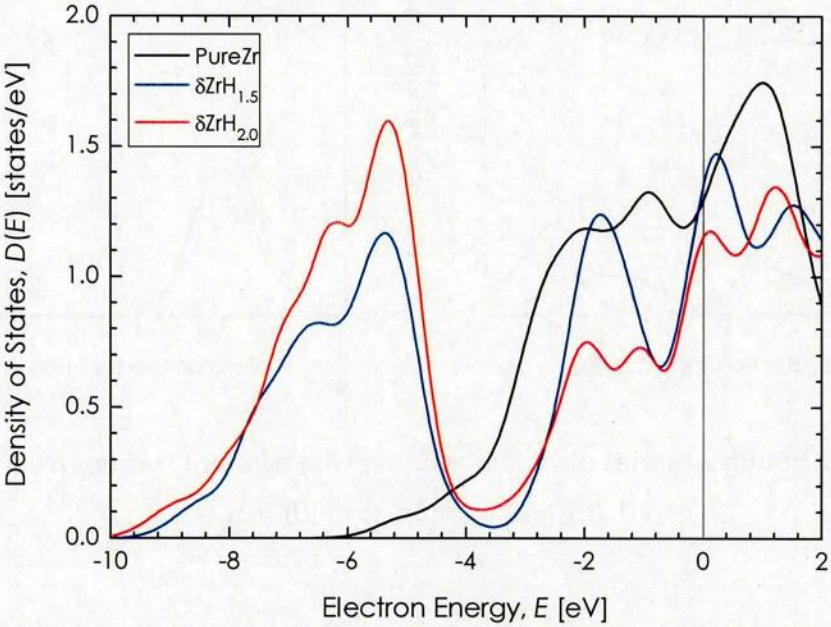


Fig. 3.21. Electron density of state of zirconium hydrides with different hydrogen contents.

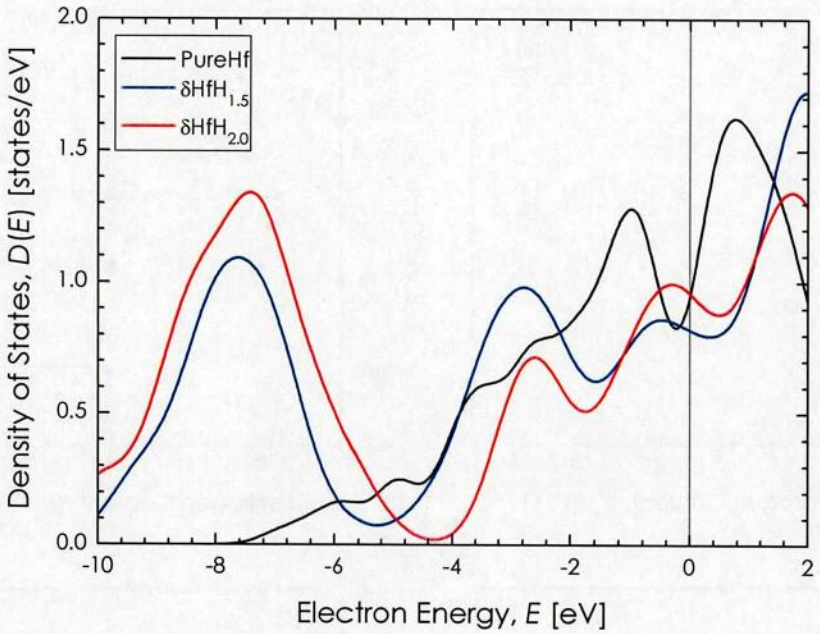


Fig. 3.22. Electron density of state of hafnium hydrides with different hydrogen contents.

Fig. 3.23(a)–(d) show the bond orders of hydrides of yttrium, titanium, zirconium, and hafnium, respectively. In the case of yttrium hydride, Y-Y bond order is smaller than that of the metal and slightly depends on the hydrogen content. The Y-H bond order is almost independent of hydrogen content. Contrary to the case, the M-M bond orders of titanium, zirconium, and hafnium hydrides decrease with hydrogen addition. Therefore, it is assumed that the reduction of M-M bond leads to the decrease of elastic moduli and Vickers hardness for the zirconium and titanium hydrides with an increase of hydrogen content, and the increase in number of Y-H bond hardens the yttrium.

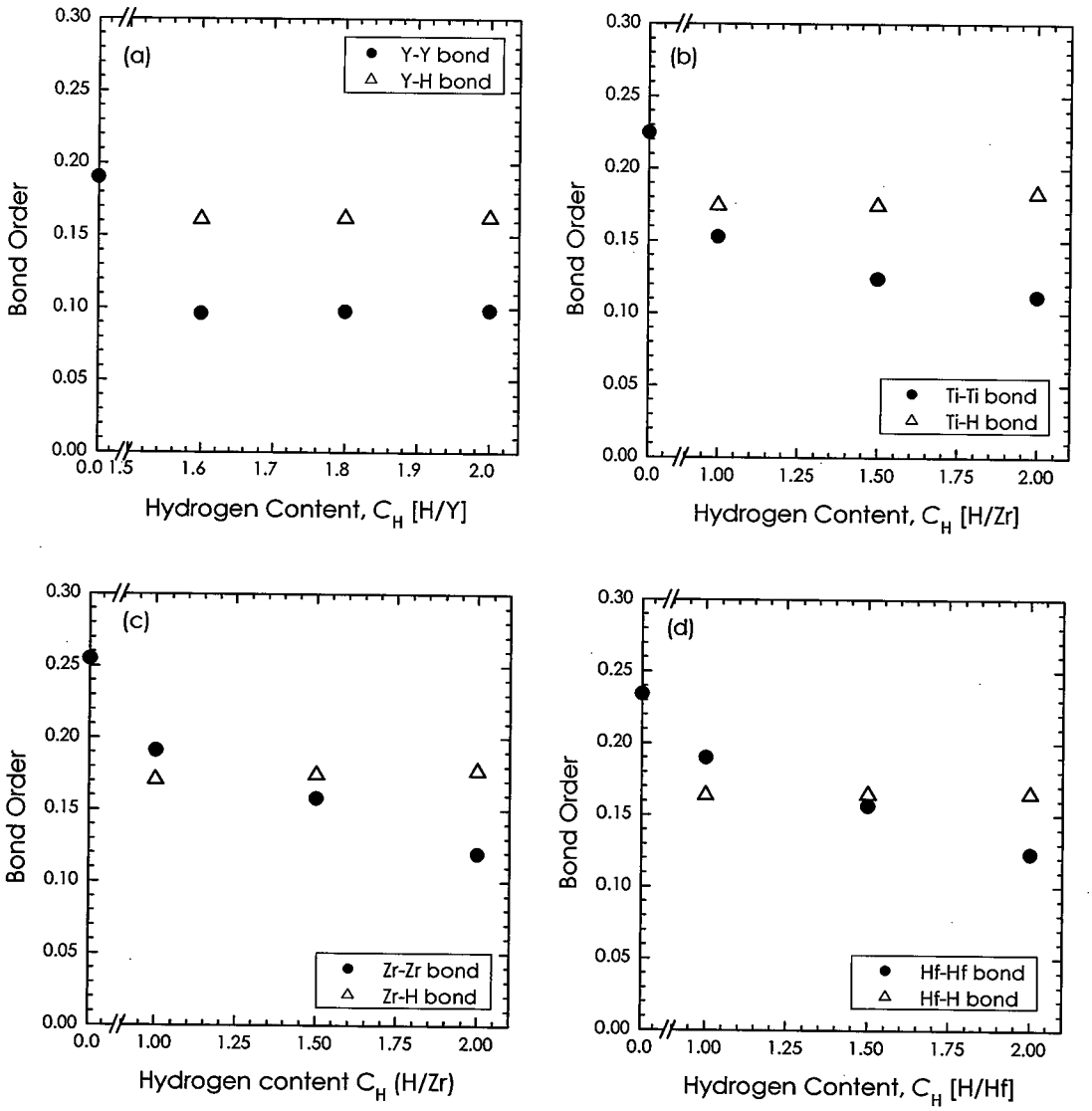


Fig. 3.23. Bond orders of metal hydrides; (a) Yttrium hydride, (b) Titanium hydride, (c) Zirconium hydride, and (d) Hafnium hydride.

From the DV-Xα calculations, the change in the mechanical properties of the metal hydride with hydrogen content can be qualitatively accounted. However, the metal-metal bond order of the yttrium hydride is quite lower than that of the pure yttrium whereas the elastic moduli and hardness of the yttrium hydride is higher than that of the pure yttrium. In the case, it is considered that the M-H-M bonding contributes to their mechanical properties. Therefore, the estimation of the absolute value of the mechanical properties by the bond order is difficult. Therefore, the total energy calculations were performed for the estimations of the thermophysical properties of the

metal hydrides. Fig. 3.24 shows the super-cell models of metal hydrides for CASTEP calculation. The hydrogen inserted sites in the fluorite-type structure were chosen from the energy minimization approach.

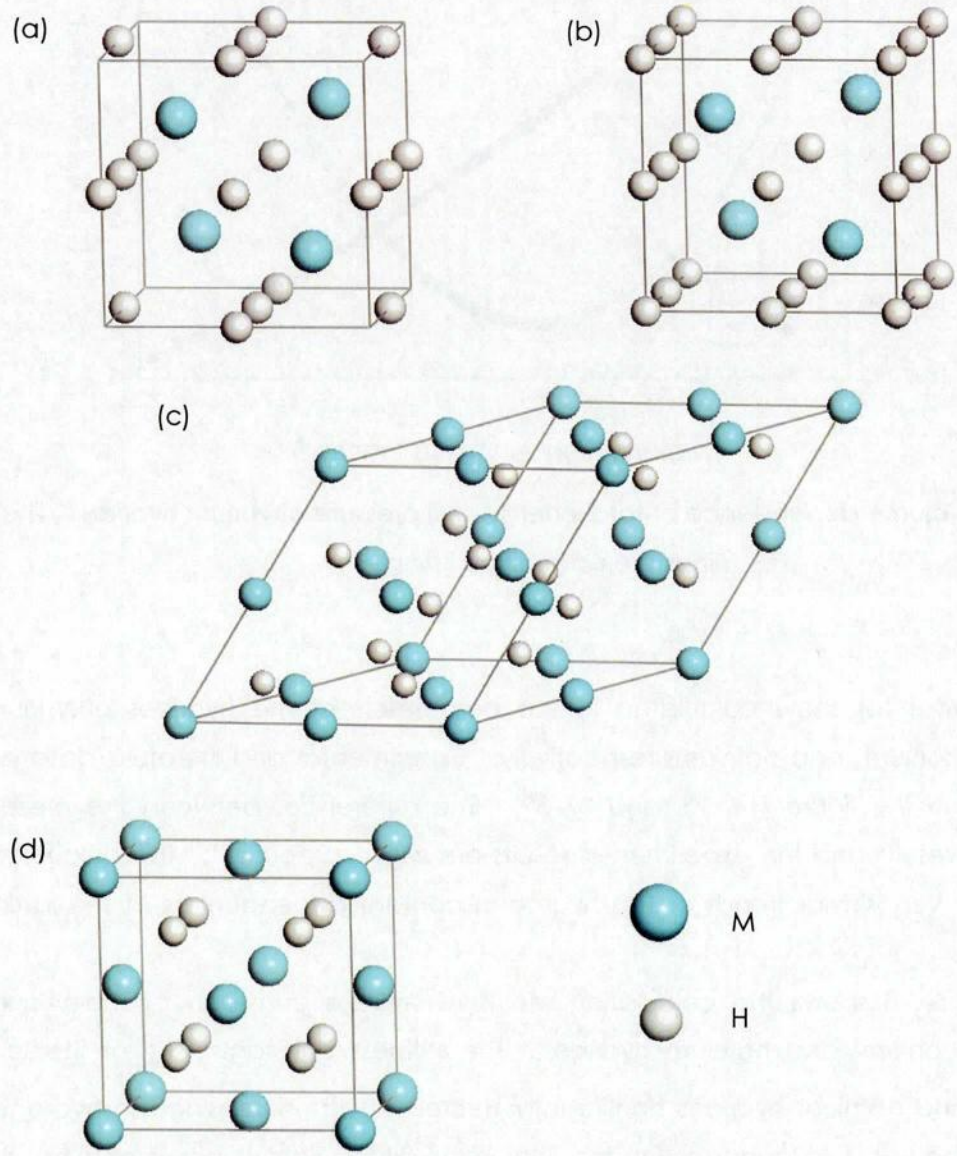


Fig. 3.24. Super-cell models of metal hydrides for CASTEP calculation; (a) $\delta MH_{1.5}$, (b) $\delta MH_{1.75}$, (c) $\delta MH_{1.875}$, and (d) $\delta MH_{2.0}$, where M = Y, Ti, Zr, and Hf.

Fig. 3.25 shows the volume dependence of total energy and pressure of yttrium hydride. From this kind of results, one can obtain the equilibrium lattice parameter at absolute zero temperature by the energy minimization principle.

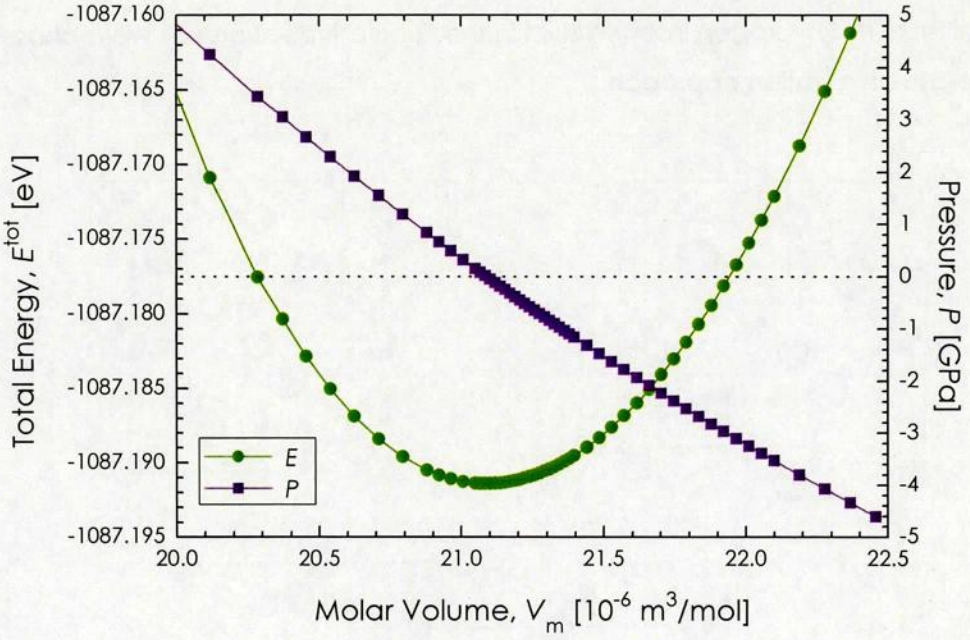


Fig. 3.25. Volume dependence of total energy and pressure of yttrium hydride. The lines are polynomial fittings.

Fig. 3.26(a)–(d) show calculated lattice parameters of the hydrides of yttrium, titanium, zirconium, and hafnium, respectively. Experimental and literature data are also shown in this figure [14, 15, and 37–52]. The differences between the present calculation results and the experimental results are within a percent. The calculation results show very similar trends of the hydrogen content dependences of the lattice parameters.

Table 3.5–3.8 shows the calculation results of stiffness constants of the yttrium, titanium, zirconium, and hafnium hydrides. The stiffness constants C_{44} of titanium, zirconium, and hafnium hydrides significantly decrease with increasing the hydrogen content, whereas the constant of the yttrium hydride slightly increases with the hydrogen content.

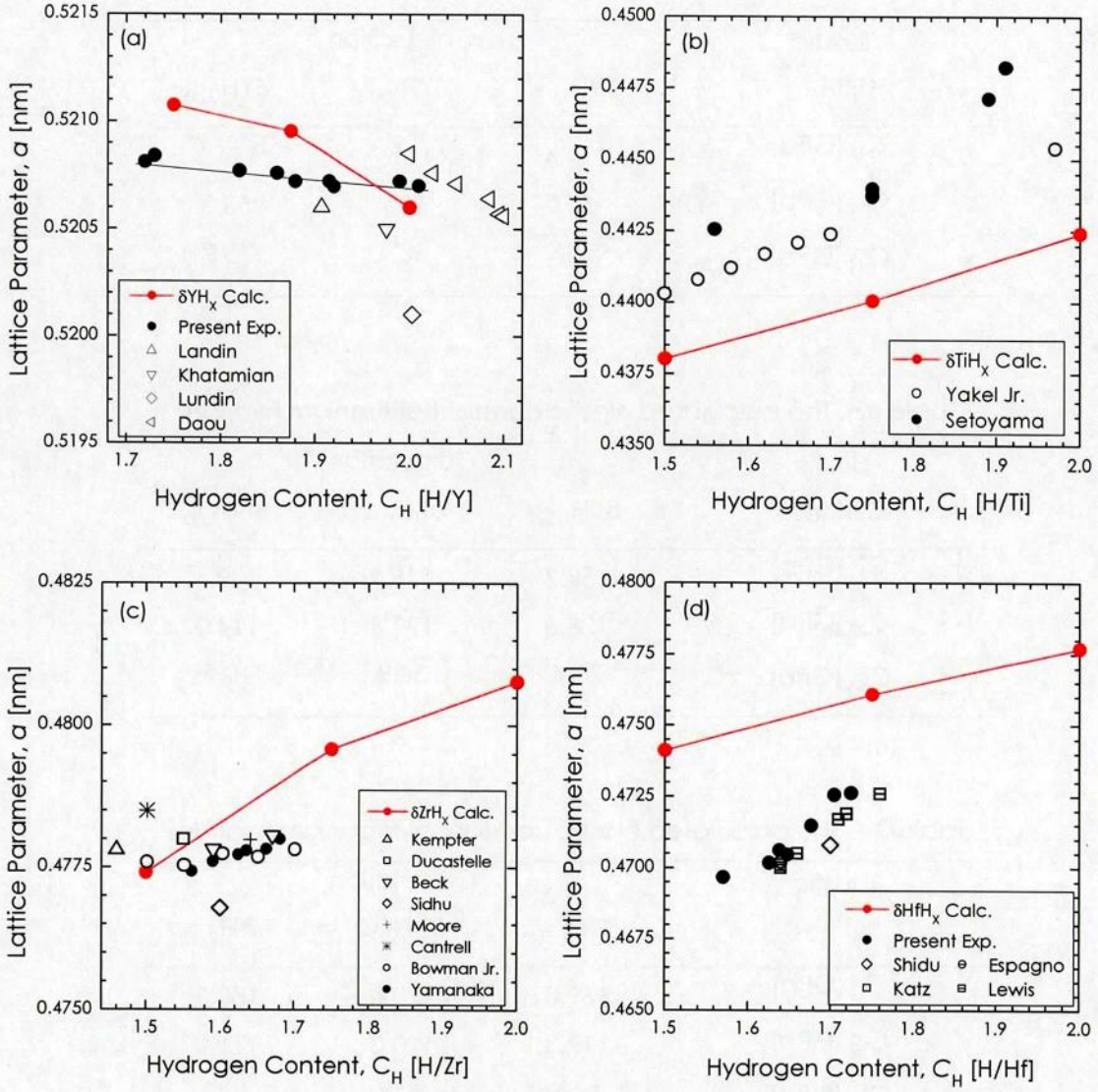


Fig. 3.26. Calculated lattice parameters of metal hydrides, together with experimental data obtained from the present study and literatures [37–52]; (a) Yttrium hydride, (b) Titanium hydride, (c) Zirconium hydride, and (d) Hafnium hydride.

Table 3.5. The calculated elastic constant of yttrium hydride.

Elastic Stiffness	Calculation		
	$\delta YH_{1.75}$	$\delta YH_{1.875}$	$\delta YH_{2.00}$
C_{11} [GPa]	111.4	111.7	116.2
C_{12} [GPa]	48.7	50.4	55.3
C_{44} [GPa]	59.5	66.1	75.9

Table 3.6. The calculated elastic constant of titanium hydride.

Elastic Stiffness	Calculation		
	$\delta TiH_{1.50}$	$\delta TiH_{1.75}$	$\delta TiH_{2.00}$
C_{11} [GPa]	159.7	145.1	139.6
C_{12} [GPa]	128.6	122.6	114.0
C_{44} [GPa]	75.4	36.9	10.5

Table 3.7. The calculated elastic constant of zirconium hydride.

Elastic Stiffness	Calculation		
	$\delta ZrH_{1.50}$	$\delta ZrH_{1.75}$	$\delta ZrH_{2.00}$
C_{11} [GPa]	169.0	170.0	180.3
C_{12} [GPa]	117.3	120.0	115.0
C_{44} [GPa]	64.5	40.7	6.43

Table 3.8. The calculated elastic constant of hafnium hydride.

Elastic Stiffness	Calculation		
	$\delta HfH_{1.50}$	$\delta HfH_{1.75}$	$\delta HfH_{2.00}$
C_{11} [GPa]	181.8	172.0	162.2
C_{12} [GPa]	154.5	146.2	138.0
C_{44} [GPa]	83.0	44.8	6.73

Fig. 3.27–30 show the calculated elastic moduli of yttrium, titanium, zirconium, and hafnium hydride, respectively. The experimental data of the hydrides obtained from the Chapter 2 in the present dissertation and literature by Setoyama [14] and Yamanaka [15] are also plotted in the figures.

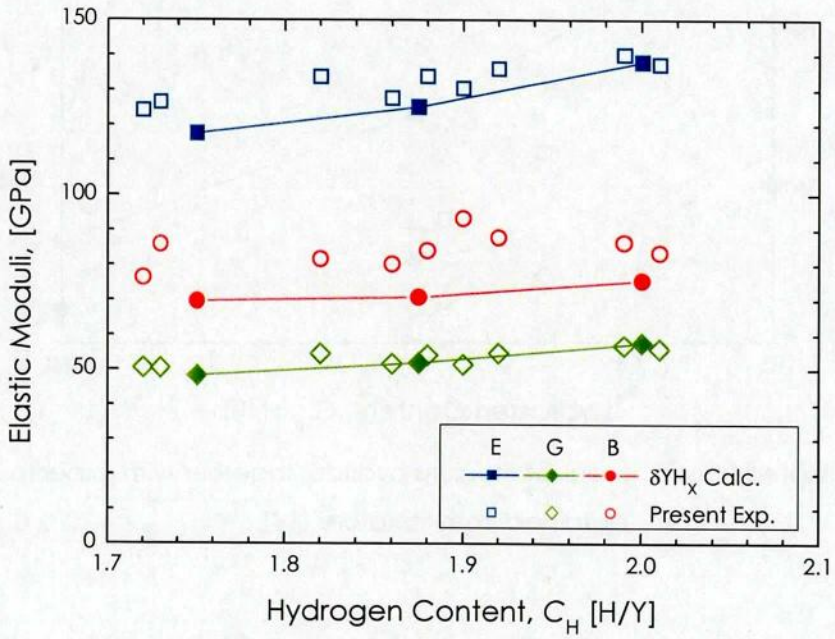


Fig. 3.27. Calculated elastic moduli of yttrium hydride, together with the present experimental results.

All the calculated bulk moduli of the hydrides are good accordance with the experimental data. The calculated Young's and shear moduli of the yttrium and hafnium hydrides are in excellent agreement with the experimental data. The calculation results of the Young's and shear moduli of the titanium and zirconium hydrides at lower hydrogen content are also good accordance with the experimental data whereas the calculated results for the higher hydrogen content somewhat differ from the experimental data. It is also found from the ab initio calculation that the elastic moduli of the yttrium hydride increase with increasing the hydrogen content, whereas those of the titanium, zirconium, and hafnium hydrides reduce due to hydrogen addition.

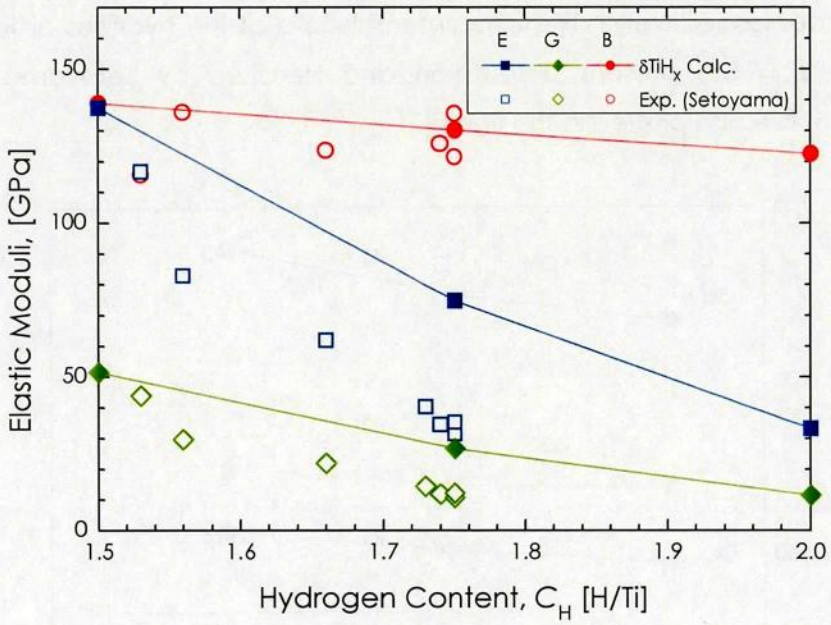


Fig. 3.28. Calculated elastic moduli of titanium hydride, together with experimental data obtained from literature [14].

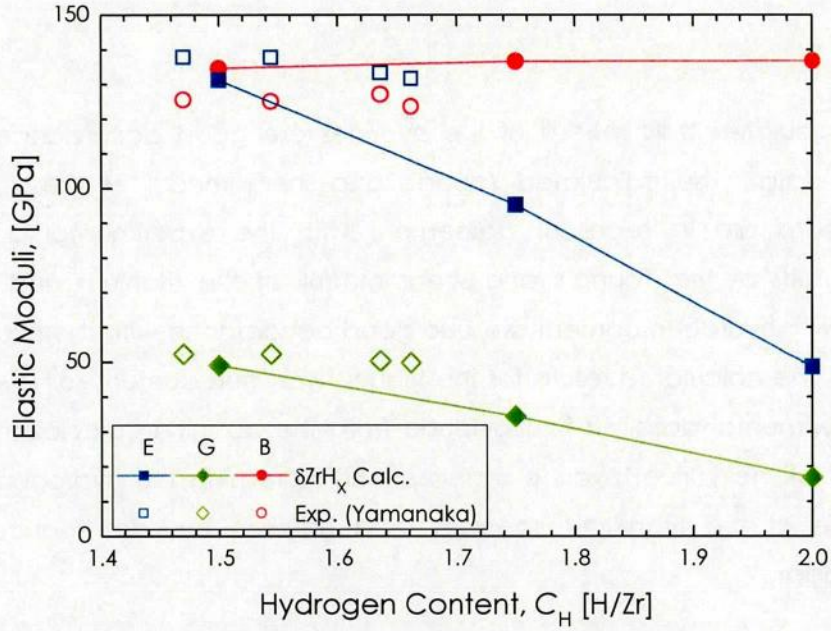


Fig. 3.29. Calculated elastic moduli of zirconium hydride, together with experimental data obtained from literature [15].

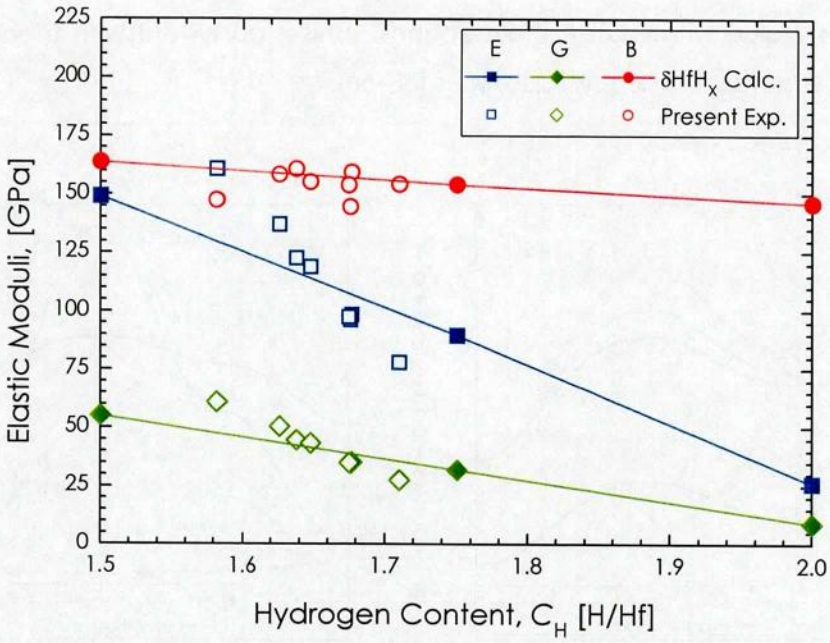


Fig. 3.30. Calculated elastic moduli of hafnium hydride, together with the present experimental results.

The Young's modulus of each direction for cubic crystal can be calculated using elastic compliance coefficient S_{ij} which is obtained by CASTEP calculation by the following equation:

$$\frac{1}{E_{ijk}} = S_{11} - 2\left(S_{11} - S_{12} - \frac{1}{2}S_{44}\right)\left(l_i^2 l_j^2 + l_j^2 l_k^2 + l_k^2 l_i^2\right) \quad (3\text{-}22)$$

The elastic compliance coefficients of the cubic crystal can be related with the elastic stiffness constant as follows:

$$C_{11} = \frac{S_{11} + S_{12}}{(S_{11} - S_{12})(S_{11} + 2S_{12})} \quad (3\text{-}23)$$

$$C_{12} = \frac{-S_{12}}{(S_{11} - S_{12})(S_{11} + 2S_{12})} \quad (3\text{-}24)$$

$$C_{44} = \frac{1}{S_{44}} \quad (3\text{-}25)$$

Fig. 3.31 shows the crystal direction dependences of Young's modulus of the yttrium, titanium, zirconium, and hafnium hydrides. For comparison, the results of the pure metals with hypothetical fcc are also shown in the figures. The average Young's modulus reduced to the polycrystalline material of the hypothetical fcc is almost same

as that of real hcp crystal of the pure metals. The Young's modulus in the [111] direction has the largest value with subset of exceptions. This is consistent with theories of the stability of pure metals for fcc crystal lattices [53–56].

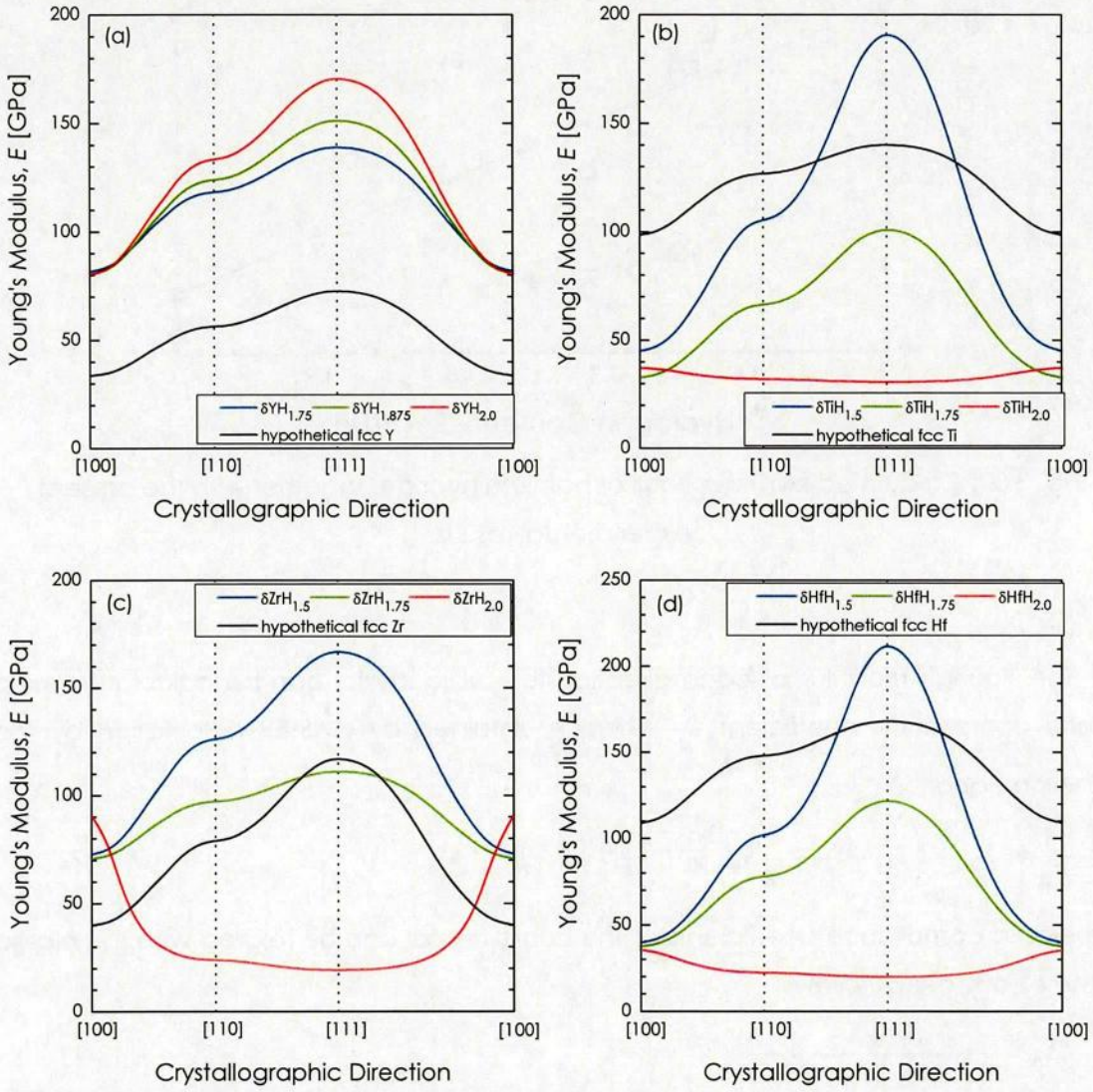


Fig. 3.31. Crystal direction dependence of Young's modulus of metal hydrides; (a) Yttrium hydride, (b) Titanium hydride, (c) Zirconium hydride, and (d) Hafnium hydride.

The direction dependences of the Young's moduli of the yttrium and zirconium hydrides are similar to those of their pure metals; the hydrides have higher elastic moduli than the pure metals. On the other hand, the direction dependences of the Young's moduli of the titanium and hafnium hydrides are quite different from those of their pure metals.

The elastic moduli in the [111] direction of the titanium, zirconium, and hafnium hydrides drastically decrease with increasing the hydrogen content whereas that of the yttrium hydride gradually increases due to hydrogen addition. For the stoichiometric di-hydrides of titanium, zirconium, and hafnium, the profile of the direction dependence of the Young's modulus turns back, which would be attributed that the δ phase of these hydrides is unstable at the hydrogen content. For this reason, it is considered that the IVa transition metal (Ti, Zr, and Hf) hydrides have similar behavior in the mechanical properties.

Fig. 3.32 shows the volume dependence of the Debye temperature and the Grüneisen parameter of yttrium hydride, together with experimental result obtained in Chapter 2. These parameters are estimated with use of the calculation result of the total energy, pressure, and the elastic moduli. The calculated Debye temperature of the yttrium hydrides are in excellent agreement with the experimental data. The Debye temperature decreases with increasing the volume. This is considered to correspond to the temperature dependence of the Debye temperature. However, since it is known that the temperature dependence of the Debye temperature is caused by the dispersion of the lattice waves and by anharmonicity [57], the Debye temperature doesn't necessarily decrease with increasing temperature. The calculated Grüneisen parameter of yttrium hydride slightly increases with increasing the volume.

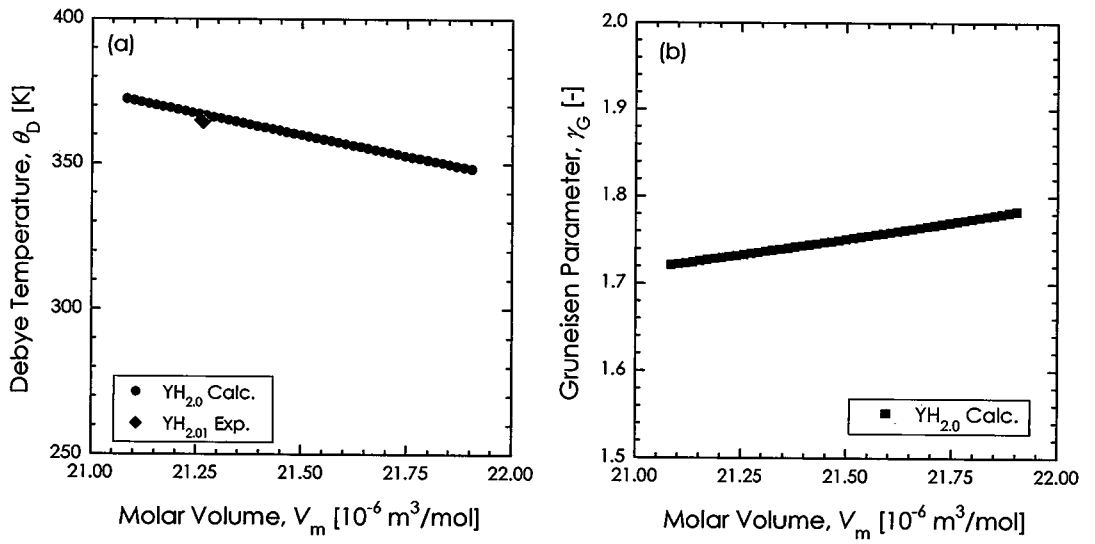


Fig. 3.32. Volume dependence of (a) Debye temperature and (b) Grüneisen parameter of yttrium hydride, together with the present experimental results.

Fig. 3.33–35 show the volume dependence of the Debye temperature and the Grüneisen parameter of the hydrides of titanium, zirconium, and hafnium, respectively. The experimental data of the hydrides obtained from the Chapter 2 in the present dissertation and literature by Setoyama [14] and Yamanaka [15] are also plotted in the figures. The calculated Debye temperature of titanium hydride is slightly higher than the experimental data whereas the calculation result of zirconium hydride is slightly lower than the experimental result.

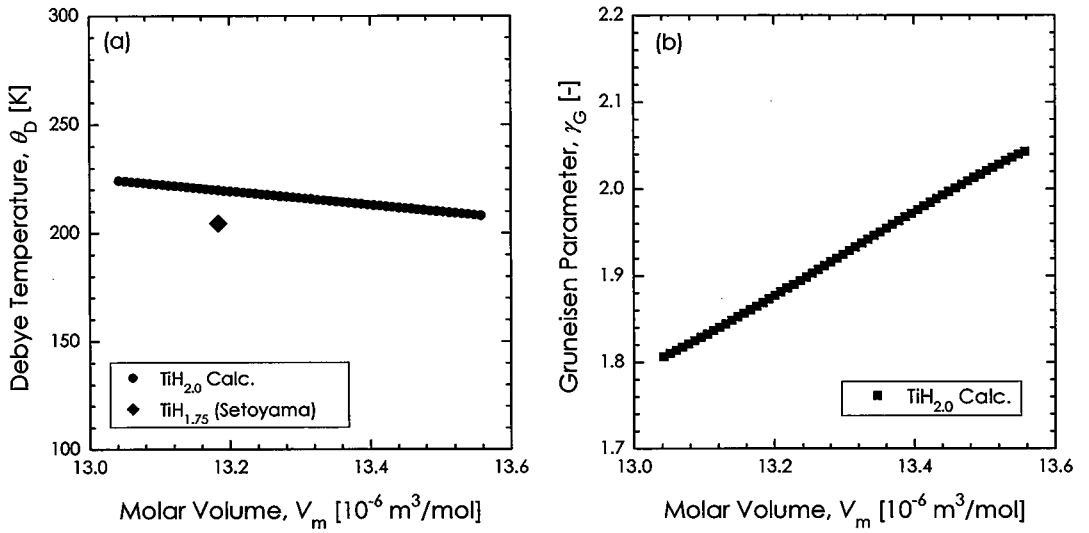


Fig. 3.33. Volume dependence of (a) Debye temperature and (b) Grüneisen parameter of titanium hydride, together with experimental data obtained from literature [14].

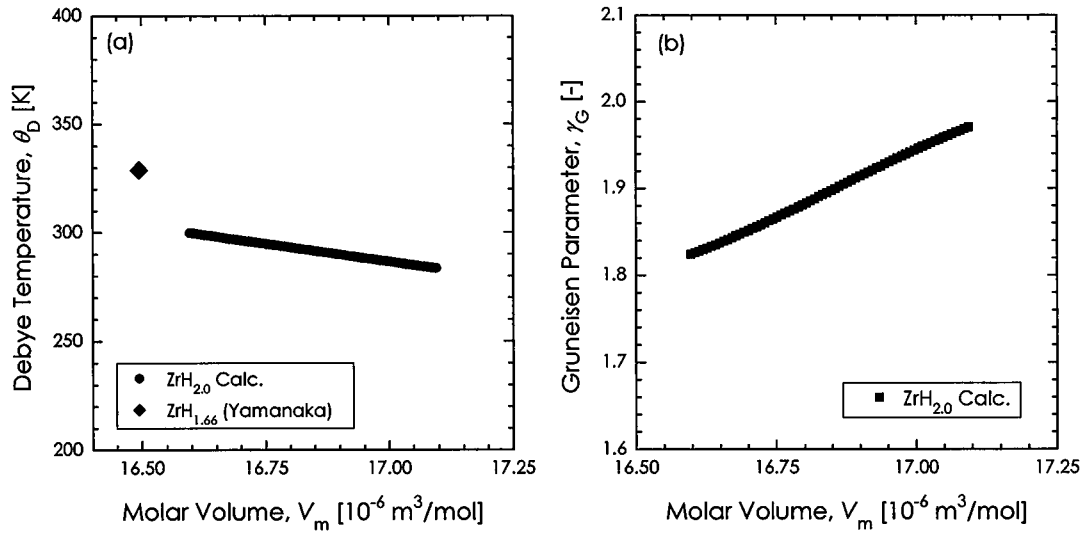


Fig. 3.34. Volume dependence of (a) Debye temperature and (b) Grüneisen parameter of zirconium hydride, together with experimental data obtained from literature [15].

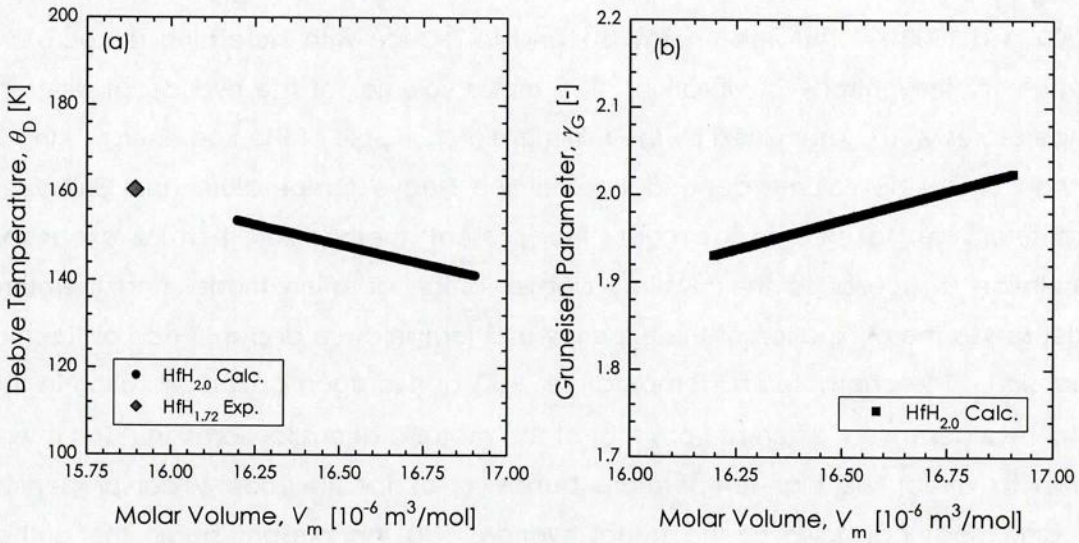


Fig. 3.35. Volume dependence of (a) Debye temperature and (b) Grüneisen parameter of hafnium hydride, together with the present experimental results.

The calculation result for the hafnium hydride is good accordance with the experimental result. These trends are corresponding to the elastic constant calculation results of the stoichiometric di-hydrides. The Grüneisen parameters of all the hydrides are about 1.8 and slightly increase with increasing the volume.

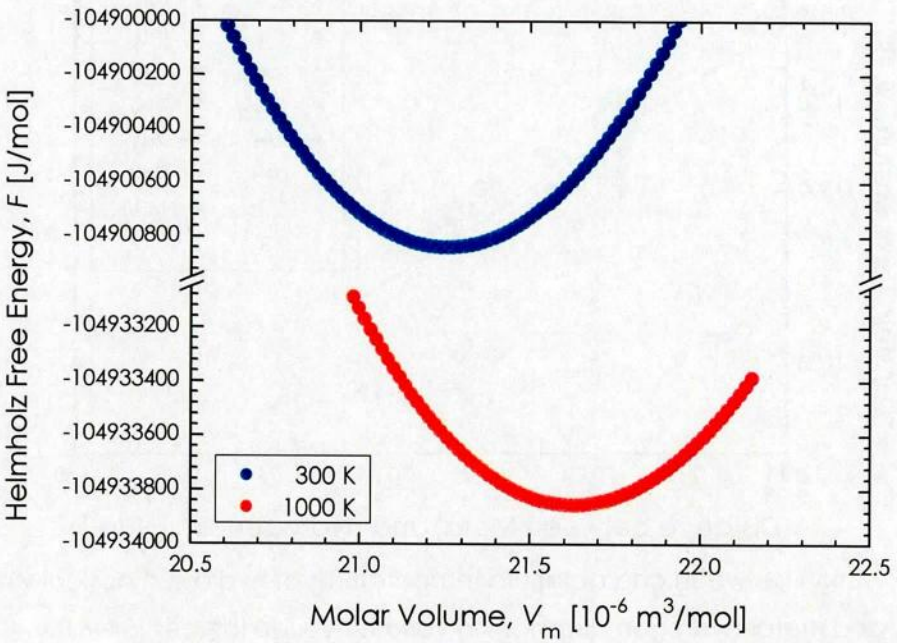


Fig. 3.36. Volume dependence of Helmholtz free energy of yttrium hydride at 300 and 1000 K.

Fig. 3.36 shows the volume dependence of Helmholtz free energy of yttrium hydride at 300 and 1000 K. The free energy is found to reduce with increasing temperature because of the entropy of vibration. The molar volumes of the hydride at different temperatures were determined by the minimization principle of the free energy. In this method, since the volume dependences of the Debye temperature and Grüneisen parameter are taken into account, the present method of thermal expansion calculation is superior to the classical Debye lattice vibration model and therefore better serves the evaluation of the experimental temperature dependence of thermal expansion. The characteristic temperature θ [K] of hydrogen optical vibration in the metal hydrides is very different from that of the metallic acoustic vibration. This is well known to affect the high-temperature behaviors of the thermophysical properties, including heat capacity, of the metal hydrides. In the present study, the author attempts to discuss the effect of hydrogen vibration on the thermal expansion of the hydrides. In 1964, Sakamoto indicated that the Einstein temperatures of several hydrides appeared to decrease with increasing metal-hydrogen distance [54]. The author surveyed later literatures of the Einstein temperature of various metal hydrides. The Einstein temperatures are plotted against the metal-hydrogen distances in Fig. 3.37.

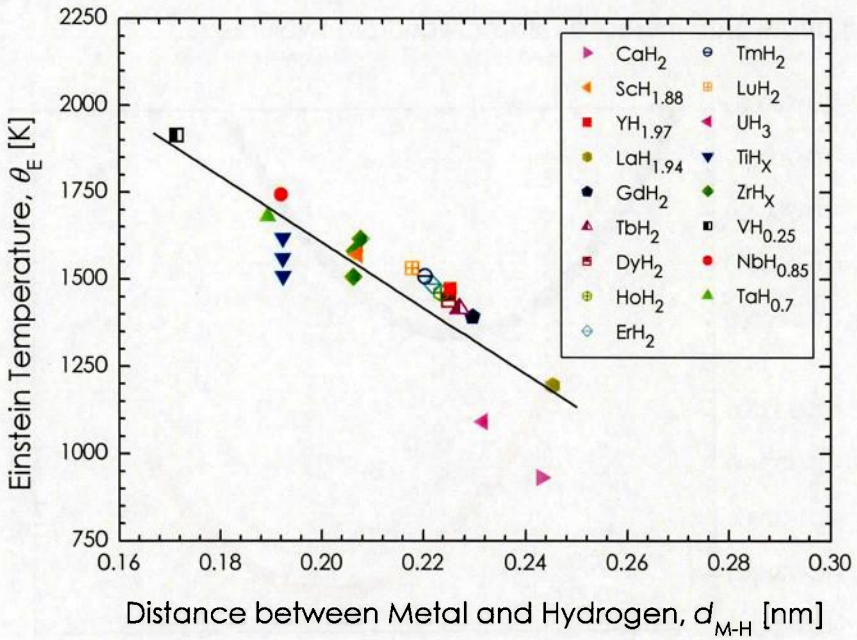


Fig. 3.37. Relation between characteristic temperatures of hydrogen optical vibrations and metal-hydrogen distances in various hydride lattices [54–64].

From this figure, the following linear relation between the Einstein temperature and the distance is empirically obtained:

$$\theta_E = -9.45 \times 10^3 \times d_{M-H} + 3.50 \times 10^3 \qquad (3\text{-}26)$$

This equation is assumed to be applicable for the case that the metal-hydrogen distance changes due to thermal expansion.

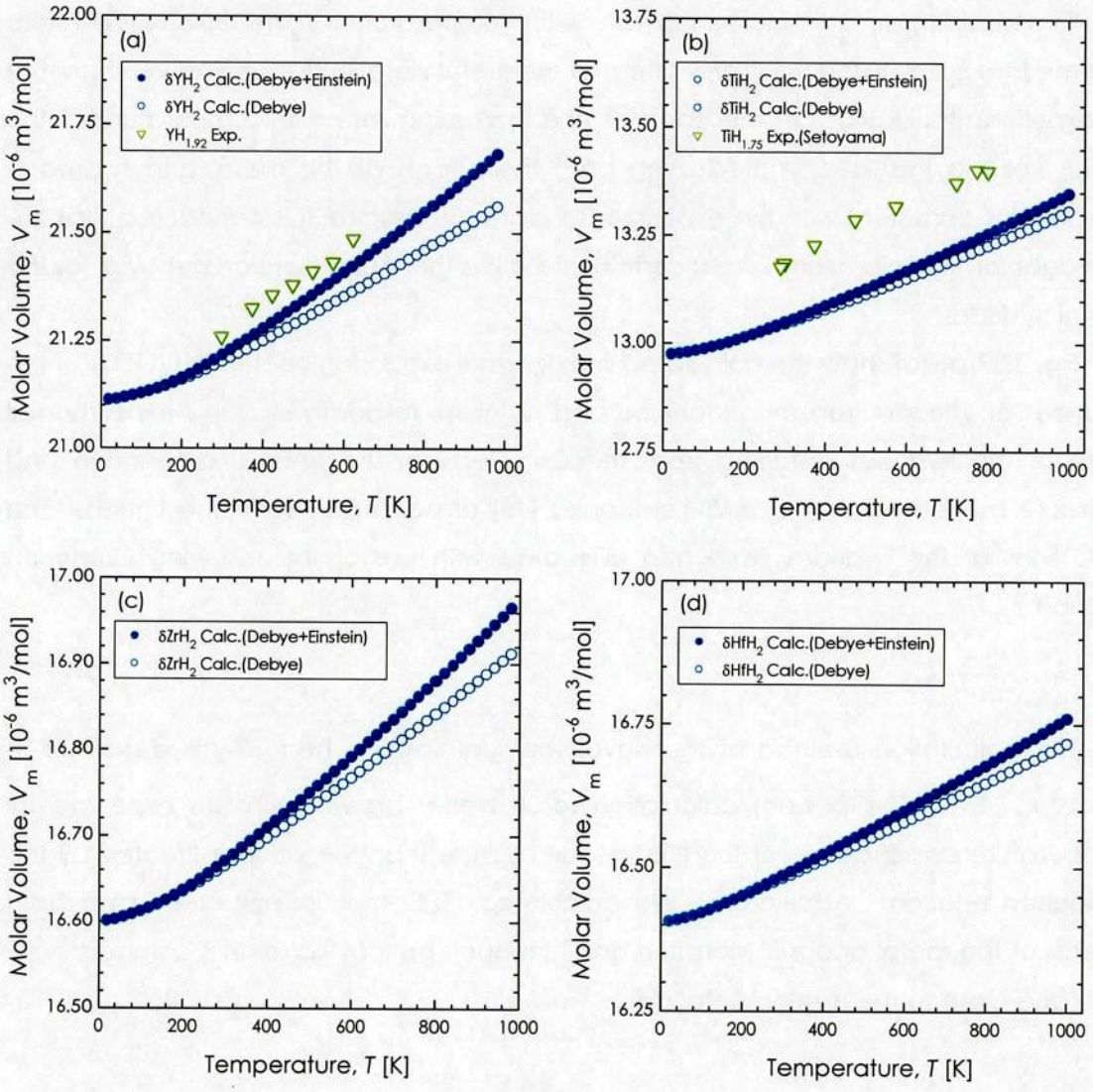


Fig. 3.38. Calculated temperature dependence of molar volume of metal hydrides, together with experimental data obtained from the present study and literature [14]; (a) Yttrium hydride, (b) Titanium hydride, (c) Zirconium hydride, and (d) Hafnium hydride.

Fig. 3.38(a)-(d) show the calculated temperature dependence of molar volume of

the hydrides of yttrium, titanium, zirconium, and hafnium, together with the experimental data obtained from the Chapter 2 in the present dissertation and literature by Setoyama [14]. The open mark indicates the volume that is calculated using only effect of the metal acoustic vibration. The solid mark indicates the calculation result in which both the effects of metal acoustic and hydrogen optical vibrations are taken into account.

The absolute values of the calculation results are good accordance with the experimental data. The increasing rate with temperature of the calculated molar volume that is estimated using only effect of the metal vibration is slightly lower than that of experimental data. On the contrary, the increasing rate with temperature of the molar volume that is estimated using both the effects of the metal and hydrogen vibrations is consistent with the experimental data. Therefore, it is considered that the hydrogen optical vibration have a certain role in the thermal expansion behavior for the metal hydrides.

Fig. 3.39(a)-(d) show the calculated liner thermal expansion coefficient (LTEC) of the hydrides of yttrium, titanium, zirconium, and hafnium, respectively. The experimental data of the hydrides obtained from the Chapter 2 in the present dissertation and literature by Setoyama [14] and Yamanaka [15] are also plotted in the figures. The LTEC lines of the hydrides were also estimated with use of the following Grüneisen relation:

$$\alpha_L = \frac{\gamma_G}{3BV_m} C_V \qquad (3\text{-}27)$$

The calculation method of the isovolumetrical specific heat C_V is described in Chapter 2-3-1. The present calculation result better agrees with the experimental temperature dependence of the LTEC of the hydride than the value estimated by the Grüneisen relation. Additionally, the calculated LTEC that is estimated using both effects of the metal acoustic vibration and hydrogen optical vibration is comparatively high and close to the experimental data.

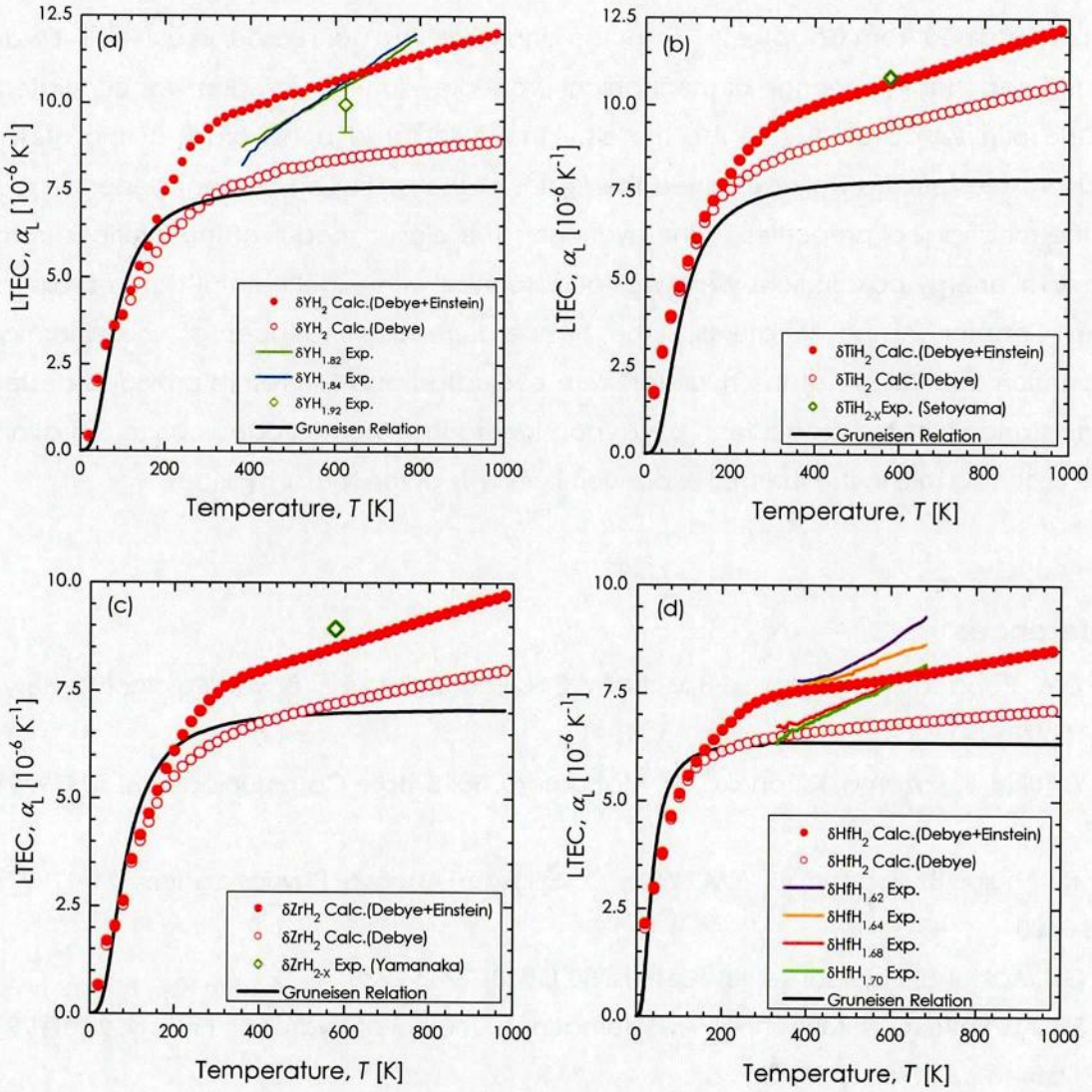


Fig. 3.39. Calculated liner thermal expansion coefficient (CLE) of metal hydrides, together with experimental data obtained from the present study and literatures [14, 15]; (a) Yttrium hydride, (b) Titanium hydride, (c) Zirconium hydride, and (d) Hafnium hydride.

3-4. Summary

In this chapter, ab initio electronic structure calculations were performed by using CASTEP code and DV- Xα method. The themophysical properties of the metal hydrogen solid solutions and hydrides were discussed from the calculation results. The elastic moduli of the yttrium hydrogen solid solution could be evaluated from the ab

initio study and the calculated results were good accordance with the experimental results obtained from Chapter 2. From the analysis of the bond order in unit-cell, it was considered that the change of mechanical properties due to hydrogen was correlated to the original covalency of the metals. The calculated bond order of the metal hydrides also qualitatively explained the trends of the hydrogen content dependence of the mechanical properties of the hydrides. The elastic moduli of the hydrides from the total energy calculations were well accordance with experimental data obtained from Chapter 2 and literatures. The temperature dependences of liner thermal expansion coefficients of the hydrides were evaluated and the results provided better understanding of the properties. It was considered that the hydrogen optical vibration had a certain role in the thermal expansion behavior of the metal hydrides.

References

[1] D.A. Papaconstantopoulos, B.M. Klein, E.N. Economou, L.L. Boyer, Physical Review, B17 (1978) 141.

[2] Y. Fukai, S. Kazama, K. Tanaka, M. Matsumoto, Solid State Communications, 30 (1979) 173.

[3] R. Ahuja, B. Johansson, J.M. Wills, O. Eriksson, Applied Physics Letters, 71 (1997) 498-3500.

[4] G.J. Ackland, Physical Review Letters, 80 (1998) 2233-2236.

[5] S.E. Kul'kova, O.N. Muryzhnikova, International Journal of Hydrogen Energy, 24 (1999) 207-215.

[6] C. Domain, R. Besson, A. Legris, Acta Materialia, 50 (2002) 3513-3526.

[7] S.J. Liu, S.Q. Shi, H. Huang, C.H. Woo, Journal of Alloys and Compounds, 330-332 (2002) 64-69.

[8] M. Morinaga, H. Yukawa, Material Science and Engineering A, 329-331 (2002) 268-275.

[9] A. Juan, C. Pistonesi, A.J. Garcia, G. Brizuela, International Journal of Hydrogen Energy, 28 (2003) 995-1004.

[10] D. Chen, Y.M. Wang, L. Chen, S. Liu, C.X. Ma, L.B. Wang, Acta Materialia, 52 (2004) 521-528.

[11] D. Setoyama, J. Matsunaga, H. Muta, M. Uno, S. Yamanaka, Journal of Alloys and Compound, 385 (2004) 156-159.

[12] S. Yamanaka, D. Setoyama, H. Muta, M. Uno, M. Kuroda, K. Takeda, T. Matsuda,

Journal of Alloys and Compounds, 372 (2004) 129-135.

[13] H.A. Wriedt, R.A. Oriani, Scripta Metallurgica, 8 (1974) 203-208.

[14] D. Setoyama, J. Matsunaga, H. Muta, M. Uno, S. Yamanaka, Journal of Alloys and Compounds, 381 (2004) 215-220.

[15] S. Yamanaka, K. Yamada, K. Kurosaki, M. Uno, K. Takeda, H. Anada, T. Matsuda, S. Kobayashi, Journal of Alloys and Compounds, 330-332 (2002) 99-104.

[16] M.D. Segall, P.J.D. Lindan, M.J. Probert, C.J. Pickard, P.J. Hasnip, S.J. Clark, M.C. Payne, Journal of Physics: Condensed Matter, 14 (2002) 2717.

[17] J.P. Perdew, K. Burke, M. Ernzerhof, Physical Review Letters, 77 (1996) 3865.

[18] R.S. Mulliken, The Journal of Chemical Physics, 23 (1955) 1833-2343.

[19] J.C. Slater, Physical Review, 81 (1951) 385.

[20] D.E. Ellis, H. Adachi, F.W. Averill, Surface Science, 58 (1976) 497.

[21] H. Adachi, M. Tsukada, C. Satoko, Journal of the Physical Society of Japan, 45 (1978) 875.

[22] O.H. Nielsen, R.M. Martin, Physical Review, B32 (1985) 3780.

[23] W. Voigt, "Lehrburch der Kristall-Phisik", Nachdruck, Teubuer, Berlin/Leipzig, (1928).

[24] V.L. Moruzzi, J.F. Janak, K. Schwarz, Physical Review, B37 (1988) 790.

[25] Y. Wang, R. Ahuja, B. Johansson, International Journal of Quantum Chemistry, 96 (2004) 501.

[26] X.–G. Lu, M. Selleby, B. Sundman, Acta Materialia, 53 (2005) 2259-2272.

[27] J.C. Slater, "Introduction to Chemical Physics," McGraw-Hill, New York, (1939).

[28] J.S. Dugdale, D.K.C. MacDonald, Physical Review, 89 (1953) 832.

[29] V.Y. Vashchenko, V.N. Zubarev, Soviet Physics. Solid State, 5 (1963) 653.

[30] J.F. Smith, J.A. Gjevre, Journal of Applied Physics, 31 (1960) 645-647.

[31] C. Elsasser, M. Fahnle, C.T. Chan, K.M. Ho, Physical Review, B49 (1994) 13975.

[32] R.W. Warren, B.I. Dunlap, Chemical Physics Letters, 262 (1996) 384.

[33] D.G. Pettifor , "Bonding and Structure of Molecules and Solids," Clarendon Press, Oxford, (1995).

[34] S. Yamanaka, K. Yamada, K. Kurosaki, M. Uno, K. Takeda, H. Anada, T. Matsuda, S. Kobayashi, Journal of Alloys and Compounds, 330-332 (2002) 313-317.

[35] C.Q. Sun, Progress in Solid State Chemistry, 35 (2007) 1-159.

[36] M. Aoki, D. Nguyen-Manh, D.G. Pettifor, V. Vitek, Progress in Materials Science, 52 (2007) 154-195.

[37] N.A. Landin, L.A. Izhvanov, A.S. Chernikov, V.P. Kalinin, Russian Journal of Inorganic Chemistry, 16 (1971) 274.

[38] D. Khatamian, W.A. Kamitakahara, R.G. Barnes, D.T. Peterson, Physical Review, B21

(1980) 2622.

[39] C.E. Lundin, J.P. Blackledge, Journal of the Electrochemical Society, 109 (1962) 838.

[40] J.N. Daou, P. Vajda, Physical Review, B45 (1992) 10907.

[41] H.L. Yakel Jr., Acta Crystallographica, 11 (1958) 46.

[42] C.P. Kempter, R.O. Elliott, K.A. Gschneidner, Jr., The Journal of Chemical Physics, 33 (1960) 837.

[43] R.L. Beck, Transactions of American Society for Metals, 55 (1962) 542.

[44] S.S. Sidhu, N.S.S. Murthy, F.P. Campos, D.D. Zauberis, Advances in Chemistry Series, 39 (1963) 87.

[45] K.E. Moore, W.A. Young, Journal of Nuclear Materials, 27 (1968) 316.

[46] F. Ducastelle. R. Caudron, P. Costa, Journal de Physique, 31 (1970) 57.

[47] J.S. Cantrell, R.C. Bowman Jr., D.B. Sullenger, The Journal of Physical Chemistry, 88 (1984) 918.

[48] R.C. Bowman, B.D. Craft Jr., J.S. Cantrell, E.L. Venturini, Physical Review, B31 (1985) 5604.

[49] S.S. Sidhu, LeRoy Heaton, D.D. Zauberis, Acta Crystallographica, 9 (1956) 607.

[50] O.M. Katz, J.A. Berger, Transaction of the Metallurgical Society of AIME, 233 (1965) 1017.

[51] L. Espagno, P. Azou and P. Bastien, Comptes Rendus, 250 (1960) 4352.

[52] F.A. Lewis, A. Aladjem, "Hydrogen Metal Systems", Scitec Publications Ltd., Balaban Publishers, Zürich, Switzerland (1996).

[53] D. C. Wallace, "Thermodynamics of Crystals," Wiley, New York, (1972).

[54] M. Sakamoto, Journal of the Physical Society of Japan, 19 (1964) 1862-1866.

[55] A. Anderson, A.W. McReynolds, M. Nelkin, M. Rosenbluth, W. Whittemore, Physical Review, 108 (1957) 108.

[56] W.L. Whittemore, A.W. McReynolds, Physical Review, 133 (1959) 806.

[57] J. Bergsma, J.A. Goedkoop, Proceedings of the Symposium on Inelastic Scattering of Neutrons in Solids and Liquids, IAEA Vienna (1961) 501.

[58] W.L. Whittemore, A.W. McReynolds, Proceedings of the Symposium on Inelastic Scattering of Neutrons in Solids and Liquids, IAEA Vienna (1961) 511.

[59] A.D.B. Woods, B.N. Brocknouse, Proceedings of the Symposium on Inelastic Scattering of Neutrons in Solids and Liquids, IAEA Vienna (1961) 487.

[60] P.H. Saunderson, S.J. Cocking, Proceedings of the Symposium on Inelastic Scattering of Neutrons in Solids and Liquids, IAEA Vienna (1963) 265.

[61] J.J. Rush, H.E. Flotow, D.W. Connor, C.L. Thaper, The Journal of Chemical Physics, 45 (1966) 3817.

[62] G. Herbst, H. Kronmüller, Physica Status Solidi, A66 (1981) 255.

[63] J.P. Burger, J.N. Daou, P. Vajda, J.N. Daou, Journal of the Less-Common Metals, 103 (1984) 381.

[64] A. Lucasson, P. Vajda, J.P. Burger, J.N. Daou, Solid State Communications, 54 (1985) 807.

CHAPTER 4

Characteristics of Zr Alloys with Precipitated Hydride and/or Solute Hydrogen

Chapter 4.
Characteristics of Zr Alloys with Precipitated Hydride and/or Solute Hydrogen

4-1. Introduction

The integrity of zirconium based alloys for fuel cladding materials has become more important because of burnup extension of nuclear fuels in the Light Water Reactors (LWR). Hence, niobium containing zirconium alloys viz., NDA, MDA, ZIRLO, and M5 have been newly introduced to improve corrosion resistance and mechanical strength. Table 4.1 shows the composition of the new niobium containing zirconium alloys. On the contrary, it was reported that zirconium alloys absorb a part of evolved hydrogen during operation by the corrosion reaction between zirconium alloy and cooling water as follows:

$$Zr + 2H_2O \rightarrow ZrO_2 + 4H \qquad (4\text{-}1)$$

If the total hydrogen concentration in the alloy exceeds the solubility limit, brittle zirconium hydrides are formed as precipitates in the alloy, which is extremely brittle (see Fig. 4.1 [1]) and therefore markedly deteriorates the material strength. Fig. 4.2 shows corrosion behaviors of the niobium containing zirconium alloys together with the Zircaloy, and Fig. 4.3 shows amount of hydrogen absorption during operation for the several cladding materials [2]. Although the niobium containing zirconium alloys have superior corrosion resistance to the Zircaloys, there is not significant difference in the amount of hydrogen absorption between the alloys. Therefore, the influence of hydrogen absorption in the fuel claddings on their integrity is considered to be not negligible at higher burnup over 60 GWd/t that will be reached near future in the LWR even if the superior corrosive-resistant Zr-Nb alloys are used.

Table 4.1. Composition of advanced Zr alloys for fuel cladding (wt%).

Additive elements	Nb	Fe	Sn	Cr	Ni
NDA	0.1	0.27	1.0	0.16	0.01
MDA	0.5	0.2	0.8	0.1	—
ZIRLO	1.0	0.1	1.0	—	—
M5	0.8 – 1.2	0.015 – 0.06	—	—	—

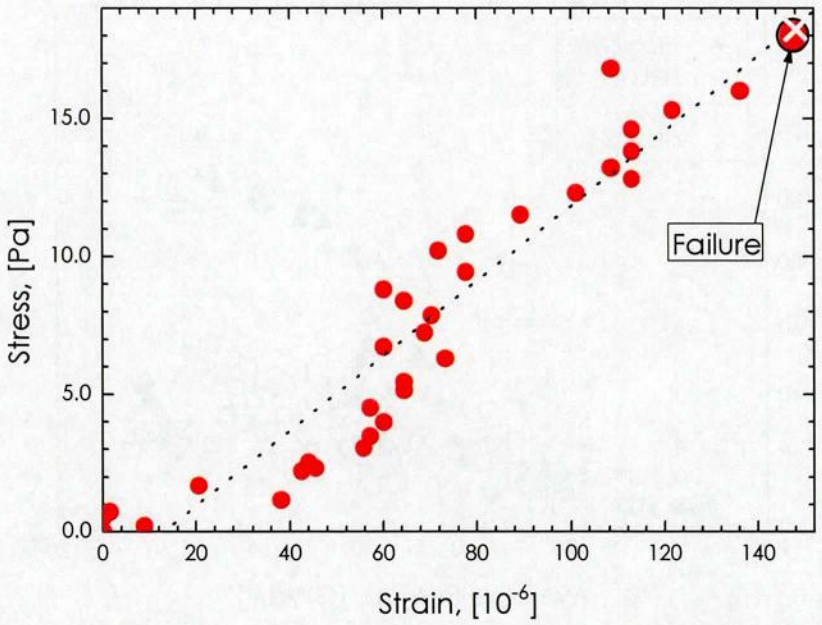


Fig. 4.1. Stress-strain curve of Zr hydride ($\delta ZrH_{1.73}$) [1].

Therefore, it is important to elucidate the terminal solid solubility of hydrogen (TSS) for the zirconium alloys. Experimental determination of the TSS is usually as follows: samples with known hydrogen contents are prepared and then their thermophysical properties were measured in order to evaluate transition temperature corresponding to end of hydride dissolution during heating process and beginning of hydride precipitation during cooling process. The TSS have been extensively studied with using several measurement such as dilatometry [3, 4], resistivity[5], internal friction [6–8], differential scanning calorimetry [9–12], small angle neutron scattering [13, 14], metallography [15], and thermal diffusion [16]. The transition temperatures are correlated with corresponding hydrogen contents in the form of a van't Hoff type relationship, from which we can obtain the pre-exponential constant and the enthalpy of the dissolution or precipitation process of hydride [17–24]. It is considered that the TSS depends on fabrication history, irradiation, and additive elements. Although several effects have been studied [25–32], there have been few reports on the effect of additive elements. Therefore, the effect of additive elements such as iron, tin, chromium, and nickel was examined separately and the influence of the additives on TSS was formulated in our previous study [33].

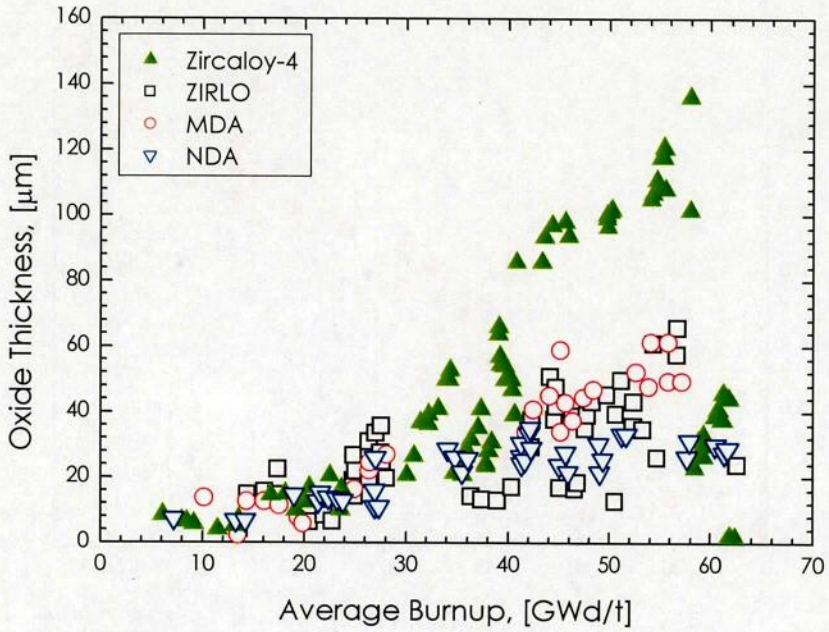


Fig. 4.2. Relation between average burnup and thickness of oxide layer generated by corrosion reaction during operation for several cladding materials [2].

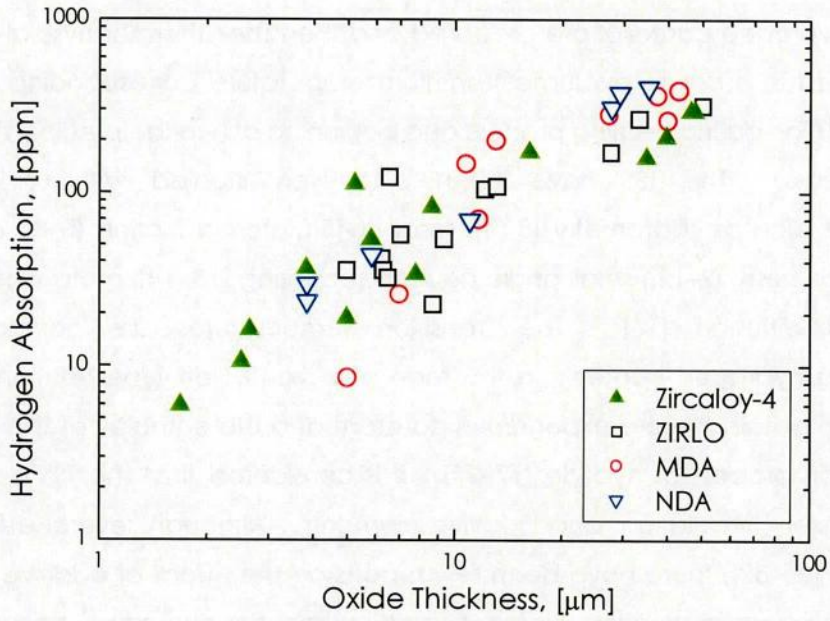


Fig. 4.3. Relation between thickness of oxide layer and amount of hydrogen absorption for several cladding materials [2].

Fig. 4.4 shows the phase diagram of Zr-Nb binary system. In the niobium modified fuel cladding, the concentration of added niobium ranges from 1 to 5 wt% contrary to the small amount of concentration of the other traditional additive element. Therefore, most of the added niobium dissolves into the matrix α phase (hcp), but a small amount of Nb-rich β Zr phase (bcc) precipitates in the alloys. Several studies on the TSS of Zr-Nb alloys have been carried out [4, 6, 11, 12, 16, 27, and 32]. However, the effect of niobium dissolution into the matrix α phase on TSS has scarcely been investigated, although the volume fraction of α phase is dominant in the alloys. Moreover, the effect of niobium addition on the TSS for the commercial fuel cladding such as the Zircaloys is still unknown.

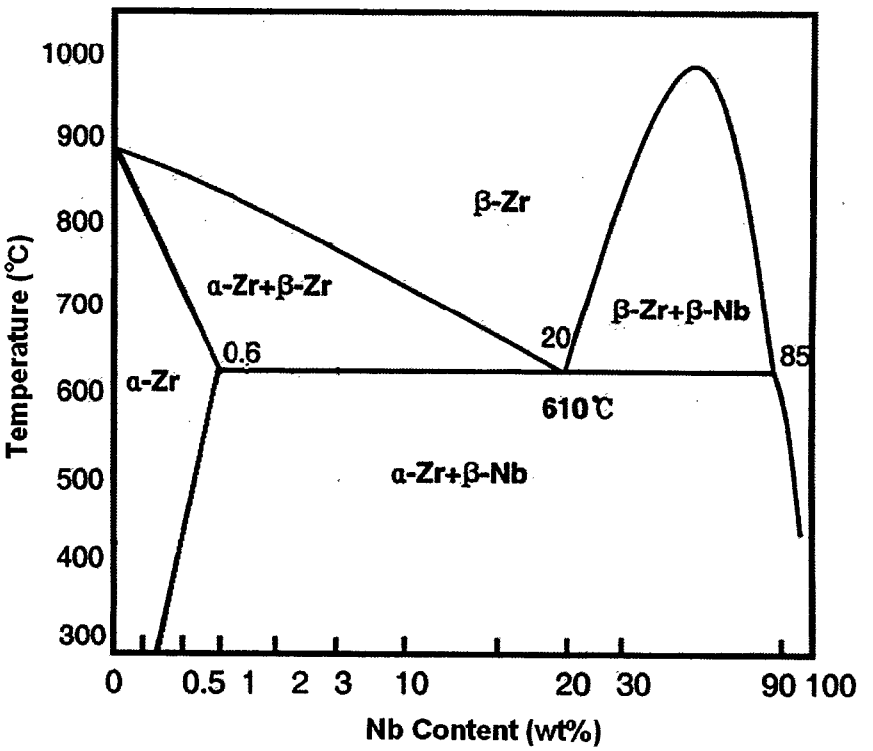


Fig. 4.4. Phase diagram of Zr-Nb binary system.

The zirconium alloys may become susceptible to the crack process known as delayed hydride cracking (DHC) depending on the several physical properties of them as well as operation conditions. The properties of the zirconium hydrogen solid solutions had been unnoticed until report [34] which indicated that solute hydrogen in metallic

lattice effected and accelerated creep rate of the zirconium alloys. Setoyama et al. [35–37] studied the mechanical properties of the zirconium and titanium hydrogen solid solutions. They revealed that solute hydrogen led reductions in the mechanical properties such as the Young's modulus and microhardness of zirconium and titanium. They also indicated probability that the solute hydrogen accelerates the creep rate by the change in the Young's modulus, not by the change in the creep mechanism. Chapter 2 and 3 in the present thesis systematically elucidated the properties of transition metal–hydrogen solid solutions. However, since these investigations are for pure metal–hydrogen systems, it is considered to be necessary to furthermore evaluate the effect of hydrogen on the Zr-Nb alloys those would be practically used for the fuel cladding. In the case of the niobium modified zirconium alloys, the phase is complex as mentioned above. It is reported that the microstructure of Zr-2.5Nb alloy for pressure tube in heavy water reactors consisted strongly elongated and textured α phase grains surrounded by very thin but nearly continuous grain-boundary network of metastable β phase. The β phase contains about 20 wt% niobium and its volume fraction is about 10% [32, 38–46]. Therefore, in-depth investigations on each particular phase of the Zr-Nb alloys are important to clarify the effect of hydrogen addition on the properties of Zr-Nb alloys. In addition, it is essential for developing this study to confirm whether consistent evaluations with Chapter 2 and 3 can be obtained or not.

From such points of view, the TSS of Zr-Nb binary alloys with different niobium contents, which were α single phase or $(\alpha+\beta)$ biphasic specimens, and Nb added Zircaloy-4 were measured and the effects of niobium addition on the TSS were discussed in section 4-4-1. The mechanical properties of the Zr-Nb alloys with different hydrogen content were evaluated in section 4-4-2.

4-2. Experimental Procedure

4-2-1. Sample Preparation

The specimens of Zr-1.0(wt%)Nb, Zr-2.5Nb, and 1.0wt% Nb added Zircaloy-4 fuel cladding alloys were produced by Sumitomo Metal Industry Ltd.. The preparation process of these alloys is the same as that for the commercially supplied recrystallized Zircaloy-4. The details of fabrication process of these specimens were shown in Table 4.2. The composition of these alloys was tabulated in Table 4.3. In addition to those specimens, pure zirconium and Zr-0.3Nb alloy were also examined in order to evaluate the variation of TSS in the matrix α phase due to niobium dissolution. This

concentration is near the niobium solubility limit at room temperature.

Table 4.2. Fabrication process of Zr -1.0Nb, Zr -2.5Nb, and Nb added Zry-4

	Process
①	Arc melting
②	β annealing and quenching : 1050 ℃×0.5 h→0 Q (in vacuum)
③	Hot rolling: 923 K×0.5 h (Ar atomsphere) T9～13 mm→T5 mm
④	Oxide layer elimination: Blast polishing by alumina shot
⑤	Interlevel annealing: 893 K×2 h (in vaccum)
⑥	Cold rolling: T5 mm→T2.5 mm
⑦	Interlevel annealing: 893 K×2 h (in vacuum)
⑧	Cold rolling: T2.5 mm→T1.0 mm
⑨	Final annealing: 850 K×3 h (in vacuum)

Table 4.3. Composition of the evaluated Zr alloys (wt%).

Sample Name	Nb	Fe	Sn	Cr	H	C	N	O	Zr
Zr-1.0Nb	1.00	0.038	0.002	0.002	0.0025	0.006	0.0047	0.100	balance
Zr-2.5Nb	2.56	0.038	0.001	0.004	0.0032	0.008	0.0031	0.181	balance
Nb added Zry-4	1.01	0.260	1.310	0.100	0.0030	0.008	0.0037	0.201	balance

Furthermore, Zr-20Nb alloy was produced for the evaluation of the mechanical properties. The principal impurities of the pure zirconium specimen included 0.001wt% Sn, 0.0083wt% Fe, 0.005wt% Cr, 0.0035wt% Ni, 0.004wt% Si, and 0.005wt% O. For preparing the Zr-0.3Nb and Zr-20Nb alloys, pure niobium of 99.95wt% and pure zirconium were used as precursor. The source materials were melted in an arc furnace under argon atmosphere at 0.05 MPa. For homogeneity, the specimen was turned over and melted more than 5 times, and then annealed in vacuum at 1273 K for 12 h. The hydrogenation was executed using a modified UHV Sieverts' apparatus under a highly

pure (7N) hydrogen gas atmosphere. Details of the Sieverts' apparatus are described in Chapter 2. After the hydrogenation at 973 K, the specimens were retained at the temperature to homogenize hydrogen distribution for 3h and then were furnace cooled with an average cooling rate of 5 K/min.

X-ray diffraction measurements were performed at room temperature using Cu-Kα radiation (RINT-2000/PC, Rigaku Corp.) to analyze the existing phases in the specimens. The absorbed hydrogen contents in the specimens were measured with a hydrogen analyser (HORIBA, EMGA-621).

4-2-2. Measurement Method

(a) Terminal Solid Solubility of Hydrogen

Their hydrogen contents range from 26 ppm to 770 ppm, and the statistical errors were within 2%. After the hydrogenation, the samples were cut into shapes approximately 5 mm square and 1 mm thick, and weighing about 40–60 mg for the TSS measurement. The hydride dissolution temperature of specimen was evaluated with a differential scanning calorimeter (ULVAC-RIKO, Triple-cell DSC) in the temperature range from 50 K to 873 K. It was reported that the dissolution/precipitation temperature was independent of heating rates in the range of 0.5–10 K/min [47]; the heating rate of 5 K/min was adopted in the present study. The apparatus has a "triple-cell" system and an adiabatic temperature control system, which was originally developed by Takahashi et al. [48]. The measurement was made in high-purity argon (6N) atmosphere with a flow rate of 100 ml/min. The accuracy of the apparatus was checked to be ±3% using an $\alpha - Al_2O_3$ standard. The transition temperature is obtained experimentally from heating or cooling. These temperatures are summarized as TSSD (TSS-dissolving) and TSSP (TSS-precipitating), respectively. Khatamian et al. [9–12] mentioned that the TSSD temperature provided more reproducible results than the TSSP. Therefore the TSSD was adopted as TSS in the present study.

(b) Mechanical Properties such as Elastic Modulus and Hardness

The longitudinal and shear sound velocity measurement was carried out by an ultrasonic pulse-echo method using Echometer1062 (Nihon Matech Corp.) at room temperature. With use of the results, the elastic moduli were evaluated. The Vickers hardness was also measured using MHT-1 (Matsuzawa Co.Ltd.) at room temperature. The applied load and load time for the indentation were 1.0 kgf and 10 sec, respectively. The measurements were repeated more than 10 times for all samples, and the average

hardness was estimated from the data obtained. The further details of these measurements are described in Chapter 2.

The high temperature elastic moduli were also obtained by using a multiple elastometer (NTP, EG-HT), based on the cantilever characteristic vibration technique. The measurement was performed under argon flow and the measuring temperature range is from room temperature to 773 K. The characteristic vibration frequencies were about 10 Hz. Young's modulus E can be derived from the following equations by the characteristic vibration method:

$$E = \frac{\omega^2 \rho S}{I \cdot k} \tag{4-1}$$

where ω is the angular frequency, ρ the density of specimen, S the cross-section of the specimen, I the moment of inertia of the specimen, and k the device parameter to lateral vibration.

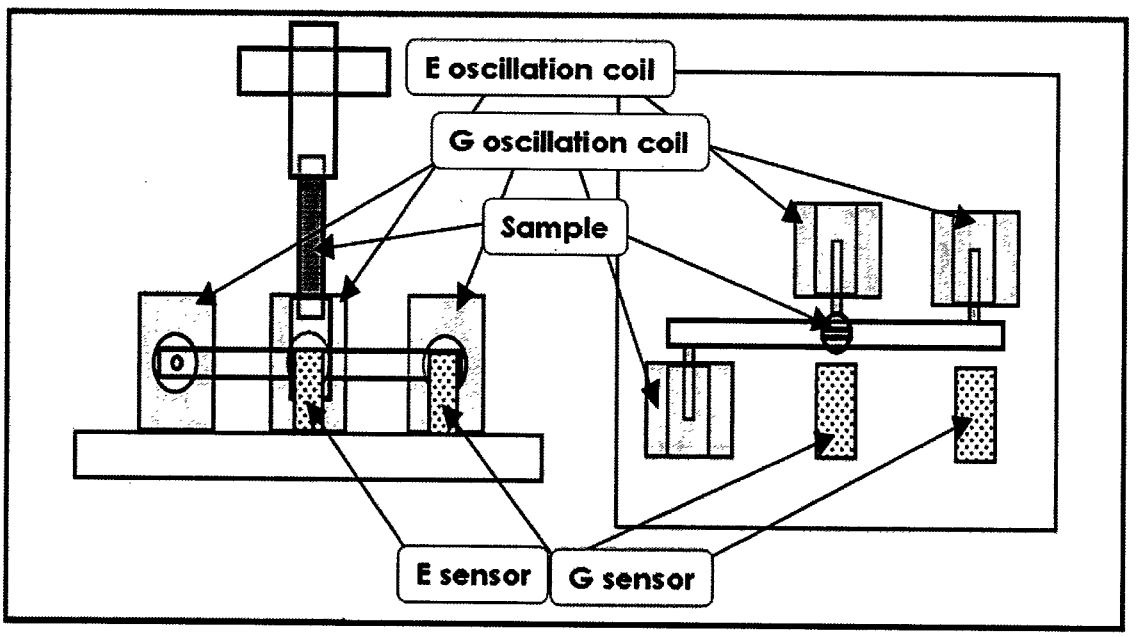


Fig. 4.5. Schematic drawing of high-temperature multiple elastometer that is based on a cantilever characteristics vibration technique.

4-3. Results and Discussion

4-3-1. Terminal Solid Solubility of hydrogen of Zr-Nb Alloys

Fig. 4.6 and Fig. 4.7 show X-ray diffraction patterns of hydrogenated Zr-0.3Nb and Nb added Zircaloy-4, respectively. Based on the X-ray diffraction analysis at room temperature, it is observed that there are two α Zr and δ ZrH_{2-X} phases in the hydrogenated pure zirconium and Zr-0.3Nb alloy. On the other hand, there exist α Zr, β Zr, and δ ZrH_{2-X} phases in the hydrogenated Zr-1.0Nb, Zr-2.5Nb, and Nb added Zircaloy-4. α Nb, γ ZrH, and ε ZrH_{2-X} phases were not detected in all the specimens. Since the niobium is a stabilizer element for β Zr, the metastable β Zr phase can exist in the specimens below the eutectic temperature of 893 K [49].

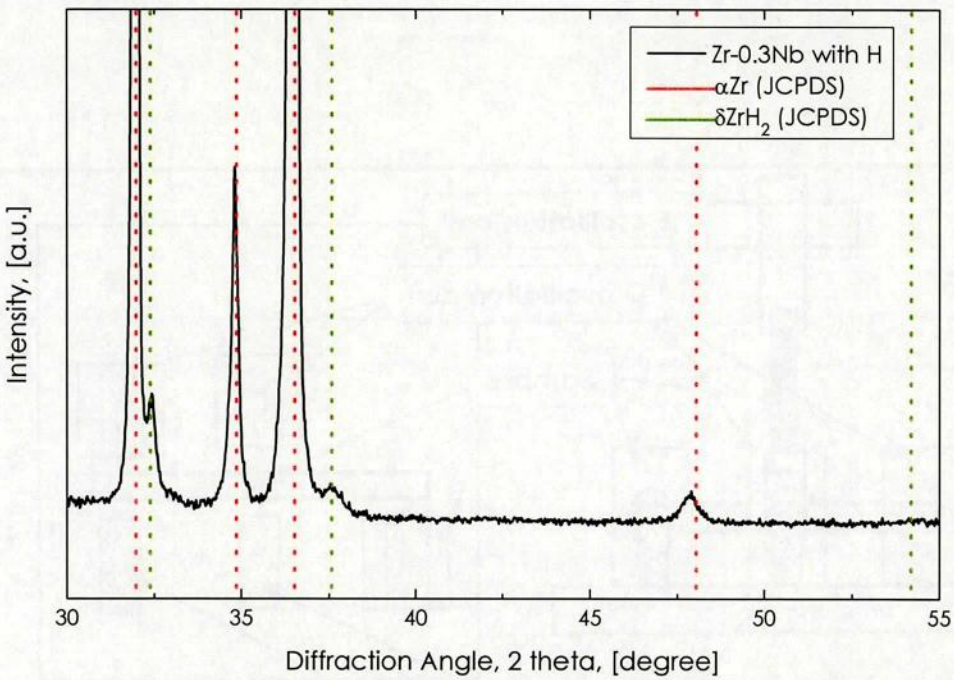


Fig. 4.6. X-ray diffraction pattern of hydrogenated Zr-0.3Nb.

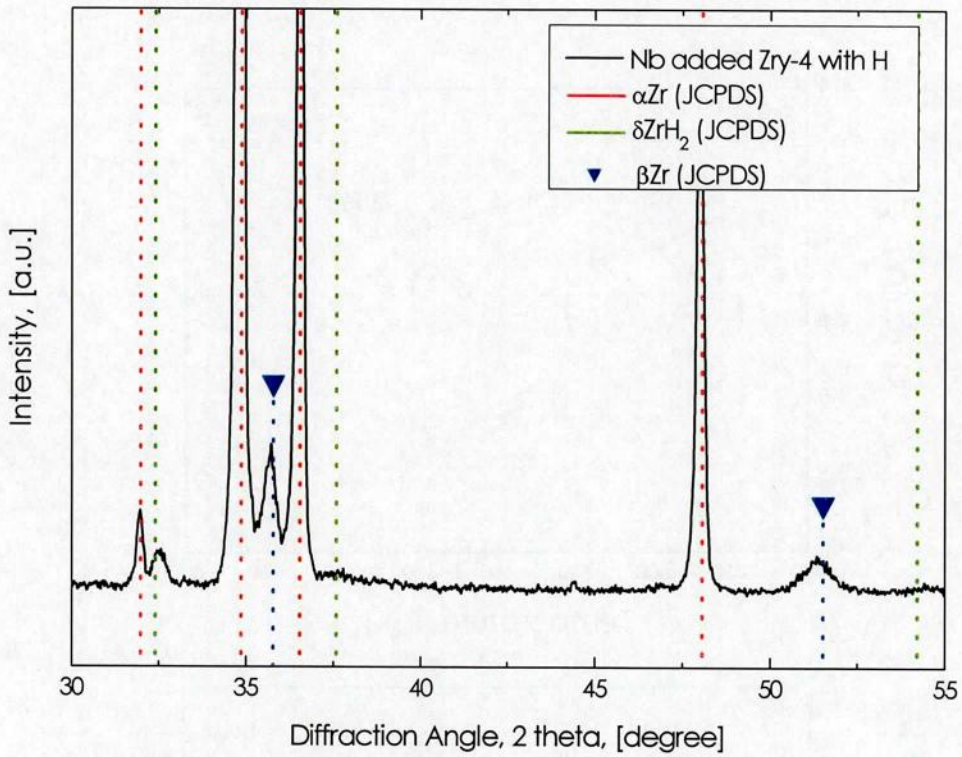


Fig. 4.7. X-ray diffraction pattern of hydrogenated Nb added Zry-4.

A typical DSC curve and heat capacity C_P for pure zirconium with 186 wtppm hydrogen are exhibited in Fig. 4.8(a) and (b), respectively. From this figure, it is found that there is an inflection point in the DSC curve at 655 K, which may be related to the complete dissolution temperature of the hydride. It is also found that the C_P increases with temperature up to 655 K due to the endothermic reaction of hydride dissolution and this termination temperature agrees with the temperature obtained from the DSC curve. The temperature is considered to signal the end of hydride dissolution. Une [31] reported that heat capacities C_P of hydrogenated zirconium alloys increase with temperature to a certain temperature, which was attributed to the hydride dissolution effect, and the end temperature agreed with the complete dissolution temperature of hydride obtained from the TSSD data. Therefore, the maximum C_P point is chosen as the complete dissolution temperature of hydride in the present study because the peak is clearer than that of DSC curve.

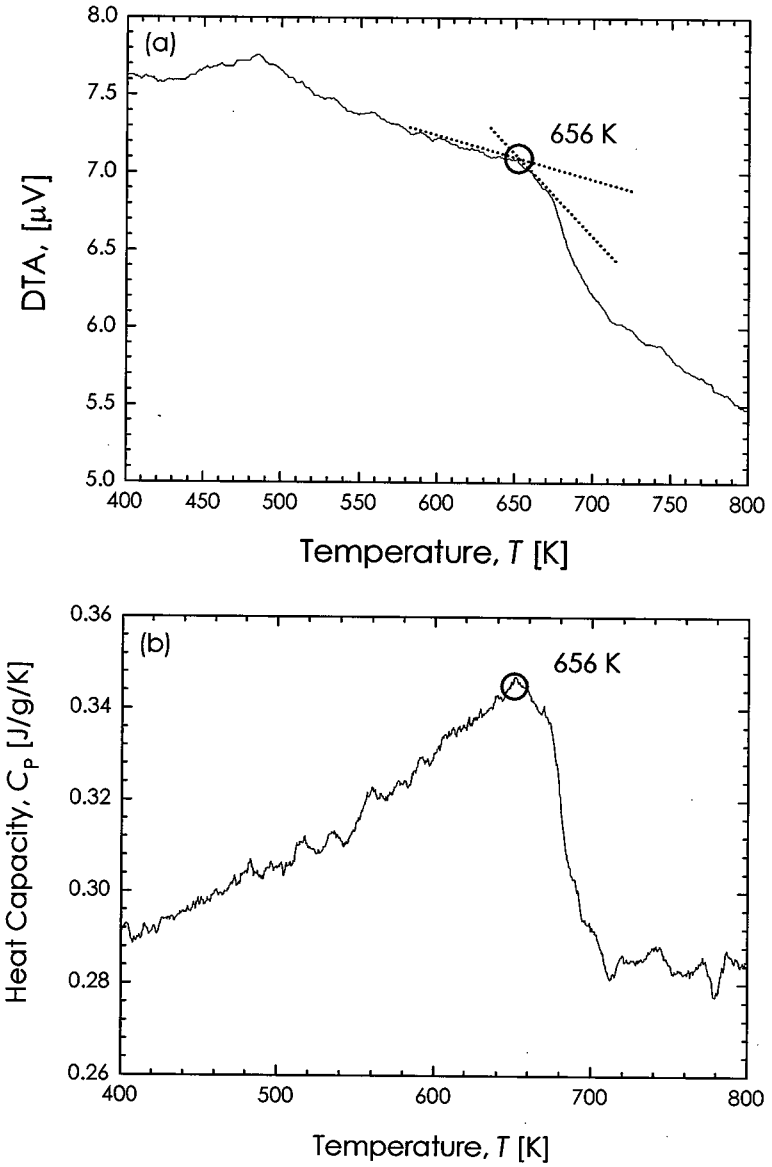


Fig. 4.8. Typical DSC (a) and C_P (b) curves of pure Zr with 186 wtppm hydrogen.

The measured TSS points for pure zirconium are plotted in Fig. 4.9 with the data by Khatamian [10] and Kearns [25]. The results in the present study are in good agreement with the previous reports. Therefore the measuring method in the present study is consistent with previous studies. The TSS shows the linear relation of $\ln C_H$ vs 1/T and can be fitted using the van't Hoff's equation:

$$C_H = A\exp\left(-\frac{Q}{RT}\right) \qquad (4\text{-}2)$$

where C_H, A, Q, R, and T are the hydrogen content, a constant related to the dissolution entropy, the dissolution enthalpy, the ideal gas constant, and the absolute temperature, respectively. The A and Q values for pure zirconium are listed with those for the other alloys in Table 4.4.

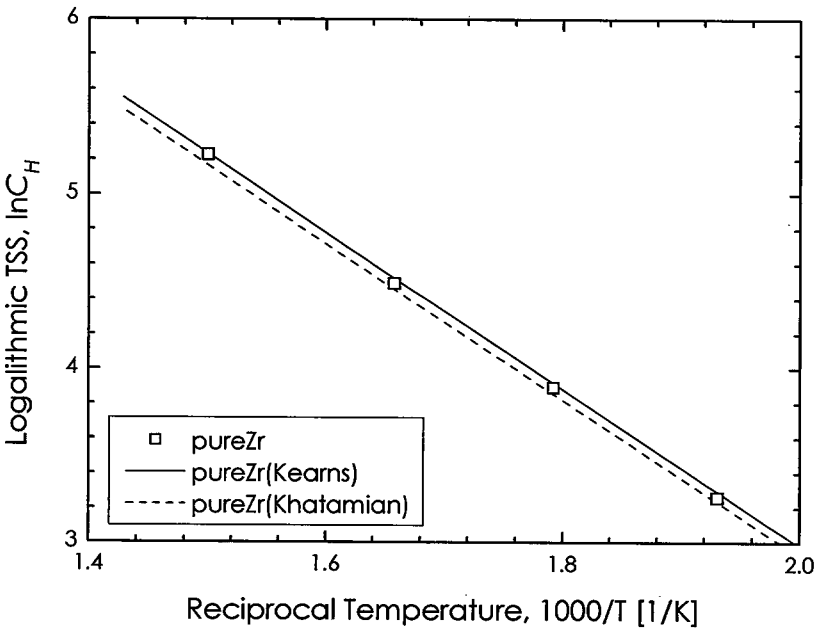


Fig. 4.9. Terminal solid solubility of hydrogen for pure Zr, together with literature data [10, 25].

Table 4.4. The van't Hoff' fit parameters of the terminal solid solubility.

Sample Name	A (wtppm)	Q (kJ/mol)
pure Zr	1.42×10^5	37.1
Zr-0.3Nb	2.89×10^5	40.4
Zr-1.0Nb	4.30×10^5	41.5
Zr-2.5Nb	3.98×10^5	40.6
Nb modified Zircaloy-4	4.27×10^5	40.1

The TSS results of Zr-Nb binary alloys, Zr-0.3Nb, Zr-1.0Nb, and Zr-2.5Nb are shown in Fig 4.10. The TSS of the α single-phase Zr-0.3Nb specimen appears to be almost same as that of pure zirconium. Therefore, it is considered that the niobium dissolution into α Zr does not affect the TSS so much. In general, the dissolved constituents lead to an entropy increase by mixing, and then the free energy decreases. Therefore the TSS increases by solute elements [33]. In the present case, the concentration of niobium is too small to bring obvious conspicuous increase in the TSS of α Zr.

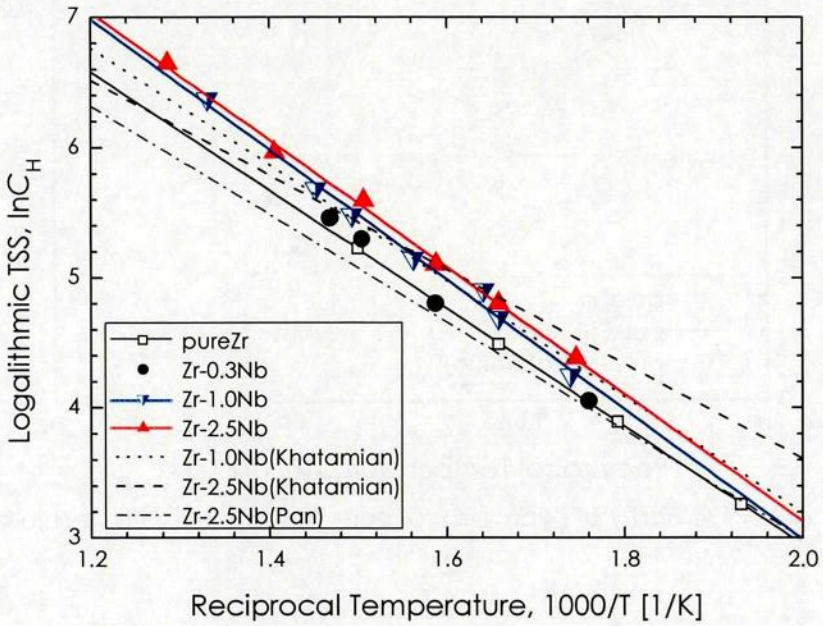


Fig. 4.10. Terminal solid solubility of hydrogen for Zr-Nb binary alloys, together with literature data [6, 12].

The literature results for Zr-1.0Nb and Zr-2.5Nb alloys are also included in Fig. 4.10. The present TSS of the Zr-1.0Nb and Zr-2.5Nb alloys are in good agreement with the data by Khatamian [12] in the temperature range from 580 K to 670 K, but higher than the data, in which the measuring method was different from the present study, by Pan [6]. This difference may be caused by the effect of β Zr decomposition, which has been revealed to decrease the TSS of Zr-Nb alloy [11]. It is also found from Fig. 4.10 that the TSS of the Zr-1.0Nb and Zr-2.5Nb alloys, which are $\alpha+\beta$ biphasic specimens, is higher than that of pure zirconium. In addition, the TSS of Zr-2.5Nb alloy is slightly higher than

that of Zr-1.0Nb alloy.

Since the TSS of the matrix α phase is unchanged by the niobium addition, the precipitation of β Zr must have a major part in increasing the TSS in Zr-Nb binary alloys. The TSS means the maximum hydrogen content of the hydrogen solid solution phase in equilibrium with the coexisting hydride phase; the concentration is determined at the point that provides a common tangent for the free energies of the solution phase and the hydride [24]. In the case of multiple systems in which three or more phases exist, the interactions between constituent elements in different phases must be taken into account in order to discuss the equilibrium. For example, the free energy of β Zr phase in the Zr-Nb-H ternary system probably decreases below the common tangent line of free energies between α Zr and hydride in the Zr-H binary system due to the niobium and hydrogen dissolution, which may result in the increase of TSS (see Fig. 4.11). Further experimental and theoretical investigations are required to address this question.

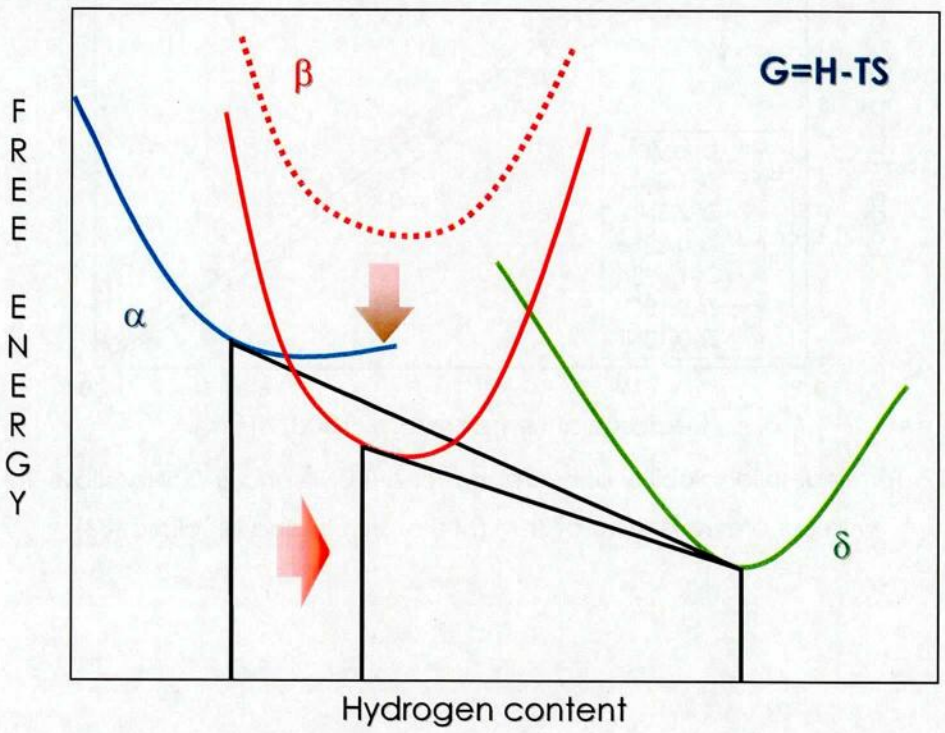


Fig. 4.11. Schematic drawing of free energy of Zr(Nb)-H system.

In Fig. 4.12, the present TSS results of Zr-Nb binary alloys are compared with the TSS results for Zr-M (M=Fe, Sn, Cr, and Ni) binary alloys obtained in our previous study [33]. The amounts of the previous additive elements are chosen based on the specifications of the Zircaloys that are actually practically used in the present commercial light-water reactors. It is found from this figure that the increase of TSS by the addition of niobium is slightly larger than that by the addition of tin, chromium, and nickel. Therefore, it is considered that niobium addition to the zirconium alloys can play an important role in terms of the TSS for increasing the life-time of cladding.

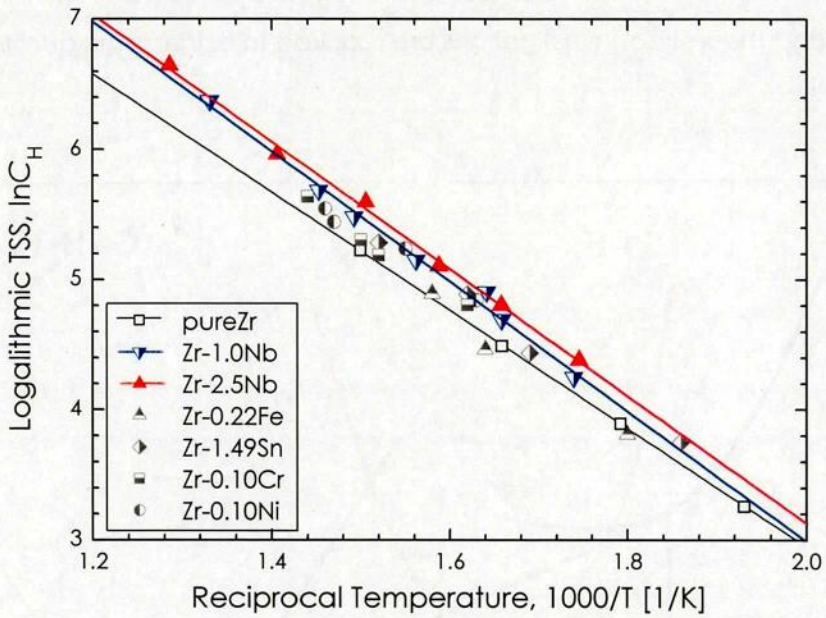


Fig. 4.12. Terminal solid solubility of hydrogen for Zr-1.0Nb and Zr-2.5Nb alloys, together with our previous data of Zr-M (M=Fe, Sn, Cr, and Ni) alloys [33].

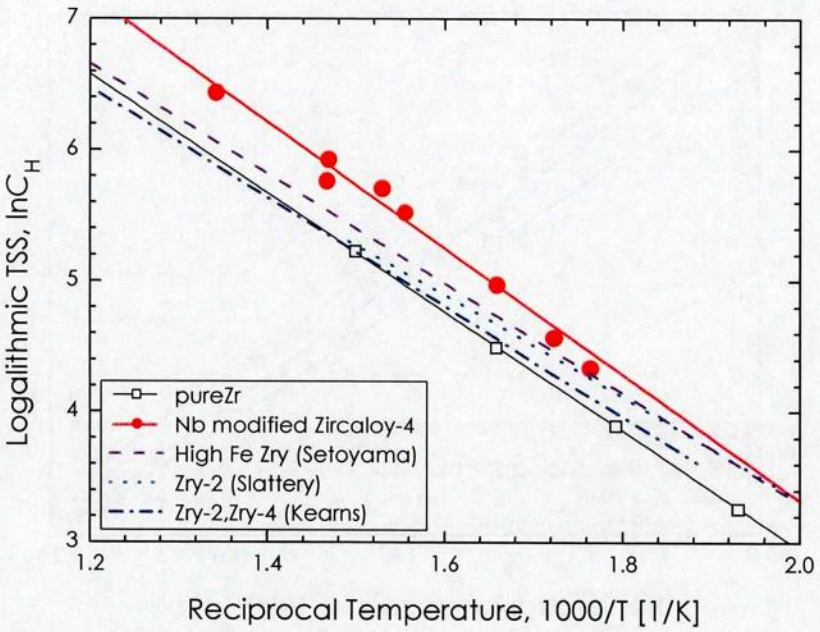


Fig. 4.13. The terminal solid solubility of 1.0wt% Nb added Zircaloy-4, together with literature data [25, 26, 33].

The TSS points of 1.0wt% Nb added Zircaloy-4 are plotted in Fig. 4.13, together with the literature data for Zircaloy-2 and Zircaloy-4 by Kearns [25], Slattery [26], and Setoyama et al. [33]. It is found from this figure that the Nb added Zircaloy-4 has higher TSS than Zircaloy-2 and Zircaloy-4. The reason why the TSS of Zircaloy is larger than that of pure zirconium have been revealed in our previous study [33] to be the effect of the tin dissolution into α Zr phase and the precipitation of intermetallic compounds of Zr-Cr and Zr-Ni alloys. The β Zr phase does not exist in the normal Zircaloy, whereas this phase exists in the present Nb-modified Zircaloy specimens. Therefore, it is considered that the increase of TSS for Zircaloy is attributed to the further effect of β Zr precipitation by niobium addition besides the traditional additive element effects. Evidently, 1.0 wt% Nb added Zircaloy indicates the higher TSS than the Zr-1.0Nb binary alloy, as shown in Fig. 4.14. Therefore, it is considered that both niobium element and the other traditional additive elements affect the TSS of hydrogen in the Nb added Zircaloy.

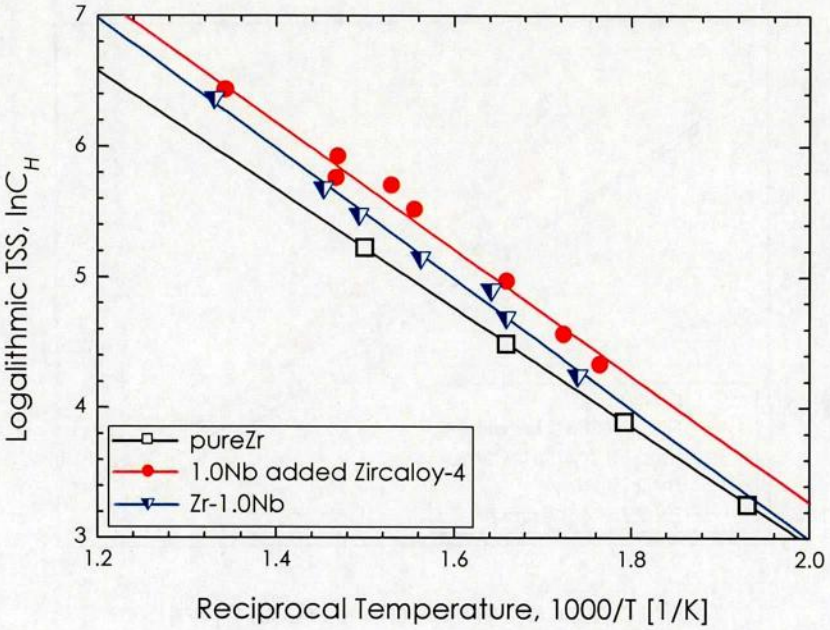


Fig. 4.14. Comparison between TSS of Zr-1.0Nb and 1.0wt% Nb added Zircaloy-4.

4-3-2. Mechanical Properties of Hydrogenated Zr-Nb Alloys

The hydrogen content of the prepared sample was in the range from 0.00 to 0.013 in the atomic ratio. Fig. 4.15 shows the X-ray diffraction patterns of the Zr-20Nb alloy. All the prepared samples were confirmed to have an bcc_A2 β Zr(Nb) single phase. Fig. 4.16 shows the lattice parameter a at room temperature as the function of hydrogen content C_H. The lattice parameter increased by hydrogen addition as expressed as follows:

$$a\,[\mathrm{nm}] = 0.3540 + 2.333\times10^{-2}\times C_H\,[\mathrm{H/M}] \qquad (4\text{-}3)$$

The present lattice parameters of β Zr-20Nb alloys without hydrogen agreed with the values estimated from the Vegard's law using the metallic radii of the zirconium and niobium at room temperature. It has been reported that hydrogen-induced volume expansions in the metals are in the range $2.6 \sim 3.2\times10^{-3}[\mathrm{nm^3/(H/M)}]$. The present hydrogen-induced volume expansion value is $(4.0\pm0.4)\times10^{-3}[\mathrm{nm^3/(H/M)}]$ and is therefore slightly higher than the literature. It is also found that the geometrical density of the sample, which is determined from the weight and dimensional measurements, is approximately equal to the theoretical density, which is determined from the lattice parameter.

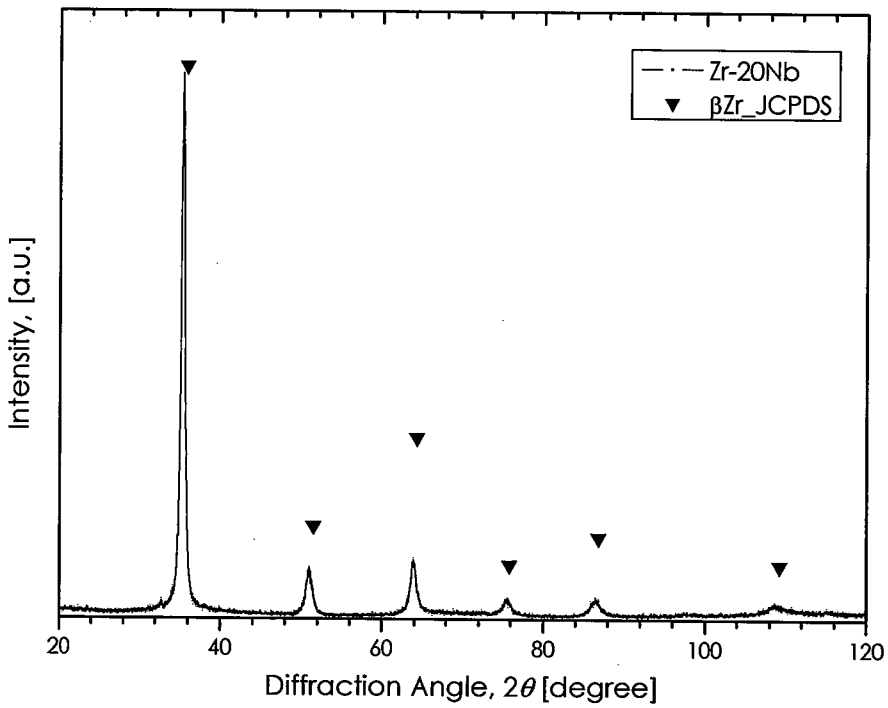


Fig. 4.15. X-ray diffraction pattern of Zr-20Nb alloy.

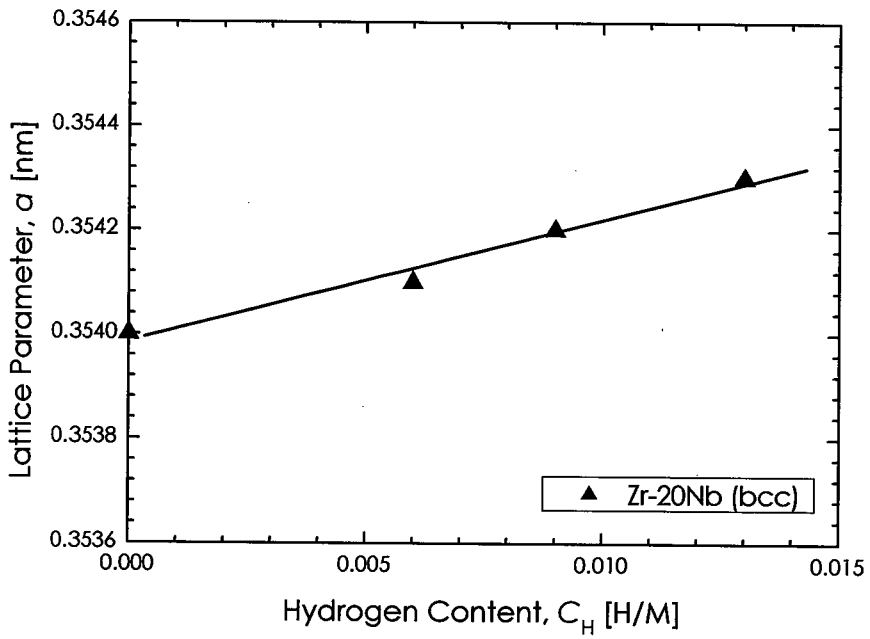


Fig. 4.16. Change in lattice parameter of hydrogen solid solution of β phase Zr-20Nb alloy with hydrogen content.

Fig. 4.17 shows the change in Young's modulus of hydrogen solid solution of β phase Zr-20Nb alloy with hydrogen content C_H. It is found from this figure that the Young's modulus of β phase Zr-20Nb alloy is almost independent of hydrogen content and empirically expressed as follows:

$$E[\mathrm{GPa}] = 102.4 - 12.0 \times C_H[\mathrm{H/M}] \quad (4\text{-}4)$$

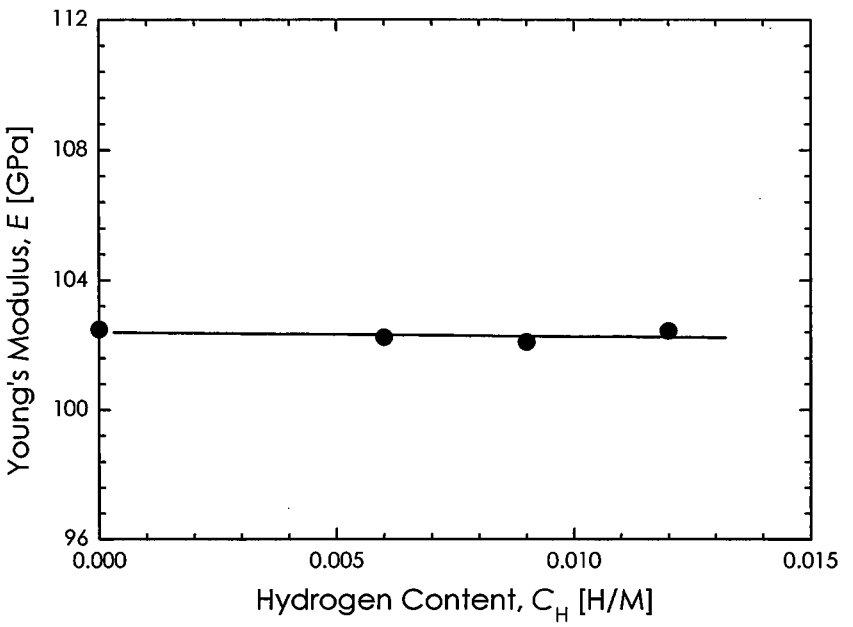


Fig. 4.17. Hydrogen content dependence of Young's modulus of hydrogen solid solution of β phase Zr-20Nb alloy.

Fig. 4.18 shows the Vickers hardness H_V of hydrogen solid solution of β phase Zr-20Nb alloy with hydrogen content C_H. As well as the elastic modulus, the hardness of β phase Zr-20Nb alloy is almost independent of hydrogen content and empirically expressed as follows:

$$H_V[\mathrm{GPa}] = 1.92 - 0.67 \times C_H[\mathrm{H/M}] \quad (4\text{-}5)$$

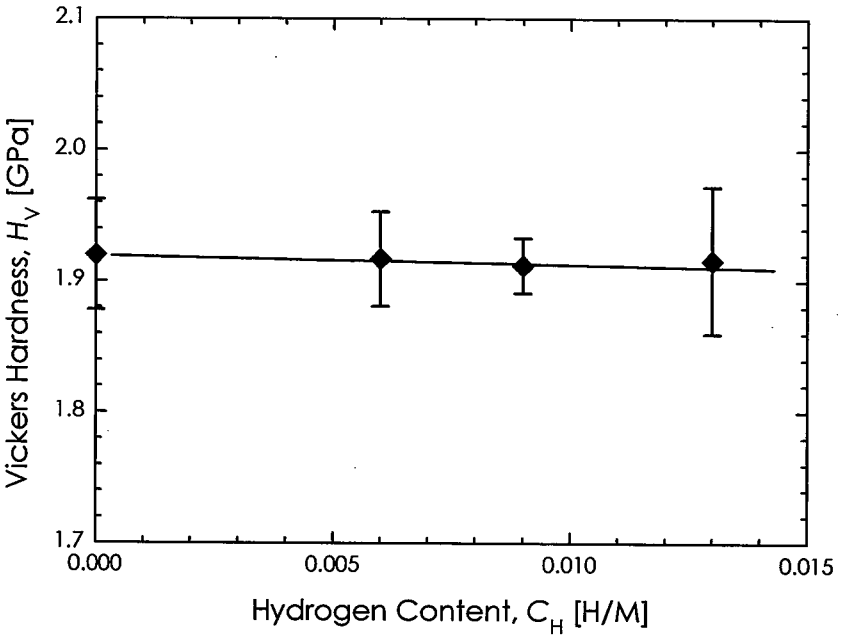


Fig. 4.18. Hydrogen content dependence of Vickers hardness of hydrogen solid solution of β phase Zr-20Nb alloy.

These results are compared to those of the Zr-H [35] and Nb-H systems for discussion. Fig. 4.19 shows the Young's modulus change due to hydrogen addition $E-E^0$, together with those data of pure zirconium and niobium. The E^0 indicates the Young's modulus without hydrogen. It is found from this figure that the changing rate of Young's modulus with hydrogen for the β Zr-20Nb hydrogen solid solution is between those of its pure metals. Fig. 4.20 shows the Vickers hardness change due to hydrogen addition $H_V - H_V{}^0$, together with those data of pure zirconium and niobium. The $H_V{}^0$ indicates the hardness without hydrogen. It is also found from this figure that the changing rate of Vickers hardness with hydrogen for the β Zr-20Nb hydrogen solid solution is between those of its pure metals. In Chapter 3, the trend of mechanical properties of transition metal–hydrogen solid solution can be explained by the electronic structure calculations. In the case of zirconium hydrogen solid solution, the 4d electrons are drawn off from the metallic bond on to the Zr-H bond, leaving less charge to participate in the Zr-Zr bonds, which consequently weakens the surrounding metallic bonds. On the other hand, it is considered that the solute hydrogen plays a role for the Nb–H–Nb bonding and consequently increases the elastic moduli and the hardness of the niobium. As a result

of analyzing the data, it is found that the hydrogen effects on the mechanical properties are not determined by crystal structure but the original bond order, which is the population of electrons participating in the covalent bonding [50], per unit cell of the elements. Therefore the present result can be compatible each other, although the β Zr-20Nb alloy has different crystal structure than the pure zirconium. On the valid assumption that the Zr-Nb solid solution alloy has the bond order per unit cell between its pure metals, the present result is considered reasonable.

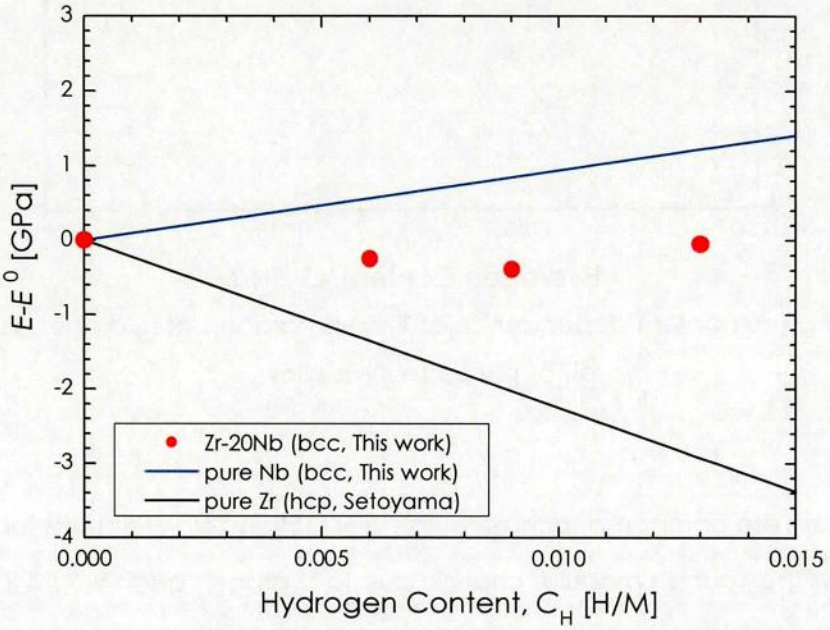


Fig. 4.19. Comparison of change in Young's modulus with hydrogen content between hydrogen solid solution of β phase Zr-20Nb alloy and its pure metals [35].

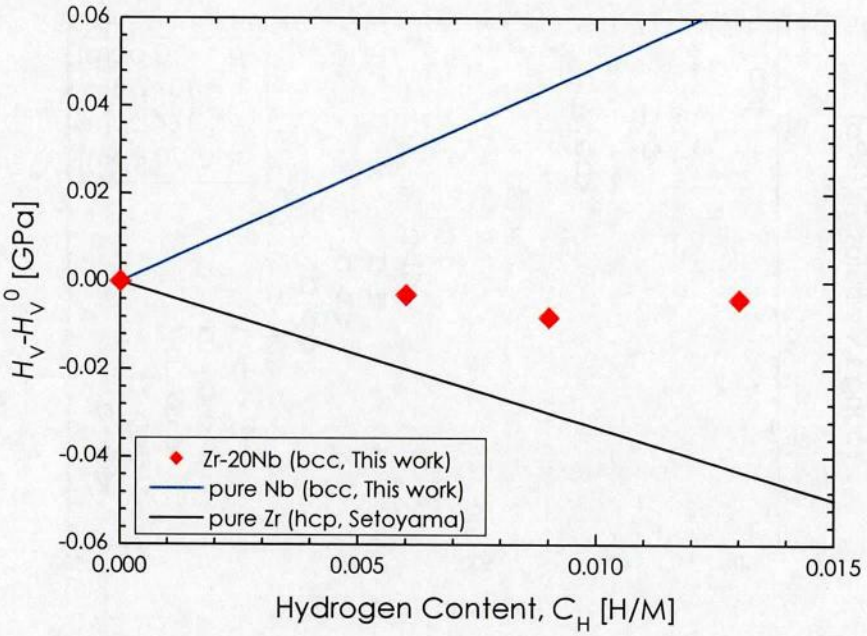


Fig. 4.20. Comparison of change in Vickers hardness with hydrogen content between hydrogen solid solution of β phase Zr-20Nb alloy and its pure metals.

Fig. 4.21 shows the temperature dependence of Young's modulus of hydrogenated Zr-1.0Nb alloy. The solid marks are in the hydrogen content region that all the hydrogen dissolves in the (α +β) metallic phase and the open ones are in the region that a part of hydrogen precipitates as δ hydride. In the two separate temperature regions, the Young's modulus and shear modulus linearly decrease with increasing temperature. The difference in the elastic modulus between the samples with different hydrogen contents is not so large in the lower temperature region, on the contrary, that appears to be clear in the higher temperature region. It is found from this figure that Young's modulus for the solid solution decrease with increasing hydrogen content and that those for the partially precipitated hydride slightly depend on the hydrogen content. This trend is also found in Zr-2.5Nb, as shown in Fig. 4.22.

Fig. 4.23 and Fig. 4.24 show the change in Young's modulus with hydrogen content of Zr-1.0Nb and Zr-2.5Nb alloys, respectively.

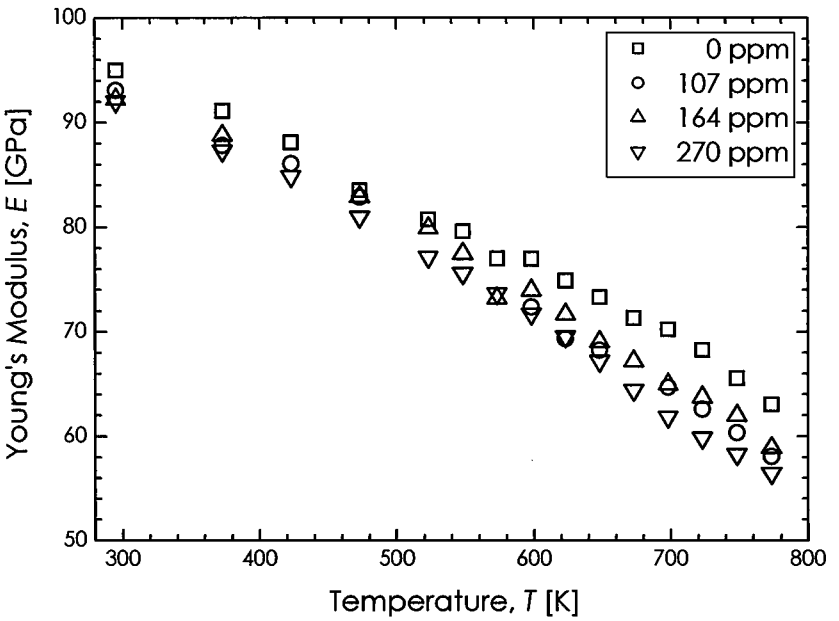


Fig. 4.21. Temperature dependence of Young's modulus of hydrogenated Zr-1.0Nb alloy.

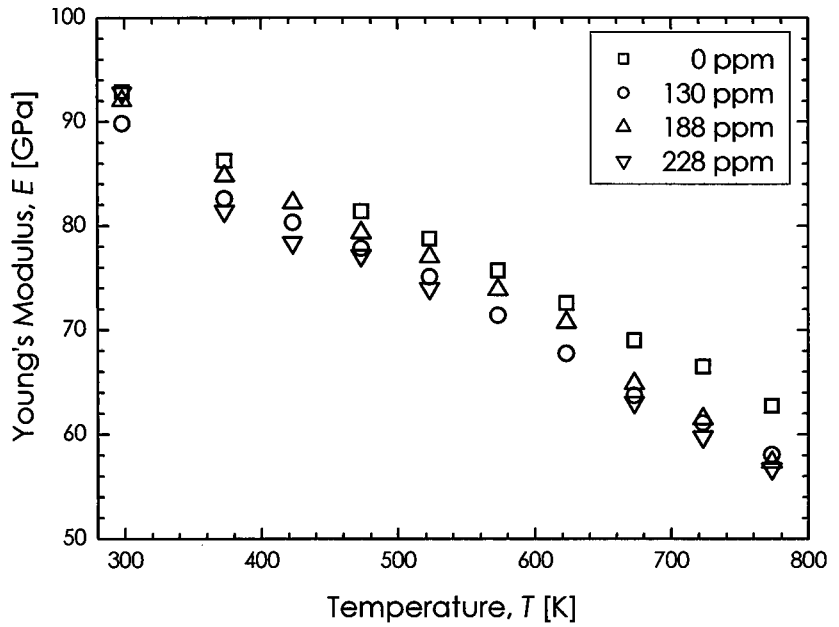


Fig. 4.22. Temperature dependence of Young's modulus of hydrogenated Zr-2.5Nb alloy.

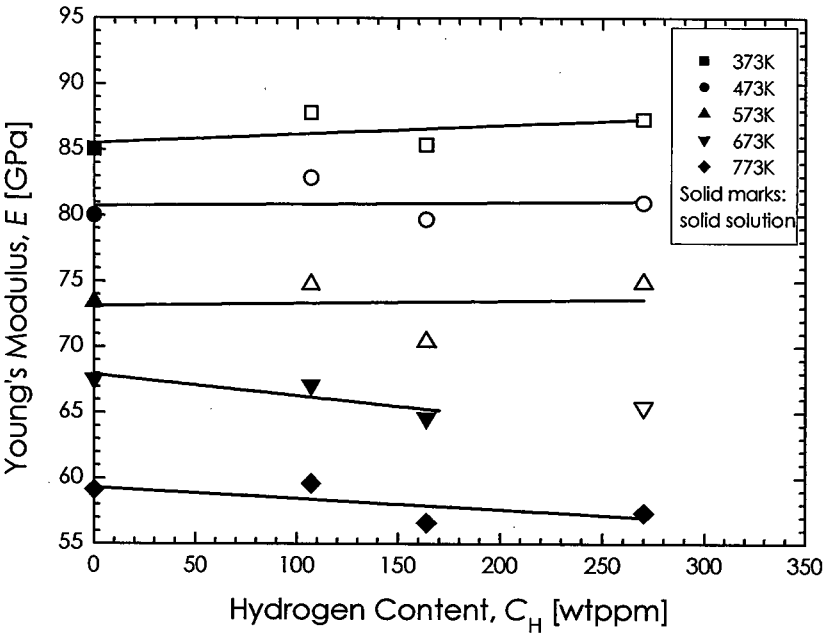


Fig. 4.23. Change in Young's modulus of Zr-1.0Nb alloy with hydrogen content.

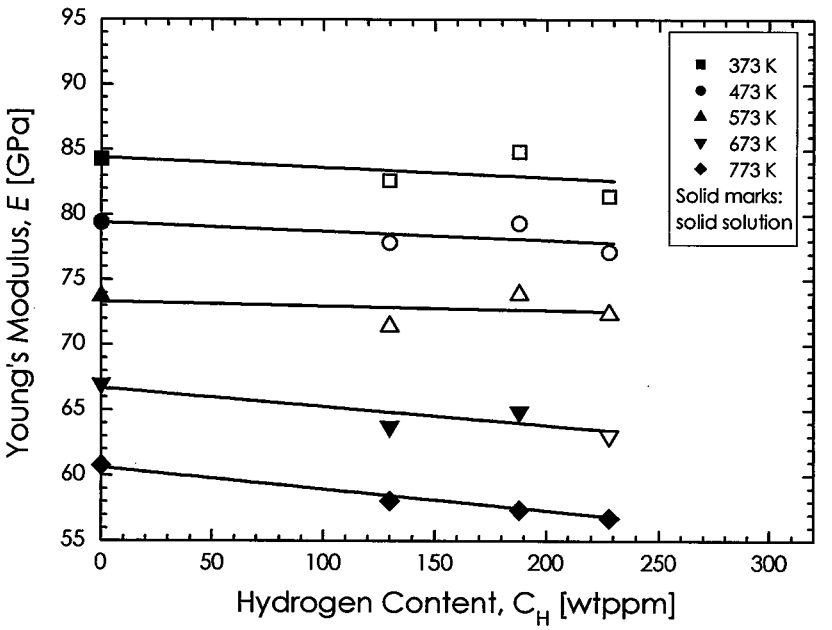


Fig. 4.24. Change in Young's modulus of Zr-2.5Nb alloy with hydrogen content.

For the solid solution it would also appear that the decreasing rates of Young's modulus against the hydrogen content are independent of the temperature. Therefore the influence of hydrogen content of the elastic moduli for the solid solution at several temperatures is compared by defining parameters E/E^0, where E^0 is Young's

modulus of the alloys without hydrogen. The E/E^0 decreased linearly with the hydrogen content, independent of temperature. The variation in Young's modulus for the solid solution with the hydrogen content is written by the following equations from the least-squares method,

$$E = E^0(1 + k_1 \times T + k_2 \times C_H) \quad (4\text{-}6)$$

where k, T, and C_H are the fitting constants, absolute temperature, hydrogen content, respectively. The variations in Young's modulus for the hydrogenated Zr-Nb alloys are written by the following equations:

$$E(\text{Zr}-1.0\text{Nb_with_Hydride}) = 94(1 - 8.2\times10^{-4} \times T + 0.7\times10^{-4} \times C_H)[\text{GPa}] \quad (4\text{-}7)$$

$$E(\text{Zr}-2.5\text{Nb_with_Hydride}) = 120(1 - 7.3\times10^{-4} \times T - 0.8\times10^{-4} \times C_H)[\text{GPa}] \quad (4\text{-}8)$$

$$E(\text{Zr}-1.0\text{Nb_with_Solute-H}) = 120(1 - 7.6\times10^{-4} \times T - 1.4\times10^{-4} \times C_H)[\text{GPa}] \quad (4\text{-}9)$$

$$E(\text{Zr}-2.5\text{Nb_with_Solute-H}) = 110(1 - 7.1\times10^{-4} \times T - 2.9\times10^{-4} \times C_H)[\text{GPa}] \quad (4\text{-}10)$$

The fitting parameters of high-temperature Young's moduli for Zr-Nb system are tabulated in Table 4.5, together with the data of zirconium hydrogen solid solutions [35].

Table 4.5. Fitting parameters of high-temperature Young's moduli for Zr-Nb system, together with the data of pure Zr hydrogen solid solutions [35].

(a) Hydrogen content region with hydride precipitant.

Material	E^0 [GPa]	$k_1 \times 10^4$ [1/K]	$k_2 \times 10^4$ [1/ppm]
Pure Zr($\alpha+\delta$)	110	-5.2	0.1
Zr1.0Nb($\alpha+\beta+\delta$)	94	-8.2	0.7
Zr2.5Nb($\alpha+\beta+\delta$)	120	-7.3	-0.8

(b) Hydrogen content region in which all the hydrogen dissolve in the metallic phase.

Material	E^0 [GPa]	$k_1 \times 10^4$ [1/K]	$k_2 \times 10^4$ [1/ppm]
Pure Zr(α)	97	-7.3	-2.7
Zr1.0Nb($\alpha+\beta$)	120	-7.6	-1.4
Zr2.5Nb($\alpha+\beta$)	110	-7.1	-2.9

In the case of the hydrogen content region that the zirconium hydride precipitates, the changing rates with hydrogen is almost zero. There is not significant difference in

the Young's modulus between α Zr and β phase Zr-20Nb. In addition, the partially precipitated hydride consists of the hydrogen solid solution phases and the hydride phase. Therefore, the Young's modulus of precipitated hydride likely influences the Young's modulus of the alloys. It is considered that the Young's modulus of the alloys which consists the hydride should slightly increase with increasing amount of hydride because the zirconium hydride has higher elastic moduli than the metal. The changing rates of the hydrogen solid solution are significantly higher than those in the region in which the hydride precipitates. The elastic moduli of pure zirconium are reduced by the solute hydrogen [35]. In addition, the solute hydrogen is found to scarcely affect the mechanical properties of β Zr-20Nb alloys as discussed above. Therefore, this reduction is due to the change of the moduli for the matrix phase.

4-4. Summary

The terminal solid solubility of hydrogen (TSS) for Zr-Nb binary alloys with different niobium concentrations, and Nb added Zircaloy-4 was measured, and the effect of niobium addition was determined in order to supply fundamental data for the integrity of new-type fuel cladding. It was found that the TSS of α Zr was not affected by the solute niobium and that the β Zr precipitant led to increase the TSS in the Zr-Nb alloys. The change in TSS by niobium addition was slightly larger than that by the traditional additive elements. The TSS of Nb added Zircaloy-4 was found to be higher than that of Zircaloy-2 and -4 due to the further effect of β Zr precipitation on top of the traditional additive element effects. Therefore, it was concluded that niobium addition to the zirconium alloys could play an important role in terms of the TSS for increasing the life-time of cladding.

The mechanical properties of hydrogenated Zr-Nb binary alloys with different phases are evaluated in order to discuss the effect of hydrogen absorption. The solute hydrogen didn't affect the mechanical properties of the single phase β Zr-20Nb alloy. In the Zr-1.0Nb and Zr-2.5Nb alloys, the solute hydrogen reduced the Young's modulus of the alloys, which was considered to be due to the change in the modulus of α Zr matrix phase. These results could be nicely accounted from the knowledge discussed in the Chapter 2 and 3.

References

[1] M. Kuroda, K. Yoshioka, S. Yamanaka, H. Anada, F. Nagase,H. Uestuka, Journal of Nuclear Science and Technology, 37 (2000) 670.

[2] T. Nishizaki, "Integrity of cladding and structural materials in nuclear reactor," PhD. Thesis, Department of Nuclear Engineering, Graduate School of Engineering, Osaka University (2002).

[3] W.H. Erickson, D. Hardie, Journal of Nuclear Materials, 13 (1964) 254.

[4] G.F. Slattery, J. Inst. Met. 95 (1967) 43.

[5] Y. Mishima, S. Ishino, S. Nakajima, Journal of Nuclear Materials, 27 (1968) 335–344.

[6] Z.L. Pan, I.G. Ritchie, M.P. Puls, Journal of Nuclear Materials, 228 (1996) 227.

[7] S. Mishra, M.K. Asundi, Zr in Nuclear Applications ASTM STP 551, American Society for Testing and Materials, (1974) 63–71.

[8] I.G. Ritchie, K.W. Sprungmann, Journal de physique, C9 (1983) 313–318.

[9] D. Khatamian, Z.L. Pan, M.P. Puls, C.D. Cann, Journal of Alloys and Compounds, 231 (1995) 488-493.

[10] D. Khatamian, V. C. Ling, Journal of Alloys and Compounds, 253 (1997) 162-166.

[11] D. Khatamian, Journal of Alloys and Compounds, 293-295 (1999) 893-899.

[12] D. Khatamian, Journal of Alloys and Compounds, 356-357 (2003) 22-26.

[13] R.W.L. Fong, S. Spooner, Scripta Metallurgica et Materialia, 30 (1994) 649.

[14]J.H. Root, R.W.L. Fong, Journal of Nuclear Materials, 232 (1996) 72–85.

[15] C.D. Cann, A. Atrens, Journal of Nuclear Materials, 88 (1980) 42–50.

[16] A. Sawatzky, B.J.S. Wilkins, Journal of Nuclear Materials, 22 (1967) 304.

[17] J.F. Freedman, A.S. Nowick, Acta Metallurgica, 6 (1958) 176.

[18] D.T. Peterson, D.G. Westlake, Transactions of the Metallurgical Society of AIME, 215 (1959) 444.

[19] D.G. Westlake, Transactions of the Metallurgical Society of AIME, 239 (1967) 1341.

[20] N.E. Paton, B.S. Hickman, D.H. Leslie, Metallurgical Transactions, 2 (1971) 2791.

[21] H.K. Birnbaum, M.L. Grossbeck, M. Amano, Journal of the Less-Common Metals, 49 (1976) 357.

[22] T. Schober, Scripta Metallurgica, 12 (1978) 549.

[23] T.B. Flanagan, W.A. Oates, S. Kishimoto, Acta Metallurgica, 31 (1983) 199-206.

[24] Y. Fukai, The Metal-Hydrogen System: Basic Bulk Properties, Springer Series in Materials Science 21 (1993).

[25] J.J. Kearns, Journal of Nuclear Materials, 22 (1967) 292.

[26] G.F. Slattery, Journal of Nuclear Materials, 32 (1968) 30.

[27] B. Cox, Journal of Nuclear Materials, 264 (1994) 283.

[28] Z.A. Matysina, S.Y. Zaginaichenko, D.V. Schur, V.K. Pishuk, Journal of Alloys and Compounds, 330-332 (2002) 85.

[29] P. Vizcaino, A.D. Banchik, J.P. Abriata, Journal of Nuclear Materials, 304(2-3) (2002) 96.

[30] K. Une, S. Ishimoto, Journal of Nuclear Materials, 322 (2003) 66.

[31] K. Une, S. Ishimoto, Journal of Nuclear Materials, 323 (2003) 101.

[32] R.N. Singh, S. Mukherjee, A. Gupta, S. Banerjee, Journal of Alloys and Compounds, 389 (2005) 102.

[33] D. Setoyama, J. Matsunaga, M. Ito, H. Muta, K. Kurosaki, M. Uno, S. Yamanaka, K. Takeda, and Y. Ishii, Journal of Nuclear Materials, 344,1-3, (2005) 291.

[34] 原子力発電技術機構燃料部, 平成 12 年度リサイクル燃料資源貯蔵施設安全性解析コード改良試験等に関する報告書 (2002).

[35] S. Yamanaka, D. Setoyama, H. Muta, M. Uno, M. Kuroda, K. Takeda, T. Matsuda, Journal of Alloys and Compounds, 372 (2004) 129–135.

[36] D. Setoyama, S. Yamanaka, Journal of Alloys and Compounds, 379 (2004) 193–197.

[37]D. Setoyama, J. Matsunaga, H. Muta, M. Uno, S. Yamanaka, Journal of Alloys and Compounds, 385 (2004) 156–159.

[38] B.A. Cheadle, C.E. Coleman, H. Litcht, Nuclear Technology, 57 (1982) 413.

[39] E.F. Ibrahim, B.A. Cheadle, Canadian Metallurgical Quarterly, 24 (1985) 273.

[40] C. Lemaignan, A.T. Motta, Nucl. Mater. 10B (1994) 1.

[41] W. Dietz, Nucl. Mater. 10B (1994) 53.

[42] D. Srivastava, G.K. Dey, S. Banerjee, Metallurgical Transactions, 26A (1995) 2707.

[43] S.A. Nikulin, V.I. Goncharov, V.A. Markelov, V.N. Shishov, Zirconium in the Nuclear Industry, ASTM STP 1295 (1996) 695-709.

[44] V.F. Urbanic, M. Griffiths, Zirconium in the Nuclear Industry, ASTM STP 1354 (2000) 695-709.

[45] L. Lanzani, M. Ruch, Journal of Nuclear Materials, 324 (2004) 165-176.

[46] K.L. Murty, I. Charit, Progress in Nuclear Energy, 48 (2006) 325-359.

[47] McMinn, E.C.Darby, J.S.Schofield, Zirconium in the Nuclear Industry: Eleventh Int. Symp., ASTM STP 1295 (1997) 338

[48] Y. Takahashi, M. Asou, Thermochimica Acta, 223 (1993) 7.

[49] A.F. Guillermet, Zeitschrift für Metallkunde, 82 (1991) 478.

[50] M. Mizuno, I. Tanaka, H. Adachi, Physical Review, B59 (1999) 15033.

CHAPTER 5

Finite Element Analysis of Hydrogen Behavior in LWR Cladding under Gradients of Hydrogen, Temperature, and Stress

Chapter 5.
Finite Element Analysis of Hydrogen Behavior in LWR Cladding under Gradients of Hydrogen, Temperature, and Stress

5-1. Introduction

As a result of power ramp tests of high burnup Boiling Water Reactor (BWR) fuels, Simada et al [1, 2] reported that breakage failures of the claddings appeared in a different form from those of the past and the power level for failure consequently decreased. Their observations revealed that cracking was initiated from outside of the cladding tubes and penetrated inwards, as shown in Fig. 5.1(a). On the contrary, several outside cracks were generated but stopped during the power ramp test of high burnup fuel cladding of Pressurized Water Reactor (PWR), as shown in Fig. 5.1(b). In order to continue the burnup extension, it is necessary to clarify the outside-in failure condition of the claddings and validate current methods of safety evaluation.

It is considered that the failure process started with an axial split by cracking of radial hydrides which were formed during the power ramp test, followed by propagation caused by step-by-step cracking of hydrides at a crack tip [1]. Fig. 5.2 shows the estimated process of the failure in high burnup fuel cladding. This process is generally called as delayed hydride cracking (DHC) [3–6], which is based on diffusion of hydrogen to the crack tip with higher tensile stress, followed by hydride nucleation, its growth, and fracture of the hydride. Iterations of these processes are considered to promote the crack propagation through the cladding materials. The crack velocity depends on time required for hydrogen to accumulate enough for growing to hydride precipitate that has critical size for breaking. Therefore, hydrogen diffusion to the crack tip from surrounding area is one of the most important factors for these processes. However, the hydrogen behavior in the fuel cladding during operation is affected by the conditions varying from hour to hour, thus being quite complex. For example, Pellet-Cladding Mechanical Interaction (PCMI) is one of the concerns related the high burn-up [7–11]. During power transients, the possibility of PCMI increases due to the narrowing gap between the pellet and cladding. In addition, in-situ measurements of crack propagation in the claddings are difficult. Therefore, it is hard to evaluate the mechanism of the DHC process only from the experimental work. Parametrical study by computer simulations should make a significant contribution to mechanism assessment of the failure process.

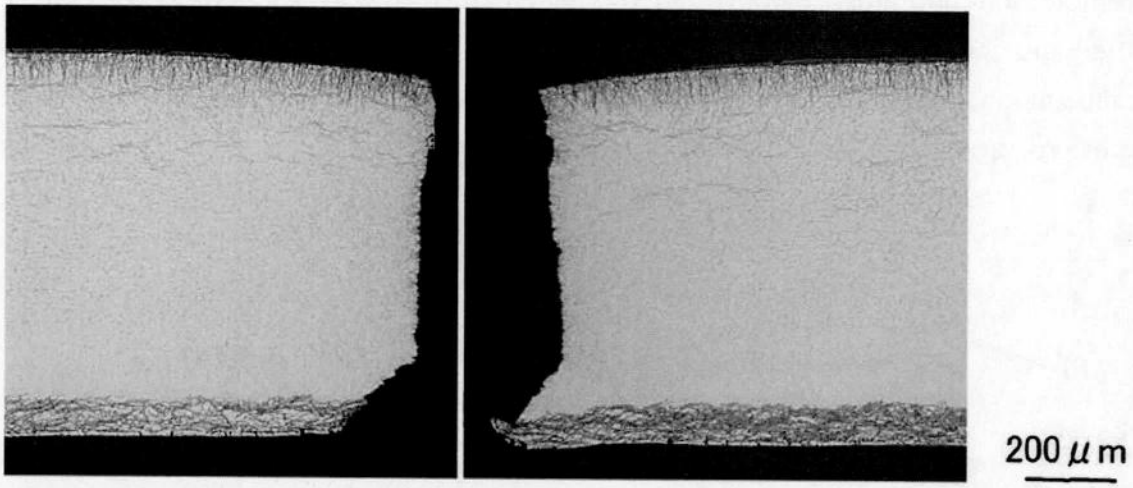


Fig. 5.1(a). Transverse view of out-side in cracking fracture of high burnup BWR cladding [1].

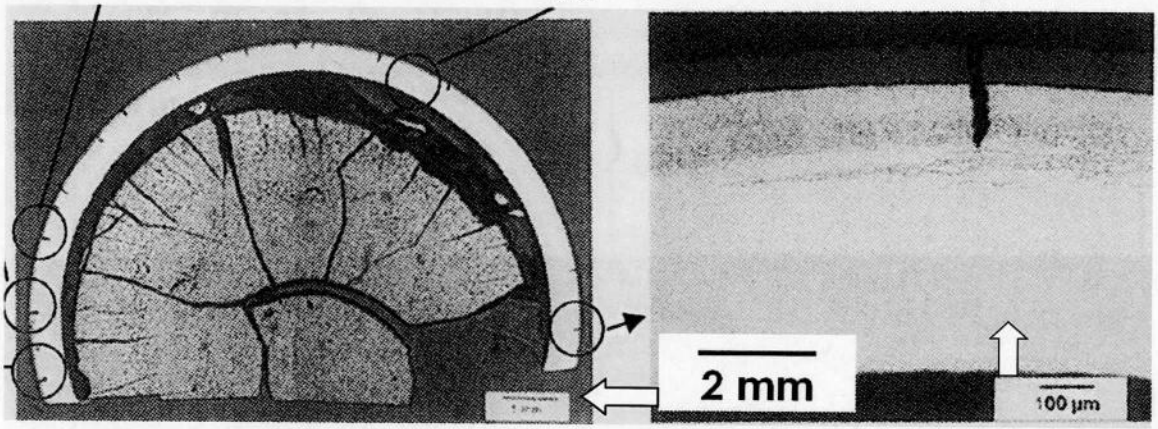


Fig. 5.1(b). Transverse view of high burnup PWR cladding after power ramp test [2].

Experimental investigations on the hydrogen diffusion behavior of zirconium alloys have been performed. Diffusion coefficient of hydrogen in the zirconium alloys are reported by number of researchers [12–17]. The redistribution of hydrogen in Zry-2 under temperature gradient was also evaluated by Sawatzky [18] and Markowitz [19]. As far as the author knows, there is only one research that quantitatively measured the hydrogen migration due to stress gradient in the zirconium alloys [20]. Recently, investigations on numerical analysis of hydrogen diffusion under stress and temperature gradient for the zirconium alloys were reported by several researchers [21–24].

In this chapter, transient hydrogen diffusion analysis which considered three effects of distributions of hydrogen concentration, temperature, and stress were performed

using finite element method (FEM) under the conditions of power ramp tests. Temperature and stress distributions of modeled claddings with cracks were calculated. Then, the calculated results of the distributions were used as condition for the hydrogen diffusion analysis to crack tip. The effects of several parameters, such as internal pressure, crack number, and its depth, were evaluated.

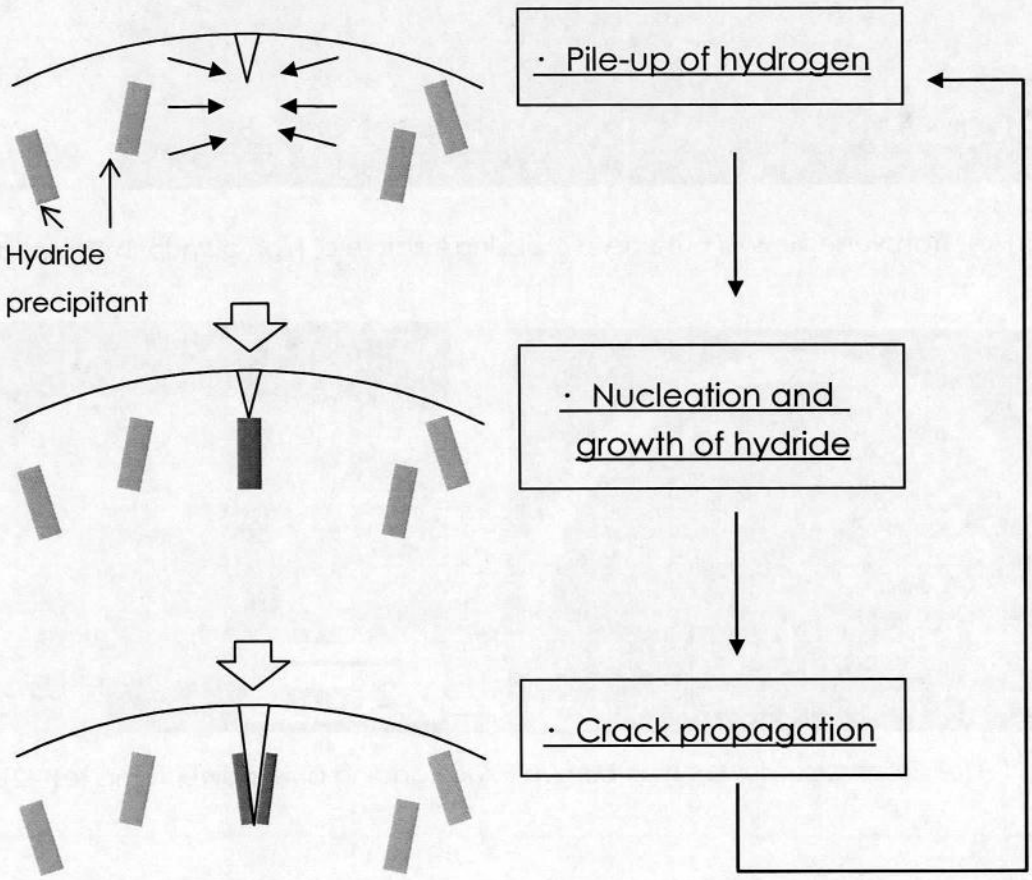


Fig. 5.2. Estimated process of the failure in high burnup fuel cladding.

5-2. Calculation

5-2-1. Finite Element Models

ABAQUS ver. 6.5 is used for the present finite element calculations. Fig. 5.3 shows the two-dimensional models and boundary conditions which were used in present calculations. Second-order isoparametric elements were used, in which corner and middle nodes are numbered, as shown in Fig. 5.4. The fuel claddings with/without outside cracks were simulated. Fig. 5.5 shows the simulated crack which have semicircular tip 1 μm in diameter. The stress gradient near crack tip would be quite sharp. Therefore, the mesh was finely divided as it approached the tip. Table 5.1 shows the thermophysical properties of postirradiated Zry-2 used in the present study [25]. Fig. 5.6 shows the hydrogen solubility used in the present calculation, which is obtained by the extrapolation of the high-temperature literature values by Yamanaka [26].

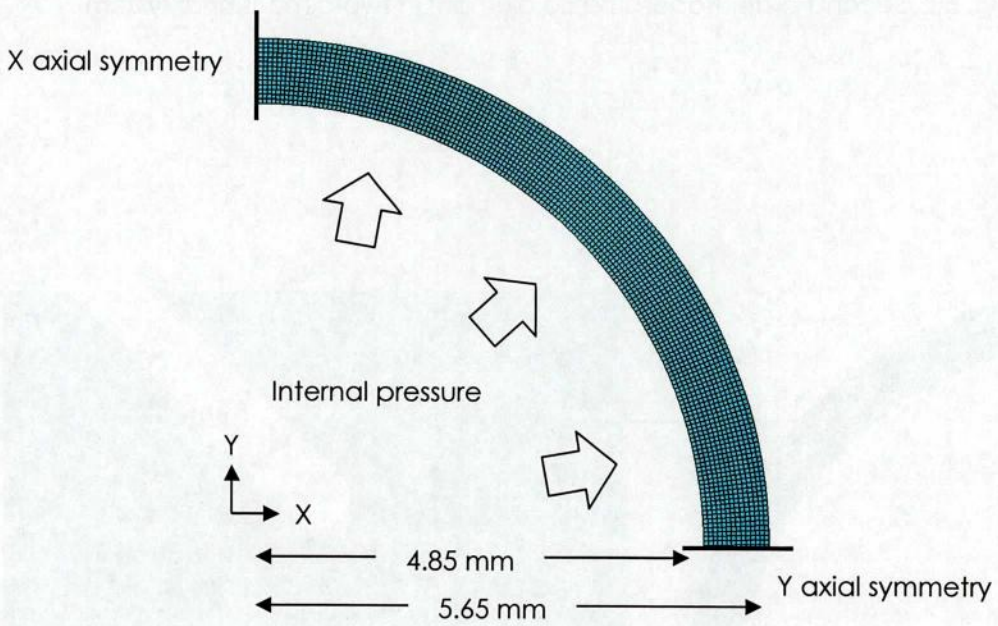


Fig. 5.3. Computational system and boundary conditions of present calculation.

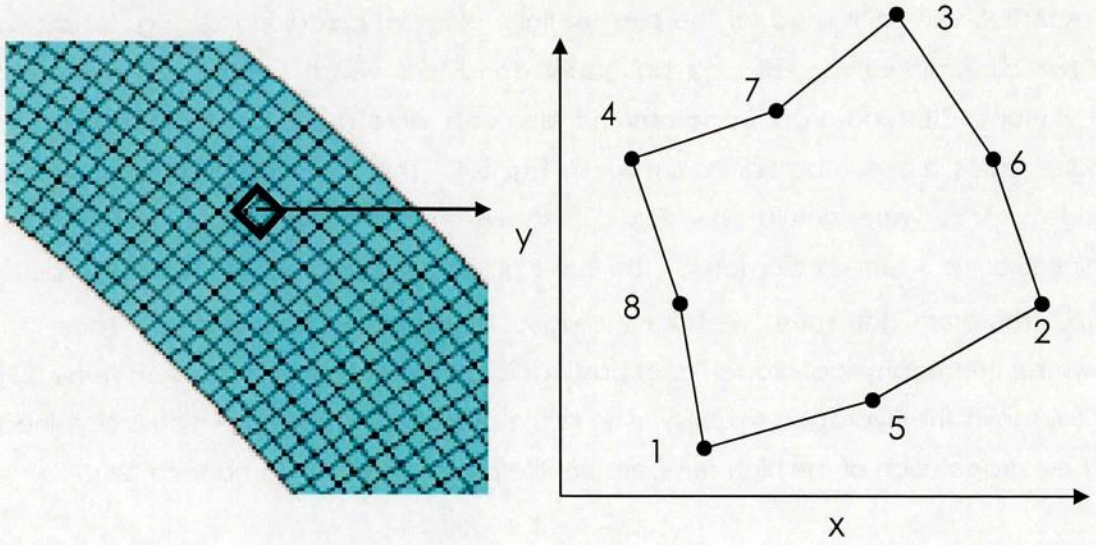


Fig. 5.4. Second-order isoparametric element in two-dimensional system.

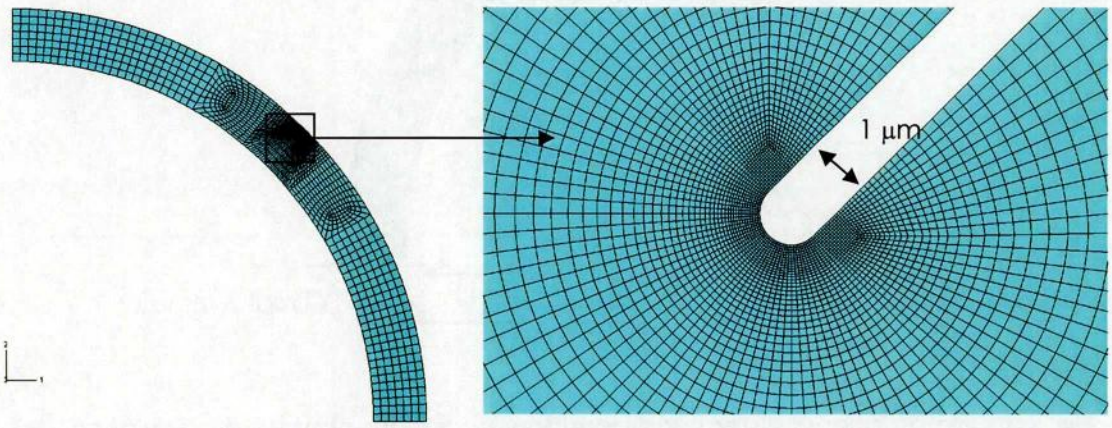


Fig. 5.5. Simulated outside crack and divided meshes in its surroundings.

Table 5.1. Thermophysical properties of postirradiated Zry-2

Temperature [K]	Young's modulus [MPa]	Poisson's Ratio [-]	Thermal conductivity [W/m/K]	Density [kg/m^3]	Linear thermal expansion coefficient [-]
298	97100	0.3676	11.28	6510	5.96×10^{-6}
773	68150	0.3311	17.46		

Temperature [K]	Specific heat capacity [J/kg/K]
273	288.7
529	324.5
745	343.5

Temperature [K]	Stress [MPa]	Plastic strain [-]	Temperature [K]	Stress [MPa]	Plastic strain [-]
298	370.3	0.00	616	150	0.00
298	405	0.02	616	210	0.02
298	436.3	0.05	616	230.3	0.05
298	473.3	0.116	616	251.5	0.097

In order to validate the modeling of crack, stress intensity factors for cracks of the same shape on flat plate were calculated and were compared with analytical solutions [27]. Fig. 5.7 (a) and (b) show the Mises stress distribution near the crack and the calculated stress intensity factors together with the analytical solutions, respectively. The calculated values are good accordance with the analytical solutions. Therefore, the modeling of cracks viz. the shape of crack and mesh division was considered to be appreciate.

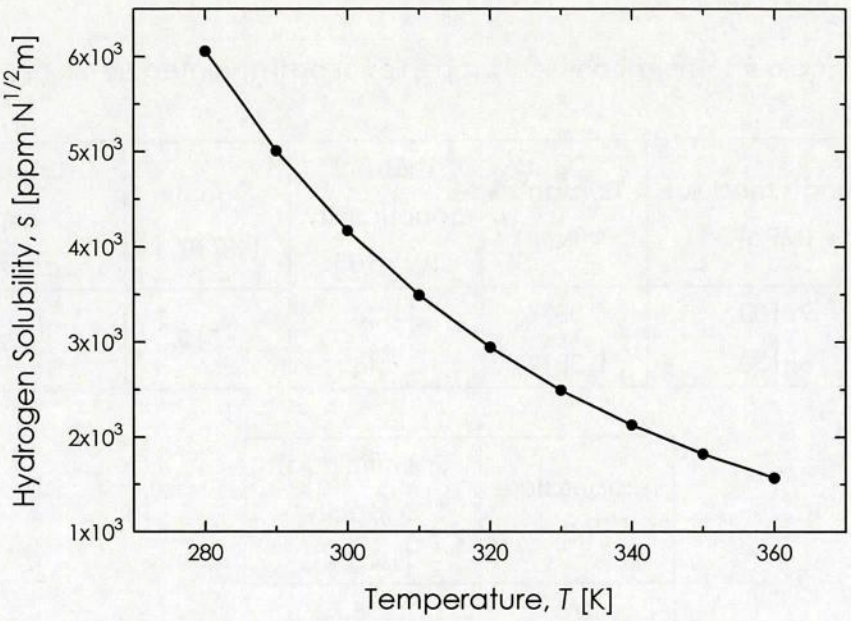


Fig. 5.6. Temperature dependence of hydrogen solubility of Zry-2 [26].

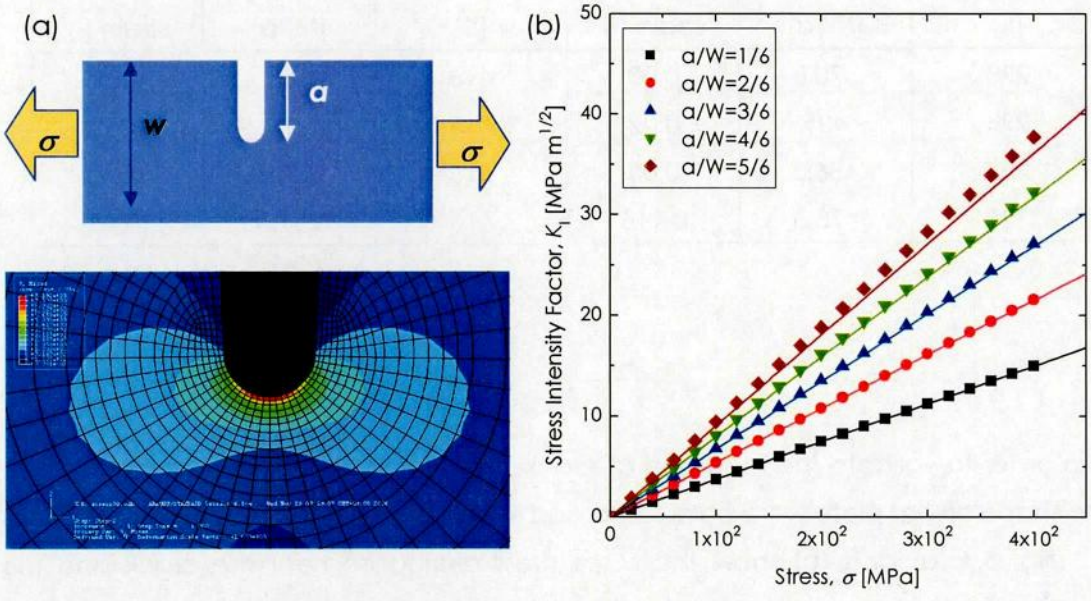


Fig. 5.7. (a) Flat plate with crack and distribution of the Mises stress near the crack tip for validation of the present crack modeling, (b) Calculated stress intensity factor together with the analytical solutions.

5-2-2. Theory of Hydrogen Diffusion Analysis

The diffusion is assumed to be driven by the gradient of a chemical potential of hydrogen. The chemical potential is defined as a partial differentiation of free energy. Gibbs free energy is defined as follows:

$$G \equiv E - TS + PV \tag{5-1}$$

where E, T, S, P, and V are internal energy, absolute temperature, entropy, pressure, and volume, respectively. The E and S of metal-hydrogen system are evaluated by classical theory as follows:

$$E = E_{METAL} + C_H E_H + C_H \cdot \Delta E_{M\text{-}Hbond} \tag{5-2}$$

$$S = S^{vib}_{METAL} + C_H S^{vib}_H + C_H \cdot \Delta S_{M\text{-}Hbond} + R \ln \frac{N!}{n!(N-n)!} \tag{5-3}$$

E_{METAL}, E_H : Molar energy of pure metal and hydrogen

S^{vib}_{METAL}, S^{vib}_H : Molar entropy of metal and hydrogen vibration

C_H : Hydrogen content

$\Delta E_{M\text{-}Hbond}$, $\Delta S_{M\text{-}Hbond}$: Change in molar energy and entropy due to creation of M-H bonds

R : Gas constant

N : Number of interstitial sites for hydrogen in lattice

n : Number of occupied sites in N

The present calculations were performed on the assumption that Sieverts' law holds. In other words, $\Delta E_{M\text{-}Hbond}$ and $\Delta S_{M\text{-}Hbond}$ are assumed to be independent of hydrogen content. In that case, we can get the chemical potential of hydrogen as follows:

$$\begin{aligned}
\mu_H &= \left(\frac{\partial G}{\partial C_H}\right) \\
&= (E_H + \Delta E_{M\text{-}Hbond}) - T \cdot (S^{vib}_H + \Delta S_{M\text{-}Hbond}) + RT \ln C_H + P\bar{V}_H \\
&= RT \ln Ks + RT \ln C_H + P\bar{V}_H \\
&= RT \ln \left(\frac{p^{1/2}}{C_H} \cdot \frac{1}{p_0^{1/2}} \right) + RT \ln C_H + P\bar{V}_H \\
&= \mu_0 + RT \ln (C_H / s) + P\bar{V}_H
\end{aligned} \tag{5-4}$$

$\bar{V}_H$: Partial molar volume of hydrogen

Ks : Sieverts' constant

p : Equilibrium hydrogen pressure at C_H

p_0 : Standard hydrogen pressure

μ_0 : Chemical potential of hydrogen at standardized condition

s : Solubility of hydrogen

The governing equations for hydrogen diffusion are an extension of Fick's equation, to allow for nonuniform solubility of the hydrogen in material. Using the Fick's equation and the equation (5-4), hydrogen diffusion flux J is calculated as follows:

$$\begin{aligned} J &= -\frac{C_H D}{RT}\cdot\frac{\partial \mu_H}{\partial x} \\ &= -\frac{C_H D}{RT}\cdot\left(\frac{RT}{C_H}\cdot\frac{\partial C_H}{\partial x} + R\ln(C_H/s)\cdot\frac{\partial T}{\partial x} + \bar{V}_H\cdot\frac{\partial P}{\partial x}\right) \\ &= -D\left(\frac{\partial C_H}{\partial x} + \frac{C_H\cdot\ln(C_H/s)}{T}\cdot\frac{\partial T}{\partial x} + \frac{C_H\cdot\bar{V}_H}{RT}\cdot\frac{\partial P}{\partial x}\right) \\ &= -D\left(\frac{\partial C_H}{\partial x} + k_1\cdot\frac{\partial T}{\partial x} + k_2\cdot\frac{\partial P}{\partial x}\right) \end{aligned} \tag{5-5}$$

where the D is hydrogen diffusion coefficient and k is proportional coefficient. In this equation, the first, second, and last terms contribute to the diffusion due to gradients of hydrogen content, temperature, and hydrostatic pressure, respectively. Based on the temperature dependence of hydrogen solubility and the partial molar volume of hydrogen, the proportionary coefficients k_1 and k_2 can be calculated. On the contrary, the hydrogen distribution due to temperature gradient is often measured for respective materials under steady state condition without stress. In that case, the Fick's equation can be expressed as follows:

$$\frac{\partial C_H}{\partial x} = -Q^*\cdot\frac{\partial T}{\partial x} \tag{5-6}$$

where Q^* is heat of hydrogen transport. In the present study, literature data of the Q^* =25.12 kJ/mol [18] is employed. Therefore, the equation (5-5) is rewritten as follows:

$$J = -D\left(\frac{\partial C_H}{\partial x} + Q^*\cdot\frac{\partial T}{\partial x} + k_2\cdot\frac{\partial P}{\partial x}\right) \tag{5-7}$$

Ideally speaking, the coefficient k_2 should be also measured because it's not always true that the heat of hydrogen transport Q^* equals to the calculated coefficient k_1. Since terminal solid solubility of hydrogen in zirconium alloys at around 600 K is quite low, there is insufficient experimental information on the hydrogen partial molar volume of them. The hydrogen partial molar volume for hcp metals is commonly about $3.0\,nm^3/(H/M)$ [28], which is adopted for calculating the coefficient k_2.

5-2-3. Analysis Procedure

The distributions of temperature and stress are required as initial field conditions for

the hydrogen diffusion analysis including the three effects of hydrogen concentration, temperature, and stress. Firstly, thermal-displacement coupled FEM calculations for the irradiated Zry-2 with crack simulating the power ramp tests were performed. Secondly, using the calculation results as the field condition, the transient analysis of hydrogen diffusion was performed.

Table 5.2 shows the boundary conditions used in the present calculations. Based on information of the power ramp test, inside and outside temperature of the cladding were fixed on 613 K and 573 K, respectively. Different parameters were employed in these calculations and influences of the parameters were elucidated. It is worth noting that the internal pressure of the BWR cladding is ranging from 1 to 4 MPa in the case of ordinal operation but much further stress is assumed to be locally applied from inner surface by the PCMI during the serious tests. By using different values of the internal pressure ranging from the 5 to 50 MPa, the present analysis simulated the case. In order to discuss the behavior of crack propagation due to the DHC, the calculations were performed for different crack lengths and numbers.

Table 5.2. Conditions of stress and hydrogen diffusion analysis.

Internal/External surface temperature (K)	613 / 573
Internal pressure (MPa)	0 ~ 50
Depth of crack (μm)	0 ~ 200

5-3. Results and Discussion

5-3-1. Stress and Strain Distribution of Fuel Cladding with Crack

Fig. 5.8 shows calculation results of hydrostatic pressure for a model without crack; (a) Contour map, (b) Radial directional distribution, (c) Dependence on internal pressure at inner and external surfaces. The hydrostatic pressure linearly decreases with increasing the distance from the inner surface even in the case that the internal pressure equals to zero due to the temperature gradient. The hydrostatic pressure has negative values except for the pressure inside of middle line of the cladding at 0 MPa of the internal pressure, and its absolute values increase by loading the internal pressure. There are two inflection points in the dependence on internal pressure: one is near 25 MPa of internal pressure and the other is near 35 MPa. The former is due to beginning of

plastic deformation and the latter is due to modulation in the true stress-true plastic strain curve. Tensile stress increases with increasing the distance from the inner surface. Therefore, hydrogen in the cladding diffuses towards outside due to not only the temperature gradient but also the stress gradient even when the cladding is smoothly shaped.

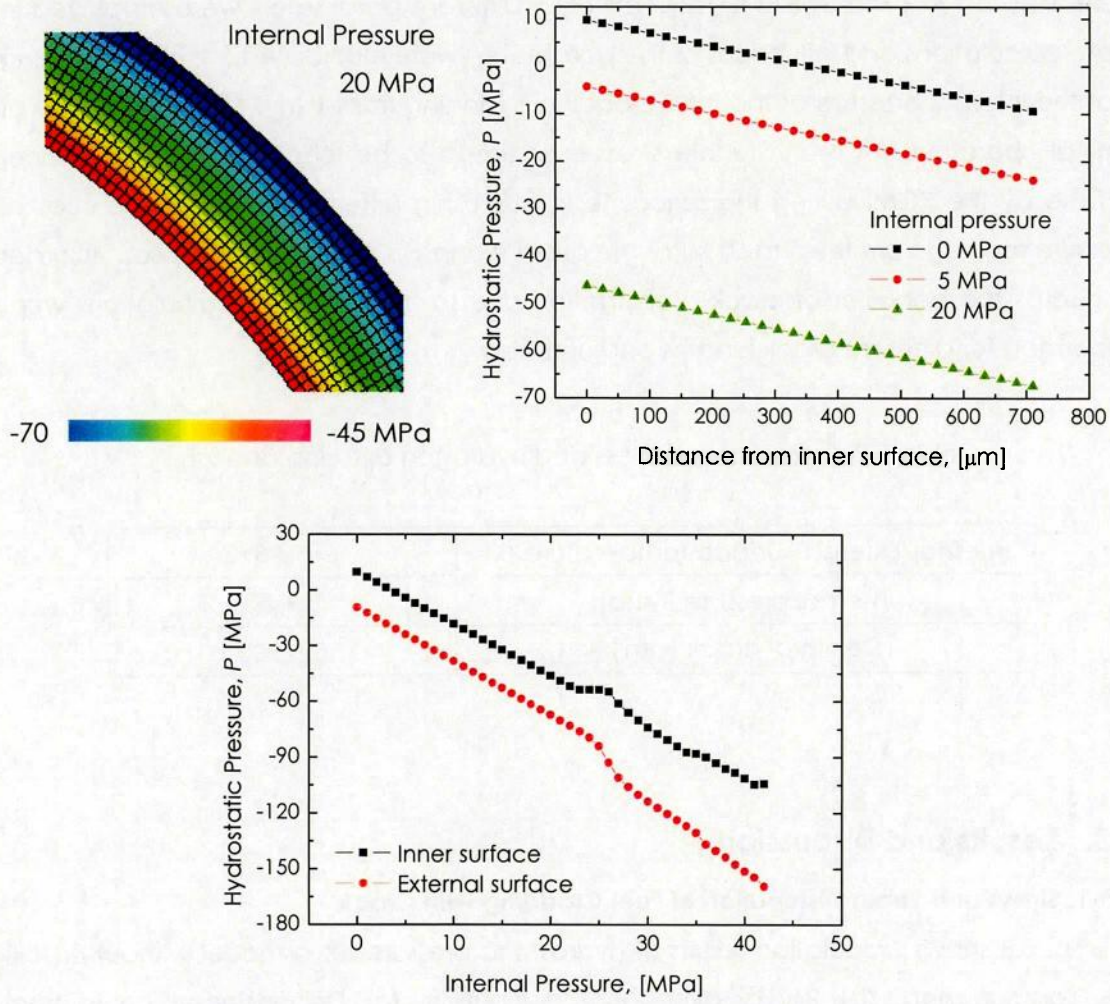


Fig. 5.8. Calculation results of hydrostatic pressure for a model without crack (a) Contour map, (b) Radial directional distribution, (c) Dependence on internal pressure.

Fig. 5.9 shows contour maps of radial stress near crack tips with different lengths. The internal pressure of all the case equals to 5 MPa. The crack length increases the

stress value and stress-focusing area near crack tip, although its distribution profile was not changed so much by the crack length.

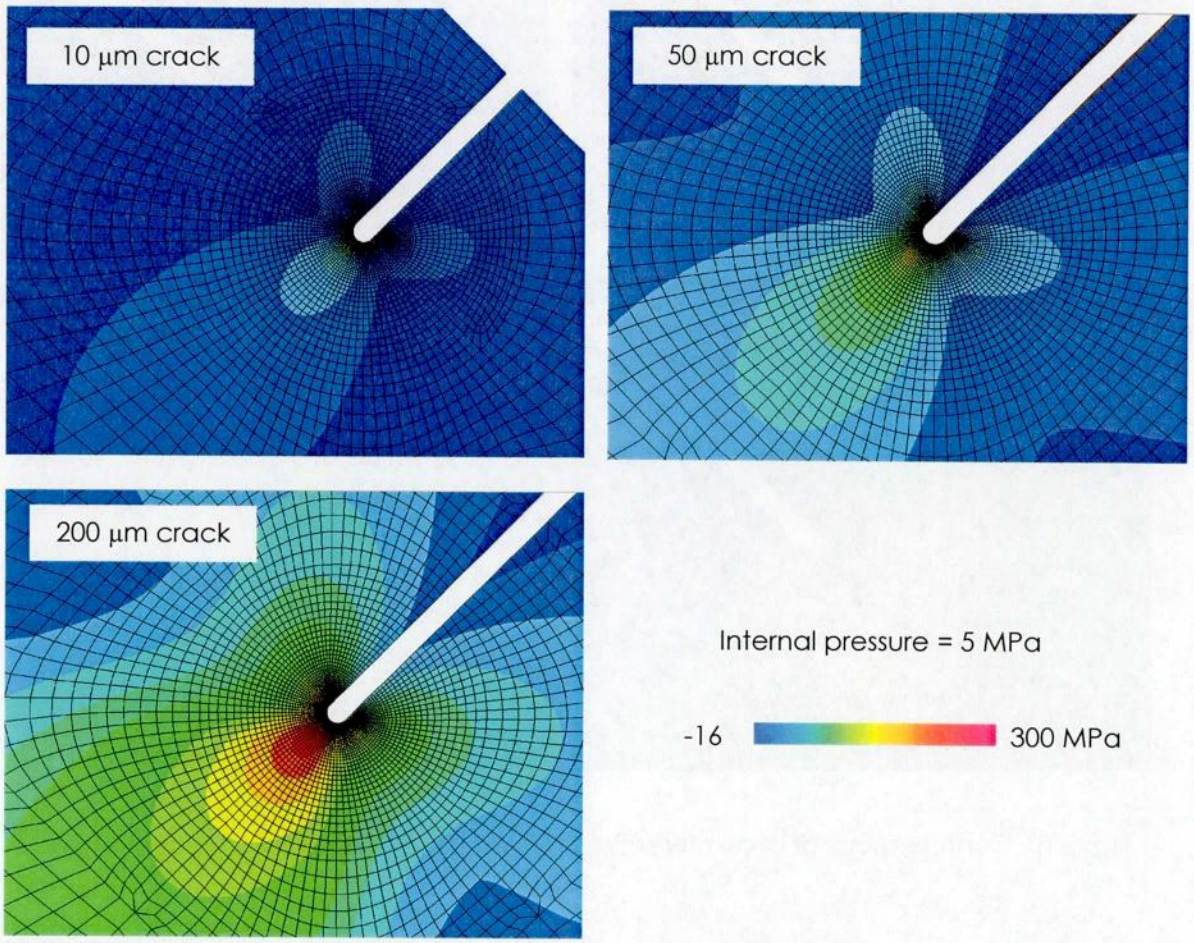


Fig. 5.9. Contour maps of radial stress near crack tips with different lengths.

Fig. 5.10 shows the contour maps of circumferential stress for the same case. It is found from this figure that there is quite higher tensile stress in circumferential direction around the crack tip than radial direction. Similar to the case of radial stress, the crack length increases the stress value and stress-focusing area near crack tip.

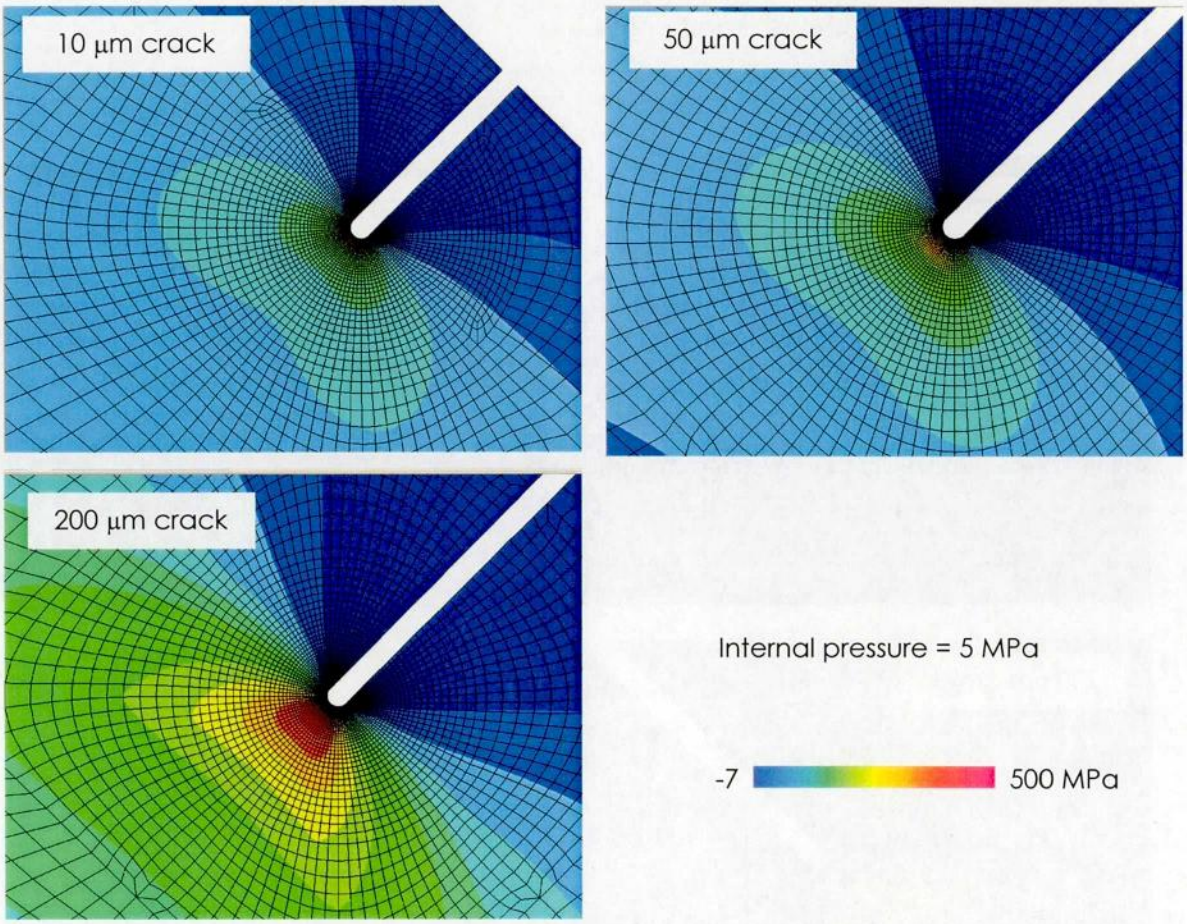


Fig. 5.10. Contour maps of circumferential stress near crack tips with different lengths.

The contour map of hydrostatic pressure that is mean value of their stresses is shown in Fig. 5.11. As has been mentioned in section 2.2, the hydrostatic pressure is responsible for the hydrogen diffusion to the crack tip. It is found from this figure that negative hydrostatic pressure spreads in a circular pattern around the crack tip. In addition, vicinity of crack surface that is slightly away from the tip has low positive hydrostatic pressure. This supposes that negative hydrostatic pressure field near crack tip, in which hydrogen piles up, shifts to the positive field when the crack would proceed. Therefore, hydrogen is considered to easily diffuse from the crack surface to the tip. It is also found that an absolute value of the hydrostatic pressure near the crack tip is quite higher than that in the smoothly shaped cladding.

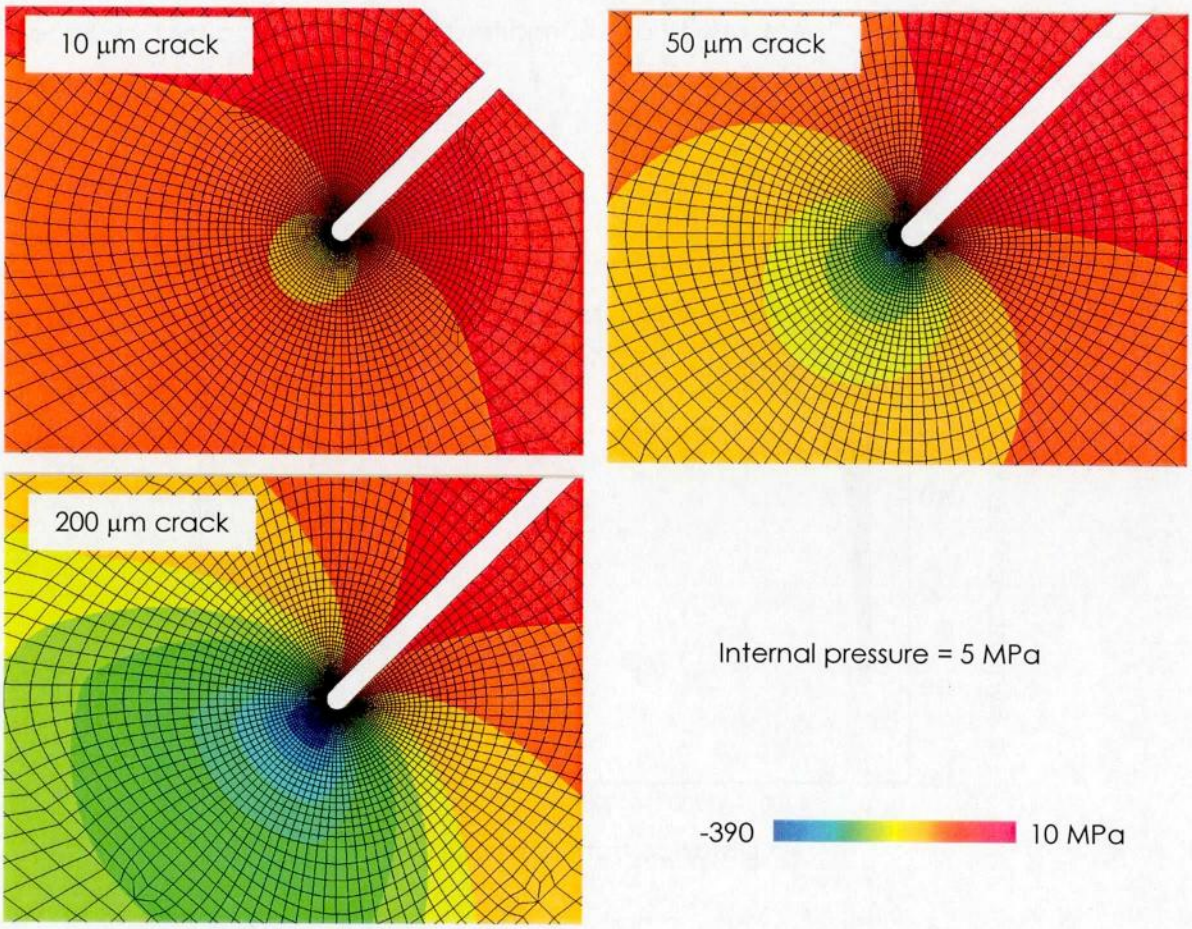


Fig. 5.11. Contour maps of hydrostatic pressure near crack tips with different lengths.

Fig. 5.12 shows the radial directional distributions of hydrostatic pressure from tips of 50 μm crack with different internal pressures. The downside is a magnified drawing near the crack tip. The hydrostatic pressure increases with increasing the internal pressure. In the case of 50 μm crack, this trend is especially-pronounced within about 100 μm distance from the crack tip. A maximum point of the hydrostatic pressure is a few micro-meters distantly-positioned from the tip. This is because the cladding near the crack tip is plastically-deformed where highly focused stress is relaxed.

Fig. 5.13 shows the radial directional distributions of hydrostatic pressure from crack tips with different lengths, in which the internal pressure is fixed to 20 MPa. The downside is again a magnified drawing near the crack tip. The hydrostatic pressure and stress-focusing area around crack tip increases with increasing the crack length. Especially in the 200μm crack, the hydrostatic pressure shifts from negative to positive

towards inner side of cladding, hence hydrostatic pressure gradient is widely spreading across the cladding. These results are considered to profoundly affect hydrogen behaviors.

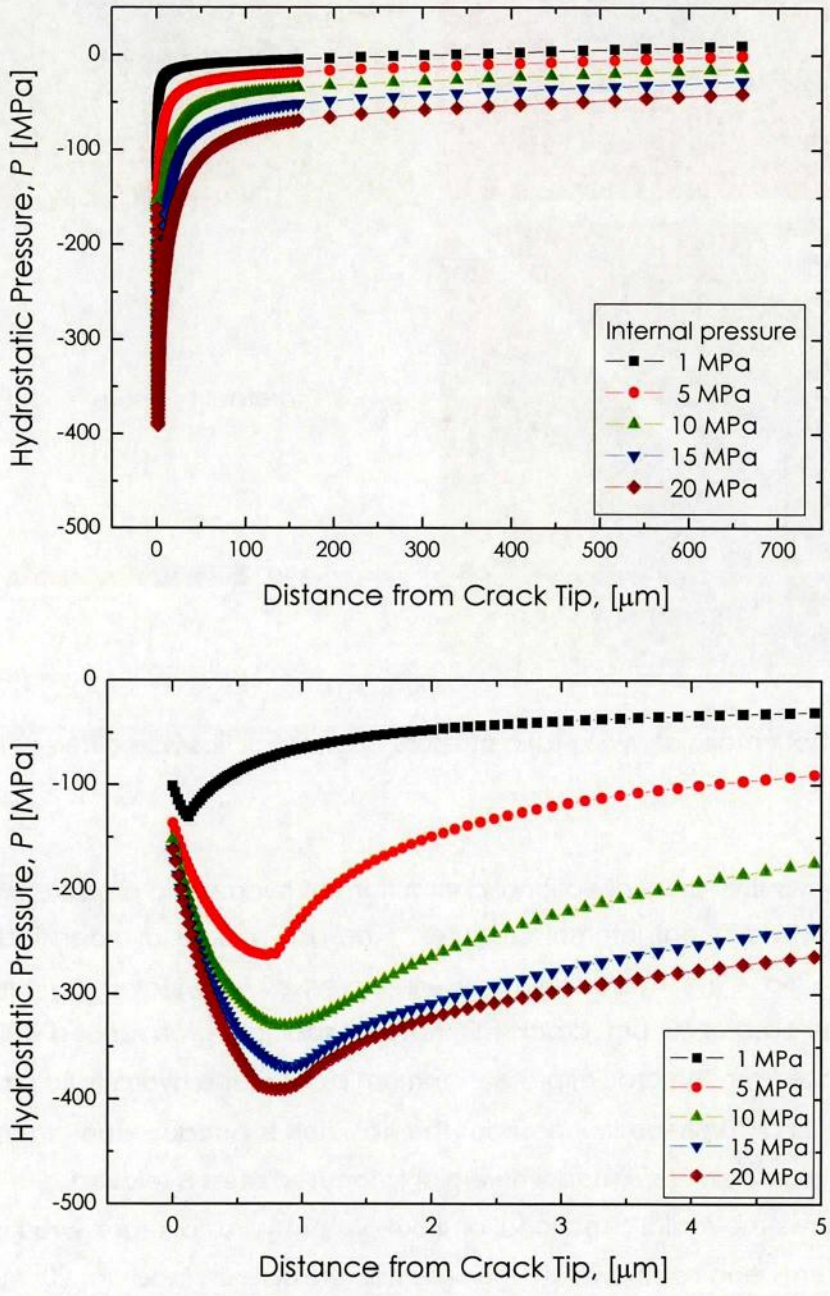


Fig. 5.12. Radial directional distributions of hydrostatic pressure from tips of 50 μm crack with different internal pressures.

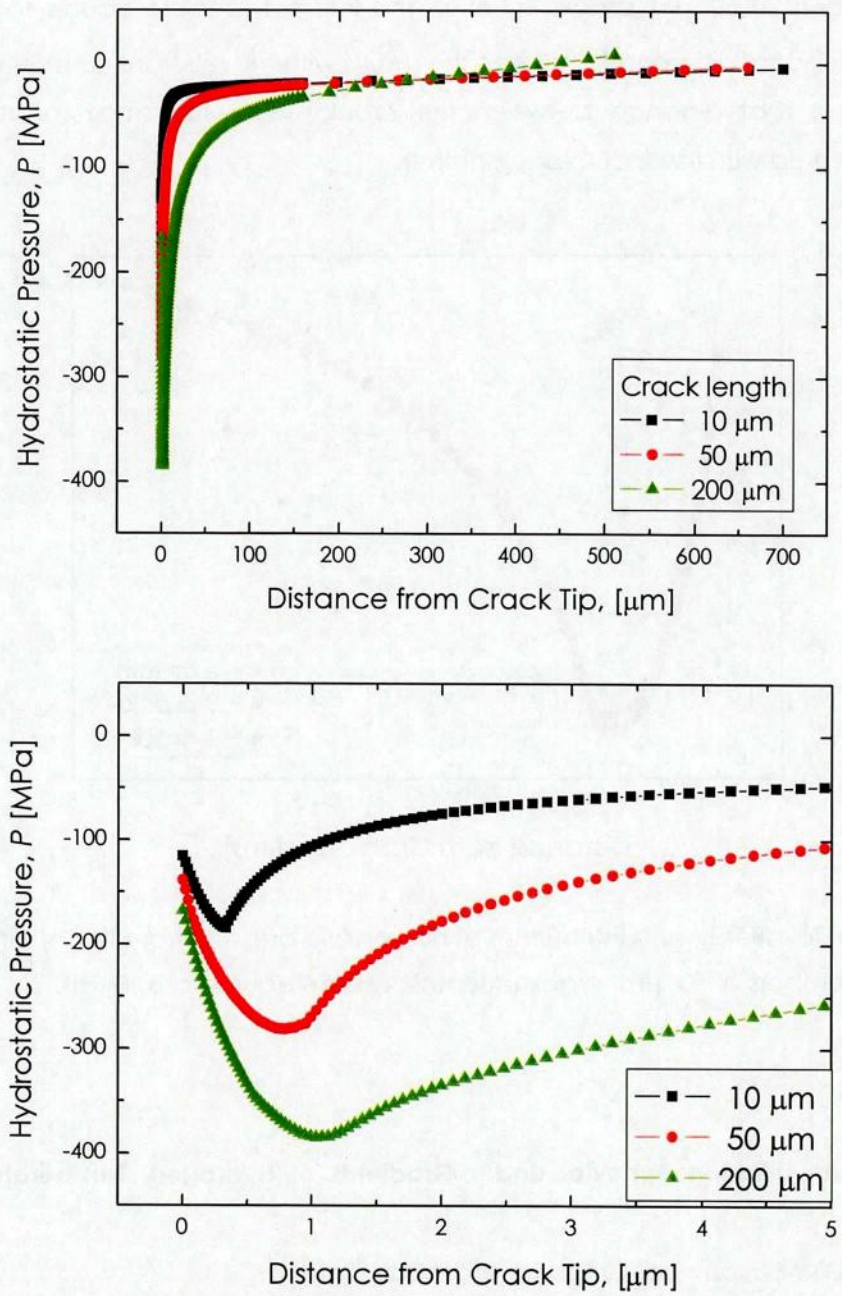


Fig. 5.13. Radial directional distributions of hydrostatic pressure from crack tips with different lengths (Internal pressure equals to 20 MPa).

Fig. 5.14 shows radial directional distributions of hydrostatic pressure from tips of different numbers of 50 μm crack, in which the internal pressure equals to 20 MPa. There is not significant difference between the results with the different number of cracks. It is considered that distance between the cracks were too small to affect the stress-focusing area with respect to one another.

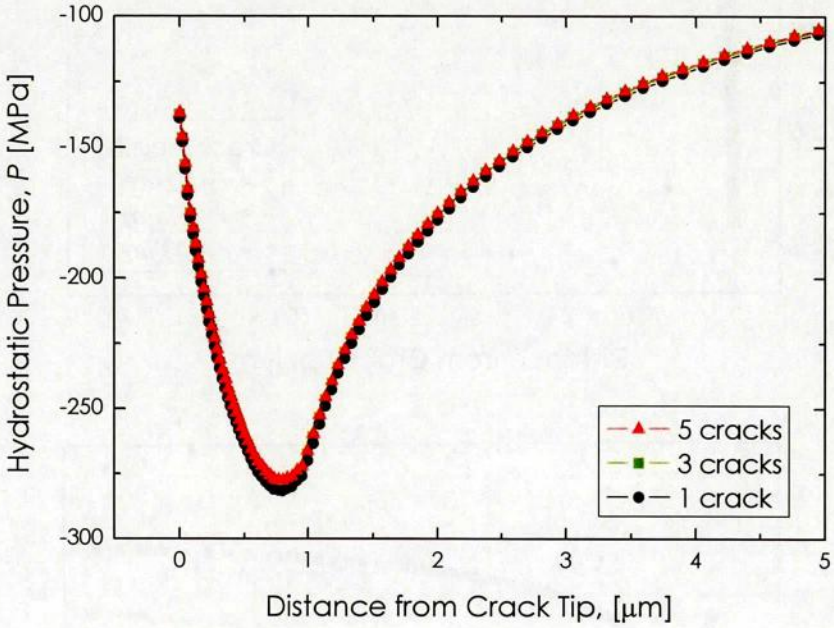


Fig. 5.14. Radial directional distributions of hydrostatic pressure from tips of different numbers of 50 μm crack (Internal pressure equals to 20 MPa).

5-3-2. Hydrogen Diffusion Behavior under Gradients of Hydrogen, Temperature, and Stress

(a) Hydrogen Distribution near Crack Tip at Steady State

Hydrogen diffusion behaviors were evaluated using the calculation results obtained in section 3.1 as field conditions. In order to discuss the effect of stress, hydrogen diffusion due to temperature gradient was analyzed and its result was used as initial hydrogen distribution. Since a zirconium liner on inner surface of the BWR cladding contains a larger amount of hydrogen than Zry-2, the zirconium liner can be a source of hydrogen. Therefore, the hydrogen diffusion analysis was performed on the boundary condition that hydrogen content of inner surface is fixed to 100 ppm. Fig. 5.15 (a) shows the contour map of hydrogen content near tip of 50 μm crack at initial state.

The hydrogen content of external side is higher than that of inner side because the hydrogen solubility of zirconium decreases with increasing temperature. In the present boundary condition, mean value of hydrogen content in the cladding approximately equals to 180 ppm.

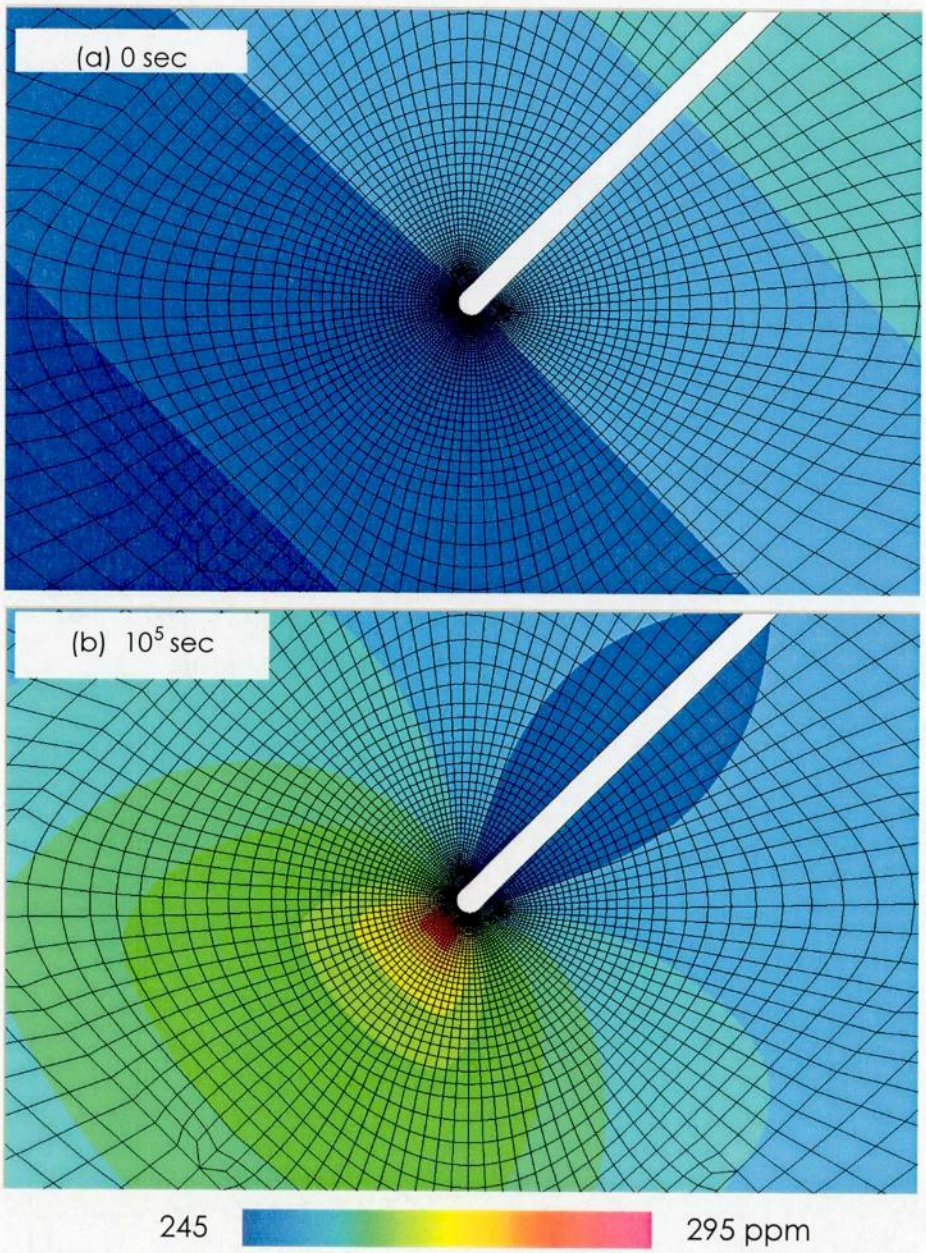


Fig. 5.15. Change in contour map of hydrogen content near tip of 50 μm crack with internal pressure of 5 MPa (a) Initial state, (b) Equilibrium state after the internal pressure loading.

Fig. 5.15 (b) shows the contour map of hydrogen content near tip of 50 μm crack with internal pressure of 5 MPa at equilibrium state after the internal pressure loading. It is found from this figure that the hydrogen distribution after the internal pressure loading is noticeably different from the initial state and a large amount of hydrogen piles up near the crack tip.

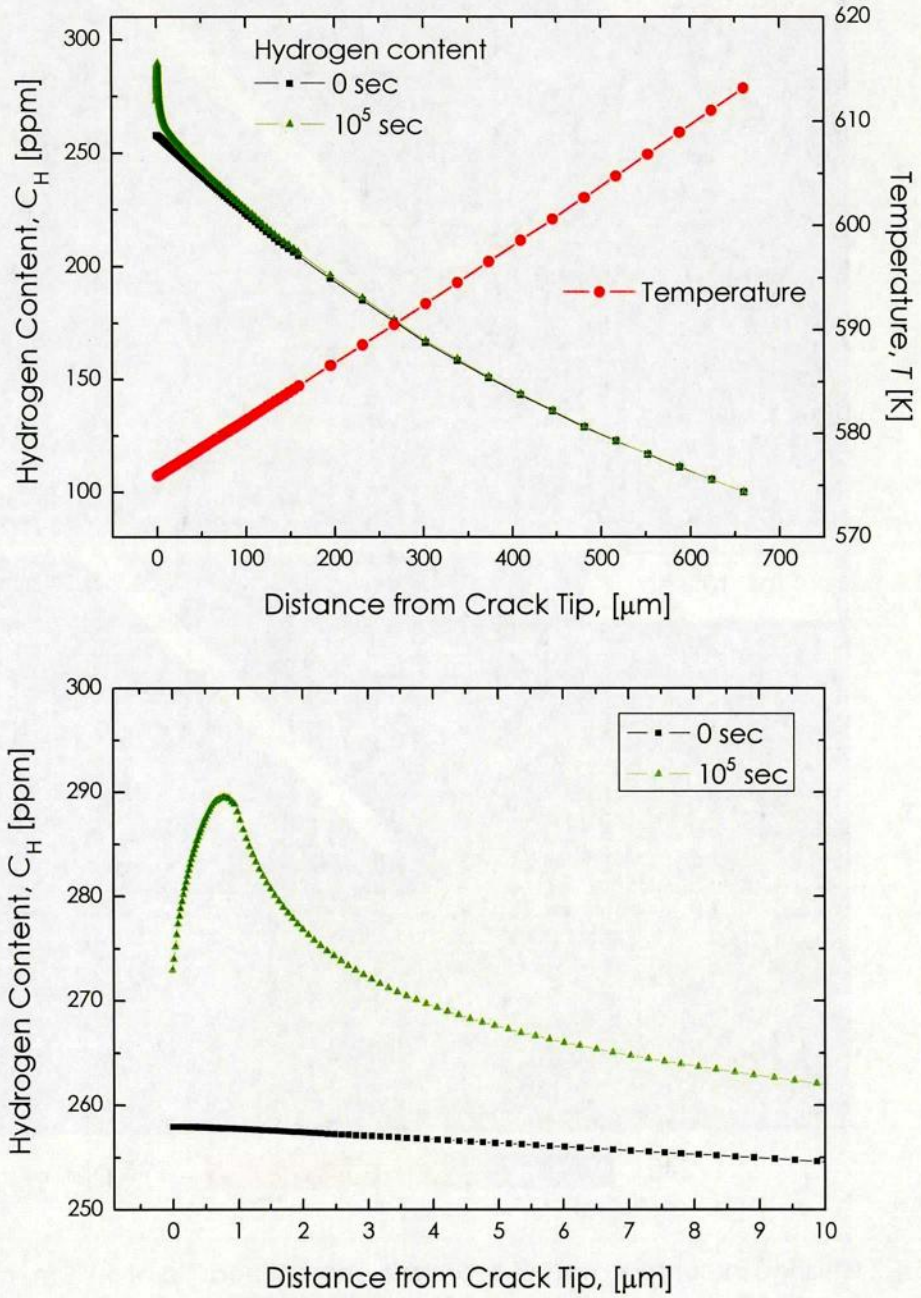


Fig. 5.16. Radial directional distributions of hydrogen content from tips of 50 μm crack with internal pressure of 5 MPa.

This is also confirmed from Fig. 5.16 that shows radial directional distributions of hydrogen content. Similar to the case of the stress distributions, the hydrogen piles up within about 100 μm distance from the crack tip and a maximum point of the hydrogen content is a few micro-meters distantly-positioned from the tip. Comparing Fig. 5.15 (a) and (b), it is also found that hydrogen content at vicinity of crack surface, where is slightly away from the tip, reduces by the internal pressure loading. These trends were corresponds to the stress distribution.

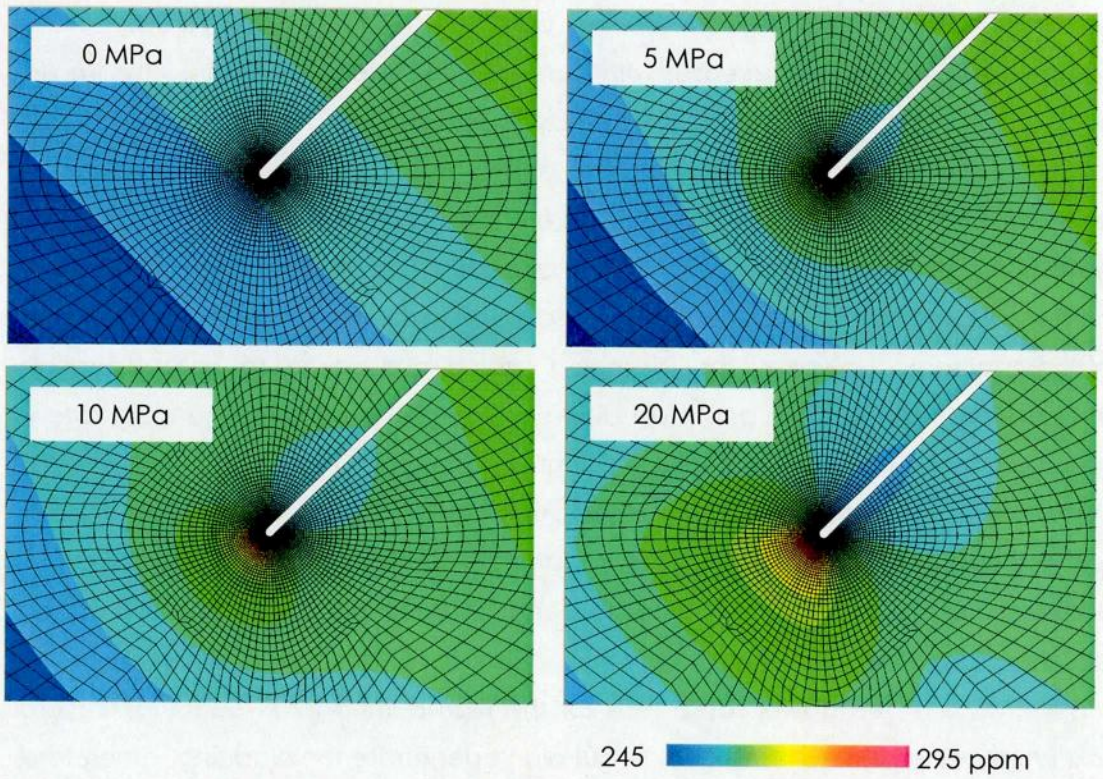


Fig. 5.17. Changes in contour map of hydrogen content near tips of 50 μm crack with different internal pressures at steady state after the internal pressure loading.

Fig. 5.17 shows changes in contour map of hydrogen content near tips of 50 μm crack with different internal pressures at steady state after the internal pressure loading. All the results with internal pressure indicate that hydrogen diffuses into the vicinity of the crack tip and the amount of piled up hydrogen increases with increasing the internal pressure. In the high burnup fuels, the hydrogen content of the cladding exceeds a terminal solid solubility of hydrogen (TSS). In such case, a matrix area which has

significantly-higher hydrogen content than around area can transform into brittle zirconium hydrides. Therefore, the difference from circumjacent hydrogen content is considered to be the most important information for determining whether the hydride precipitates or not. In the present study, a changing rate in the hydrogen content is evaluated on the basis of the hydrogen content distribution of the smoothly-shaped cladding model.

Fig. 5.18 shows the changing rate in radial directional distributions of hydrogen content from crack tips with different internal pressure, in which the crack lengths equal to 50 μm. Although the distribution profile and the maximum point of the hydrogen content are not so changed by the internal pressure, the amount of hydrogen that is piled up near the crack tip increases with increasing the internal pressure. This implies that the PCMI during the power ramp tests may encourage the DHC breakage failure.

Fig. 5.19 shows changes in contour map of hydrogen content near crack tips with different lengths, in which the internal pressure is fixed to 20 MPa. It is found from this figure that the distribution profile of hydrogen apparently changed by the crack length. Since the crack length is different, the change in the hydrogen content can not make easy comparison. However, the changing rate is considered to be substantially compared even in this case as stated above. Fig. 5.20 shows the changing rate in radial directional distributions of hydrogen content from crack tips with different lengths. With increasing the crack length, the more amount of hydrogen piled up around the crack tip and the hydrogen-focusing area significantly spreads. Therefore, it is considered that the crack easily comes to penetration if the length reaches a certain level.

In the case of the power ramp tests for the high burnup PWR claddings, several cracks were generated from the outside but didn't penetrate the cladding. Therefore, the crack number may affect propagation of the DHC. Fig. 5.21 shows radial directional distributions of changing rate in hydrogen content from tips of different numbers of 50 μm crack, in which the internal pressure equals to 20 MPa. There is not significant difference between the results with the different number of cracks, which is correspond to the hydrostatic pressure. The irradiation influence minifies the difference in the thermophysical properties between the Zry-2 and the Zry-4 [25]. In addition, it was reported that average hydrogen contents of the high burnup claddings of the PWR was rather higher than those of the BWR [2]. Therefore, the other factors, such as temperature condition, presence of the liner, and so on, are considered to be important.

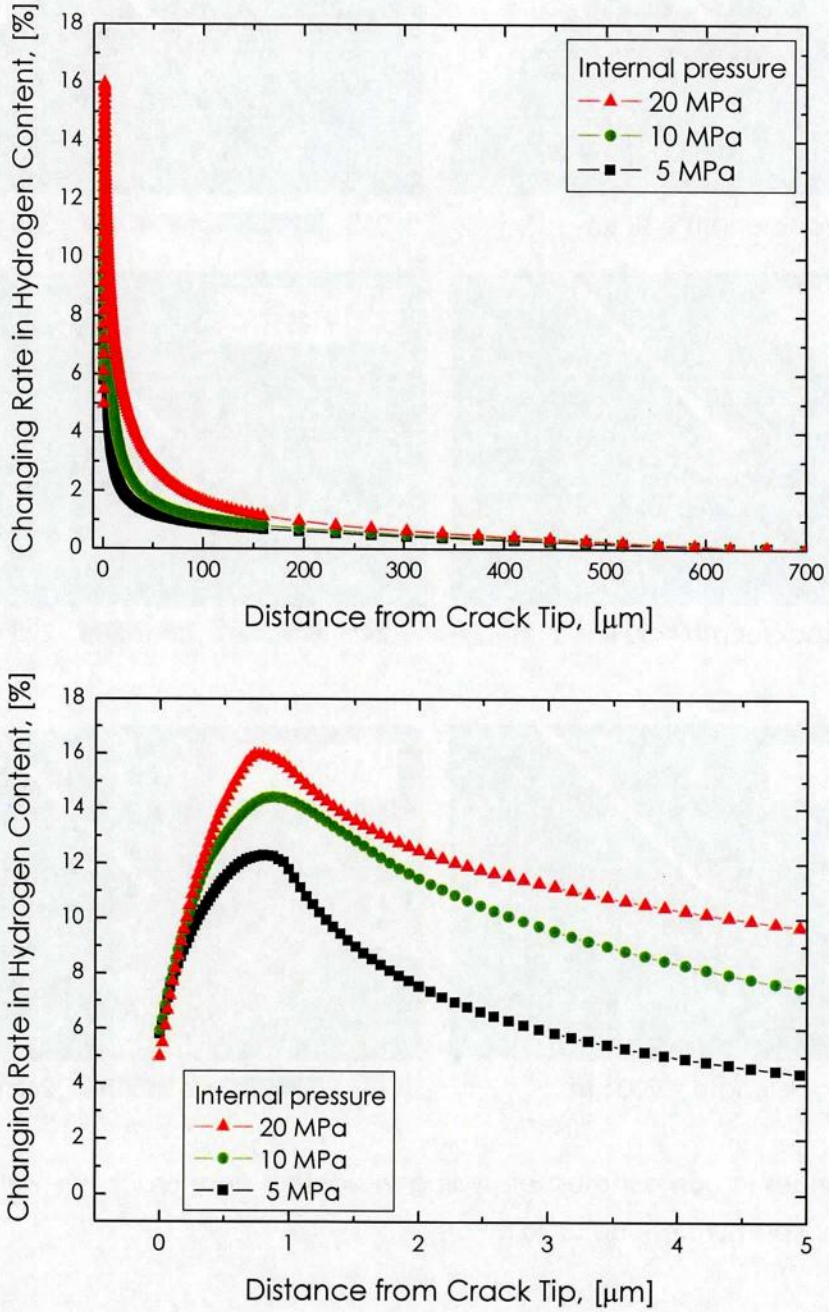


Fig. 5.18. Changing rate in radial directional distributions of hydrogen content from crack tips with different internal pressure (Crack lengths equal to 50 μm).

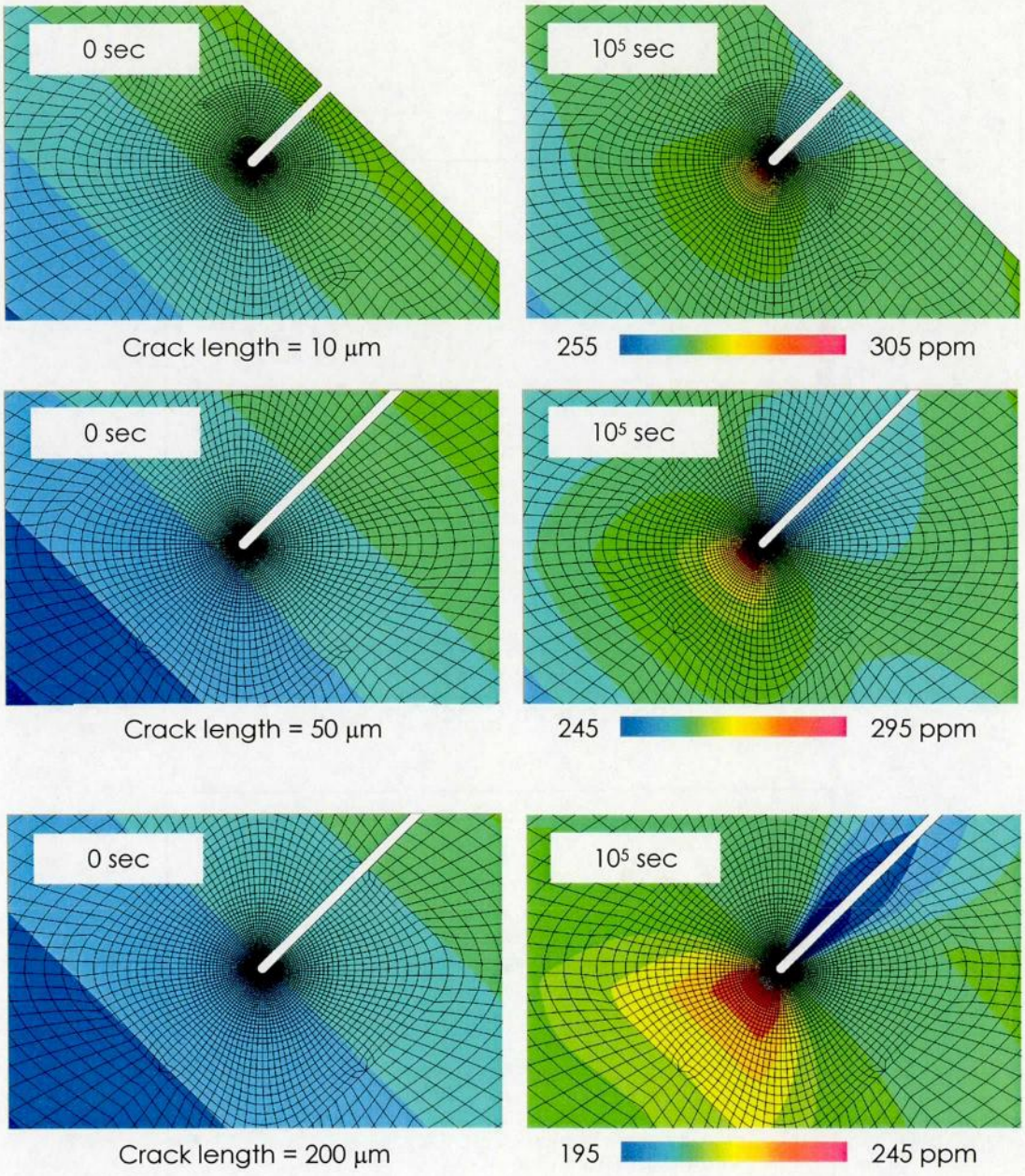


Fig. 5.19. Changes in contour map of hydrogen content near crack tips with different lengths (Internal pressure equals to 20 MPa).

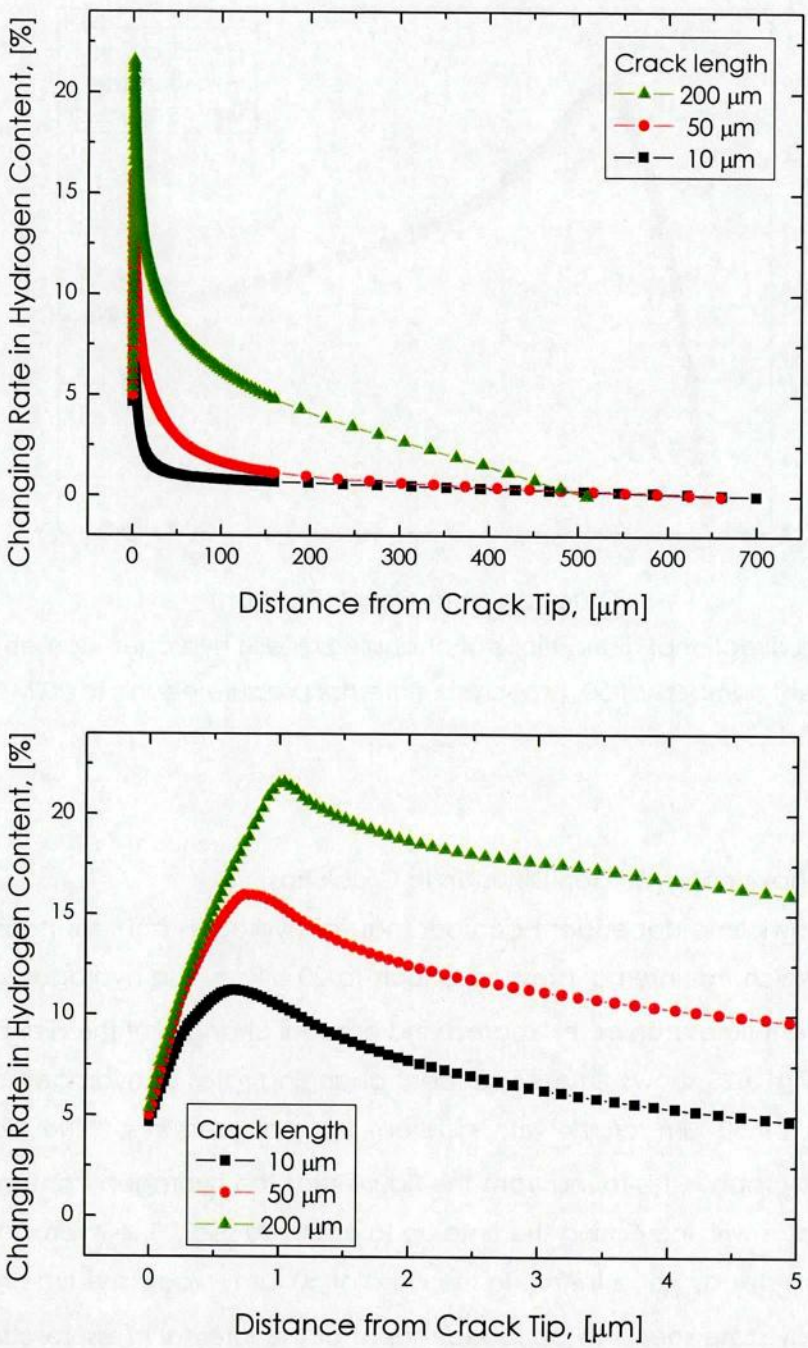


Fig. 5.20. Changing rate in radial directional distributions of hydrogen content from crack tips with different lengths (Internal pressure equals to 20 MPa).

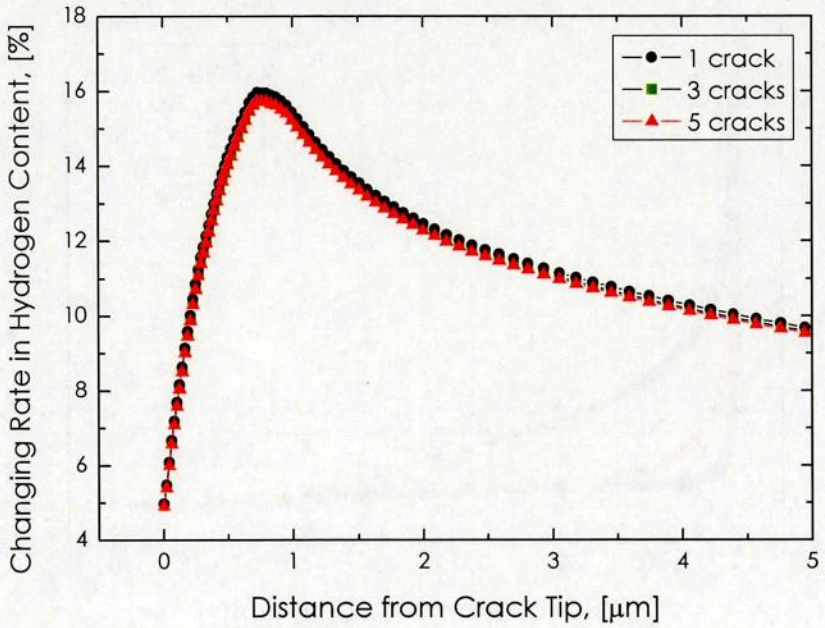


Fig. 5.21. Radial directional distributions of changing rate in hydrogen content from tips of different numbers of 50 μm crack (Internal pressure equals to 20 MPa).

(b) Transient Behavior of Hydrogen Diffusion to Crack Tips

Fig. 5.22 shows time-dependent contour map of hydrogen content near tips of 50 μm crack, in which the internal pressure equals to 20 MPa. The hydrogen distribution profiles at different times can be estimated and gradual changes of the distributions are confirmable. Fig. 5.23 shows time-dependent changing rates of hydrogen content at maxima points of 50 μm crack with different internal pressures. The downside is semilogarithmic graph. It is found from the figure that the hydrogen content near the crack tip increases with increasing the time up to about 20 sec. The hydrogen diffusion becomes almost steady since then. In the case of 50 μm crack, the time required to reach the steady state seems to be independent of the internal pressure although the changing rate increases by the internal pressure. Fig. 5.24 shows time-dependent changing rates of hydrogen content at maxima points with different crack lengths, in which the internal pressure is fixed to 20 MPa. In the case of 10 μm crack, the hydrogen diffusion almost reach steady state in 1 sec. In the case of 50 μm crack, the hydrogen content near the crack tip increases with increasing the time up to about 20

sec. In the case of 200 μm crack, it takes a few ten thousands sec to reach the steady state. As just described, it takes more time to converge the hydrogen content change, the crack becomes longer. The hydrostatic pressure gradient covers a wider range of the cladding in the case of the longer crack (see section 5-3-1), hence it takes longer time. However, it should be noted that hydrogen increasing rate per unit time increases with growing the crack length, and the changing rate from the initial state reaches over 10 % for a given short time. The present study successfully provided tangible information on hydrogen behavior during the power ramp test and the effects of the several conditions were revealed. There is marked variability in the literature data of hydrogen diffusion coefficient. In addition, the diffusion coefficient and solubility of hydrogen would change due to the external stress. Therefore, the sensitivity analysis will be important in the next step for the investigation.

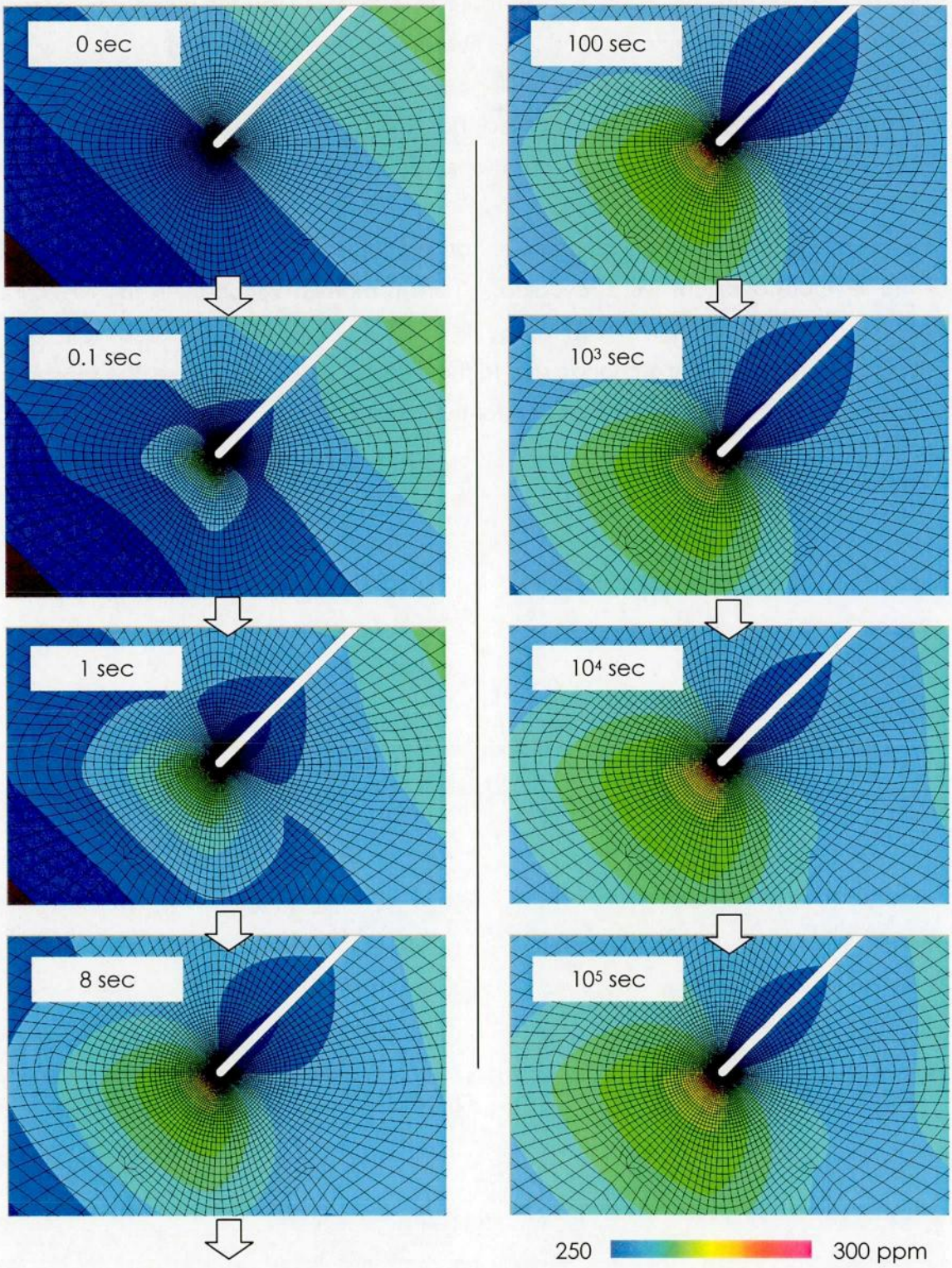


Fig. 5.22. Time-dependent contour map of hydrogen content near tip of 50 μm crack (Internal pressure equals to 20 MPa).

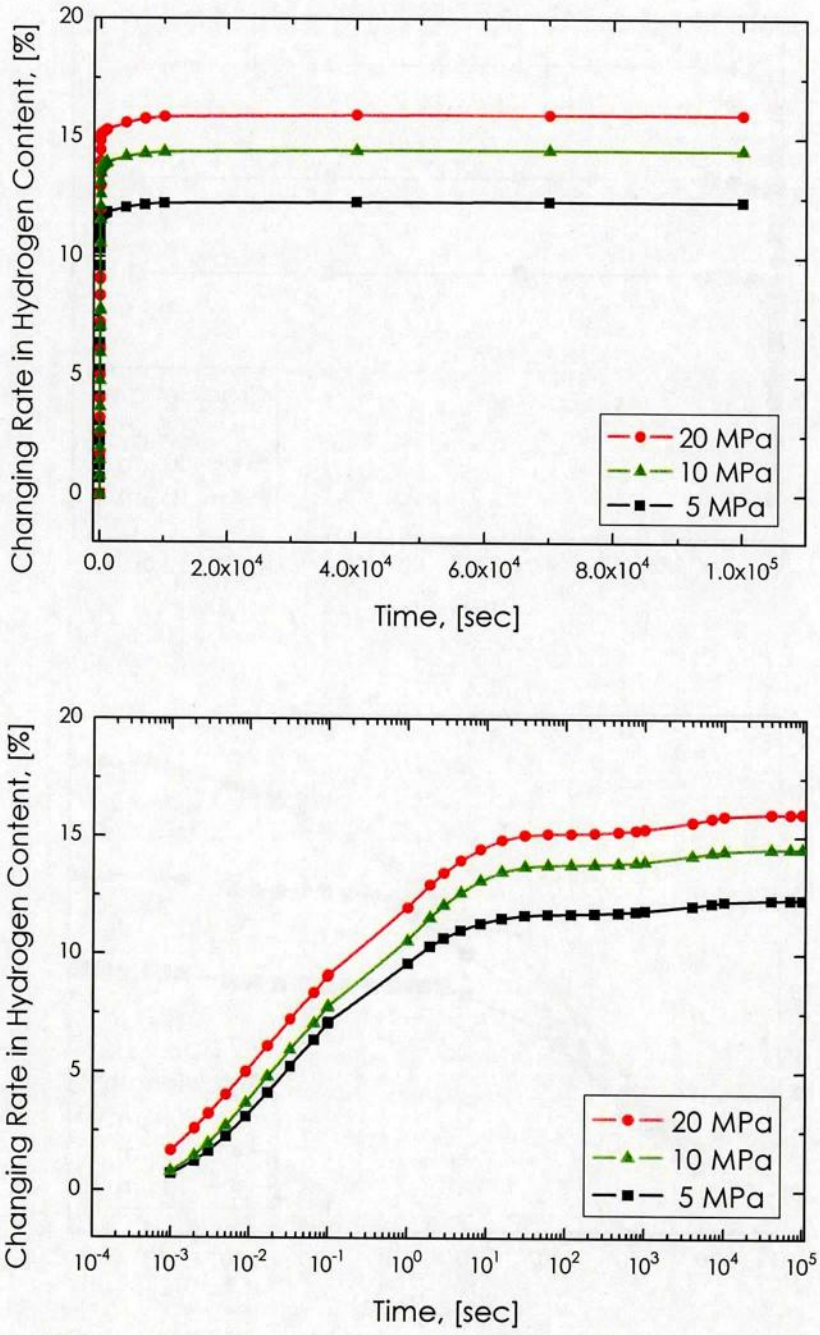


Fig. 5.23. Time-dependent changing rates of hydrogen content at maxima points of 50 μm crack with different internal pressures.

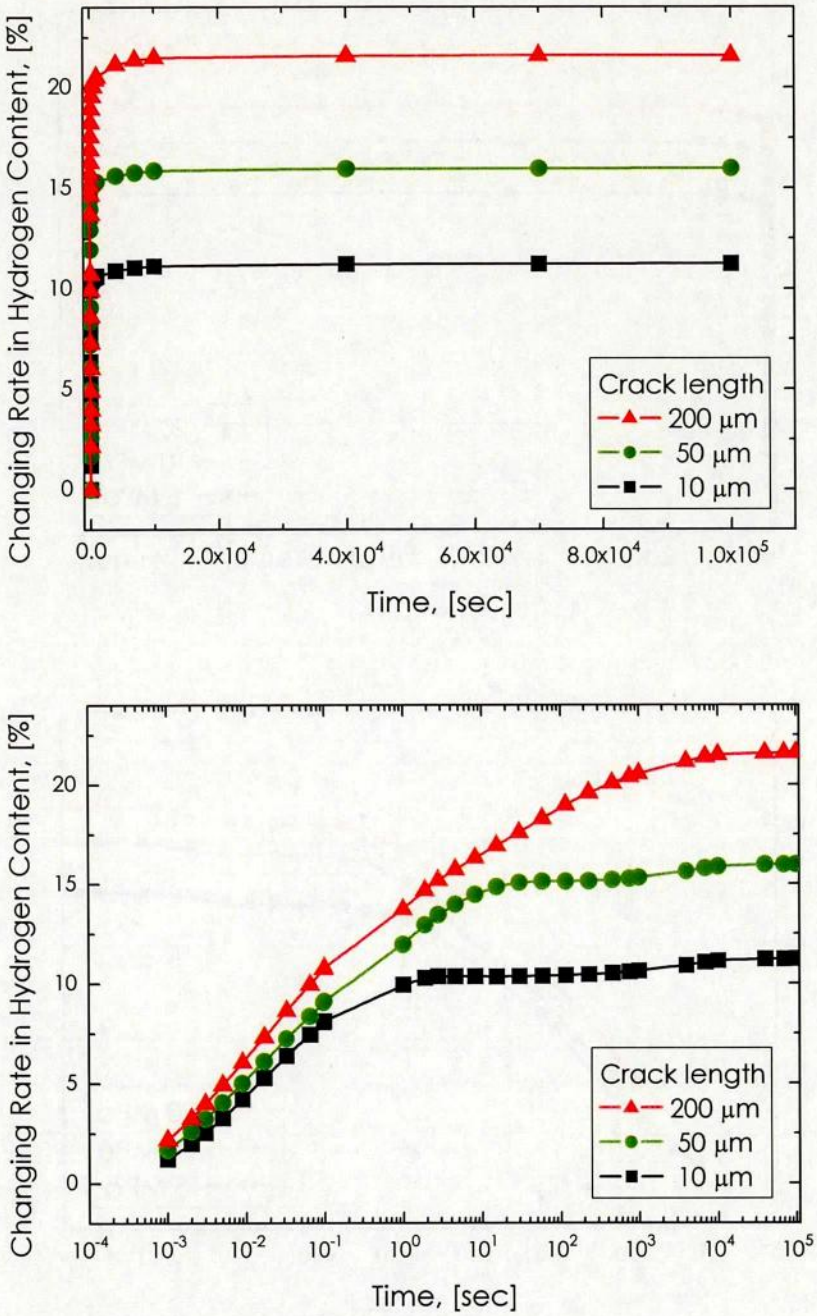


Fig. 5.24. Time-dependent changing rates of hydrogen content at maxima points with different crack lengths (Internal pressure equals to 20 MPa).

5-4. Summary

The thermal-displacement coupled analysis was performed for models of the BWR cladding using the finite element method. The negative hydrostatic pressure spread in a circular pattern around the crack tip. The absolute value of the hydrostatic pressure near the crack tip was quite higher than that in the smoothly shaped cladding, which would be responsible for the hydrogen pile up around the crack tip of the cladding. The hydrostatic pressure increased with increasing the internal pressure. The hydrostatic pressure and the stress-focusing area around crack tip increased with increasing the crack length. The crack number didn't affect the stress distribution near the crack tip.

With use of these results, the transient hydrogen diffusion analysis, including the three effects of hydrogen concentration, temperature, and stress, was performed. The effects of several parameters, such as internal pressure, crack number, and its depth, were evaluated. The hydrogen distribution after the internal pressure loading was noticeably different from the initial state and a large amount of hydrogen piles up near the crack tip. The hydrogen diffused into the vicinity of the crack tip and the amount of piled up hydrogen increased with increasing the internal pressure. With increasing the crack length, the more amount of hydrogen piled up around the crack tip and the hydrogen-focusing area significantly spread. The crack number didn't affect the hydrogen behavior near the crack tip. All the results were corresponding to the distribution of the hydrostatic pressure because the contribution of the stress gradient to hydrogen diffusion near the crack tip was larger than the other contributions. It was found that hydrogen increasing rate per unit time increased with growing the crack length and increasing the internal pressure. It was also found that the changing rate from the initial state reached over 10 % for a given short time from the several seconds to several thousands of seconds. For future work on crack propagation prediction due to the DHC, it was considered to be important that the time for hydrogen to pile-up near the crack tip could be objectified.

References

[1] S. Shimada, E. Etoh, H. Hayashi, Y. Tukuta, Journal of Nuclear Materials, 327 (2004) 97-113.

[2] M. Yamawaki, K. Konashi, S. Shimada, Journal of the Atomic Energy Society of Japan,

46 (2004) 457.

[3] C.E. Coleman, S. Sagat, G.K. Shek, D.B. Graham, M.A. Durand, International Journal of Pressure Vessels and Piping, 43 (1990) 187-204.

[4] S.Q. Shi, G. K. Shek and M. P. Puls, Journal of Nuclear Materials, 218 (1995) 189-201.

[5] Y.S. Kim, S.B. Ahn, Y.M. Cheong, Journal of Alloys and Compounds, 429 (2007) 221-226.

[6] R.N. Singh, S. Roychowdhury, V.P. Sinha, T.K. Sinha, P.K. De, S. Banerjee, Materials Science and Engineering A, 374 (2004) 342-350.

[7] B. Cox, Journal of Nuclear Materials, 172 (1990) 249.

[8] T. Fuketa, H. Sasajima and T. Sugiyama, Nuclear Technology, 133 (2001), p. 50.

[9] T. Nakamura, K. Kusagaya, T. Fuketa, H. Uetsuka, Nuclear Technology, 138 (2002), p. 246.

[10] K. Ito, M. Sogame, M. Ichikawa, T. Nakajima, T. Okubo, H. Saito, Res Mechanica, 2 (1981) 109–121.

[11] J.S. Cheon, B.H. Lee, Y.H. Koo, J.Y. Oh, D.S. Sohn, Nuclear Engineering and Design, 231 (2004) 39-50.

[12] M. Someno, Nihon Kinzoku Gakkaishi, 24 (1960) 249-253.

[13] A. Sawatzky, Journal of Nuclear Materials, 2 (1960) 62-68.

[14] M.W. Mallet, W.M. Albrecht, Journal of the Electrochemical Society, 104 (1957) 142.

[15] C.R. Cupp, P. Flubacher, Journal of Nuclear Materials, 6 (1962) 213-228.

[16] M. Mazzolai, J. Ryll-Nardzewski, Journal of the Less Common Metals, 49 (1976) 323-327.

[17] J.J. Kearns, Journal of Nuclear Materials, 43 (1972) 330-338.

[18] A. Sawatzky, Journal of Nuclear Materials, 2 (1960) 321.

[19] J.M. Markowitz, Transactions of the Metallurgical Society of AIME, 221 (1961) 819.

[20] B.F. Kammenzind, B.M. Berquist, R. Bajaj, P.H. Kreyns, D.G. Franklin, Zirconium in the Nuclear Industry, ASTM STP 1354 (2000) 113-127.

[21] A.G. Varias, A.R. Massih, Journal of Nuclear Materials, 279 (2000) 273-285.

[22] A.G. Varias, A.R. Massih, Journal of the Mechanics and Physics of Solids, 50 (2002) 1469-1510.

[23] S.Q. Shi, Journal of Nuclear Materials, 275 (1999) 318-323.

[24] J. Lufrano, P. Sofronis, H.K. Birnbaun, Journal of the Mechanics and Physics of Solids, 44 (1996) 179.

[25] SCDAP/RELAP5/MOD3.1 Code 4. MATPRO, INEL Report NUREG/CR-6150 EGG-2720, Idaho Falls, (1993).

[26] S. Yamanaka, M. Miyake, M. Katsura, Journal of Nuclear Materials, 247 (1997) 315.

[27] T.L. Anderson, Fracture Mechanics (2nd Edition), CRC Press LLC, (2000).

[28] Y. Fukai, The Metal-Hydrogen System: Basic Bulk Properties, Springer Series in Materials Science 21 (1993).

CHAPTER 6

Concluding Remarks

Chapter 6

Concluding Remarks

In the present dissertation, the properties of metal hydrides and hydrogen behavior in the fuel cladding were studied in order to contribute to the advancement of the nuclear power plant systems.

In Chapter 2, the basic bulk properties of the metal-hydrogen systems, i.e. the mechanical properties of metal hydrogen solid solutions and the thermophysical properties of metal hydrides, were evaluated.

The mechanical properties of single phase hydrogen solid solutions of the yttrium and niobium were measured. The elastic moduli of the hydrogen solid solutions increased with increasing hydrogen content. The Vickers hardness of the hydrogen solid solutions also increased with increasing hydrogen content. Therefore, it was considered that the yttrium and niobium were elastically and plastically hardened by the effect of hydrogen dissolution. This trend differed from the titanium and zirconium hydrogen solid solutions, whose elastic moduli and hardness reduced by hydrogen addition. The interstitial hydrogen effect appeared to be independent of crystal structures.

The author succeeded in the production of bulk metal hydrides of yttrium, hafnium, niobium, and Zr-Gd alloy, without cracks and voids. The yttrium and niobium hydrides had higher elastic moduli and Vickers hardness than the respective pure metals, whereas the mechanical properties of the hafnium hydride were lower than those of the pure hafnium. Additionally, the mechanical properties of the yttrium and niobium hydrides increased with increasing hydrogen content, on the contrary those of the hafnium hydride decreased with increasing hydrogen content. The thermal conductivity of yttrium hydride was significantly higher than that of pure yttrium although the hydrides of hafnium and niobium had almost same or less thermal conductivities than the respective pure metals. The thermal conductivity of hydride of Zr-Gd alloy, which was polyphasic material, was higher than that of the zirconium hydride. Investigation on the gadolinium hydride was considered to be important. It was found from the preset study and the literatures that although yttrium, titanium, zirconium, and hafnium were adjacent in the periodic table and their hydrides exhibited the same crystal structures, they possessed polymorphic physical properties. It was considered that these results were mutually comparable and they revealed the characteristic nature of metal hydrides since their crystal structure was same. The several important correlations between the basic bulk properties of metal hydrides were

found from the present and previous studies.

In Chapter 3, ab initio electronic structure calculations were performed by using CASTEP code and DV- Xα method. The themophysical properties of the metal hydrogen solid solutions and hydrides were discussed from the calculation results. The elastic moduli of the yttrium hydrogen solid solution could be evaluated from the ab initio study and the calculated results were good accordance with the experimental results obtained from Chapter 2. From the analysis of the bond order in unit-cell, it was considered that the change of mechanical properties due to hydrogen was correlated to the original covalency of the metals. The calculated bond order of the metal hydrides also qualitatively explained the trends of the hydrogen content dependence of the mechanical properties of the hydrides. The elastic moduli from the total energy calculation were well accordance with experimental data obtained from Chapter 2 and literatures. The temperature dependence of liner thermal expansion coefficient was evaluated and the results provided better understanding of the properties. It was considered that the hydrogen optical vibration had a certain role in the thermal expansion behavior of the metal hydrides.

In Chapter 4, the terminal solid solubility of hydrogen (TSS) for pure Zr, Zr-Nb binary alloys with different niobium concentrations, and Nb added Zircaloy-4 was measured, and the effect of niobium addition was determined in order to supply fundamental data for the integrity of new-type fuel cladding. It was found that the TSS of αZr was not affected by the solute niobium and that the β Zr precipitant led to increase the TSS in the Zr-Nb alloys. The change in TSS by niobium addition was slightly larger than that by the traditional additive elements. The TSS of Nb added Zircaloy-4 was found to be higher than that of Zircaloy-2 and -4 due to the further effect of β Zr precipitation on top of the traditional additive element effects. Therefore, it was concluded that niobium addition to the zirconium alloys could play an important role in terms of the TSS for increasing the life-time of cladding. The mechanical properties of hydrogenated Zr-Nb binary alloys with different phases were evaluated in order to discuss the effect of hydrogen absorption. The solute hydrogen didn't affect the mechanical properties of the single phase β Zr-20Nb alloy. In the Zr-1.0Nb and Zr-2.5Nb alloys, the solute hydrogen reduced the Young's modulus of the alloys, which was considered to be due to the change in the modulus of αZr matrix phase. These results could be nicely accounted from the knowledge discussed in the Chapter 2 and 3.

In Chapter 5, the thermal-displacement coupled analysis was performed for models of the BWR cladding using the finite element method. The negative hydrostatic

pressure spread in a circular pattern around the crack tip. The absolute value of the hydrostatic pressure near the crack tip was quite higher than that in the smoothly shaped cladding, which would be responsible for the hydrogen pile up around the crack tip of the cladding. The hydrostatic pressure increased with increasing the internal pressure. The hydrostatic pressure and the stress-focusing area around crack tip increased with increasing the crack length. The crack number didn't affect the stress distribution near the crack tip. With use of these results, the transient hydrogen diffusion analysis, including the three effects of hydrogen concentration, temperature, and stress, was performed. The effects of several parameters, such as internal pressure, crack number, and its depth, were evaluated. The hydrogen distribution after the internal pressure loading was noticeably different from the initial state and a large amount of hydrogen piles up near the crack tip. The hydrogen diffused into the vicinity of the crack tip and the amount of piled up hydrogen increased with increasing the internal pressure. With increasing the crack length, the more amount of hydrogen piled up around the crack tip and the hydrogen-focusing area significantly spread. The crack number didn't affect the hydrogen behavior near the crack tip. All the results were corresponding to the distribution of the hydrostatic pressure because the contribution of the stress gradient to hydrogen diffusion near the crack tip was larger than the other contributions. It was found that hydrogen increasing rate per unit time increased with growing the crack length and increasing the internal pressure. It was also found that the changing rate from the initial state reached over 10 % for a given short time from the several seconds to several thousands of seconds. For future work on crack propagation prediction due to the DHC, it wais considered to be important that the time for hydrogen to pile-up near the crack tip could be objectified.

In conclusion, the fundamental and practical information on the metal-hydrogen systems was obtained with unprecedented detail, which is desperately-required in the nuclear field. Several trends proposed in the present study is considerable to be applied to the material science and engineering.

Acknowledgement

The author couldn't have carried out the present study without tremendous help from many people. I would like to graceful thanks to Prof. Dr. Shinsuke Yamanaka for his heartfelt encouragement and valuable advice. I was fortunate to join Yamanaka laboratory and study the thermodynamics and solid state physics in the research process. Prof. Dr. Toshikazu Takeda and Prof. Dr. Akira Yamaguchi in Division of Sustainable energy and Environmental Engineering, Graduate School of Engineering, Osaka University, were appreciated very much for their important and kind advices for the present study. Prof. Dr. Takao Yamamoto in Management of Industry and Technology, Graduate School of Engineering, Osaka University is greatly appreciated for his valuable and important advices for the present study. I also wish to express appreciation to Assoc. Prof. Dr. Masayoshi Uno for his helpful suggestions and discussion in many aspects such as interpretation of data.

I would like to thank Assist. Prof. Dr. Ken Kurosaki and Dr. Muta Hiroaki for their precious guidance for the study. I'm indeed humble and grateful to Dr. Daigo Setoyama and Mr. Junji Matsunaga for their great help and support in technical matters, informative suggestion and discussion. The author could carry out the present study with their steady instructions and tender encouragements. Dr. Bun Tsuchiya in Tohoku University is greatly appreciated for his guidance and advice with regard to the investigation of metal hydride. Dr. Shijo Nagao in Helsinki University of Technology is specially acknowledged for his valuable guidance for ab initio electronic structure calculations. I would like to thank Mr. Kazuhira Ko and Mr. Shunichiro Nishioka, who have helped to perform this work on the light water reactor fuel cladding. I wish to thank Mr. Yuki Kitano, who has helped to perform this work on the metal hydride. The author wishes to make an address of thanks to Mr. Hiroyuki Nagai for belonging to the same research group in a short period. I want to express my great appreciation for Ms. Kazuko Terasoma's kind supports for administrative matter. I would like to extend my appreciation to all of the members of Yamanaka laboratory. Finally, I appreciate my family's concern for my growth and making me the person I am today.

November, 2007 Masato Ito

Research Activities

List of Publications

1. "Mechanical Properties of Yttrium Hydrogen Solid Solution," Masato Ito, Daigo Setoyama, Junji Matsunaga, Hiroaki Muta, Masayoshi Uno, Shinsuke Yamanaka, Journal of Alloys and Compounds, 394, 1-2 (2005), 58-62.
2. "Mechanical Properties of Yttrium Hydride," Daigo Setoyama, Masato Ito, Junji Matsunaga, Hiroaki Muta, Masayoshi Uno, Shinsuke Yamanaka, Journal of Alloys and Compounds, 394, 1-2 (2005) 207-210.
3. "Thermal Properties of Titanium Hydrides," Daigo Setoyama, Junji Matsunaga, Masato Ito, Hiroaki Muta, Ken Kurosaki, Masayoshi Uno, Shinsuke Yamanaka, Journal of Nuclear Materials, 344, 1-3, (2005) 298-300.
4. "Thermal Properties of Yttrium Hydride," Masato Ito, Junji Matsunaga, Daigo Setoyama, Hiroaki Muta, Ken Kurosaki, Masayoshi Uno, Shinsuke Yamanaka, Journal of Nuclear Materials, 344, 1-3, (2005) 295-297.
5. "Influence of Additive Elements on the Terminal Solid Solubility of Hydrogen for Zirconium Alloy," Daigo Setoyama, Junji Matsunaga, Masato Ito, Hiroaki Muta, Ken Kurosaki, Masayoshi Uno, Shinsuke Yamanaka, Journal of Nuclear Materials, 344, 1-3, (2005) 291-294.
6. "Thermodynamic Modeling of the Uranium-Zirconium-Iron-Oxygen System," Masato Ito, Ken Kurosaki, Masayoshi Uno, Shinsuke Yamanaka, Proceedings in Actinides 2005, The Royal Society of Chemistry, Cambridge, UK (2006), 412-415.
7. "Electrical and Thermal Properties of Titanium Hydrides," Masato Ito, Daigo Setoyama, Junji Matsunaga, Hiroaki Muta, Ken Kurosaki, Masayoshi Uno, Shinsuke Yamanaka, Journal of Alloys and Compounds, 420,1-2 (2006) 25-28.
8. "Characteristics of Niobium Hydrogen Solid Solution," Masato Ito, Hiroaki Muta, Masayoshi Uno, Shinsuke Yamanaka, Journal of Alloys and Compounds, 425, 1-2 (2006) 164-168.
9. "Effect of Electronegativity on the Mechanical Properties of Metal Hydrides with a Fluorite Structure," Masato Ito, Daigo Setoyama, Junji Matsunaga, Hiroaki Muta, Ken Kurosaki, Masayoshi Uno, Shinsuke Yamanaka, Journal of Alloys and Compounds, 426, 1-2 (2006) 67-71.
10. "Effect of Nb Addition on the Terminal Solid Solubility of Hydrogen for Zr and Zircaloy-4," Masato Ito, Kazuhira Ko, Hiroaki Muta, Masayoshi Uno, Shinsuke Yamanaka, Journal of Alloys and Compounds, 446-447 (2007) 451-454.

11. "Nanoindentation Studies of High-Temperature Oxidized Zircaloy-4 with and without Hydrogen," Masato Ito, Hiroaki Muta, Daigo Setoyama, Masayoshi Uno, Shinsuke Yamanaka, Journal of Alloys and Compounds, 446-447 (2007) 639-642.
12. "Indentation Study of Titanium, Zirconium, and Hafnium Hydrides," Masato Ito, Shunichiro Nishioka, Hiroaki Muta, Ken Kurosaki, Masayoshi Uno, Shinsuke Yamanaka, Proceedings of Material Research Society 2007 Fall Meeting, accepted.
13. "Effect of Hydrogen Absorption on the Mechanical Properties of Zr-Nb Alloys," Shunichiro Nishioka, Masato Ito, Hiroaki Muta, Masayoshi Uno, Shinsuke Yamanaka, Proceedings of Material Research Society 2007 Fall Meeting, accepted.
14. "Experimental and Theoretical Study on Thermophysical Properties of Hafnium Hydride," Masato Ito, Yuki Kitano, Ken Kurosaki, Masayoshi Uno, Shinsuke Yamanaka, Journal of Nuclear Materials, to be submitted.
15. "Experimental and Theoretical Study on Mechanical Properties of Niobium Hydride," Masato Ito, Hiroaki Muta, Masayoshi Uno, Shinsuke Yamanaka, Journal of Physics: Condensed Matter, to be submitted.
16. "Thermal and Electrical Properties of Niobium Hydride," Masato Ito, Hiroaki Muta, Masayoshi Uno, Shinsuke Yamanaka, Journal of Alloys and Compounds, to be submitted.

List of Presentations

International Conference and Symposium

1. "Thermal Properties of Yttrium Hydrogen Solid Solutions and Yttrium Hydrides," Masato Ito, Junji Matsunaga, Daigo Setoyama, Hiroaki Muta, Ken Kurosaki, Masayoshi Uno, Shinsuke Yamanaka, 11th Symposium on Thermodynamics of Nuclear Materials (STNM 11), SC27, Karlsruhe, September 6-9, 2004.
2. "Thermodynamic Modeling of the Uranium-Zirconium-Iron-Oxygen System," Masato Ito, Ken Kurosaki, Masayoshi Uno, Shinsuke Yamanaka, Actinide-2005, 4P19, Manchester, July 4-8, 2005.
3. "Effect of Nb Addition on the Terminal Solid Solubility of Hydrogen for Zr and Zircaloy-4," Masato Ito, Kazuhira Ko, Hiroaki Muta, Masayoshi Uno, Shinsuke Yamanaka, International Symposium on Metal-Hydrogen Systems (MH2006), O-101, Lahaina, Maui, October 1-6, 2006.
4. "Ab initio Electronic Structure Calculation of Metal Hydride –Nano Scale Analysis on

Hydrogen Behavior," Masato Ito, Hiroaki Muta, Ken Kurosaki, Masayoshi Uno, Shinsuke Yamanaka, 4th 21st COE International Symposium, Toba, November 18-19, 2005.

5. "Evaluation of Hydrogen Behavior in Stressed Nuclear Fuel Cladding using Ab initio Calculation," Masato Ito, Hiroaki Muta, Masayoshi Uno, Shinsuke Yamanaka, 5th 21st COE International Symposium, Awaji, December 8-9, 2006.
6. "Nanoindentation Studies of Ti, Zr, and Hf Hydrides," Masato Ito, Shunichiro Nishioka, Hiroaki Muta, Ken Kurosaki, Masayoshi Uno, Shinsuke Yamanaka, Material Research Society 2007 Fall Meeting, Boston, November 26-30, 2007.

Domestic Meeting

1. "イットリウム水素固溶体の基礎物性," 伊東 正登, 松永純治, 瀬戸山 大吾, 牟田浩明, 黒崎 健, 宇埜正美, 山中伸介, 日本金属学会 2004 年春期大会 No. 284, 東京工業大学, 03/29-04/01.
2. "イットリウム水素化物の基礎物性（1）," 伊東 正登, 松永純治, 瀬戸山 大吾, 山中伸介, 日本金属学会 2004 年秋季大会 P016-1, 秋田大学, 09/28-30.
3. "ニオブ水素固溶体の基礎物性," 伊東 正登, 松永純治, 瀬戸山 大吾, 山中伸介, 日本金属学会 2005 年春期大会 No. 65, 横浜国立大学, 03/29-31.
4. "Zr, Ti および Y 水素化物の物性 ー機械的性質ー," 伊東 正登, 瀬戸山 大吾, 松永 純治, 宇埜 正美, 山中 伸介, 日本原子力学会 2005 年秋の大会 IV 401, 八戸工業大学, 09/13-15.
5. "βNb 水素化物の機械的性質," 伊東 正登, 牟田 浩明, 黒崎 健, 宇埜 正美, 山中 伸介, 日本金属学会 2005 年秋期大会 No. 205, 広島大学, 09/28-30.
6. "Nb-H 系の熱的・電気的特性," 伊東 正登, 牟田 浩明, 黒崎 健, 宇埜 正美, 山中 伸介, 日本金属学会 2005 年秋期大会 P030-1, 広島大学, 09/28-30.
7. "Ti 及び Nb 水素化物のナノ領域における機械的性質," 伊東 正登, 永井 宏之, 牟田 浩明, 黒崎 健, 宇埜 正美, 山中 伸介, 日本金属学会 2006 年春期大会 No. 173, 早稲田大学, 03/21-23.
8. "Zr 合金の水素固溶限におよぼす Nb 添加の影響," 伊東 正登, 瀬戸山 大吾, 松永 純治, 宇埜 正美, 山中 伸介, 日本原子力学会 2006 年秋の大会 I43, 北海道大学 09/27-29.
9. "第一原理計算による金属水素化物の物性評価," 伊東 正登, 顧 和平, 牟田 浩明, 黒崎 健, 宇埜 正美, 山中 伸介, 日本原子力学会 2007 年春の年会 L38, 名古屋大学 03/27-29.
10. "ナノインデンテーションによる Ti, Zr, Hf 水素化物の機械的性質評価," 伊東 正登, 西岡 俊一郎, 牟田 浩明, 黒崎 健, 宇埜 正美, 山中 伸介, 日本金属学会 2007 年岐阜大会 No. 513, 早稲田大学, 03/21-23.

11. "高燃焼度燃料安全裕度確認試験総合評価 -(8)被覆管の水素化物によるき裂進展挙動解析-," 伊東 正登, 牟田 浩明, 黒崎 健, 宇埜 正美, 山中 伸介, 緒方 恵造, 日本原子力学会 2007 年秋の大会 G36, 北九州国際会議場他, 09/27-29.

Award

1. 2006 年度日本原子力学会関西支部学生賞, 金属水素化物の物性ならびに燃料被覆管中における水素挙動に関する研究, 伊東 正登.

Research Grants

1. 平成 17 年度 産研・原子力専攻 21 世紀 COE 若手研究(B)
   タイトル：金属水素化物中における水素挙動のナノレベル解析並びに電子状態評価
   助成金額：48 万円
2. 平成 18 年度 産研・原子力専攻 21 世紀 COE 若手研究(B)
   タイトル：第一原理電子状態計算および EBSP 法による応力負荷燃料被覆管中の水素化物析出挙動解析
   助成金額：50 万円
3. 平成 19 年度科学研究費補助金（特別研究員奨励費）
   タイトル：応力下水素拡散係数測定ならびに破壊挙動解析による高燃焼度燃料被覆管の寿命評価
   助成金額：90 万円